The Dissertation Committee for Bharadwaj Narayanan
certifies that this is the approved version of the following dissertation:

Dynamical Phenomena In Multicomponent Polymers

Committee:

Venkat Ganesan, Supervisor

Roger T. Bonnecaze

Isaac C. Sanchez

Peter J. Rossky

Peter F. Green

Dynamical Phenomena In Multicomponent Polymers

by

Bharadwaj Narayanan, B.S.

DISSERTATION

Presented to the Faculty of the Graduate School of

The University of Texas at Austin

in Partial Fulfillment

of the Requirements

for the Degree of

DOCTOR OF PHILOSOPHY

THE UNIVERSITY OF TEXAS AT AUSTIN

December 2006

Dedicated to my parents Thiruvengadasami and Aruna Narayanan, and my grandparents Sripathy and Indira Iyengar.

Acknowledgments

I would like to thank all the people that helped me get to this point. My journey to and through graduate school would certainly not have been possible without the encouragement and innumerous sacrifices of my family, especially my parents and my brother. My parents taught me the value of knowledge and instilled in me, the desire to learn.

My teachers from primary through secondary education and my professors at the Indian Institute of Technology (Madras), have contributed greatly to help me reach every milestone. They gave me the confidence and motivation to keep aiming high.

My journey through graduate school would certainly not have been possible without the able guidance of Prof. Ganesan. His guidance and support kept me focused on my research during times of trouble. His high expectations, inspired me to achieve higher goals.

I would like to thank all my friends for making it an enjoyable journey. Thanks to Anil, Rhutesh, Kasu, Jada, Anshu, Maha, Megha, Chris, Scott, Shawn, Cecile and the G-Hauser's for being there. They have helped more than they realize.

Lastly, I express my appreciation to members of our research group. I would especially like to thank Dr. Victor Pryamitsyn for his insightful sugges-

tions and guidance at various points throughout my research.

Dynamical Phenomena In Multicomponent Polymers

Publication No. _____

Bharadwaj Narayanan, Ph.D.
The University of Texas at Austin, 2006

Supervisor: Venkat Ganesan

This research concerns with different aspects of dynamical phenomena in the context of multicomponent polymeric systems. The polymer melts under investigation include polymer blends of varying compositions of two homopolymers (A and B), polymer emulsions of homopolymers blended with block copolymers (AB) and pure block copolymer systems. A novel computation algorithm termed the Self-Consistent Brownian Dynamics (SCBD) was developed and employed to explore the flow effects encountered in the aforementioned polymeric systems. Our contributions in polymer blend systems include, quantification of the slip phenomena at the interface of phase separated symmetric and asymmetric blends. We have also quantified the slip suppression phenomena by the addition of copolymer compatibilizers to the polymer blend interfaces. We have also used the SCBD approach to study the effect of copolymer characteristics on the dynamics of an isolated polymer droplet embedded in a matrix of another polymer. In the case of ternary

polymer blend systems, we have studied the flow-induced phase transitions in the microemulsion phases. We provide molecular viewpoint suggesting that the interplay between polymer chain conformations and their flow deformations can lead to novel flow effects upon the phase, structure and rheological behavior of ternary blend systems. In the case of pure copolymer systems, we have studied the effect of oscillatory shear on the lamellar orientation of phase separated multiblock copolymers.

Table of Contents

Acknowledgments **v**

Abstract **vii**

List of Figures **xiii**

Chapter 1. Introduction and Dissertation Overview **1**

1.1 Motivation 2
1.2 Challenge 8
1.2.1 Existing Polymer Modeling and Theoretical Approaches 9
1.3 Layout of the Thesis 11
1.4 Development of a Hybrid Brownian Dynamics Approach (Chapter 2) 12
1.5 Interfacial Phenomena in Polymer Blends (Chapter 3) 12
1.6 Flow Deformation of Polymer Blend Droplets And The Role of Block Copolymer Compatibilizers (Chapter 4) 13
1.7 Shear Induced Phase Transition in Ternary Polymer Blend Systems (Chapter 5) 13
1.8 Composition Field Dynamics in Ternary Polymer Blends (Chapter 6) 14
1.9 Rheology of Ordered Phases of Multiblock Copolymers (Chapter 7) 14
1.10 Summary 15

Chapter 2. Self Consistent Brownian Dynamics **16**

2.1 Gaussian Thread Model 17
2.2 Self-Consistent Field Theory 19
2.3 Kinetic Theory Models 25
2.4 Coarse-Grained Simulations of Polymers 28
2.4.1 Coarse-Grained Models 28

2.4.2 Brownian Dynamics Simulations for Polymer Dynamics 32
2.4.3 The Rouse Model 33
2.4.4 The FENE Model 36
2.5 Some Recent Developments 37
2.6 The Self Consistent Brownian Dynamics Approach 38
2.6.1 Single Chain Evolution 40
2.6.2 Self Consistent Velocity Field $\mathbf{v}(\mathbf{r})$ Evolution 43
2.6.3 Schematic Representation of SCBD 45
2.7 Numerical Implementation of Brownian Dynamics: Special Cases 47
2.7.1 Brownian Dynamics of FENE chains 47
2.7.2 Oscillatory Shear 49
2.8 Summary 51

Chapter 3. Interfacial Phenomena in Polymer Blends 53
3.1 Introduction 53
3.2 Simulation Details 61
3.3 Equilibrium Results 63
3.4 Slip & Shear Flow in Polymer Blends 66
3.4.1 Results 67
3.5 Effect of Block copolymer Compatibilizers on Slip 81
3.5.1 The Brinkman Model and The Friction Parameters . . . 87
3.5.2 Comparison to the Brinkman Model 87
3.5.3 Drainage Time Computation in The Brinkman Model . 92
3.5.4 Compatibilizer Effects on Drainage Times: Results . . . 96
3.6 Summary 99

Chapter 4. Flow Deformation of Polymer Blend Droplets and The Role of Block Copolymer Compatibilizers 101
4.1 Introduction 101
4.2 Simulation Details 107
4.3 Qualitative Aspects of The Deformation Behavior of Droplets . 111
4.4 Quantitative Aspects of The Deformation Behavior of Droplets 123
4.5 Rheology 134
4.6 Conclusion 143

Chapter 5. Dynamical Phenomena in Ternary Polymer Blends 145
5.1 Introduction 145
5.2 Simulation Algorithm & Details 151
5.3 Equilibrium Microemulsion Structure 153
5.4 Effect of Shear on Structure 156
5.4.1 Effect of Viscoelastic Asymmetry 162
5.4.2 Effect of Copolymer Size 165
5.5 Effect of Morphology on Rheology 167
5.5.1 Effect of Copolymer Size 173
5.5.2 Effect of Viscoelastic Asymmetry 175
5.6 Mechanism for Shear-Induced Phase Transitions 178
5.7 Conclusion 184

Chapter 6. Composition Field Dynamics in Ternary Polymer Blends 186
6.1 Introduction 186
6.2 Derivation of Free Energy Expression 189
6.3 Cell Dynamics 193
6.4 Results for Disordered Phase 196
6.5 Ordered System Results: Cell Dynamics 211
6.6 Summary and Conclusions 226

Chapter 7. Rheology of Ordered Phases of Multiblock Copolymers 229
7.1 Introduction 229
7.1.1 Simulation Details 237
7.2 Oscillatory Shear Rheology of Diblock Copolymer Lamellar: Role of Viscoelastic Asymmetry 239
7.3 Oscillatory Shear Rheology: Multiblock Copolymers 247
7.4 Summary and Conclusions 255

Chapter 8. Summary and Future Directions **257**
8.1 Summary and Conclusions 257
8.2 Recommendations for Future Work 262
8.2.1 Entanglements 263
8.2.2 Transients 264
8.2.3 Parallelization of Algorithm To Enable 3D Simulations . 265
8.2.4 Model Development 267

Bibliography **268**

Vita **282**

List of Figures

1.1 Droplets of polystyrene (PS) in a matrix of polymethylmethacrylate (PMMA) in a mixture of 30/70 (PS/PMMA) by volume. . 3

1.2 Morphologies for linear ABC triblock copolymers obtained by varying the block sequences (ABC,ACB,BAC), composition and molecular weights. 3

1.3 Phase diagram of AB diblock copolymer obtained from (a) Self-consistent mean field theory and (b) Experimental system of poly(isoprese-styrene) diblock copolymers. The x-axis represents the block composition f and the y-axis represents the incompatibility parameter χN. The morphologies obtained are spherical (S), cylindrical (C), gyroid (G), and lamellar (L) phases. 5

1.4 Polypropelene (PP) drops in polystyrene (PS) matrix (with viscosity ratio = 2.4), for strain values of (a)γ=0, (b)γ=2, (c)γ=3, (d)γ=5, (e)γ=9 and (f)γ=13. 6

2.1 The Gaussian thread representation of a polymer chain and its equivalent *bead-spring* representation. 18

2.2 Bridges and loops formed in lamellar phase separated multiblock copolymers. 26

2.3 (a)Slip in the velocity at the interface of two immiscible homopolymers and (b) The linear simple shear velocity profile assumed by kinetic theory models. 26

2.4 Various levels of coarse-graining of a polymer molecule into (a) Atomistic resolution, (b) United atom (CH_2), (c) Bead-rod model, (d) Bead-spring model and (e) Dumbell model. 29

2.5 Coarse-graining of the simulation box into a 2D lattice with the positions and number of polymeric beads inside a *bin* dictating the values of the quantities of interest (like composition and/or stress fields) at each lattice point. 43

2.6 Schematic representation of the dynamical evolution of a polymeric system using self-consistent Brownian dynamics. The four steps shown in the figure, are carried out at each timestep, in the order displayed. 46

3.1 (a) Composition profiles of A and B components plotted as a function of spatial position for a symmetric blend with $\chi N = 7.0$. The points represent the results of our simulations, while the solid lines represent the numerical results of self consistent field theory. (b) Coexistence curves (binodals) for symmetric and asymmetric ($\alpha = 2.0$) blends. The points represent the results of our simulations, while the solid lines represent the numerical results of Flory Huggins theory. 65

3.2 The steady state velocity profiles during shear of a symmetric, segregated polymer blend: (a) $\chi N = 4.5$; (b) $\chi N = 6$; (c) $\chi N = 7.5$. 70

3.3 The velocity gradient plots as a function of the position for $\chi N = 4.5, 6$ and 7.5. Due to the periodicity of the box, the interface is shifted from $y = 0$. 70

3.4 Extrapolation lengths (represented as the ratio $L_e/\sqrt{\chi N}$ as a function of the degree of segregation χN. The points depict the values obtained from our simulation for a symmetric blend and the solid line represents the theoretical prediction of FG [56]. . 72

3.5 (a) Velocity profile (b) Velocity gradients for an asymmetric blend with $\alpha = 2.0$ and $\chi N_A = 7.5$. In (b) the plots have been shifted such that the interface is located at $y = 0$. The noise evident in (b) is due to statistical noise in averaging and the numerical evaluation of gradients. The solid line in (b) is a guide to the eye. 74

3.6 Slip lengths (normalized by R_g of the A chain) plotted as a function of χN_A for different degrees of asymmetries between the blend components: (a) $\alpha = 1.5$; (b) $\alpha = 2.0$; (c) $\alpha = 2.5$, where $\alpha \equiv N_A/N_B$. The points depict the values obtained from our simulation for a symmetric blend and the solid line represents the theoretical prediction of FG [56]. 77

3.7 Interfacial viscosities η_I normalized by the square of their interfacial widths, a_I. 79

3.8 Velocity gradient profiles near the interface in the presence of block copolymeric compatibilizers for different coverages Γ of block copolymers. Γ is expressed as number of chains per R_g^2 of the block copolymer. The average shear rate in the bulk is 0.3 and is indicated as a dashed line in the plot. The profiles have been plotted only in the region close to the interfacial region. 81

3.9 Molecular weight dependence of the minimum coverage of block copolymers needed to suppress slip. The molecular weights of the blend components are kept a constant at 20 beads each. . 84

3.10 Velocity profiles in the presence of the compatibilizer for coverages higher than the minimum coverage required for suppression of slip. Plot (a) corresponds to a coverage $\Gamma = 3.2$ and $N_{AB} = 30$; (b) $\Gamma = 2.3$ and $N_{AB} = 40$; (c) $\Gamma = 2.7$ and $N_{AB} = 30$. 86

3.11 (a) Two bulk homopolymer phases, separated by an interface filled with copolymers is modeled as two bulk viscous media with a Brinkman medium between them representing the copolymer layers. (b) The velocity profile obtained by solving the Brinkman model equations. 88

3.12 (a) The Brinkman layer thickness, l as a function of the copolymer lengths; (b) The Brinkman friction thickness δ plotted for three different molecular weights of copolymer as a function of the copolymer coverages at the interface (expressed as number of chains/R_g^2). Lines are drawn as a guide to the eye. 90

3.13 Schematics of our hydrodynamic model. (a) Drainage between droplets. The droplets are assumed to be flattened due to the capillary forces. (b) Closer view of the drainage between droplets. l_1 and l_2 respectively represent the thickness of the Brinkman layers exterior and interior to the droplet. 95

3.14 Nondimensionalized drainage times (t_d) plotted as a function of capillary number (Ca): (a) For three different copolymer coverages Γ (expressed as number of chains per R_g^2 at the interface. $\Gamma = 0$ corresponds to the absence of compatibilizer; and (b) For two different molecular weight of copolymer, N_{AB}. 98

4.1 Steady state composition profiles of the droplet phase polymers: (a) $\Gamma = 3.18, \dot{\gamma} = 0.0$, Wi=0.0; (b) $\Gamma = 3.18, \dot{\gamma} = 0.15$, Wi=0.18; (c) $\Gamma = 3.18, \dot{\gamma} = 1.0$, Wi=1.2; (d) $\Gamma = 0.0, \dot{\gamma} = 1.0$, Wi=1.2. "$D$" denotes the deformation parameter for the droplet (The black color denotes the droplet phase). 113

4.2 Steady state composition profiles of the copolymers: (a) $\Gamma = 3.18, \dot{\gamma} = 0.0$, Wi=0.0; (b) $\Gamma = 3.18, \dot{\gamma} = 0.15$, Wi=0.18; (c) $\Gamma = 3.18, \dot{\gamma} = 1.0$, Wi=1.2; (d) $\Gamma = 0.477, \dot{\gamma} = 1.0$, Wi=1.2 (The white color denotes the copolymer phase). 117

4.3 Steady state streamline profiles: (a) $\Gamma = 0.0, \dot{\gamma} = 2.0$; (b) $\Gamma = 0.0, \dot{\gamma} = 3.5$; (c) $\Gamma = 0.0, \dot{\gamma} = 2.0$; (d) $\Gamma = 3.18, \dot{\gamma} = 2.0$. 120

4.4 Droplet deformation parameters D as a function of applied shear rate $\dot{\gamma}$ for different compatibilizer coverages Γ. 123

4.5 Effective surface tension σ (note: the interfacial energy is nondimensionalized with energy scale $k_BT = 1.0$ and length scale of $R_g = 1.0$) plotted as a function of the copolymer coverage Γ. 126

4.6 Droplet deformation parameter D is displayed as a function of capillary number Ca. In the above, theory refers to the predictions of [94]. 128

4.7 The variations of copolymer composition C (normalized by its uniform value, C_0) as a function of the meriodonal angle θ for two different copolymer coverages Γ. 130

4.8 (a) Droplet deformation parameter D displayed as a function of the capillary number Ca at a coverage $\Gamma = 3.18$ for different copolymer lengths N_A-N_B; (b) Normalized copolymer compositions as a function of the meriodonal angle θ for three different copolymer lengths N_A-N_B. 133

4.9 Low shear viscosities η_0 as a function of coverage for two different copolymer lengths. The thin line indicates the theoretical prediction for the emulsion viscosity [127] at zero copolymer coverage. 136

4.10 Normalized shear viscosity as a function of shear rate $\dot{\gamma}$ for different coverages and for copolymer chain lengths: (a) $N_{AB} = 1.3N$; (b) $N_{AB} = 0.6N$. 137

4.11 Normalized shear viscosity as a function of capillary number Ca for different coverages and for copolymer chain lengths: (a) $N_{AB} = 1.3N$; (b) $N_{AB} = 0.6N$. 138

4.12 First normal stress difference obtained at a copolymer coverage of 3.18 is compared with the results of small deformation theory (SDT [119]), Polymer component of normal stress difference [40] (indicated above by Polym Comp) and the polymer corrected normal stress difference (SDT+Polym). 141

5.1 Phase diagram for a ternary PEE-PDMS system, at a constant 1:1 ratio of PEE and PDMS homopolymer. A bicontinuous microemulsion phase exists in a narrow composition channel at a total homopolymer concentration of around 90% by volume (adapted from [140]) (The white and black colors denote the two components in the inset). 150

5.2 (a) Equilibrium phase diagram of a ternary system obtained using Field Theoretic Simulations [112] (FTS), (b) Two dimensional composition profiles obtained from SCBD at various homopolymer compositions indicated (The gray areas denote the total composition of component A). 154

5.3 Two dimensional composition profiles obtained at various shear rates, (a) $\dot{\gamma}\tau$=0.0, Equilibrium; (b) $\dot{\gamma}\tau$=0.0081; (c) $\dot{\gamma}\tau$=0.081; (d) $\dot{\gamma}\tau$=0.81; (e) $\dot{\gamma}\tau$=2.025 (The white areas denote the total composition of component A). 157

5.4 Two dimensional composition profiles of just the block copolymers in the system, at shear rates (a) $\dot{\gamma}\tau$=0.2; (b) $\dot{\gamma}\tau$=2.025 (The grayscale denotes the composition of component A of the copolymer). 158

5.5 Microphase structures predicted by Krishnan and coworkers at (a) Low; (b) High and (c) Intermediate, shear rates. 159

5.6 One dimensional averaged composition profiles at shear rates (a) $\dot{\gamma}\tau$=0.081; (b) $\dot{\gamma}\tau$=0.81. 161

5.7 Two dimensional compositional profiles obtained for viscoelastically symmetric (left column) and viscoelastically asymmetric (right column) system with $\beta = 10.0$, at shear rates (a) $\dot{\gamma}\tau$=0.04; (b) $\dot{\gamma}\tau$=0.6; (c) $\dot{\gamma}\tau$=1.21 (The grayscale denotes the total composition of component A). 163

5.8 One dimensional, total (thin line) and copolymer (thick line) composition profiles at a shear rate of $\dot{\gamma}\tau$=0.61, for three different values of copolymer lengths characterized by (a) $\alpha = 2.5$, (b) $\alpha = 5.0$ and (c) $\alpha = 7.0$. 167

5.9 Velocity profiles for a system with $\alpha = 5.0$ and $\beta = 1.0$, for shear rate values of (a) $\dot{\gamma}\tau$=0.0081, (b) $\dot{\gamma}\tau$=0.081 and (c) $\dot{\gamma}\tau$=4.05. . 170

5.10 Shear viscosities normalized by low shear viscosity of an ordered ternary blend, for the cases of pure homopolymer, ordered ternary blend, pure homopolymer and disordered ternary blend. The rings denote the approximate shear rate where the respective systems begin to shear thin. 170

5.11 Shear thinning viscosity for PEE-PDMS ternary blend (adapted from [130]). 171

5.12 Two dimensional composition and 1D averaged viscosity profiles for shear rate of $\dot{\gamma}\tau$=0.081, for systems with two different copolymer lengths given by, (a) $\alpha = 5.0$ and (b) $\alpha = 7.0$. . . . 174

5.13 Shear viscosities (normalized by the respective low shear viscosity) for systems with three different copolymer lengths, given by, (a) $\alpha = 2.5$, (b) $\alpha = 5.0$ and (c) $\alpha = 7.0$. 175

5.14 Two dimensional composition and 1D averaged viscosity profiles for a viscoelastically asymmetric system with $\beta = 10.0$ and $\alpha = 5.0$. 177

5.15 Shear viscosities (normalized by the respective low shear viscosity) for systems with three different viscoelastic asymmetries, given by, (a) $\beta = 1.0$, (b) $\beta = 5.0$ and (c) $\beta = 10.0$. 177

5.16 Shear rate dependencies of R_{gy} of the copolymer chains and the enthalpic overlap functions defined as: $\Theta = \int_L dy[\phi_A^C(y)\phi_B^C(y) + \phi_A^C(y)\phi_B^H(y) + \phi_A^H(y)\phi_B^C(y)]$, where the integration is over an AB interface. The superscripts H and C denote the homopolymer and copolymer respectively. L denoted the lamellar phase and T denotes the nonperiodic lamellar and macrophase separated phase. Both Θ and R_{gy} are normalized by their zero shear values. 180

5.17 Shear stress dependence of R_{gy} of the copolymer for different viscosity contrast systems. Solid symbols correspond to L phase and open symbols correspond to T phase. 181

5.18 Enthalpic cost displayed as a function of shear rate for two values of α. 184

6.1 (a) Order disorder transition for ternary blend system with $\alpha = 2.22$ (b) Cell dynamics solution of the equilibrium composition profile at various homopolymer compositions indicated. 197

6.2 Equilibrium structure factor in the disordered phase, for homopolymer compositions of (a) $\phi^H = 0.2$ and (b)$\phi^H = 0.67$. . . 199

6.3 Structure factor for ternary blend with $\phi^H = 0.67$ at four different shear rates of (a) $\dot{\gamma} = 0.0$; (b) $\dot{\gamma} = 0.005$; (c) $\dot{\gamma} = 0.05$ and (d) $\dot{\gamma} = 0.1$. 200

6.4 The structure factor weighted second moments displayed as a function of the shear rate, obtained from cell dynamics in (a) and the experimental and numerical scheme results of [17] in (b) & (c) respectively. 203

6.5 Normalized anisotropy Δ and orientation angle θ displayed as a function of shear rate, obtained from cell dynamics in (a) and the experimental and numerical scheme results of [17] in (b) & (c) respectively. 204

6.6 (a) Normalized intensity obtained from cell dynamics, at equilibrium and under shear ($\dot{\gamma} = 0.1$) for a viscoelastically symmetric system; (b) Normalized intensity under shear for a PEE-PDMS ternary blend, adapted from [17]. 206

6.7 (a) Normalized intensity obtained from cell dynamics, at equilibrium and under shear rates indicated, for a viscoelastically asymmetric system; (b) Normalized intensity under shear for a PEE-PDMS ternary blend, adapted from [17]. 208

6.8 The structure factor weighted second moments displayed as a function of the shear rate, obtained from cell dynamics (for a viscoelastically *asymmetric* system) in (a) and the experimental and numerical scheme results of [17] in (b) & (c) respectively. 209

6.9 Normalized anisotropy Δ and orientation angle θ displayed as a function of shear rate, obtained from cell dynamics (for a viscoelastically *asymmetric* system) in (a) and the experimental and numerical scheme results of [17] in (b) & (c) respectively. 210

6.10 Two dimensional composition profiles obtained using the first protocol for a ternary blend with $\phi^H = 0.68$, at equilibrium in (a) and at four different shear rates of (b) $\dot{\gamma} = 0.001$; (c) $\dot{\gamma} = 0.005$; (d) $\dot{\gamma} = 0.05$ and (e) $\dot{\gamma} = 0.5$. 212

6.11 Two dimensional composition profiles obtained using the first protocol for a ternary blend with $\phi^H = 0.71$, at equilibrium in (a) and at four different shear rates of (b) $\dot{\gamma} = 0.001$; (c) $\dot{\gamma} = 0.005$; (d) $\dot{\gamma} = 0.05$ and (e) $\dot{\gamma} = 0.5$. 213

6.12 Two dimensional composition profiles (of just the copolymers) obtained using the first protocol for a shear rate $\dot{\gamma} = 0.5$ for a ternary blend with homopolymer composition of (a) $\phi^H = 0.68$; (b) $\phi^H = 0.71$; (c) $\phi^H = 0.73$ and (d) $\phi^H = 0.77$. 215

6.13 Two dimensional composition profiles obtained using the first protocol for a ternary blend with $\phi^H = 0.73$, at equilibrium in (a) and at four different shear rates of (b) $\dot{\gamma} = 0.001$; (c) $\dot{\gamma} = 0.005$; (d) $\dot{\gamma} = 0.05$ and (e) $\dot{\gamma} = 0.5$. 216

6.14 Two dimensional composition profiles obtained using the first protocol for a ternary blend with $\phi^H = 0.77$, at equilibrium in (a) and at four different shear rates of (b) $\dot{\gamma} = 0.001$; (c) $\dot{\gamma} = 0.005$; (d) $\dot{\gamma} = 0.05$ and (e) $\dot{\gamma} = 0.5$. 217

6.15 Two dimensional composition profiles obtained using the second protocol for a ternary blend with $\phi^H = 0.68$, at equilibrium in (a) and at three different shear rates of (b) $\dot{\gamma} = 0.001$; (c) $\dot{\gamma} = 0.005$ and (d) $\dot{\gamma} = 0.05$. 218

6.16 Two dimensional composition profiles obtained using the second protocol for a ternary blend with $\phi^H = 0.71$, at equilibrium in (a) and at three different shear rates of (b) $\dot{\gamma} = 0.001$; (c) $\dot{\gamma} = 0.005$ and (d) $\dot{\gamma} = 0.5$. 219

6.17 Two dimensional composition profiles obtained using the second protocol for a ternary blend with $\phi^H = 0.73$, at equilibrium in (a) and at three different shear rates of (b) $\dot{\gamma} = 0.001$; (c) $\dot{\gamma} = 0.005$ and (d) $\dot{\gamma} = 0.05$. 220

6.18 Two dimensional composition profiles obtained using the second protocol for a ternary blend with $\phi^H = 0.77$, at equilibrium in (a) and at three different shear rates of (b) $\dot{\gamma} = 0.001$; (c) $\dot{\gamma} = 0.005$ and (d) $\dot{\gamma} = 0.5$. 221

6.19 Two dimensional composition profiles obtained using the first protocol for a ternary blend (*with viscosity contrast*) with $\phi^H = 0.68$, at equilibrium in (a) and at four different shear rates of (b) $\dot{\gamma} = 0.001$; (c) $\dot{\gamma} = 0.005$; (d) $\dot{\gamma} = 0.05$ and (e) $\dot{\gamma} = 0.5$. . . 222

6.20 Two dimensional composition profiles obtained using the first protocol for a ternary blend (*with viscosity contrast*) with $\phi^H = 0.71$, at equilibrium in (a) and at four different shear rates of (b) $\dot{\gamma} = 0.001$; (c) $\dot{\gamma} = 0.005$; (d) $\dot{\gamma} = 0.05$ and (e) $\dot{\gamma} = 0.5$. . . 223

6.21 Two dimensional composition profiles obtained using the first protocol for a ternary blend (*with viscosity contrast*) with $\phi^H = 0.73$, at equilibrium in (a) and at four different shear rates of (b) $\dot{\gamma} = 0.001$; (c) $\dot{\gamma} = 0.005$; (d) $\dot{\gamma} = 0.05$ and (e) $\dot{\gamma} = 0.5$. . . 224

6.22 Two dimensional composition profiles obtained using the first protocol for a ternary blend (*with viscosity contrast*) with $\phi^H = 0.77$, at equilibrium in (a) and at four different shear rates of (b) $\dot{\gamma} = 0.001$; (c) $\dot{\gamma} = 0.005$; (d) $\dot{\gamma} = 0.05$ and (e) $\dot{\gamma} = 0.5$. . . 225

7.1 Schematic representing the (a) parallel and (b) perpendicular orientations of block copolymer lamellae under shear. 230

7.2 (a) Schematic of a *triblock* copolymer lamella displaying the alternate *bridges and loops* layer and *slip* layer; (b)Schematic of a *pentablock* copolymer lamella displaying the *bridges and loops* in every layer. 232

7.3 Storage($G^{'}$) and loss ($G^{''}$) moduli as a function of oscillatory shear frequency, for lamellae oriented in parallel and perpendicular directions. 239

7.4 Storage($G^{'}$) and loss ($G^{''}$) moduli as a function of oscillatory shear frequency, for lamellae oriented in parallel and perpendicular directions, for four different viscoelastic asymmetries characterized by (a) $\beta = 2.0$; (b) $\beta = 4.0$; (c) $\beta = 5.0$ and (d) $\beta = 6.0$. 242

7.5 Complex modulus for parallel and perpendicular orientations of lamellae as a function of frequency, comparing three different viscoelastic asymmetries, (a) $\beta = 1.0$ & $\beta = 2.0$; (b) $\beta = 3.0$ & $\beta = 4.0$; (c) $\beta = 5.0$ & $\beta = 6.0$. Here, ω_c is the crossover frequency defined in the text. 245

7.6 Phase diagram for parallel and perpendicular orientation selection as a function of viscoelastic asymmetry β and crossover frequency ω_c. 246

7.7 (a) Storage modulus of viscoelastically symmetric, di-, tri- and penta-block copolymer as a function of frequency. (b) Loss modulus of viscoelastically symmetric, di-, tri- and penta-block copolymer as a function of frequency. 249

7.8 Time averaged link distribution as a function of the distance between the links, for a pentablock copolymer system oriented in the parallel direction, at equilibrium (thick line) and under shear with $\omega\tau = 8.0$ (thin line). 250

7.9 Time averaged link distribution as a function of the distance between the links, for a pentablock copolymer system oriented in the perpendicular direction, at equilibrium (thick line) and under shear with $\omega\tau = 8.0$ (thin line, coincides with the thick line). 251

7.10 Complex modulus as a function of frequency for parallel and perpendicular orientations of (a) diblock (b) triblock and (c) pentablock copolymer systems. 254

8.1 A chart depicting the main contributions and issues addressed in the thesis. 258

Chapter 1

Introduction and Dissertation Overview

The main objectives of the research detailed in this dissertation were to gain insights into the interplay between molecular level dynamics and thermodynamical interactions in compositionally and/or dynamically inhomogeneous multicomponent polymeric systems. To achieve these objectives, we have followed the steps outlined below.

a) Developed a hybrid multiscale coarse-grained simulation approach to study the interplay between molecular-level dynamics and thermodynamical characteristics of inhomogeneous polymeric systems.

b) Employed the above approach to effect microscale dynamical studies in binary homopolymer blends, block copolymer melts and ternary blends of homopolymers and copolymers.

c) Attempted to bridge the external flow induced changes in molecular conformations to the macroscopic rheological properties and the phase behavior of the multicomponent polymers.

d) Used our results alongside dynamical models to predict macroscale behavior and the response of inhomogeneous phase separated polymeric systems such as, multicomponent polymer blends, self-assembled blockcopolymer

systems etc. to externally applied flow conditions.

Broadly, we expect this research to help exploit the flow behavior to attain tailor made morphologies in multicomponent systems for specific applications.

1.1 Motivation

For the past few decades, melt blending of two or more polymeric systems has been used extensively as a route to develop advanced polymeric materials which possess a desirable combination of the properties of the individual components of the blend [27]. However, most polymers are immiscible and hence simple physical blending of the polymeric systems lead to an array of micro and macro phase separated morphologies [30–34]. These phase separated structures range from simple polymer droplets embedded in a matrix of another polymer, as seen in binary homopolymer blends as shown in Fig. 1.1, to extremely complex self assembled structures attained in multiblock copolymer systems (cf. Fig. 1.2, adapted from Zheng and Wang [1], for the various morphologies attainable by varying the compositions in a triblock copolymer melt). In such multicomponent, phase separating polymeric systems, the properties (mechanical, optical and electrical) of the final product depend not only on the properties of the individual constituents but also crucially on their morphological characteristics [27–29].

Research in multiphase complex fluids has ranged from understanding the structure-property relationships in various polymeric fluids to exploring

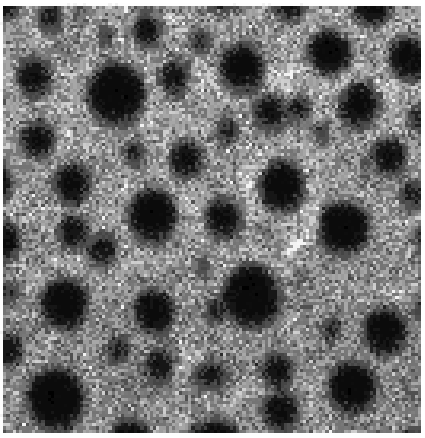

Figure 1.1: Droplets of polystyrene (PS) in a matrix of polymethylmethacrylate (PMMA) in a mixture of 30/70 (PS/PMMA) by volume.

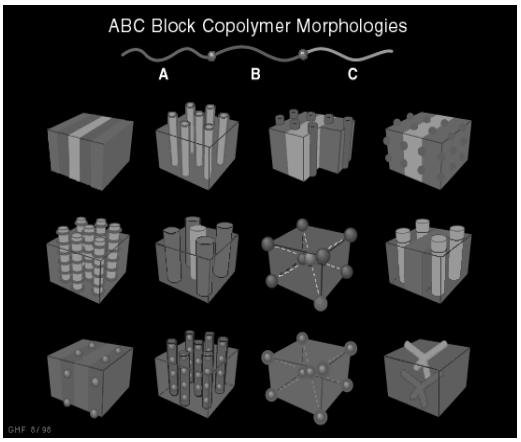

Figure 1.2: Morphologies for linear ABC triblock copolymers obtained by varying the block sequences (ABC,ACB,BAC), composition and molecular weights.

novel, inexpensive techniques to attain specific microstructures which can lead to the desired properties [27–34]. Early attempts at understanding multicomponent polymeric systems involved models and theories aimed at predicting the equilibrium morphologies [2–5]. Many pioneering advances have now led theoretical developments which are capable of predicting various equilibrium domain shapes and dimensions [2–4, 65]. For instance, Fig. 1.3 shows the complete phase diagram including the various morphologies attained in an AB diblock copolymer melt. While Fig. 1.3a displays the four different morphologies predicted by polymer self consistent mean field theory [2, 3], viz. spherical (S), cylindrical (C), gyroid (G), and lamellar (L), which depend on the composition f (of block A) and the interaction parameter χN. Figure 1.3b displays the corresponding experimental phase diagram of poly(isoprene-styrene) diblock copolymers [6]. The resemblance and comparisons between the experimental and the theoretical phase diagrams are indeed striking.

In more recent years, flow processing of multicomponent polymeric systems has emerged as an inexpensive and versatile route to control the microstructure. Intriguing experimental results have been reported in the literature, documenting the novel behaviors arising from an interplay between flow and thermodynamical characteristics in multicomponent polymers. In binary polymer blend systems, these effects range from flow-induced mixing, demixing, phase transitions [35, 36, 60, 61], network formation, interfacial slip and low mixing viscosities [62, 63], slip suppression in compatibilized polymer blends with block copolymer compatibilizers [102, 103] etc. Furthermore, droplet de-

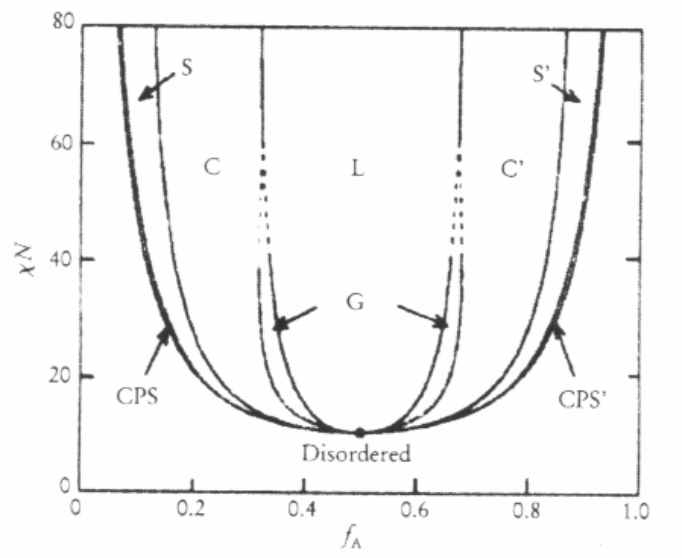

(a)

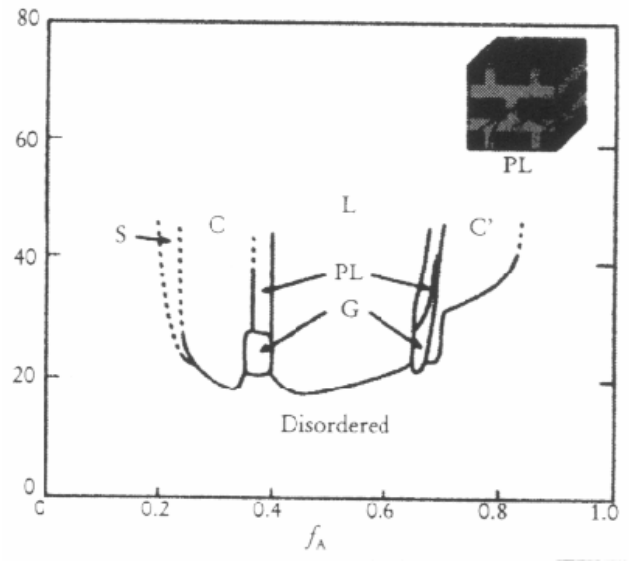

(b)

Figure 1.3: Phase diagram of AB diblock copolymer obtained from (a) Self-consistent mean field theory and (b) Experimental system of poly(isoprese-styrene) diblock copolymers. The x-axis represents the block composition f and the y-axis represents the incompatibility parameter χN. The morphologies obtained are spherical (S), cylindrical (C), gyroid (G), and lamellar (L) phases.

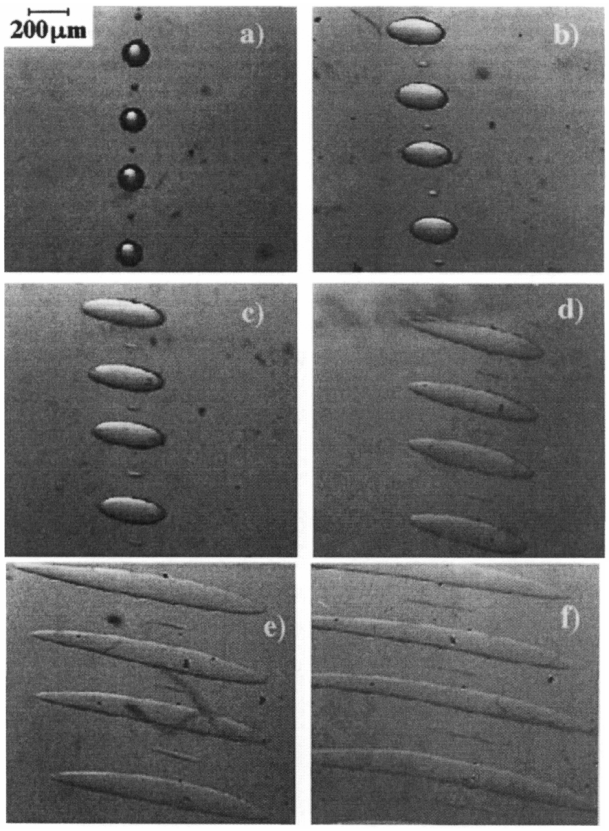

Figure 1.4: Polypropelene (PP) drops in polystyrene (PS) matrix (with viscosity ratio = 2.4), for strain values of (a)γ=0, (b)γ=2, (c)γ=3, (d)γ=5, (e)γ=9 and (f)γ=13.

formation, coalescence, breakup and formation of sheet-like morphologies under external shear flows have also been witnessed in polymer blend systems with droplet morphology. For instance, Fig. 1.4 shows digital video micrographs of a coexisting blend of PS/PP (60/40) blend (adapted from [7]). Figures 1.4a-f display the morphology under steady shear, for the four different strains specified. At the lowest strain (=0), the system retains its equilibrium morphology with the droplets of the minority phase (PP) in a matrix of the majority phase (PS). At moderate strains, the droplets in the system are elongated under shear and at high strain values the elongated drops give way to highly anisotropic stringlike morphologies.

In block copolymer systems, flow-induced ordering and disordering transitions, shear induced alignment and shift in copolymer orientation have been observed [8, 9, 30, 33, 34]. Oscillatory shear has been found to induce long range order in the normally defect prone block copolymer systems. For instance until about a decade ago flow was observed to lead to only parallel orientation of block copolymer lamellae. However, Koppi et al. [10] discovered the perpendicular alignment in poly(ethylene-propylene)-poly(ethylene-ethylene) (PEP-PEE) by increasing the frequency of the applied oscillatory shear. On the other hand, completely contradictory results have been obtained by Winey and coworkers [11, 12] for polystyrene-polyisoprene system wherein they have witnessed a flip in orientation from perpendicular to parallel by increasing the shear frequency. These apparently contradicting results highlight the complexity of the underlying flow-structure relationship. More

recent experiments have highlighted the subtleties in multiblock copolymer systems, for instance, lamellae-forming triblock and pentablock copolymers have exhibited reciprocating shear-induced lamellar reorientation [8, 34]. Evidently, understanding the interplay between the applied flow and the resulting morphology would allow us to use the flow field as a control parameter towards achieving the desired structure.

Some important questions that arise in understanding above phenomena include: How does the external flow-field affect the conformational statistics of the polymer?, How do the flow induced changes in molecular conformations relate to the resulting morphology?, How do the chain conformations and system morphology affect the rheological properties of the viscoelastic system? These questions have provided us with the motivation towards pursuing research aimed at understanding the rheology-morphology relationship in multicomponent polymeric systems.

1.2 Challenge

Successful theories that could correctly predict the interplay between various flow parameters and the structural characteristics in multicomponent systems should necessarily incorporate polymer-polymer thermodynamics as well as polymer rheological characteristics. Furthermore, note that such materials are inherently inhomogeneous, and in many cases the inhomogeneities in the system (characterizing the inherent structure of the underlying multicomponent system) are on the scale of molecules themselves. Hence, modeling

the dynamics of phase separating and self assembling systems requires one to account for the interaction between individual polymers in the molecular scale to accommodate (in a thermodynamically consistent manner) the resulting compositional inhomogeneity.

1.2.1 Existing Polymer Modeling and Theoretical Approaches

Early attempts at studying the rheology and flow characteristics of viscoelastic, complex fluid systems (like polymer solutions and polymer melts) employed kinetic theory based continuum approaches. These conventional approaches were based on solving the conservation equations of mass, momentum and energy along with constitutive equations for polymer stress. These constitutive equations, obtained by approximate models based on kinetic theory, have provided quantitative predictions for the velocity and stress distributions in complex flows of homogeneous polymeric systems including polymer solutions and melts. However, such approaches have limited applicability in multiphase flows of polymer melts since they do not incorporate molecular scale enthalpic interactions between different monomer entities.

Computer simulation methods have emerged as a useful tool in studying the morphology of multiphase polymeric systems. In the most detailed *classical* simulations, interactions are parametrized at the atomistic level by a combination of bonded and nonbonded potentials typically formulated at the level of two or three-body interactions. These interactions are incorporated into computer simulation techniques like Monte Carlo (MC) and mole-

cular dynamics (MD) simulations to deduce the equilibrium characteristics of materials. While the non-equilibrium versions of such atomistic simulations have proven useful to gain insights into the rheology of simple fluids [69], direct application of such simulations to study the dynamics in multicomponent polymeric systems proves computationally very expensive [13, 14]. Mainly, the long relaxation times of individual polymer chains and the high density in polymer melts render the equilibration in simulations very difficult. This drawback becomes particularly severe for studying dynamical flow phenomena in compositionally inhomogeneous systems where, in addition to the above time scales, the time scale due to the imposed flow becomes relevant.

Recently, there have been advances in developing coarse-grained, hybrid, multi-scale models which overcome some of the above-mentioned drawbacks of the traditional models. The present research is also similar in spirit, and focuses on the development of a mutli-scale, hybrid simulation approach, which (detailed in the next chapter) uses efficient coarse-grained models for polymer chains and their interactions, in turn considerably reducing the computational costs and enabling the study of dynamical phenomena in multiphase polymeric systems. An important component of this dissertation was the development of this new simulation technique (termed self-consistent Brownian dynamics) for application in different contexts. The second aspect of our research was in its application in different contexts. In the following chapters we outline our efforts in both these contexts.

1.3 Layout of the Thesis

As mentioned earlier, our foremost objective is to gain understanding of dynamical phenomena in multicomponent polymeric systems. To effect this objective we have classified our research on the basis of two categories,

a) *Polymeric systems under consideration:* Here we have classified the systems studied into three categories,

(i) Homopolymer Blends (A+B) [Chapters 3 and 4]

(ii) Ternary Blends (A + B + AB) [Chapters 5 and 6]

(iii) Block copolymer melts (AB, ABA etc) [Chapter 7]

b) *Dynamical phenomena under consideration:* Here we have classified the interplay between rheology and morphology as:

(i) Effect of morphology (or compositional inhomogeneity) on the induced flow field or macroscopic rheology of the system. These include studies of interfacial slip in polymer blends, slip suppression in compatibilized polymer blends [Chapter 3] and rheology of ordered block copolymer phases [Chapter 7].

(ii) Effect of applied flow field on the morphological characteristics such as, droplet deformation, shear induced order-disorder transitions [Chapter 6], shear effect on orientational characteristics [Chapter 7]. Here we summarize the contents of each following chapter.

1.4 Development of a Hybrid Brownian Dynamics Approach (Chapter 2)

We elaborate on our recently developed, hybrid multiscale simulation approach. This approach generalizes Doi's dynamical mean field theory for rod-like polymers by combining single chain Brownian dynamics algorithms with phenomenological prescriptions for the dynamics of coarse-grained velocity and composition fields.

1.5 Interfacial Phenomena in Polymer Blends (Chapter 3)

We present a detailed analysis of interfacial phenomena in symmetric and asymmetric polymer blend systems using the above simulation approach. Specifically, we study the influence of the bulk rheological properties of the polymer blend components upon slip at unentangled polymer interfaces. Our results in this chapter provide a microscopic explanation of the negatively deviating viscosities of polymer blends. We also present results elucidating the *slip suppressing* influence of block compatibilizers, and suggest some new effects that might account for the effect of compatibilizers in the suppression of coalescence during polymer blending.

1.6 Flow Deformation of Polymer Blend Droplets And The Role of Block Copolymer Compatibilizers (Chapter 4)

We study the influence of block copolymer compatibilizers upon the dynamics of a nanoscale polymer droplet in a matrix of another polymer. This study focuses on the influence of the physical characteristics of the copolymer, viz. its coverage and chain lengths upon the droplet deformation characteristics and the rheological properties of the polymer blend system. We also studied the rheological effects arising from the presence of block copolymers. Our results suggest increased shear thinning with either increasing the copolymer coverage or the copolymer chain lengths. Moreover, the normal stresses of the mixture are found to be dominated by the inherent normal stresses of the matrix and the droplet phases. The rheological results are rationalized by invoking the interplay between deformation characteristics and the dynamical effects of block copolymers at polymer blend interfaces.

1.7 Shear Induced Phase Transition in Ternary Polymer Blend Systems (Chapter 5)

This chapter presents a study of flow-induced phase transitions in microemulsion phases of ternary polymer blends. Our results match qualitatively with the recent experimental observation on such polymeric systems but differ from the behavior expected and observed in the analogous system of surfactants. We rationalize this contrast from a molecular viewpoint suggesting that

the interplay between polymer chain conformations and their flow deformations can lead to novel flow effects upon the phase, structural and rheological behavior of multicomponent polymeric systems.

1.8 Composition Field Dynamics in Ternary Polymer Blends (Chapter 6)

We study the effect of composition fluctuations on both the ordered and disordered phases of ternary polymer blends. We develop a more accurate description of the ternary blend system by developing a three order parameter model. Cell dynamics simulations [15, 16] were employed to obtain structure factor under shear in disordered system. Our results had better quantitative agreement with the experiments [17] than the existing single parameter model of Patzold and Dawson [18]. However, we found no evidence of shear-induced phase transitions or instabilities in the ordered phase.

1.9 Rheology of Ordered Phases of Multiblock Copolymers (Chapter 7)

In this chapter we study oscillatory shear rheology of block copolymer lamellae oriented in different directions with respect to the applied shear. We compare and contrast the rheological behavior of different orientations and varying viscoelastic contrast between the block copolymer components. Moreover, we also compare the rheological characteristics of di-, tri- and penta-block copolymer lamellae and rationalize the results using the internal chain confor-

mation in the form of bridges and loops. Furthermore, we also provide an approximate phase diagram for lamellar reorientation with increasing oscillatory shear frequency.

1.10 Summary

Pioneering contributions by various researchers have resulted in the equilibrium phenomena in multicomponent polymeric systems and dynamical phenomena in homogeneous polymeric systems being reasonably well understood. However, despite focused research for over a decade, we still face a lot of challenges (both numerical and conceptual) in understanding the dynamical phenomena in multicomponent, phase separated, polymeric mixtures. In summary, this dissertation elaborates our contributions in that area. We have developed a hybrid multiscale model capable of capturing dynamical phenomena in multiphase systems. We have borrowed ideas from both equilibrium thermodynamical concepts and numerical polymer modeling approaches to achieve this objective (elaborated in the following chapter). Complex dynamical phenomena in an array of polymeric systems, mentioned above, have been studied in detail and the results are provided in the later chapters of this dissertation.

Chapter 2

Self Consistent Brownian Dynamics

Many seminal advances have occurred in the context of modeling the thermodynamical and dynamical properties of polymeric materials. Pioneering work by Edwards, Helfand, Sanchez and Leibler [2–4, 19] have immensely contributed to the general understanding of phase separation and phase behavior in polymeric systems under equilibrium. Early theories for modeling polymer molecules have employed a variety of microscopic mechanical models such as the lattice model, bead-spring models, Gaussian thread models etc. for describing the connectivity and interactions of polymer molecules. Statistical thermodynamics based ideas are then used to predict the density profiles, geometry, size and stability of microstructural domains. The resulting models have been cast into attractive numerical approaches that can enable the prediction of the thermodynamics and self-assembly characteristics of a variety of multicomponent polymers. These approaches [2, 3] have been used with great success to predict the equilibrium thermodynamical features of multiblock copolymers, blends of block copolymers with homopolymers, thin films of polymers etc.

2.1 Gaussian Thread Model

Much of the research outlined in this thesis is based on the Gaussian thread model [40]. To set the stage for the same, we briefly explain the Gaussian thread model for the description of a polymer chain. The latter can be considered as the *continuous* mathematical representation of the bead-spring model where a polymer chain is represented by a set of beads connected by springs. The chain conformation is represented by the $(N+1)$ position vectors $\mathbf{R}_{\bar{s}} \equiv (\mathbf{R}_0 ... \mathbf{R}_N)$ or alternatively by a set of bond vectors $\mathbf{r}_{\bar{s}} \equiv (\mathbf{r}_1 ... \mathbf{r}_N)$ (cf. Fig. 2.1) with a bond length distribution which follows a Boltzmann distribution of the form,

$$\psi(\mathbf{r}) = \left[\frac{3}{2\pi b^2}\right]^{3/2} \exp\left(-\frac{3\mathbf{r}^2}{2b^2}\right), \tag{2.1}$$

so that,

$$\left\langle \mathbf{r}^2 \right\rangle = b^2, \tag{2.2}$$

where b is an effective bond length, termed in the polymer literature as the Kuhn segment length. The overall conformational distribution function of such a chain is given by,

$$\begin{aligned} \Psi(\{\mathbf{r}_{\bar{s}}\}) &= \prod_{\bar{s}=1}^{N} \left[\frac{3}{2\pi b^2}\right]^{3/2} \exp\left(-\frac{3\mathbf{r}_{\bar{s}}^2}{2b^2}\right), \\ &= \left[\frac{3}{2\pi b^2}\right]^{3N/2} \exp\left(-\sum_{\bar{s}=1}^{N} \frac{3(\mathbf{R}_{\bar{s}} - \mathbf{R}_{\bar{s}-1})^2}{2b^2}\right). \end{aligned} \tag{2.3}$$

Within the framework of the bead-spring model, this corresponds to a situation wherein the spring potential energy is given by a simple Hookean harmonic

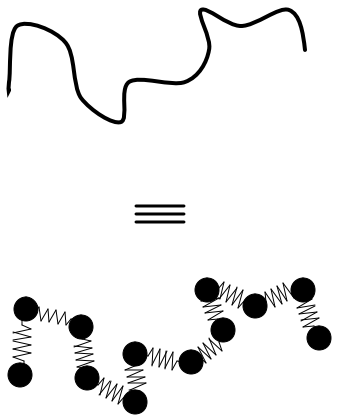

Figure 2.1: The Gaussian thread representation of a polymer chain and its equivalent *bead-spring* representation.

form:

$$U_o(\{\mathbf{R}_{\bar{s}}\}) = \frac{3}{2b^2} k_B T \sum_{\bar{s}=1}^{N} (\mathbf{R}_{\bar{s}} - \mathbf{R}_{\bar{s}-1})^2 \tag{2.4}$$

Such a chain is called the Gaussian chain, whose distribution function can be recast into the continuous formalism when the suffix $\bar{s}$ is considered as a continuous variable. In such a case, $\mathbf{R}_{\bar{s}} - \mathbf{R}_{\bar{s}-1}$ is replaced by $d\mathbf{R}_{\bar{s}}/d\bar{s}$ and $\sum_{\bar{s}=1}^{N}$ is replaced by $\int_0^N d\bar{s}$. The above equation (2.3) could then be written as,

$$\Psi(\{\mathbf{r}_{\bar{s}}\}) = \left[\frac{3}{2\pi b^2}\right]^{3N/2} \exp\left[-\frac{3}{2b^2}\int_0^N d\bar{s}\left(\frac{\partial \mathbf{R}_{\bar{s}}}{\partial \bar{s}}\right)^2\right] \tag{2.5}$$

2.2 Self-Consistent Field Theory

To illustrate the development of our model for multicomponent polymers, we consider as an example, the formulation of self-consistent field theory for a system of a binary blend of homopolymer A and homopolymer B [2, 3]. While studying multicomponent polymeric systems, in addition to employing a polymer chain model incorporating the connectivity of the monomers, we need to account for nonbonded monomer interactions. For that purpose, we use the interaction energy functional obtained by extending the Flory-Huggins (FH) theory [20], a model originally developed for polymeric solutions. In this model, the interaction energy is approximated by the heat of mixing of dissimilar polymer components, the latter is computed by enumerating the number of unlike monomer contacts in a lattice model of the polymer. Within a continuum formalism, the interaction energy between the A and B components can be written as,

$$U_1 [\mathbf{R}_A, \mathbf{R}_B] = \frac{k_B T \chi}{\rho_o} \int d\mathbf{r} \hat{\rho}_A \hat{\rho}_B, \tag{2.6}$$

where χ is termed the Flory-Huggins interaction parameter [20] representing the unfavorable costs of $A - B$ interactions relative to the $A - A$ and $B - B$ interactions. $\hat{\rho}_A$ and $\hat{\rho}_B$ denote the individual microscopic monomer densities defined as,

$$\hat{\rho}_k = \sum_{\alpha=1}^{m_k} \int_0^{N_k} d\bar{s} \delta \left(\mathbf{r} - \mathbf{R}_{\alpha k} \left(\bar{s} \right) \right), \tag{2.7}$$

where m_K is the number of chains of species K(=A or B) within the volume V and α indexes the chain number. The average density ρ_o is defined as,

$$\rho_o \equiv (m_A N_A + m_B N_B)/V. \tag{2.8}$$

Within the Gaussian thread model, the bonded interactions for a binary polymer blend system are represented by an interaction potential obtained from equation (2.4), generalized to the case of two components,

$$U_o\left[\mathbf{R}_A, \mathbf{R}_B\right] = \frac{3k_BT}{2b_A^2}\sum_{\alpha=1}^{m_A}\int_0^{N_A} d\bar{s}\left(\frac{d\mathbf{R}_{\alpha A}(\bar{s})}{d\bar{s}}\right)^2 + \frac{3k_BT}{2b_B^2}\sum_{\alpha=1}^{m_B}\int_0^{N_B} d\bar{s}\left(\frac{d\mathbf{R}_{\alpha B}(\bar{s})}{d\bar{s}}\right)^2. \tag{2.9}$$

Upon non-dimensionalizing the above equation so that the arc length variable s $(=\bar{s}/N)$ runs from 0 to 1 instead of 0 to N_k, we can rewrite the above equation as,

$$U_o\left[\mathbf{R}_A, \mathbf{R}_B\right] = \frac{k_BT}{4\mathbf{R}_{g,A}^2}\sum_{\alpha=1}^{m_A}\int_0^{1} ds\left(\frac{d\mathbf{R}_{\alpha A}(s)}{ds}\right)^2 + \frac{k_BT}{4\mathbf{R}_{g,B}^2}\sum_{\alpha=1}^{m_B}\int_0^{1} ds\left(\frac{d\mathbf{R}_{\alpha B}(s)}{ds}\right)^2. \tag{2.10}$$

In addition to the above interactions, in many cases, polymer melts have very low compressibility and can be modeled to be incompressible (albeit, compressibility effect can play an important role in some situations [19]). This incompressibility constraint is imposed by a delta functional $\delta\left(\hat{\rho}_A + \hat{\rho}_B - \rho_o\right)$, constraining that the sum of the microscopic individual densities, $\hat{\rho}_A\left(\mathbf{r}\right) + \hat{\rho}_B\left(\mathbf{r}\right)$, at every position in space $\mathbf{r}$, equals the average total monomer density ρ_o. This constraint can also be viewed as an approximate way to account for the hard-core repulsive short range interactions in the system.

The partition function for the system is then written by assembling all the above interactions as,

$$Z = \int D\left[\mathbf{R}_A\right] \int D[\mathbf{R}_B] \delta\left(\hat{\rho}_A + \hat{\rho}_B - \rho_o\right) \exp\left(-U_o - U_1\right). \tag{2.11}$$

The above model involving conformation path integrals of the chains is then converted into a field theory where the fundamental degrees of freedom are fluctuating chemical potential fields. For this purpose it is convenient to express the microscopic densities appearing in Z in terms of the linear combination fields as,

$$\hat{\rho}_{\pm}(\mathbf{r}) \equiv \hat{\rho}_A(\mathbf{r}) \pm \hat{\rho}_B(\mathbf{r}) \tag{2.12}$$

The incompressibility constraint on $\hat{\rho}_A + \hat{\rho}_B = \rho_o$ allows us to rewrite the interaction term U_1 as,

$$U_1 = -v_o \chi / 4 \int d\mathbf{r} [\hat{\rho}_-(\mathbf{r}) - (\rho_{A0} - \rho_{B0})]^2 \tag{2.13}$$

This expression can be transformed into a field-theory using a *Hubbard-Stratanovich* transformation. *Hubbard-Stratanovich* transformation, is essentially a functional generalization of the following equality regarding Gaussian integrals,

$$\exp(\frac{\beta}{4} \int d\mathbf{r} \zeta^2(\mathbf{r})) = \int Dw(\mathbf{r}) \exp\left[\frac{-1}{\beta} \int d\mathbf{r} w^2(\mathbf{r}) + \int d\mathbf{r} \zeta(\mathbf{r}) w(\mathbf{r})\right] \tag{2.14}$$

the value of which at the saddle point corresponds to the original functional form $\exp(\frac{\beta}{4} \int d\mathbf{r} \alpha^2(\mathbf{r}))$. By employing this transformation, along with equation (2.13) for U_1, the expression for $\exp(-U_1)$ could be written as,

$$\exp(-U_1) = \int D[w] \exp\left(\int d\mathbf{r} \left[(\hat{\rho}_- - \rho_{A0} + \rho_{B0}) w - 1/(\chi v_o) w^2\right]\right) \tag{2.15}$$

Note that, the saddle point of the above functional, obtained by the functional differentiation of the expression with respect to the field w would lead back to the original equation for U_1 (equation (2.13)). The δ function itself could be rewritten in the exponential representation as,

$$\delta(\hat{\rho}_+ - \rho_o) = \int D[\pi] \exp[-i \int d\mathbf{r}\pi[\hat{\rho}_+ - \rho_o]] \tag{2.16}$$

In the above formulation w can be viewed as an exchange potential conjugate to $\hat{\rho}_A - \hat{\rho}_B$ and π is the chemical potential field conjugate to the total monomer density $\hat{\rho}_A + \hat{\rho}_B$. Note here that the potential fields, $\pi(\mathbf{r})$ and $w(\mathbf{r})$, *decouple* the quadratic $\hat{\rho}_-$ interactions in U_1. In such a framework equation (2.11) can be reexpressed as,

$$Z = \int D\left[w\right] \int D[\pi] \exp\left(-H\left[w, \pi\right]\right), \tag{2.17}$$

where, the *Hamiltonian* $H\left[w, \pi\right]$ is,

$$H\left[w, \pi\right] = \frac{-\rho_o}{\chi N_A^2} \int dr w^2(\mathbf{r}) - \frac{i\rho_o}{N_A} \int dr \pi(\mathbf{r}) + m_A \ln Q_A + m_B \ln Q_B. \tag{2.18}$$

In the above,

$$Q_A = \int D\mathbf{R}_A \exp\left[\frac{-1}{4\mathbf{R}_{g,A}^2} \int_0^1 ds \left(\frac{d\mathbf{R}_A(s)}{ds}\right)^2 + \int_0^1 ds \left(i\pi\left(\mathbf{R}_A(s)\right) + w\left(\mathbf{R}_A(s)\right)\right)\right], \tag{2.19}$$

and

$$Q_B = \int D\mathbf{R}_B \exp\left[\frac{-1}{4\mathbf{R}_{g,B}^2} \int_0^1 ds \left(\frac{d\mathbf{R}_B(s)}{ds}\right)^2 + \frac{1}{\alpha} \int_0^1 ds \left(i\pi\left(\mathbf{R}_B(s)\right) - w\left(\mathbf{R}_B(s)\right)\right)\right],$$

represents the partition function of a single polymer chain of type A and B respectively in potential fields given by,

$$\begin{aligned} \psi_A &= -i\pi(\mathbf{r}) - w(\mathbf{r}), \quad \text{for } A \text{ chains} \\ \psi_B &= -i\pi(\mathbf{r}) + w(\mathbf{r}), \quad \text{for } B \text{ chains} \end{aligned} \tag{2.20}$$

In equation (2.2), α is a parameter characterizing asymmetry, with $\alpha = N_A/N_B = \mathbf{R}^2_{g,A}/\mathbf{R}^2_{g,B}$. In a continuum implementation, the above single chain partition functions are evaluated as, $Q_K[\psi_K] = V^{-1}\int d\mathbf{r} q_K(\mathbf{r}, 1)$, where $q_K(\mathbf{r}, s)$ is the solution of the diffusion equation,

$$\frac{\partial}{\partial s} q_K(\mathbf{r}, s) = R^2_{go,K}\nabla^2 q_K(\mathbf{r}, s) - N_K \psi_K q_K(\mathbf{r}, s) \tag{2.21}$$

subject to the initial condition $q_K(\mathbf{r}, 0) = 1$.

While the above formulation is exact, a *mean-field* approximation is typically made for computing the equilibrium characteristics (the model resulting from the approximation being termed as the self-consistent field theory [3]). In this approximation, the potentials, ψ_K are computed using the saddle point values of the fields w, π (denoted by w^*, π^*) given by,

$$w^* = \frac{\chi\rho_o}{2}\left[\phi_A(\mathbf{r}) - \phi_B(\mathbf{r})\right], \tag{2.22}$$

and π^* being a solution of

$$\phi_A(\mathbf{r}) + \phi_B(\mathbf{r}) - 1 = 0, \tag{2.23}$$

where, ϕ_k denotes the individual local (microscopic) composition field defined as, $\phi_K \equiv \hat{\rho}_k/\rho_o$. These compositions in the system are computed from the

solution of the above field theory as,

$$\langle \phi_K \rangle = \frac{1}{Q_K} \int_0^1 ds q_K(\mathbf{r}, s) q_K(\mathbf{r}, 1-s) \tag{2.24}$$

In this mean-field approximation, the free energy is given by,

$$F[\phi_A(\mathbf{r}), \phi_B(\mathbf{r})] = -m_A \ln Q_A(w^*, \pi^*) - m_B \ln Q_B(w^*, \pi^*) + \tag{2.25}$$

$$\int d\mathbf{r}[(\rho_{Ao} - \rho_{Bo}) w^*(\mathbf{r}) - i\rho_o \pi^*(\mathbf{r}) + \rho_o \chi^{-1} w^{*2}(\mathbf{r})]. \tag{2.26}$$

where the above can be viewed as a *density functional* approximation to the free energy.

In summary, the self-consistent field theory is a mean-field approach in which the bonded and non-bonded interactions in a polymeric system are converted into a field theory, and the partition function of the overall system is reduced to the partition function of a single chain under the influence of a fictitious potential fields (equations (2.22) and (2.23)). The equilibrium in this field theory entails self-consistent solutions of the potentials. Indeed, the potential fields are themselves functions of compositions (see equations (2.22), (2.23)). However, the compositions, ϕ_A and ϕ_B, are themselves determined by the potential field (2.24). Hence, equation (2.21) is evolved self-consistently, with the potentials being updated at every step, to their saddle point values ((2.22) and (2.23)), until convergence. More pertinently, the self-consistent field theory idea is equivalent to the physical representation, where self-consistent potential fields act on single chains, with the compositions of

the monomers themselves determined from the potential fields. This idea is exploited in our hybrid simulation approach (detailed in a later section).

2.3 Kinetic Theory Models

Despite the successes of mean-field theories for predicting equilibrium phenomena, they have had only limited success in studying dynamical behavior [39, 40]. In the last decade there have been isolated efforts to extend the above approaches to dynamical, non-equilibrium phenomena in multicomponent polymeric systems [50]. Most of these approaches are based upon a simple *diffusion equation* like perspective, with the time evolution of compositions evolved as,

$$\frac{\partial \phi}{\partial t} + \nabla \cdot (\mathbf{v}\phi) = D\nabla^2 \frac{\delta F}{\delta \phi}, \tag{2.27}$$

where, D is the diffusion constant for composition relaxation and $\mathbf{v}(\mathbf{r})$ represents the externally imposed flow field and F is the composition dependent free energy from mean-field theory (equation (2.26)), where the saddle point values of the potentials can be written in terms of composition values. In polymeric systems, the diffusion constants are typically nonlocal and the above equation is more appropriate in the generalized form,

$$\frac{\partial \phi}{\partial t} + \nabla \cdot (\mathbf{v}\phi) = \int dt' \int d\mathbf{r}' \Lambda \left(\mathbf{r}, \mathbf{r}'; t, t'\right) \frac{\delta F[\phi]}{\delta \phi \left(\mathbf{r}', t'\right)} \tag{2.28}$$

where $\Lambda(\mathbf{r}, \mathbf{r}'; t, t')$ is a generalized diffusion constant. Although the above continuum approaches are computationally efficient, they do suffer from fundamental shortcomings. Some limitations include the neglect of chain-chain

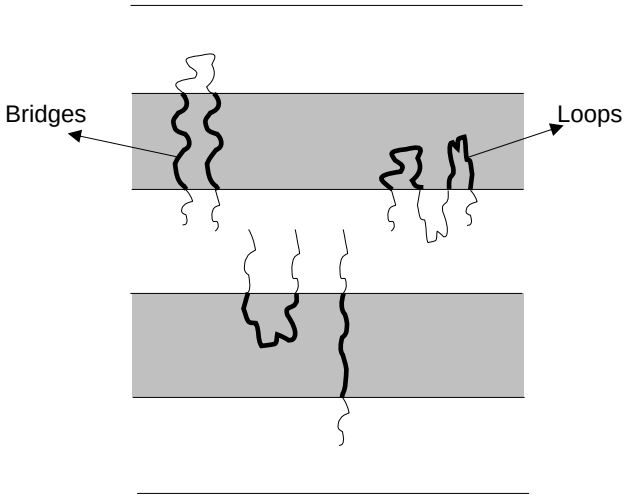

Figure 2.2: Bridges and loops formed in lamellar phase separated multiblock copolymers.

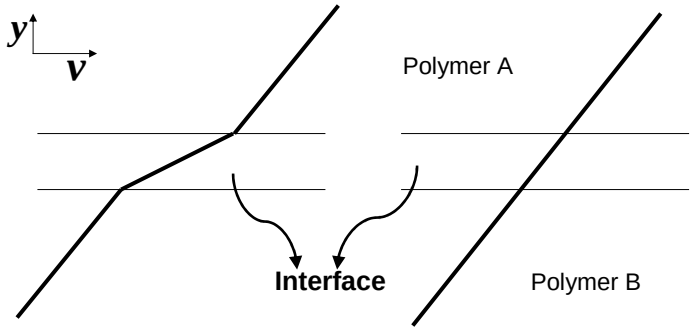

Figure 2.3: (a)Slip in the velocity at the interface of two immiscible homopolymers and (b) The linear simple shear velocity profile assumed by kinetic theory models.

interactions owing to the separation of entropic and energetic effects. Lack of such interchain interactions also ignores the topological constraints such as entanglements in dense polymer systems. Moreover, the collective evolution of order parameter ignores the molecular level dynamics. For instance, in phase separating multiblock copolymer (with number of blocks greater than 2) melts, the polymer chains in their lamellar phases, could have either a loop or a bridge configuration (see the schematic in Fig. 2.2). The number of loops and bridges in the lamellar phase (which depends strongly on the externally applied flow field) dictates both the mechanical and rheological properties of the system. However, the continuum models ignore the different chain conformational statistics, and their potentially different dynamics. Explicitly, the free energy in equation (2.26) is computed using the Gaussian chain partition functions (equations (2.19) and (2.2)), although the chains are clearly stretched (and do not follow Gaussian chain statistics) under external flow fields such as shear or extensional flows. Owing to the lack of a *constitutive equation*, it is also relatively complicated in such models to incorporate the compositional inhomogeneities induced changes in the velocity fields. At the simplest level, these models have used the viscous constitutive equations for computing the stress fields, which predict (for a symmetric system with identical bulk viscosities), linear simple shear flow (Fig. 2.3b). For instance, one of the effects of such composition inhomogeneities is the apparent slip at the interface of two immiscible polymers [55, 56, 103]. Figure 2.3a shows the slip velocity profile of two phase separated polymers (of equal viscosities). However, the lack of

chain conformation information and the lack of stress equations would make these models unsuitable to capture such effects.

2.4 Coarse-Grained Simulations of Polymers

2.4.1 Coarse-Grained Models

With the development of modern supercomputers and the computational power available today, there have been significant advances in the development of computer simulation approaches to study dynamics in simple fluids [13, 14, 21, 22]. Atomistic efforts have been undertaken in the context of polymeric systems involving (in the most detailed case), a complete description of polymer molecules with atomistic resolution of the interactions. Interactions typically include bonded and non-bonded intermolecular interactions typically parametrized as pair interaction potentials (such as spring forces, Lennard-Jones potentials etc.). For instance, a complete atomistic description of a polyethylene homopolymer chain is displayed in Fig. 2.4a, where the polymer molecule is modeled as a bonded carbon backbone with hydrogen atoms bonded to the carbon atoms. Equilibrium and non-equilibrium sampling of the system is usually performed by simulating the system using Monte Carlo (MC) or molecular dynamics (MD) simulation techniques. One of the shortcomings of such simulations is the enormous computational power required to evolve sufficiently large systems at realistic densities [13, 14]. Even simulation of equilibrium systems to study structure and thermodynamics of multicomponent polymers proves an enormous challenge. It is particularly

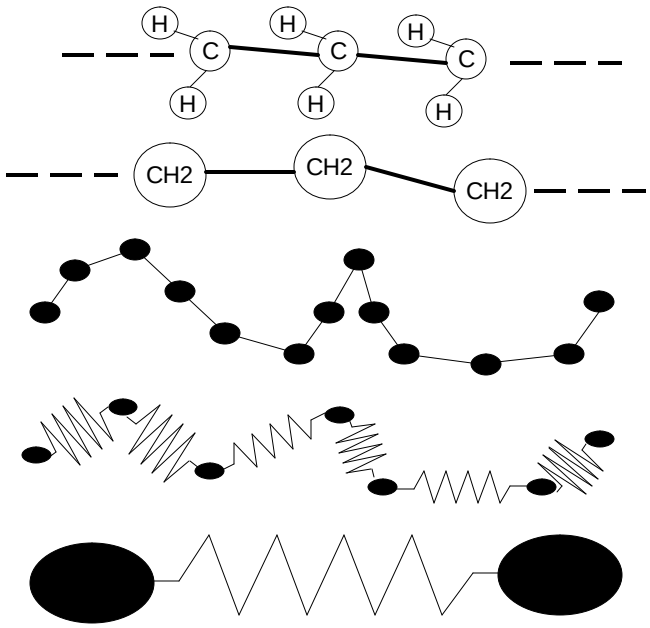

Figure 2.4: Various levels of coarse-graining of a polymer molecule into (a) Atomistic resolution, (b) United atom (CH_2), (c) Bead-rod model, (d) Bead-spring model and (e) Dumbell model.

difficult to study dynamical properties in multiphase, inhomogeneous systems owing to the long time scales for composition dynamics.

An array of research has focused on reducing the computational requirement of atomistic scale models. This has given rise to various particle based approaches in which the polymer chain is modeled at a coarse-grained level [22, 80]. At the simplest level of coarse-graining, early researches have employed a united atom approach wherein each CH_2 unit of a polyethylene molecule is grouped together as a single effective particle (see Fig. 2c) with *ef-*

fective interactions between various CH_2 units. Standard Monte Carlo or molecular dynamics techniques can then be employed to evolve the coarse-grained particles, and track their equilibrium/dynamical properties. Typically, further coarse-graining of single polymer molecule is carried out, where the chemical details of the polymer are ignored and instead the polymer is replaced by different micromechanical models [45]. The extent of coarse-graining could range from a bead-rod representation of the polymer to bead-spring models to dumbell model (in the increasing order of coarse-graining). In the bead-rod model (also refered to as the freely jointed chain model), the distance between two adjacent beads in the polymer chains is assumed a constant [23, 40]. Each bead in the bead-rod model constitutes a fixed number of monomeric entities ($\sim$5), with the rod representing the average bond length between the *sub-molecules* represented by the beads. More extensive coarse-graining results in the bead-spring model in which each bead representing 10 or more backbone atoms lumped into a bead. The statistical fluctuations in the bond lengths of such entities appear as a spring force between the beads. At the coarsest level, polymer chains have been just modeled as a dumbell with 2 beads connected by a spring (Fig. 2.4e). Such models have been used to probe, at the simplest level, the effect of flexibility and connectivity upon the equilibrium and dynamical properties of simple fluid systems.

Each of these coarse-grained descriptions of polymer molecule has been employed to address different types of phenomena in polymeric systems. For instance, the dumbell model for polymer molecule has been widely used to

study complex flow situations of homogeneous polymeric systems [45]. The dumbell model provides the simplest avenue to incorporate the effects of viscoelasticity in the study of dynamical phenomena. However, the lack of detailed information on polymer chain conformations in a dumbell model makes it largely unfit for the study complex viscoelastic phenomena, as well as the structure and thermodynamics in multiphase systems. The bead-rod model on the other hand has typically been used to study the single polymer chain phenomena under external flow fields including extensional flow and shear flows [23]. The relatively detailed description of polymer molecule conformation and interactions makes the bead-rod model suited for studying dynamics involving many polymeric degrees of freedom such as the study of single polymer/DNA/protein molecule deformations under external flow fields. However the model proves too detailed to study realistically dense systems and thermodynamics in multicomponent systems. The bead-spring model provides a compromise between the preceding models and have been used to study a wide range of systems, including complex flows in viscoelastic homopolymer systems and single molecule deformations under external flow fields. These versatile features of the bead-spring model have prompted us to use this model for the multiscale hybrid simulation approach detailed later. Moreover, the previously outlined mapping of the bead spring model to the Gaussian thread model allows us to incorporate this model in the study of multicomponent polymeric systems.

2.4.2 Brownian Dynamics Simulations for Polymer Dynamics

The Brownian dynamics simulation technique is used extensively in the researches outlined for the study of dynamical phenomena in such bead spring systems. In this section, we review the Brownian dynamics simulations approach for bead-spring polymers.

The monomeric entities in polymer molecules change their positions randomly due to the thermal agitation arising from molecular collisions with both the solvent molecules and other monomers in the system. This motion, termed as the Brownian motion, is the dominant dynamical process in polymer solutions and melts. Models of Brownian motion can be studied by developing coupled dynamical equations for the motion of the Brownian particles and the surrounding fluid molecules [40]. However, due to the separation of timescales controlling the dynamics of the solvent molecules and polymeric monomers, the solvent dynamics is usually *projected* out, leading to an effective phenomenological equation of motion for the monomers [40]. One such phenomenological equation for the Brownian motion, is termed the Langevin equation and describes the dynamics of a Brownian particle (whose position is denoted as $x(t)$) [40].

$$\zeta \frac{dx}{dt} = -\frac{\partial U}{\partial x} + f(t) \tag{2.29}$$

In the above equation, the right hand side includes the contributions from, $f(t)$, the random force due to the collision of fluid molecules with the Brownian particle and the potential gradient driving the motion, dU/dx (with U including all inter-molecular and intra-molecular interactions and externally

applied potentials). Physically, the above equation represents a force balance, with the left hand side being the drag force, with ζ, the mobility coefficient (for Stoke's drag $\zeta = 6\pi\eta_s a$), balanced by the potential and random forces, where a and η_s are the spherical radius of the particle and the solvent viscosity respectively. In Brownian dynamics, the random force $f(t)$ is usually assumed to be Gaussian distributed and characterized by the following moments,

$$\langle f(t) \rangle = 0,$$

$$\left\langle f(t) f(t^{'}) \right\rangle = 2\zeta k_B T \delta(t - t^{'}) \tag{2.30}$$

The above Brownian dynamics model can be coupled with the various single chain models for polymer molecule (described in the previous subsection) in order to study dynamical phenomena in polymers. In most of our research, we have employed the Rouse model description of polymer chain. Some of our research have also used an alternate bead-spring model known as the FENE model. In the following section we provide a brief description of the Rouse and FENE bead-spring models under the Brownian dynamics framework.

2.4.3 The Rouse Model

The Brownian dynamics model for the case of bead-spring model without hydrodynamical interactions and other intermolecular interactions is known as the Rouse model [24]. In the Rouse model, the polymer chain is represented as a set of N identical beads connected via $N-1$ Hookean springs. This model, first developed by Rouse, was used to model the dynamics of dilute polymeric

solutions. The equation of motion of the beads is described by the generalized Langevin equation (see equation (2.29) above) as [40],

$$\frac{\partial}{\partial t}\mathbf{R}_n(t) = \sum_m \mathbf{H}_{nm} \cdot \left(-\frac{\partial U}{\partial \mathbf{R}_m} + f_m(t) \right) + \frac{1}{2} k_B T \sum_m \frac{\partial}{\partial \mathbf{R}_m} \cdot \mathbf{H}_{nm} \qquad (2.31)$$

where $(\mathbf{R}_1, \mathbf{R}_2, ..., \mathbf{R}_N) = \mathbf{R}_n$are the positions of the beads and $\mathbf{H}_{nm}$ and U are the mobility tensor and the interaction potential between the beads respectively. In the Rouse model, the only interactions between different beads are spring forces between adjacent beads, and hence the interaction potential is given by the potential energy stored in the spring as,

$$U = \frac{k}{2} \sum_{n=2}^{N} (\mathbf{R}_n - \mathbf{R}_{n-1})^2. \qquad (2.32)$$

Rouse model neglects interactions, and the mobility tensor is given as,

$$\mathbf{H}_{nm} = \frac{\mathbf{I}}{\zeta} \delta_{nm}, \qquad (2.33)$$

where ζ is the friction coefficient of the bead and k, the spring constant given by,

$$k = \frac{3 k_B T}{b^2}, \qquad (2.34)$$

mimics the Gaussian thread model (see equation (2.3)). Using the above equations, the dynamics of the internal beads $(2, 3, ..., N-1)$ is given by,

$$\zeta \frac{d\mathbf{R}_n}{dt} = -k(2\mathbf{R}_n - \mathbf{R}_{n+1} - \mathbf{R}_{n-1}) + f_n, \qquad (2.35)$$

and for the end beads ($n = 1$ and N),

$$\begin{aligned} \zeta \frac{d\mathbf{R}_1}{dt} &= -k(\mathbf{R}_1 - \mathbf{R}_2) + f_1 \qquad (2.36) \\ \zeta \frac{d\mathbf{R}_N}{dt} &= -k(\mathbf{R}_N - \mathbf{R}_{N-1}) + f_N. \end{aligned}$$

Here f_n is the random force characterized by the moments described in equation (2.30).

While the dynamics of Rouse model is a simple, easy to implement and a computationally efficient model, it suffers from some shortcomings. The neglect of hydrodynamical interactions makes the model inappropriate for the study of dilute polymer solutions. However it has emerged as a successful model in the dynamics of polymer melts, where hydrodynamic interactions are expected to be screened [40]. The lack of non-bonded interparticle interactions also neglects excluded volume interactions and makes the Rouse model inappropriate to capture effects due to topological constraints such as entanglements. Moreover, the Hookean springs could in principle be stretched infinitely under external flow fields which creates computational artifacts making the model inappropriate for strong flow conditions. For the same reason, viscoelastic effects such as shear thinning are not captured in the Rouse model. However, methods have been developed to address the above shortcomings, for instance, it is straightforward to incorporate finite extensibility through the FENE model detailed in the following section. The reptation motion of entangled systems can easily be incorporated into a Rouse model by choosing higher mobility coefficients for the motion of the bead along the polymer chain and a lower value perpendicular to it. The simplicity and effectiveness of the Rouse model in representing polymeric melts have prompted us to employ this model in our hybrid simulation approach (detailed in a later section).

2.4.4 The FENE Model

As mentioned in the preceding section, in Rouse model the Hookean springs are infinitely extensible, which prevents observation of viscoelastic features present in real systems. These discrepancies arise from the physical feature that real polymer molecules could at most only be extended to their fully stretched length under external flow. Hence, the linear spring force law in Rouse model is inapplicable at large extensions of polymer chains. This feature is improved upon by introducing a finitely extensible nonlinear spring force, which incorporates a *spring-extension* dependent spring constant. A new parameter b_f is introduced which governs the maximum allowed extensibility of each FENE spring. The spring force in a FENE model reads [45],

$$\mathbf{F}_S = \frac{k\mathbf{Q}}{1 - \mathbf{Q}^2/(b_f k_B T/k)} \tag{2.37}$$

where $b_f k_B T/k$ is the square of the maximum allowed spring extension and the FENE b_f-parameter is a dimensionless parameter describing the finite extensibility of the FENE springs. In the limit $b_f \to \infty$, the Rouse model is regained with a spring constant k. The $\mathbf{Q}^2$ dependent prefactor of $\mathbf{Q}$ in the above equation is the effective spring constant of the FENE spring. Note that the b_f parameter is chosen in accordance with the physical nature of the particular polymer molecule under consideration. An estimate of the parameter was derived by Ottinger for a polymer with pure carbon backbone by making use of the number of carbon bonds and the bond angles between two carbon bonds in the polymer molecule. It was shown that the b_f paramater was roughly equal to the number of monomer units represented by a single bead.

While FENE model has been widely used to study viscoelastic behavior in a variety of polymeric systems, the singularity in equation (2.37) of the model requires some computational precautions. Indeed, for a finite time step, there is a non-zero probability that the spring extension could exceed the maximum prescribed extension. In our simulations, we have employed a semi-implicit, predictor-corrector technique developed by Shaqfeh and coworkers [25]. We provide the details of this technique in a later section.

2.5 Some Recent Developments

Before we present our approach, we discuss briefly some more recent developments for addressing dynamics in multicomponent polymers. Few of the more promising numerical approaches developed in the last decade include novel techniques like dissipative particle dynamics (DPD) [80], cell dynamics [15, 16] etc. Dissipative particle dynamics is a mesoscale simulation in which a set of interacting particles (beads) is considered, whose time evolution is governed by Newton's equation of motion. DPD uses artificial soft-core repulsive potentials to model interactions between different beads [80]. This results in an effective speeding up of simulations typically by an order of magnitude. The DPD approach has been successfully used for qualitative investigations of microphase separated ordered structures in block copolymer melts. The Hookean and FENE bead-spring (with DPD potentials) models have been used to obtain various equilibrium mesophases in symmetric and asymmetric block copolymer melts. Although the DPD approach shows enormous prospect in studying

equilibrium and dynamical phenomena in multicomponent polymeric systems, they have some shortcomings. For instance, the artificial soft-core potentials employed in DPD system lead to artificially high fluid phase compressibilities, loss of topological constraints between the chains, high fluctuation effects and often a loss of connection to the chemical details of the underlying complex fluid.

More recently, Kawakatsu and coworkers [52] proposed a new approach which combines polymer self-consistent field theory with reptational dynamics arising due to entanglements. The latter method has been used successfully to model the fast flow dynamics and molecular conformational changes occurring in the shear of entangled polymer brushes, however this method is extremely expensive and further applications have not been reported. Schnidman and coworkers [53] have also been developing a dynamical version of the self-consistent field theory which allows for a versatile simulation of dynamical properties of multicomponent polymeric materials. Here again, studies beyond the first application have not been reported.

2.6 The Self Consistent Brownian Dynamics Approach

As seen from the overview in the previous section, development of numerical approaches to study equilibrium, dynamical and rheological phenomena in multicomponent polymeric systems has been the focus of many recent researches. In the following, we elaborate our contributions in developing a simulation technique [54, 103] called the *Self-consistent Brownian Dynam-*

ics (SCBD) approach, which combines single-chain based Brownian dynamics simulations along with a field-theoretical approach to address the rheology of inhomogeneous polymeric systems. In this approach, the polymer chain is modeled at a coarse-grained level, as a set of beads and springs, with however, the interactions between different beads are now accounted for by a potential acting on each bead. As will be explained below, this method is founded upon polymer self-consistent field theory [2, 3], and the potential is computed in a self consistent manner to render this mapping exact at equilibrium. One of the advantages of this framework is that it avoids the need to simulate many chains and instead non-interacting copies of single polymer chain are evolved in combination with a hybrid continuum-molecular framework. Moreover, it is also possible to incorporate this framework within alternate single-chain Brownian dynamics simulation approaches to capture (approximately) the effects arising from entanglements, hydrodynamical interactions etc.

Our approach combines the idea behind Doi's dynamical mean field theory [40] (for rodlike polymers) along with self consistent field theory [2] for flexible polymers to develop a method that can predictively model the dynamical characteristics of flexible inhomogeneous polymeric systems. In Doi's theory, the dynamical properties of *interacting* rodlike molecules are modeled by the dynamics of *non-interacting* macromolecules, which are instead acted upon by the influence of an external potential field. This potential field is an explicit function of the distribution function and is specified by Onsager's self-consistent mean field theory for interacting rods. Along same lines, in our

approach for flexible polymers the interplay between the thermodynamics and dynamical properties are tracked by the Brownian motion of a single polymer molecule in a potential field $W(r)$ which account for the interactions between unlike polymer molecules. This prescription for the self consistent potential ($W(r)$), is dictated by consideration of polymer self-consistent field theory of the appropriate polymeric system under investigation. However, in contrast to rodlike systems, an explicit relation between self consistent potential and the distribution function of molecules cannot be derived for flexible interacting polymers and hence an analytical theory similar to Doi cannot be developed for flexible polymers. Instead, we employ the self-consistent field theory idea (developed in section 2.2 for a system of a binary asymmetric blend) in a numerical framework to complement this idea. Hence, our approach incorporated the two main ingredients to capture dynamical phenomena in multicomponent systems, namely, the interactions (through self-consistent field theory) that accommodate the phase separation phenomena and the automatic inclusion of chain conformation dynamics using Brownian dynamics simulation alongside single chain models. In the following subsections, we detail a hybrid simulation scheme that computes the potentials on the fly based on the statistics of the flexible polymers.

2.6.1 Single Chain Evolution

Self-consistent field theory is an equilibrium theory predicting the equilibrium properties of interacting polymer chains. To extend the above theory

to predict non-equilibrium properties, we propose to perform non-equilibrium Brownian dynamics simulations. In the field theory developed in section 2.2, each polymer chain is assumed to be a continuous Gaussian curve. However, to model the dynamics of polymer chain we need to resort to one of the various single-chain Brownian dynamics models discussed earlier. In the Rouse bead-spring model for example, the polymer chain is modeled as a set of N beads connected linearly by $N-1$ springs. This model, in its continuous limit (large N limit) corresponds to the Gaussian thread representation of the polymer. To model the dynamics of the polymer chain in the presence of a potential field, the dynamical equation of motion for the beads are specified by the Langevin equation [40],

$$\zeta\left(\frac{d\mathbf{R}_\alpha^i}{dt}\right) = \mathbf{F}_s + \mathbf{F}_P + \mathbf{F}_R \tag{2.38}$$

where, $\mathbf{R}_\alpha^i$ is the coordinate of the i^{th} bead of α^{th} chain, ζ is the mobility coefficient. In the above equation, terms on the right hand side express a balance between the frictional force experienced by a bead moving at a velocity $d\mathbf{R}/dt$ and other internal forces acting on the bead, viz., $\mathbf{F}_R$, a white noise mimicking the random collisions, $\mathbf{F}_s$, the spring force in the bead-spring model $\equiv 3k_BT[\mathbf{R}_\alpha^{i+1} - 2\mathbf{R}_\alpha^i + \mathbf{R}_\alpha^{i-1}]/b^2$ acting on each bead and $\mathbf{F}_P$ represents the external potential force arising from the self-consistent field. Recall, for a polymer blend, our earlier derivation resulted in the expression for the potential field. At a given instant the potential $W(\mathbf{R}_\alpha^i)$ on each bead (statistical

segment) is given by the field theory developed in section 2.2 as,

$$W(\mathbf{R}_\alpha^i) = -\pi(\mathbf{r}=\mathbf{R}_\alpha^i) - w(\mathbf{r}=\mathbf{R}_\alpha^i), \qquad \text{for type } A \text{ chains} \quad (2.39)$$

$$= -\pi(\mathbf{r}=\mathbf{R}_\alpha^i) + w(\mathbf{r}=\mathbf{R}_\alpha^i), \qquad \text{for type } B \text{ chains} \quad (2.40)$$

where, α indexes different chains. Note further that the potentials π and w themselves in the saddle point approximation, are explicit functions of volume fractions, given by the equations (2.22) and (2.23). To accommodate this characteristic, we propose a phenomenological prescription for the evolution of the chemical potentials such that they take their saddle point values at equilibrium. Explicitly, they are evolved on the discretized lattice, by the following equations,

$$\frac{dw(\mathbf{r})}{dt} = \Gamma_1 \left[\frac{\chi\rho_o}{2} \left(\phi_A(\mathbf{r},t) - \phi_B(\mathbf{r},t) \right) - w(\mathbf{r}) \right] \quad (2.41)$$

$$\frac{d\pi(\mathbf{r})}{dt} = \Gamma_2 \left[\phi_A(\mathbf{r},t) + \phi_B(\mathbf{r},t) - 1 \right] \quad (2.42)$$

where, Γ_1, Γ_2 are fictitious mobilities that drive the potential evolution appropriately such that, the collective fields (w, π) are evolved slower than the individual beads. The idea is quite similar to the one employed in Car-Parrinello methods [158], where the electron response is evolved with a fictitious mass. Note here, that our system consists of many copies of discrete bead-spring chains. We adopt a space fixed lattice discretization of the volume to determine the volume fractions $\phi_k(\mathbf{r},t)$, by explicitly counting the number of beads of type A and B, at any given instant t. For example the composition of A beads at the lattice point i, j is proportional to sum over all the beads inside

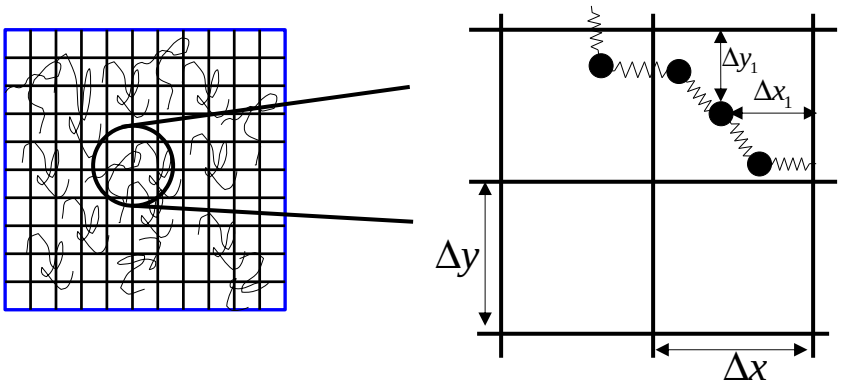

Figure 2.5: Coarse-graining of the simulation box into a 2D lattice with the positions and number of polymeric beads inside a *bin* dictating the values of the quantities of interest (like composition and/or stress fields) at each lattice point.

the four bins surrounding this lattice point. A better way to compute the composition would be to include a bead position dependent weight fraction into the summation. This is explained schematically in Fig. 2.5, where the contribution of the bead to the composition at lattice point i, j is given by the ratio of the area ΔA_1 ($=\Delta x_1 \times \Delta y_1$) to the total area of the bin ΔA ($=\Delta x \times \Delta y$). Note that, the bead inside a bin contributes to the composition at all the four lattice points defining the bin.

2.6.2 Self Consistent Velocity Field $\mathbf{v}(\mathbf{r})$ Evolution

In order to study dynamical phenomena in polymeric systems under the influence of external flow field, we need to incorporate a velocity term into

the evolution equation (2.43) as,

$$\zeta\left(\frac{d\mathbf{R}_\alpha^i}{dt}-\mathbf{v}\left(\mathbf{R}_\alpha^i\right)\right)=\mathbf{F}_s+\mathbf{F}_P+\mathbf{F}_R \tag{2.43}$$

Here, the left hand side denotes the frictional force experienced by a bead moving at a velocity $d\mathbf{R}/dt$ with respect to a medium moving at a velocity $\mathbf{v}(\mathbf{r})$. For inhomogeneous systems, the velocity field $\mathbf{v}(\mathbf{r})$ in the above equation can, in general, be different from the macroscopically imposed velocity field. For example, in situations of slip at polymer-polymer interfaces, the velocity field is a complex function of the distance from the interface, whereas the applied flow is a simple shear field. In general, these differences can be attributed to the interplay between compositional inhomogeneity and molecular level dynamics, necessitating a self-consistent determination of the velocity field.

In our system, the composition field evolves due to the evolution of the potential fields and the individual chains. To determine the self-consistent velocity field we propose a phenomenological evolution for the computation of velocity field $\mathbf{v}(\mathbf{r})$ (defined on the coarse-grained lattice) such that, at steady state the Cauchy stress equation [45] is satisfied, *.i.e.* $\nabla\cdot\tau(\mathbf{r})=\sum_i\phi_i\nabla W_i(\mathbf{r})$, where $\tau(\mathbf{r})$ corresponds to the total elastic stress and $W_i(\mathbf{r})$ represents the potential acting on the component i. Note that, in a completely homogeneous system (where $\nabla W(\mathbf{r})=0$), this expression enforces the Cauchy stress equation inside the system at steady state. We compute the stress, $\tau(\mathbf{r})$, at each lattice cell using Kramer's expression for elastic stress given by [45],

$$\tau(\mathbf{r})=\langle\sum_{i,\alpha}[(\mathbf{R}_\alpha^{i+1}-\mathbf{R}_\alpha^i)(\mathbf{R}_\alpha^{i+1}-\mathbf{R}_\alpha^i)]\delta(\mathbf{r}-\mathbf{R}_\alpha^i)\rangle/(2\Delta s) \tag{2.44}$$

where Δs denotes the discretization of the contour variable s and the δ function ensures the computation of the quantity inside the summation, within the vicinity of $\mathbf{r}$. In our simulations, this is performed within every bin of the coarse-grained lattice (similar to the computation of $\phi(\mathbf{r})$ described earlier). The velocity field $\mathbf{v}(\mathbf{r})$ is then evolved through an iterative procedure of the form,

$$\nabla^2 \mathbf{v}_{m+1}(\mathbf{r}) = \nabla^2 \mathbf{v}_m(\mathbf{r}) - \epsilon[\nabla \tau_m(\mathbf{r}) - \nabla W_m(\mathbf{r})] \tag{2.45}$$

until convergence. Here, ϵ denotes a phenomenological time scale for self consistent velocity field evolution similar to the mobilities Γ_1 and Γ_2 (in equations (2.41) & (2.42)), and is chosen along same lines it ensures that the collective velocity fields are evolved slower than the individual beads. Here, the subscript m denotes the current iteration number. Note that, such a phenomenological evolution ensures the convergence of velocity to a steady state value such that the Cauchy stress equation is satisfied at steady state. This renders such an approach not directly suitable to capture the unsteady state characteristics and transients.

2.6.3 Schematic Representation of SCBD

The preceding steps of SCBD are put together in an algorithm and is explained schematically in the flow chart representation on Fig. 2.6. In the first step, the beads are evolved from random initial conditions using the Langevin equation. In step 2 we carry out a binning procedure in the system and the coarse-grained volume fractions at each lattice point are computed

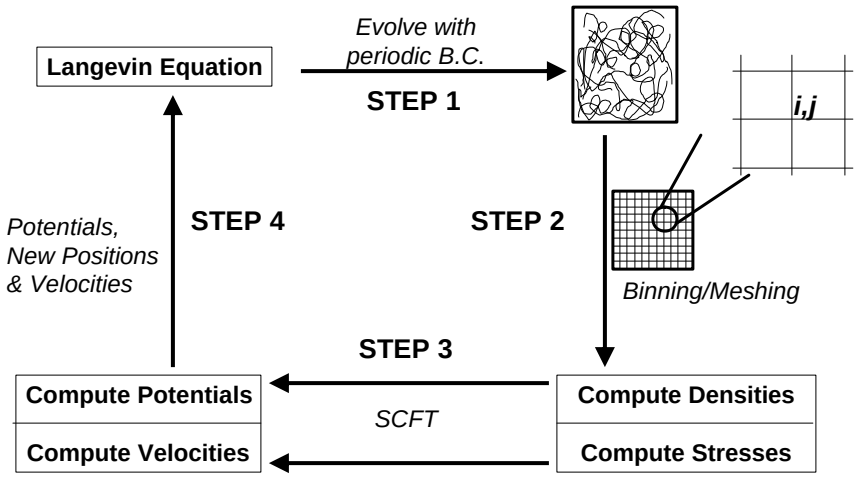

Figure 2.6: Schematic representation of the dynamical evolution of a polymeric system using self-consistent Brownian dynamics. The four steps shown in the figure, are carried out at each timestep, in the order displayed.

instantaneously based on the number and position of the beads within the 4 bins surrounding lattice point. The stress at each lattice point inside the system is then computed using the Kramer's expression for stress (equation (2.44)) for all the beads within the vicinity of the lattice point i, j (i.e. inside the four bins surrounding i, j). Once the composition and stress fields inside the system are computed, the self-consistent potentials are evolved using equations (2.41) and (2.42) in step 3. In the final step, the updated values of self-consistent potentials and velocities are used in the Langevin equation to evolve the beads.

2.7 Numerical Implementation of Brownian Dynamics: Special Cases

2.7.1 Brownian Dynamics of FENE chains

The evolution procedure for a FENE system of chains is computationally tricky owing to the singularity encountered in the FENE spring force law (see equation (2.37)). Moreover, as mentioned earlier, for a finite value of the time step there exists a non-zero probability that the springs could stretch beyond their maximum allowed extension. In order to ensure that such a situation is not realized, the first step of our algorithm, namely, the Brownian dynamics evolution of the beads is split into three separate steps: a) Brownian dynamics evolution of center of mass of the single chain; b) Evolution of the connector vectors (Q_i) of the single chain; and c) Reformation of the chain using the evolved center of mass and connector vectors. The dynamical equation of motion of the center of mass is now specified by the Langevin equation,

$$\zeta\left(\frac{d\mathbf{R}_{cm,\alpha}}{dt} - \mathbf{v}(\mathbf{R}_{cm,\alpha})\right) = \frac{1}{N}\left(\sum_{i=1}^{N}(\mathbf{F}_S^i + \mathbf{F}_P^i + \mathbf{F}_R^i)\right) \tag{2.46}$$

where $\mathbf{R}_{cm,\alpha}$ is the center of mass of the polymer chain and $\mathbf{v}_{cm}$ is the velocity of the center of mass. The right hand side of the above equation gives the bead averaged forces representing the effective spring force, potential force and random force acting on the center of mass of the chain. After the evolution of the center of mass, the connector vectors are now evolved to obtain the new connector lengths. This is effected by a semi-implicit, predictor-corrector method developed by Shaqfeh and coworkers [25]. The predictor step is the

first explicit step in obtaining the new connector vectors. This step is given as,

$$\zeta\left(\frac{d\mathbf{Q}_{\alpha}^{i}}{dt}-v(\mathbf{Q}_{\alpha}^{i})\right)=\mathbf{F}_{Q,S}^{i}+\mathbf{F}_{Q,P}^{i}+\mathbf{F}_{Q,R}^{i} \tag{2.47}$$

where $\mathbf{F}_{Q,R}$, $\mathbf{F}_{Q,S}$, and $\mathbf{F}_{Q,P}$ specify the random, spring and the potential forces acting along the connector spring,

$$\begin{aligned}\mathbf{F}_{Q,S}^{i} &= \mathbf{F}_{S}^{i+1}-\mathbf{F}_{S}^{i}\\ \mathbf{F}_{Q,P}^{i} &= \mathbf{F}_{P}^{i+1}-\mathbf{F}_{P}^{i}\\ \mathbf{F}_{Q,R}^{i} &= \mathbf{F}_{R}^{i+1}-\mathbf{F}_{R}^{i}\end{aligned} \tag{2.48}$$

At the end of the explicit step, the length of the connector springs could be greater than the maximum allowed extension for the FENE spring. The following corrector step is applied to help overcome this problem. The corrector step, detailed in [25], requires the solution of the following cubic equation,

$$\left|\bar{\mathbf{Q}}_{i}\right|^{3}-R\left|\bar{\mathbf{Q}}_{i}\right|^{2}-b_{f}(1+\frac{1}{2}(\delta t))\left|\bar{\mathbf{Q}}_{i}\right|+b_{f}\times R=0 \tag{2.49}$$

Here, $\left|\bar{\mathbf{Q}}_{i}\right|$ specifies the magnitude of the new set of connector vectors, b_f is the dimensionless extensibility and R is the magnitude of the connector vectors at the end of the explicit step. Note that the above cubic equation has a unique solution between 0 and $\sqrt{b_f}$. Choosing this solution gives the magnitude or the length of the connector vector. The direction of the connector vector however is specified by the explicit, predictor step outlined above. Once the new set of connector vectors is obtained, the polymer chain is re-created using

the following two equations,

$$\begin{aligned} \mathbf{R}_{\alpha}^{1} &= \mathbf{R}_{cm,\alpha} - \sum_{j=1}^{N-1} \frac{N-j}{N} \mathbf{Q}_{j}, \\ \mathbf{R}_{\alpha}^{\nu} &= \mathbf{R}_{\alpha}^{1} + \sum_{j=1}^{\nu-1} \mathbf{Q}_{j}, \quad \text{for } \nu = 2, 3, ..., N \end{aligned} \tag{2.50}$$

2.7.2 Oscillatory Shear

In chapter 7, we have applied the above self-consistent Brownian dynamics algorithm to simulate the oscillatory shear on block copolymers. The algorithm detailed in section 2.6 focuses on the simple, steady shear version. In the present section, we elaborate on the modifications for the computation of the self-consistent velocity field in order to incorporate an oscillatory shear field. We consider the situation of an externally applied oscillatory strain of the form,

$$\gamma = \gamma_o \sin(\omega t). \tag{2.51}$$

The shear rate and the applied oscillatory shear velocity is then given by,

$$\dot{\gamma} = \gamma_o \omega \cos(\omega t). \tag{2.52}$$

$$v_x(y) = y \gamma_o \omega \cos(\omega t). \tag{2.53}$$

where γ_o is the strain amplitude, ω is the shear frequency, x denotes the direction of velocity and y is the shear gradient direction. For our polymeric system, we assume that the self-consistent velocity at any instant would comprise of two components, an in-phase component (with amplitude = $v_{x,1}(y)$)

and an out-of-phase component (with amplitude = $v_{x,2}(y)$). The total velocity is then given by the sum of the two components as,

$$v_x(y) = v_{x,1}(y)\cos(\omega t) + v_{x,2}(y)\sin(\omega t) \tag{2.54}$$

Note that $v_x(y)$ is used to find the center of mass velocity (in equation (2.46)) and the connector velocity (in equation (2.47)). The velocity amplitudes are then evolved self-consistently using a phenomenological dynamical prescription which prescribes that at steady state, the ensemble and *time averaged*, y-gradients of both the in-phase and out-of-phase components of the shear stress $\tau_{xy}(\mathbf{r})$ vanish, where $\tau_{xy}(\mathbf{r})$ corresponds to the total elastic shear stress computed at each lattice cell using Kramer's expression for elastic stress (equation (2.44)). Note here that the in-phase and out-of-phase components of the shear stress (σ_1 and σ_2 respectively) must be time averaged for a integral multiple of the time period T($= 2\pi/\omega$).

$$\begin{aligned}\sigma_1(y) &= \frac{2}{T}\int_0^T \tau_{xy}(y)\cos(\omega t) \\ \sigma_2(y) &= \frac{2}{T}\int_0^T \tau_{xy}(y)\sin(\omega t)\end{aligned} \tag{2.55}$$

The velocity amplitudes are then evolved self-consistently using the following iterative procedure of the form,

$$\begin{aligned}\nabla^2 v_{x,1}^{m+1}(y) &= \nabla^2 v_{x,1}^{m}(y) - \epsilon\nabla\sigma_1^m(y)] \\ \nabla^2 v_{x,2}^{m+1}(y) &= \nabla^2 v_{x,2}^{m}(y) - \epsilon\nabla\sigma_2^m(y)]\end{aligned} \tag{2.56}$$

Such a phenomenological approach ensures the constancy of stress throughout the system at steady state, and captures other time-periodic behavior. After the steady state is attained we compute the storage and loss modulus of the system using the following equations,

$$G^{'}(y) = \frac{1}{\gamma_o}\frac{2}{T}\int_0^T \tau(y)\sin(\omega t),$$
$$G^{''}(y) = \frac{1}{\gamma_o}\frac{2}{T}\int_0^T \tau(y)\cos(\omega t). \tag{2.57}$$

2.8 Summary

In summary, we have developed a novel computational approach to simulate the dynamics and rheology of inhomogeneous polymer phases of multicomponent polymers. By combining a hybrid bead-spring model for polymer chain, field theoretical framework for polymer interactions and a self-consistent procedure for determining $\mathbf{v}(\mathbf{r})$, the above simulation technique incorporates three features which are essential to capture the dynamics in inhomogeneous polymeric systems, viz., (i) A microscopic description for the dynamics of polymer chains, capable of coarsely capturing polymer conformation statistics; (ii) The intermolecular interactions responsible for the compositional inhomogeneity; (iii) Compositional inhomogeneity induced changes to the velocity fields. In the following chapters we display our results pertaining to the equilibrium and dynamical properties of homopolymer blends, compatibilized polymer droplet deformation, shear induced phase behavior in ternary

(homopolymers+block copolymer) polymer blends and shear induced reorientation in block copolymer systems.

Chapter 3

Interfacial Phenomena in Polymer Blends

3.1 Introduction

Blending of two or more polymers is commonly used to enhance the technological applications of polymers. Melt blending of polymers allows one to create novel materials with advanced properties which result in their enhanced performance and marketability [27–29]. However, blending dissimilar polymers often leads to immiscible phase separated systems, with the resulting inhomogeneous system comprising of many interfaces between regions of different compositions. The static and dynamical properties of such interfaces typically differ from the corresponding bulk properties of either of the homopolymers, and play a crucial role in determining the material properties and processing of the blend [27, 28, 67]. Consequently, it is important to develop a fundamental understanding of different parameters on these characteristics.

A large literature of theoretical and experimental studies has focused on the understanding of interfacial properties of polymer blends [2, 3, 28, 40, 67, 68, 103]. Static/equilibrium properties of polymer-polymer interfaces in binary polymer blends are well described by self consistent field theory approaches [3] detailed earlier. Specifically, Helfand and Tagami [111] were the first to

consider interfaces of $A + B$ polymer blends and use self-consistent field theory to predict the composition profile, interfacial thickness and the interfacial tension of such interfaces. Their expressions for interfacial thickness (a_I) and interfacial tension (γ) in polymer blends read,

$$a_I = 2b/(6\chi_{AB})^{1/2} \tag{3.1}$$

$$\gamma = \frac{k_B T}{b^2}(\chi_{AB}/6)^{1/2} \tag{3.2}$$

where, χ_{AB} is the Flory interaction parameter characterizing the degree of incompatibility. While the above mean field theories typically represent phase separation phenomena in incompressible systems, more refined *equation of state* theories such as the Sanchez-Lacombe lattice fluid models [19] have generally accounted for finite compressibility effects by developing pressure-volume-temperature relationships for the components and their mixtures using an equation of state.

While the above models predict the equilibrium characteristics as a function of the degree of immiscibility of the components (characterized at the simplest level by the Flory interaction parameter, χ_{AB}), the nonequilibrium response of polymer blend interfaces is much less understood. In contrast, experiments are replete with intriguing observations on dynamics of polymer blend interfaces. These include, shear-induced mixing, demixing and closed-loop miscibility curves [35, 36, 60, 61], network formation in phase separated polymer blends, slip and low mixing viscosities in polymer blends [62, 63] etc. While phenomena such as shear-induced mixing, demixing and network forma-

tion result from the effect of viscoelasticity upon thermodynamical and structural properties [9], slip and low mixing viscosities in polymer blends result from the impact of compositional inhomogeneity on the dynamical properties [56]. While the former class of problems has had some microscopic and phenomenologically based theoretical efforts [60, 61], the latter has had comparatively fewer microscopic theories and predictions [56]. Moreover, there is still a lack of a unified predictive approach that can account for both classes of phenomena. In contrast, the SCBD approach developed in this thesis (and elaborated in the previous chapter) can in principle account for both the effects, namely, the effect of viscoelasticity on thermodynamics and vice-versa. In the present chapter, we study the slip phenomena in polymer blend interfaces, an issue which embodies the latter effect.

Motivation for the present study comes from the anomalously low viscosities which have been observed in various experimental investigations involving immiscible polymer blends [62, 63] wherein, the blend viscosity is found to be much lower than either of the pure components' viscosity. Such low viscosities were lower than that predicted by the commonly employed linear mixing rules [64] leading to these mixtures being termed as negatively deviating blends. A hypothesis advanced to rationalize these deviations has implicated slip at the polymer blend interface [65]. Direct experimental measurements of slip have been complicated due to the difficulties in isolation of this specific phenomenon from other dynamical phenomena in polymer blends. However, recently, Zhao and Macosko [67] provided, probably the first comprehensive

investigation of the slip phenomena. They considered the extrusion of a multilayered polymer blend laminate with different numbers of layers and determined the apparent shear viscosity of the samples. Their experimental results confirmed qualitatively, the predictions of the above theories, while the quantitative values were somewhat lower than the theoretical predictions. Also, Lam and coworkers [68] used rheological measurements and confocal microscopy to determine the slip at the interface between HDPE (high density polyethylene) and Polystyrene. Using confocal microscopy they demonstrated conclusively that there is an apparent discontinuity in the velocity profile at the interface, and that a smaller interfacial thickness between the blend components accentuates the slip phenomena (again in qualitative agreement with the theoretical predictions).

There have been some prior theoretical works addressing the issue of polymer slip. When a phase separated system of unentangled chains is subjected to a simple shear flow parallel to the interface, the bulk material exhibits a viscosity scaling characteristic of Rouse chains as [40],

$$\eta_{\text{BULK}} \sim \zeta b^2 N/v_o \sim \zeta R_g^2/v_o. \tag{3.3}$$

where ζ is the friction coefficient and v_o is the segmental volume in the melt as defined in the previous chapter. deGennes and coworkers [65], suggested that slip results from a layer of low interfacial viscosity η_I, sandwiched between the two bulk layers with their corresponding viscosities. Further, they proposed that for unentangled interfaces, η_I can be estimated as the Rouse

viscosity corresponding to the number of monomers in the overlapping region of the interface (analogous to the bulk viscosity which is proportional to N). In the regime where the interfacial width a_I is large compared to the segmental length b, the number of monomers in the interfacial region can be estimated by balancing the enthalpic costs and the entropic gain for a loop of s segments of A entering the B rich region. This yields that the average segmental length s^* inside the interface scales as $1/\chi$. Using this expression, the interfacial viscosity can be expressed as $\eta_I \sim \zeta b^2 s^*/v_o \sim \zeta b^2/v_o\chi$ (cf. equation (3.3)), or in terms of interfacial thickness, a_I, (cf. equation (3.1)) as $\eta_I \sim \zeta a_I^2/v_o$. In a nutshell, the theoretical predictions suggest that (for an unentangled interface) the interfacial slip for blends at different thermodynamic conditions are determined by the interfacial thickness, which in turn is a thermodynamical property. The above scaling predictions have been confirmed by Fredrickson and Goveas [56] who started from a formal Fokker-Planck equation, and then used a combination of projection operators and phenomenological proposals to derive the constitutive equations for an inhomogeneous Rouse melt. More recently, Barsky and Robbins[66] used molecular dynamics simulations to probe slip phenomena in symmetric polymer blends, and indicated qualitative agreement with the scaling predictions of deGennes [65] and theoretical results of Fredrickson [56].

More intriguing dynamical behavior has been witnessed in the context of compatibilized polymer blends. Compatibilization is a term referring to the addition of small quantities block copolymers to the homopolymer blend sys-

tem. It is common in many industrial applications to improve the properties of polymer blends by using trace amounts of block copolymers which promote the mixing of the blend components [28]. While the precise mechanisms by which block copolymers (commonly referred to as compatibilizers) affect the morphology of blends is still under debate, at least two dominant mechanisms have been suggested. The first mechanism purports that the copolymers affect the deformation characteristics of the blend droplets by either contributing to the Marangoni stresses and/or by influencing the equilibrium and dynamical characteristics of the blend interfaces, such as their interfacial tension and slip phenomena [59, 71]. As evidence for this mechanism, experimental studies [72] probing the shear deformation behavior of polymer droplets have indeed confirmed significant increases in the surface areas of the deforming droplets in the presence of copolymeric compatibilizers. The second mechanism proposes that the copolymers suppress coalescence and coarsening of the droplets, and hence affects the morphologies of blending. The latter was physically rationalized by Sundararaj and Macosko [73] as arising from the steric repulsion of the copolymer layers upon close approach of the droplets. Milner and Xi [59] on the other hand, proposed that the suppression of coalescence was due to a suppression of drainage arising from the Marangoni stresses at the interface. Milner and Xi's theory is purely dynamical in nature and is supported by recent experiments by Leal and co-workers [58], who demonstrated that in the presence of block copolymers the drainage times can be enhanced by upto an order of magnitude.

While a full scale simulation of droplet coalescence and coarsening processes would enable a resolution of the above issues, such an effort is still computationally expensive. In the following, we use the molecular perspective that can be gleaned from the self-consistent Brownian dynamics approach to probe the role of block copolymer compatibilizers in modifying the dynamical properties of the polymer blend interfaces. We focus on two main issues:

(a) The suppression of slip by block copolymers: Many recent experiments which have probed the rheology (the viscosity) of polymer blends containing block copolymeric additives have demonstrated concomitant increases in the viscosities in compatibilized blends. For instance, Zhao and Macosko [67] measured the shear viscosities for compatibilized and incompatibilities phase separated PP and PS blend, and showed that with the addition of block copolymer compatibilizers, the negative deviations of viscosities of blends (the signature of slip phenomena) were reduced considerably. Block copolymers are believed to effect a suppression of slip by increasing the number of entanglements at the interface [67]. However, very few studies have systematically examined the role of different controlling parameters such as the volume fraction, molecular weight of the block copolymers etc. in modifying the slip characteristics. Our studies probe if indeed block copolymers suppress the slip at polymer blend interfaces, and the role of the amount of compatibilizer added and the block copolymer molecular weight in influencing these characteristics;

(b) Dynamics of compatibilized polymer blend interfaces: We also study the dynamics of polymer blend interfaces at compatibilizer coverages

higher than that required for the suppression of slip. The main motivation for these studies is towards the resolution of mechanisms by which block copolymers suppress coalescence. While the Milner-Xi hypothesis postulating the dynamical inhibition of drainage seems consistent with many experimental results, unresolved issues still linger. For instance, their theory predicts that the critical copolymer concentrations required to prevent coalescence should increase linearly with the applied shear rate. However, experiments [74] show that there was only either a weak or absolutely no dependence between the critical concentration and the shear rate. Other experimental results have suggested that suppression was pronounced in cases where longer copolymers were dangling from the droplet surface into the continuous matrix phase [26]. Such dependencies cannot be explained by dynamical theories, and suggests that, unlike small molecule surfactants the thickness of the copolymer layer could have a non-trivial effect in suppressing coalescence.

In this chapter, our main focus is on the study of interfacial slip at polymer-polymer interface. A detailed quantitative investigation of the interfacial slip phenomena in symmetric as well as asymmetric polymer blends is carried out by employing the self-consistent Brownian dynamics approach developed and elaborated in the previous chapter. In the second part of this chapter, we employ the self-consistent Brownian dynamics approach to effect a quantitative study of the effect of copolymer compatibilizers at the interface, mainly focusing on the two issues discussed above. The rest of this chapter is arranged as follows. The chapter is presented in three parts. The first part

provides details of parameters used in the simulation algorithm presented earlier. Section 3.3 deals with the equilibrium results of binary polymer blend system and section 3.4 focuses on the slip phenomena within the context of symmetric and asymmetric polymer blends. These results are compared with related experimental and theoretical researches. The final part of the chapter is devoted to studying the role of block copolymers as compatibilizers. It focuses on suppression of slip by copolymers (section 3.5) and its role in coalescence phenomena (section 3.5.4).

3.2 Simulation Details

The simulation algorithm used corresponds to that detailed in the previous chapter (section 2.6). Our simulations for the case of a symmetric polymer blend used a simulation box of size $16\times8\times8$ (in R_g units) containing 8000 chains. Each chain was discretized into 20 beads each and a Hookean spring law was used. The initial conditions were generated by randomly assigning the positions for all beads, while ensuring that none of the springs were excessively stretched. We quantify the length units in terms of the radius of gyration of the polymer in the blend. We also non-dimensionalize our Brownian dynamics algorithm by expressing time in terms of the reciprocal of friction coefficient ζ and setting the energy scale $k_BT = 1.0$. All our simulations were performed in two dimensions with the assumption that the steady state self-consistent potential (equations (2.22) and (2.23)) exhibits no axial variations. However, this does not impose any constraint on the motion of the beads, and the beads

were assigned positions inside a three dimensional box and were allowed to execute Brownian motion in all three dimensions. For such a 2D simulation, we chose the lattice cell dimensions for coarse-graining as 0.25 R_g units in x and y directions. Random initial conditions were assigned for the potentials w and π at all the lattice points. (equations (2.22) and (2.23))

In the non-dimensionalized formulation, the parameters in our problem are: $\chi N-$ the Flory interaction parameter representing the repulsion between unlike monomers, Γ_1, Γ_2 the phenomenological mobilities for the evolution of $w(r)$ and $\pi(r)$ potentials, and $\epsilon-$ the parameter for velocity field evolution (see equation (2.45)). In our runs we used 0.05, 0.1 and 0.0016 (in the units discussed above) for Γ_1, Γ_2 and ϵ respectively. To ensure the validity of this method and to maintain stability, the mobility coefficient Γ_2 has to be greater than Γ_1 [42]. Moreover, Γ_1, Γ_2 and ϵ must be positive. As mentioned earlier, Γ_1 and Γ_2 arise due to the finite density of monomers, and fluctuations do arise due to the fact that the number of chains per unit volume is finite. By choosing a reasonably dense system of chains per unit volume, we minimize such effects. We chose Γ_1 and Γ_2 such that the properties computed (at steady-state) did not exhibit any significant variations with the parameters. The time step for the Brownian dynamics was chosen as 0.01.

We use convergence of the composition profile to monitor whether equilibrium has been achieved. In case of shear flow, both the convergence of the velocity and the composition profiles were used as criteria which signal the attainment of steady state. The convergence was assumed to be achieved

when there was less than 0.5% change in the composition and velocity profiles for two consecutive block averaging performed for an interval of $125\tau_R$. The simulations were performed for a further period of $625\tau_R$ after convergence to sample all the desired quantities. Here τ_R denotes the Rouse relaxation time of the chain. Our simulations employed a shear rate $\dot{\gamma}\tau_R$ of 1.2. We choose a moderately high shear rate in order to reduce any fluctuations appearing in the velocity profile. Moreover, we do not study shear rate dependence since all the quantities computed are expected to be independent of shear rate in a Gaussian chain framework. The computational time for our runs took on an average around 48hrs in a single 2.5GHz processor system.

3.3 Equilibrium Results

Before presenting our results on the *dynamics* of polymer blends we validate the phenomenology underlying our simulation by examining the *equilibrium* properties of a binary polymer blend system. We first consider the case of *symmetric* polymer blends where the physical properties of the two polymers, such as, chain length, segment length, friction coefficient and segmental volumes are identical to each other. Figure 3.1(a) plots the composition profile obtained from our Brownian dynamics approach for a symmetric immiscible blend where $\chi N = 6.0$. It is evident that there are two interfaces, one situated near $x = 0$ and the other near the boundary of the simulation box. The existence of the second interface is a consequence of the periodic boundary conditions imposed. We also display the equilibrium composition

profiles computed from the numerical solution of the self-consistent field theory. The latter was obtained using the real space method of Fredrickson and Drolet [42] using the same discretization of space and chain lengths as our Brownian dynamics simulations. As is evident from the displayed results, the results of our hybrid Brownian dynamics simulation match well with the numerical results of the self-consistent field theory. Using our simulations, we also computed the coexistence curves for the symmetric polymer blend. The coexistence compositions of each phase was discerned by averaging the composition values at the plateau region of the composition profile. The coexisting composition values are displayed as a function of χN in Fig. 3.1(b). We were not able to get reliable coexistence compositions for shallow quenches (low $\chi N's$) because of finite size effects which precluded the existence of a plateau region in the composition profile. Shown on the same figure is the coexistence curve computed (by equating the chemical potentials and osmotic pressures in the two phases) from a Flory-Huggins form for the free energy: $-\beta F = \phi_A \ln \phi_A + \phi_B \ln \phi_B + \chi N \phi_A \phi_B$, where, $\beta = 1.0/k_B T$. We note excellent agreement between coexistence compositions obtained from our hybrid algorithm and that obtained from Flory-Huggins theory [20]. Note that, as expected for a symmetric blend, the coexistence curve is symmetric along the $\phi = 0.5$ line.

We have also studied the above equilibrium properties for the case of a polymer blend mixture where the two components differ in their chain lengths. We denote the asymmetry in the chain lengths by the parameter $\alpha = N_A/N_B$.

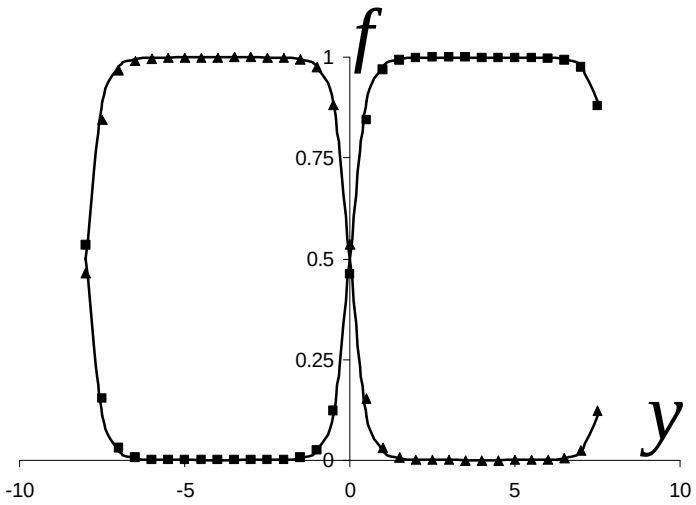

(a)

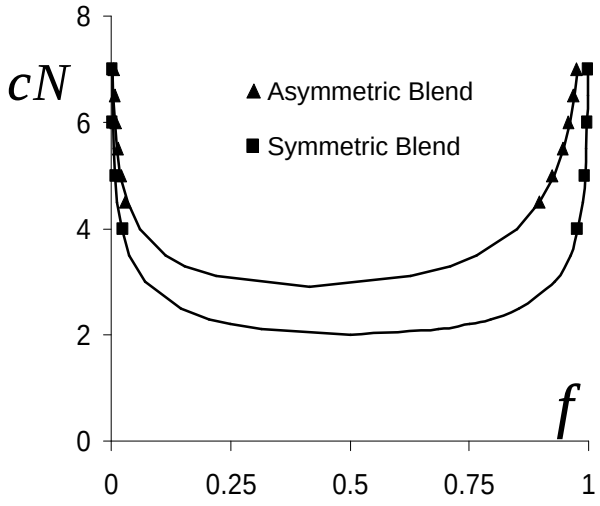

(b)

Figure 3.1: (a) Composition profiles of A and B components plotted as a function of spatial position for a symmetric blend with $\chi N = 7.0$. The points represent the results of our simulations, while the solid lines represent the numerical results of self consistent field theory. (b) Coexistence curves (binodals) for symmetric and asymmetric ($\alpha = 2.0$) blends. The points represent the results of our simulations, while the solid lines represent the numerical results of Flory Huggins theory.

Figure 3.1(b) displays the coexistence curve, computed as explained in the previous paragraph, for an asymmetric blend with $\alpha = 2.0$. Shown alongside in the plot is the coexistence curve computed using the Flory-Huggins theory. The asymmetry in the plot is the consequence of asymmetry in chain lengths. We again find excellent agreement between simulation and theory.

In summary, we have successfully demonstrated the applicability of our *dynamical approach* in capturing the equilibrium properties of symmetric and asymmetric blends. The results indicate a very good agreement between our simulations and the existing theories predicting equilibrium properties. While certainly our method is computationally more time consuming and hence is not most appropriate to study equilibrium properties, nevertheless the above exercise demonstrates the applicability of the phenomenological equations (2.41) and (2.42).

3.4 Slip & Shear Flow in Polymer Blends

In this study, we used our Brownian dynamics simulation approach to study slip phenomena in polymer blends. Our focus was on validating the theoretical predictions viz., whether slip correlates directly with interfacial thickness for these systems. To this effect, we examined the slip length and the interfacial viscosities of both symmetric and asymmetric (in MWs) polymer blends. The latter involves asymmetric bulk rheological properties, and hence can provide a sensitive test to the theoretical prediction that the interfacial viscosity correlates only with the thermodynamically determined

interfacial thicknesses. We note that while our Brownian dynamics simulations are on systems involving unentangled bulk components and interfaces, *our results are nevertheless equally applicable to the linear rheological regime of polymer blends with entangled bulk components with unentangled interfaces.* The latter situations are representative of high MW blends encountered in practical applications, where due to the strong degree of segregation between the blend components, the interfaces are often disentangled. In such situations, the bulk viscosity is proportional to [40] $N^{3-3.4}$, while the interfacial viscosity would correspond to the viscosity of the unentangled chains in the overlapping interfacial region which is calculated in our simulations.

3.4.1 Results

In our Brownian dynamics simulation, we first equilibrate the two layer phase separated melt as explained in the previous section. Subsequently, a homogeneous shear field is applied on the system using a Lee-Edwards boundary condition [69]. As mentioned earlier, the applied shear rates in all simulations was kept a constant value with $\dot{\gamma}\tau_R = 1.2$. The initial velocity of all beads (at the start of shear) is specified as $\dot{\gamma} r_x$ where r_x denotes the x position of the beads, and $\dot{\gamma}$ the applied shear rate. For the case of shear flow, we evolved the self consistent velocities using equation (2.45). We compute both the self-consistent velocity field and the *non-equilibrium* composition profiles. The former quantifies slip at the interface, while the latter quantifies the role of shear upon the phase behavior. Since our simulations were performed for

unentangled polymer melts, there is no coupling between the configurational statistics of the chains in the lateral and normal direction to shear, and consequently, shear does not have any effect upon the compositional characteristics of the blend. We first examine the effect of the degree of incompatibility between the polymers upon the slip and dynamics in a binary polymer blend system. Figures 3.2(a)-(c) displays the velocity profiles of a symmetric blend for three different values of the incompatibility parameters χN corresponding to weak ($\chi N = 4.5$), intermediate ($\chi N = 6.0$) and stronger ($\chi N = 7.5$) segregations. It is evident that the self-consistent velocity profiles deviate from the homogeneous shear profile, with the deviations becoming more pronounced with an increase in the degree of incompatibility. In order to render these slip effects more explicit, we plot in Fig. 3.3 the observed shear rate as a function of position, for the different degrees of incompatibility. It is seen from the results that the bulk shear rates asymptote to the same value, as expected for a symmetric polymer blend system. On the other hand, the shear rates at the interface displays an increased value which becomes more pronounced with an increase in the degree of incompatibility between the polymers. The latter effect corresponds to a decrease in the effective viscosity of the interface, serving as an evidence of the slip phenomena. It is to be noted that since we have considered only Gaussian chains, shear thinning behavior is absent, and hence any lowering of viscosity is attributed to slip.

To facilitate a direct comparison with the theoretical predictions we compute two related quantities from our results: (i) An effective slip length

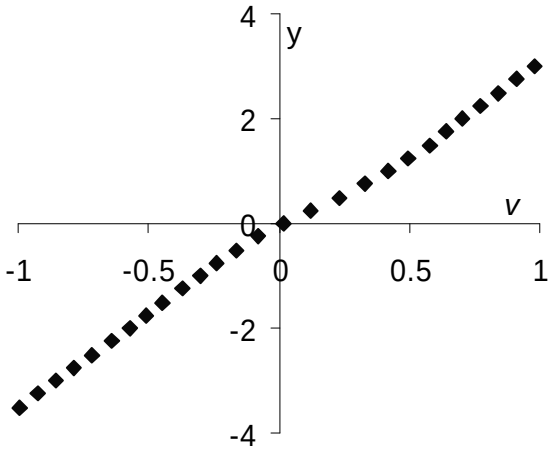

(a)

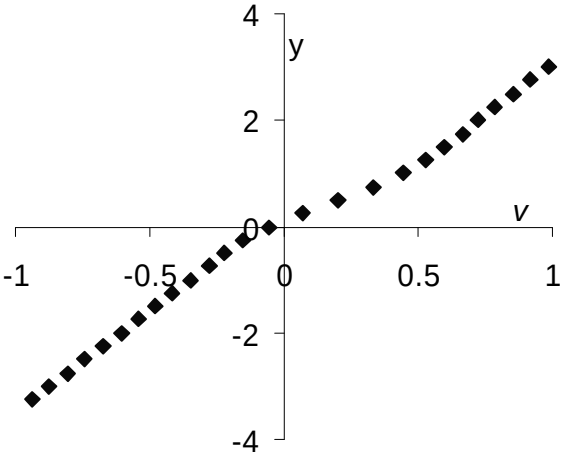

(b)

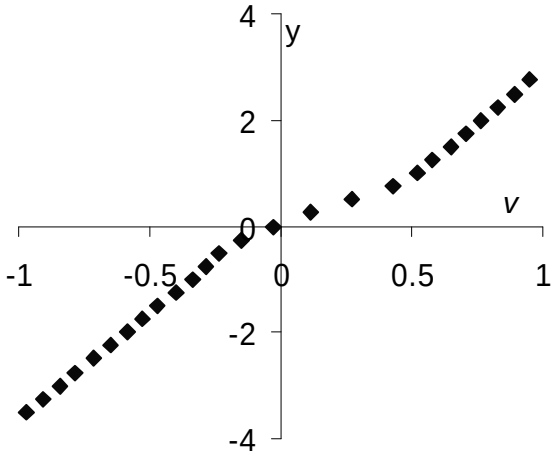

(c)

Figure 3.2: The steady state velocity profiles during shear of a symmetric, segregated polymer blend: (a) $\chi N = 4.5$; (b) $\chi N = 6$; (c) $\chi N = 7.5$.

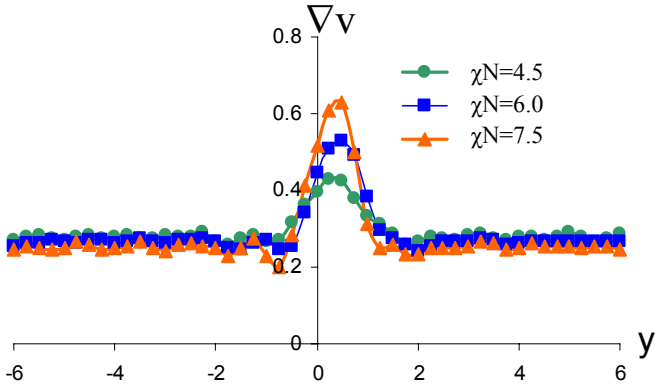

Figure 3.3: The velocity gradient plots as a function of the position for $\chi N = 4.5, 6$ and 7.5. Due to the periodicity of the box, the interface is shifted from $y = 0$.

(or extrapolation length) L_e which quantifies the apparent viscosity of the system, and (ii) the interfacial viscosity η_i. For the case of symmetric blends, it is possible to relate this slip length L_e directly to the discontinuity in the velocity at the interface Δv as, $L_e \equiv \Delta v/\dot{\gamma}$, where $\dot{\gamma}$ represents the observed shear rate. On the other hand, as explained below, for asymmetric blends the L_e computed in our simulations has a more complicated dependence on the velocity profile values. Experimental [67], theoretical [56, 70] and earlier computational studies [66] have all focused on the dependence of this slip length L_e on the degree of incompatibility between the various components. Scaling arguments [65] of deGennes suggests that the magnitude of slip should increase with an increase in the degree of incompatibility and that $L_e \sim \sqrt{\chi N}$. Fredrickson and Goveas (FG) [56], theory predicts $L_e/\sqrt{\chi N} \simeq R_g/6.0$ for symmetric polymer blends under simple shear parallel to the interface.

We computed the slip length in our simulations for symmetric polymer blends, and is displayed in Fig. 3.4 as the ratio $L_e/\sqrt{\chi N}$ as a function of χN. It is observed that consistent with the scaling arguments of deGennes [65] that the slip length asymptotes to a constant value at strong segregation limit. Shown on the same plot is the theoretical prediction of FG [56]. It is observed that their predictions agree extremely well with our simulation results for the entire range of incompatibilities. However, unlike both the deGennes and FG predictions, our results (Fig. 3.4) show a weak, albeit noticeable dependence on the degree of segregation χN. These discrepancies could most likely be due to the inapplicability of the theoretical predictions for weak incompatibilities,

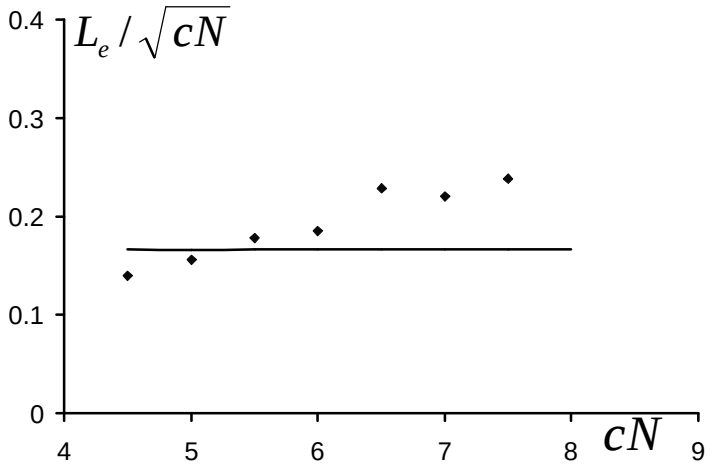

Figure 3.4: Extrapolation lengths (represented as the ratio $L_e/\sqrt{\chi N}$ as a function of the degree of segregation χN. The points depict the values obtained from our simulation for a symmetric blend and the solid line represents the theoretical prediction of FG [56].

since, one of the underlying assumptions of the FG theory was the existence of an interface whose thickness was small compared to R_g.

To allow for a more stringent test of the theoretical predictions, we examine slip in the context of asymmetric blends. Practical situations almost always involves blend components which are asymmetric, with asymmetries resulting from unequal chain lengths (N_A, N_B), unequal chain stiffness (segmental volumes), unequal segmental friction coefficients or a combination of one or more of these factors. In the following, as a representative example, we study the case where the asymmetry results from the asymmetries in the chain lengths. This represents a simple case where the bulk rheological properties are asymmetric, and hence the slip phenomena is expected to be impacted.

We effect numerical simulations for three different degrees of asymmetries in chain lengths between the blend components, corresponding to $\alpha \equiv N_A/N_B = 1.5, 2$ and 2.5. Figure 3.5(a) displays the numerically computed velocity profile for an asymmetric blend with $\alpha = 2.0$. The bulk phase for $y < 0$ corresponds to shorter chains (or lower viscosity polymer). Due to the asymmetry in the rheological properties of the blend, the velocity gradients in the two phases also display an asymmetry characteristic of the constancy of shear stress. To render the slip at the interface more explicit, we display the shear rates in Fig. 3.5(b) as computed from the velocity profile. We confirm that indeed the values of average shear rates in the bulk phases are different and asymptote to the ratio of the bulk viscosities of the unentangled components. More interestingly, there is a jump in the observed shear rate at the interface, which confirms the lower viscosity and the manifestation of interfacial slip in these systems.

To quantify the above trends, in each of the above cases we determine the apparent viscosity of the blend η_{app} by using the (constant) shear stress values and the applied shear rate. This apparent viscosity is converted to an effective slip length L_e using the following relationship:

$$L_e = L(\frac{\eta_{\text{eff}}}{\eta_{\text{app}}} - 1), \tag{3.4}$$

where η_{eff} represents the effective viscosity of a 2 layered polymer blend in the absence of any slip effects, and L denotes the size of the system. Despite the apparent dependence of (3.4) on the size of the system, the L_e values are actually independent of the size L and asymptotes to a constant independent of

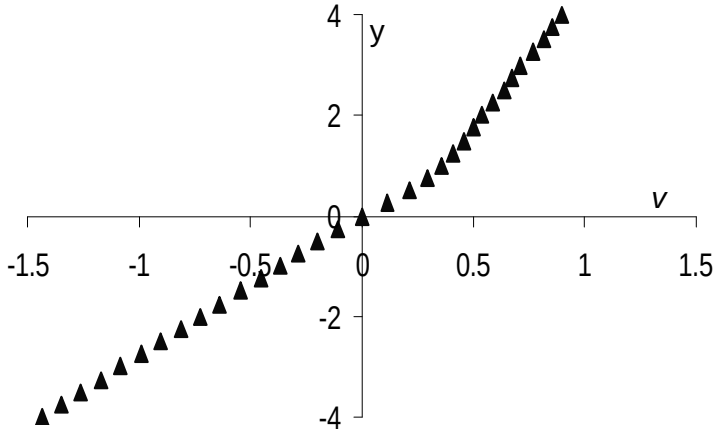

(a)

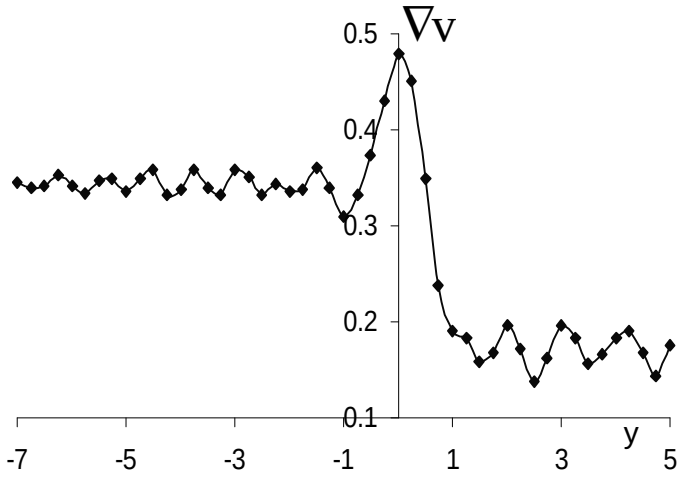

(b)

Figure 3.5: (a) Velocity profile (b) Velocity gradients for an asymmetric blend with $\alpha = 2.0$ and $\chi N_A = 7.5$. In (b) the plots have been shifted such that the interface is located at $y = 0$. The noise evident in (b) is due to statistical noise in averaging and the numerical evaluation of gradients. The solid line in (b) is a guide to the eye.

L. Moreover, L_e provides a direct quantification of the "negative" deviations in viscosity of our blend system. The computed slip lengths L_e for the above systems for various degrees of incompatibility are plotted as a function of χN_A in Fig. 3.6. As evident, the slip effects increase (and the apparent viscosity decreases) with an increase in the degree of incompatibility, and correspondingly the parameter L_e increases with χN. Note however that the parameter L_e for asymmetric blends embody both the velocity difference across the interface as well as the asymmetric bulk viscosities of the system. While Fig. 3.6 suggests that the values of L_e for asymmetric blends are comparable in magnitude to the values of L_e determined for symmetric systems, the extrapolated velocity differences across the interface (results not displayed) of an asymmetric blend (determined from Fig. 3.5 for instance) tended to be much lower than the values determined for symmetric blends. This suggests that the slip manifests in a much less pronounced manner in asymmetric polymer blends due to the asymmetric nature of their rheological properties. Also displayed on Fig. 3.6 are the theoretical predictions obtained by solving the integral equation of Fredrickson and Goveas phenomenological theory. It is seen that while qualitatively the theoretical predictions match extremely well with our simulation results, quantitatively the theoretical predictions tend to be somewhat different than our numerical results. The latter suggests that the phenomenological constitutive equation proposed by Fredrickson and Goveas [56] might need to be embellished to account for the asymmetric rheological properties of the blend components.

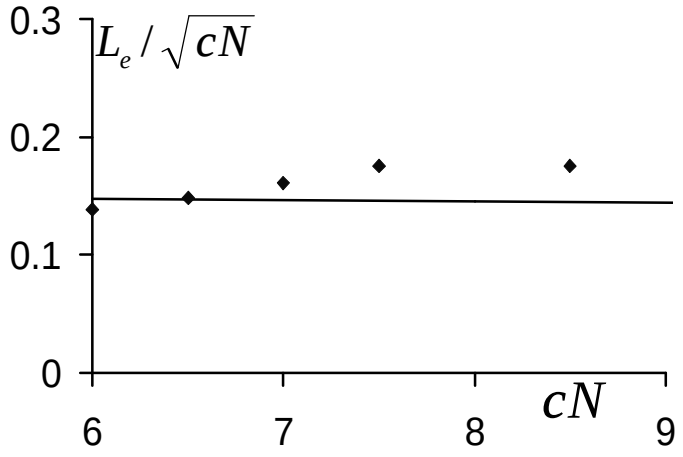

(a)

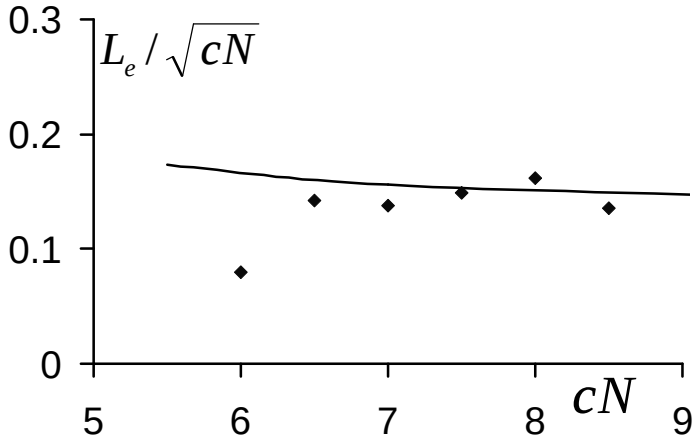

(b)

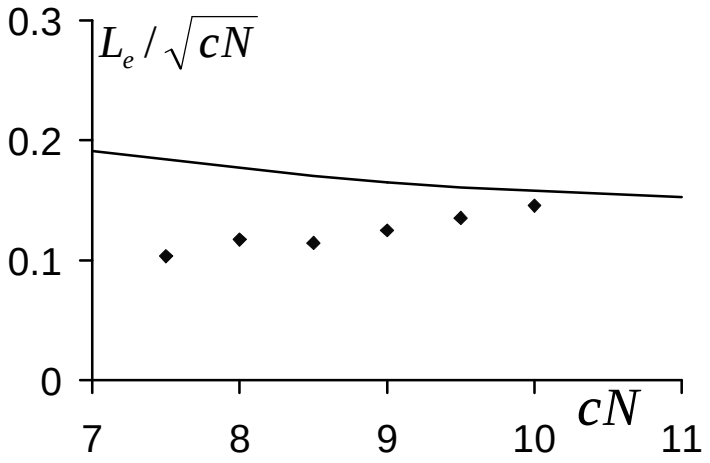

(c)

Figure 3.6: Slip lengths (normalized by R_g of the A chain) plotted as a function of χN_A for different degrees of asymmetries between the blend components: (a) $\alpha = 1.5$; (b) $\alpha = 2.0$; (c) $\alpha = 2.5$, where $\alpha \equiv N_A/N_B$. The points depict the values obtained from our simulation for a symmetric blend and the solid line represents the theoretical prediction of FG [56].

Next, we verify if our above results for symmetric and asymmetric blends can be collapsed onto a single curve when plotted in terms of the interfacial viscosities and the interfacial thicknesses of the blends. To do this, we solve the continuum problem with two bulk media and a single interfacial medium in between with a reduced viscosity. By fitting the velocity profile obtained in our simulations with the continuum problem, we extract $\eta_I/\eta_{\text{BULK}}$. Next, we compute the interfacial thickness a_I from the knowledge of the composition profiles. Explicitly, we find the composition gradient $d\phi/dx$ at the interface and compute interfacial thickness as $a_I \simeq \Delta\phi/(d\phi/dx)$. Here, $\Delta\phi$ is the difference in the compositions of the component in the two phases.

According to the scaling arguments proposed by deGennes [65], the interfacial viscosity η_I depends only on the number of monomers in the interfacial region and hence should scale a_I^2. As mentioned earlier, the scaling predictions of deGennes is expected to be valid only at strong degrees of segregation where the interfacial width is smaller than that of the unperturbed radius of gyration of the chains. Figure 3.7 displays the ratio η_I/a_I^2 obtained from our simulations plotted as a function of the parameter χN in those blend components. We find that at weak segregations the value of η_I/a_I^2 is small and nonuniversal, confirming that the slip effects are negligible for partially miscible blends. In such situations, the interfacial widths are large and the interfacial viscosity matches that of homogeneously mixed phases. However, at stronger degrees of segregation the different plots plateau to a constant value *independent of the asymmetry or the degree of segregations*. Our results

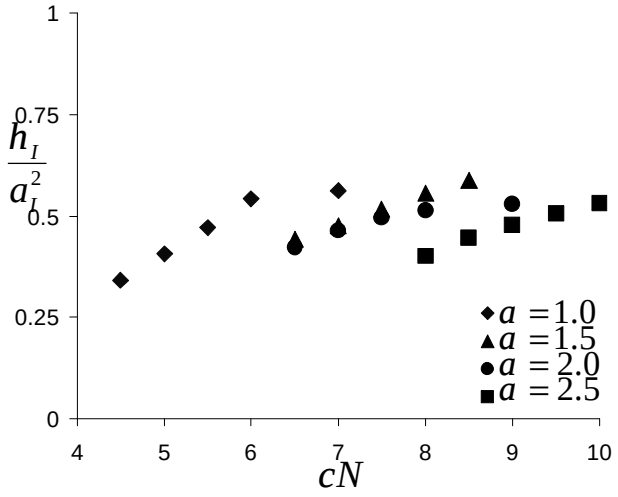

Figure 3.7: Interfacial viscosities η_I normalized by the square of their interfacial widths, a_I.

quantitatively reinforce the scaling description of slip provided by deGennes and suggests that for *unentangled interfaces*, the interfacial viscosity can be deduced based on a *thermodynamic* approach by correlating it to the interfacial width. These results also suggest that for segregated systems with small interfacial widths, the interfacial viscosity can be a very small value. As mentioned earlier, our simulations pertain to the situation involving unentangled bulk components with unentangled interfaces. Consequently, the extrapolations lengths L_e determined from our simulations are small in magnitude (of the order of a few R_g) compared to the macroscopic length scales typically encountered. In such situations, while the apparent viscosity of the blend is still lower than the bulk viscosities, the magnitude of lowering is hard to detect

in experiments. On the other hand, for the more practically relevant cases of entangled bulk components with unentangled interfaces, our results for the interfacial viscosity are still applicable. In these situations, our results suggests $\eta_I \sim a_I^2$, while the bulk viscosities $\eta_B \sim N^{3-3.4}$. The apparent viscosity $\eta_{\rm app}$ can be estimated using a simple 3 layer model as $\eta_{\rm app} \sim L\eta_I/a_I \sim La_I$, and hence $L_e \sim \eta_B/a_I$ which can be very large in magnitude. These results suggest that for entangled components with unentangled interfaces, the slip effects deduced from our simulations can lead to pronounced discontinuities in the velocity profiles at the interface and concomitantly to a significant lowering of the apparent viscosity of blends as seen in experiments.

In summary, our simulation results clearly display the occurrence of slip phenomena during the shear flow of polymer blends. The slip effects increase with an increase in the degree of segregation or a decrease in the interfacial thickness between the blend components. These results qualitatively agree with the experimental results of Lam and coworkers [68]. We do find that the degree of slip and its variation with the incompatibility between the components becomes less pronounced when the blends have asymmetric rheological properties. We have verified the latter result by additional simulations (not displayed) probing a wider range of asymmetry between the blend components. We also find that the phenomenological theories and scaling arguments agree remarkably well with our simulation results for both symmetric and asymmetric blends. Importantly, our simulations do confirm the scaling prediction of deGennes that the interfacial viscosity scales as the interfacial width of the

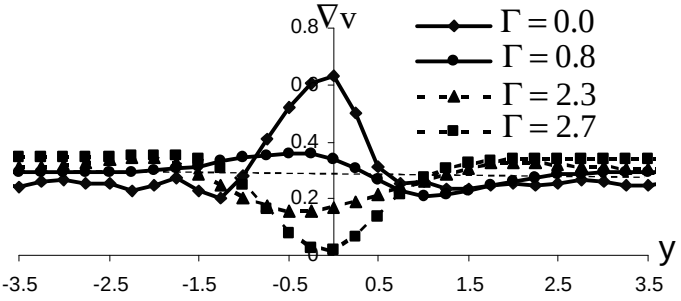

Figure 3.8: Velocity gradient profiles near the interface in the presence of block copolymeric compatibilizers for different coverages Γ of block copolymers. Γ is expressed as number of chains per R_g^2 of the block copolymer. The average shear rate in the bulk is 0.3 and is indicated as a dashed line in the plot. The profiles have been plotted only in the region close to the interfacial region.

polymer blend components for strongly segregated systems.

3.5 Effect of Block copolymer Compatibilizers on Slip

The simulations probing the role of copolymers were begun for a symmetric phase separated blend ($A + B$), by explicitly positioning all the block copolymers (AB) at the interface. The system is then allowed to equilibrate until the composition profiles of the homopolymer and the copolymer converge. To ensure that the system has equilibrated, we checked the resulting equilibrium composition profiles against the predictions of self-consistent field theory. Homogeneous shear is then applied using the Lee-Edwards [69] boundary condition, and the self-consistent velocity profiles were obtained for a compatibilized polymer blend for various volume fractions and molecular weights of copolymers. To display the dynamical effects of block copolymers, we first

focus on the qualitative characteristics of the gradients of the self-consistent velocities (i.e., the local shear rates) as a function of the block copolymer coverage at the interface (Fig. 3.8). In this context, slip is manifested as a reduction in viscosity or a corresponding increase in the observed shear rate. As is evident from the displayed results, for trace or no amount of copolymers at the interface, the qualitative characteristics of the velocity profile is unchanged from that of the pure blend, displaying slip at the interface. On the other hand, for slightly higher volume fractions copolymers (corresponding to a coverage of 0.78 copolymers/R_g^2, which is still lower than the typical experimental values), our results manifest the slip suppressing feature of block copolymer. At this coverage, the local shear rates acquire an almost uniform value throughout the bulk and interface. Upon further increase in the coverage of the block copolymer, the velocity profiles display two dynamically distinct interfacial regions. The first region is near $x = 0$ (interface) and corresponds to an increased viscosity layer arising from the block copolymers, while the second layer is the slip layer at the block copolymer-matrix interfaces. At even these low values of the block copolymer concentration, the slip at the polymer blend interface has been completely suppressed. An even further increase in the volume fraction of the copolymer eliminates slip in its entirety leaving just a single increased viscosity layer at the interface.

Our results above suggests that the copolymer layer suppresses the slip by providing an additional mechanism of friction. Note that all our above results were obtained for a Rouse system of chains where entanglements are

absent. Further, all the volume fractions involved here are less than or equal to that used in experimental studies of droplet deformation in the presence of a compatibilizer. For instance, the highest coverage of copolymer (Fig. 3.8) is 2.73 copolymers/R_g^2. The main conclusions we draw from the above results is that, even small fractions of copolymer can counterbalance the slip present in polymer blends. *Moreover, while entanglements probably affect the quantitative details of this suppression, entanglements with the compatibilizers is not an essential ingredient for suppressing slip.*

We investigate quantitatively the role of the different features of the compatibilizers by first probing the role of the molecular weight of the block copolymer in influencing the coverages required to completely suppress the slip. Figure 3.9 plots the critical interfacial coverage (normalized as number of chains per R_g^2) as a function of the molecular weight of the copolymer. We deduce this critical volume fraction by determining the coverage at which the average velocity gradient across the interface matches the velocity gradient in the bulk. As is evident from the plot, the minimum coverage of the block copolymer decreases with increasing molecular weight, and for the highest MWs of copolymers considered, coverages as low as 0.6 chains/R_g^2 suffice to suppress slip. The dependence of this minimum coverage on the MW can be understood as a result of the increase in the number of monomers of the blend components present in the volume spanned by the block copolymer chains at the interface. In the unentangled polymers we consider, the friction due to the copolymer layer is expected to scale as the number of monomers spanning the

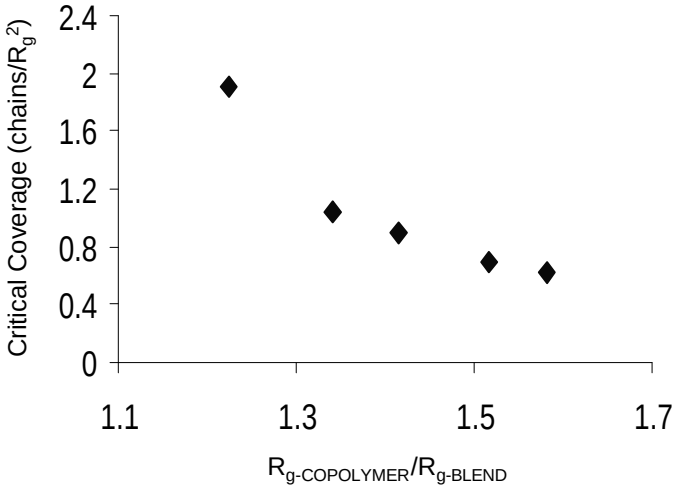

Figure 3.9: Molecular weight dependence of the minimum coverage of block copolymers needed to suppress slip. The molecular weights of the blend components are kept a constant at 20 beads each.

copolymer layer. Consequently, higher molecular weights of copolymer leads to an enhanced friction effect, which leads to a corresponding decrease in the coverage needed for suppression of slip.

We next consider the regime where the volume fractions of block copolymers, albeit low, are higher than the minimum coverages required to suppress slip. This regime corresponds to the situations where the copolymers have been reported to suppress coalescence [58, 105]. Our results presented in Fig. 3.8 suggested that in this regime, the copolymers qualitatively act as a layer of additional friction for the flow of blend components. These effects are displayed in Fig. 3.10, where we illustrate explicitly the changes in the steady state velocity profiles of compatibilized blends with changing MW and the

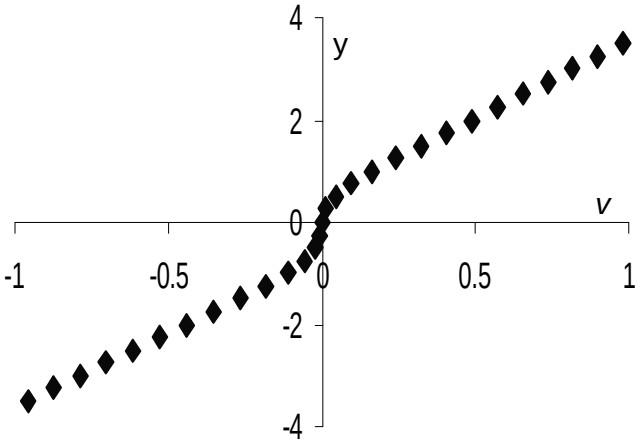

(a)

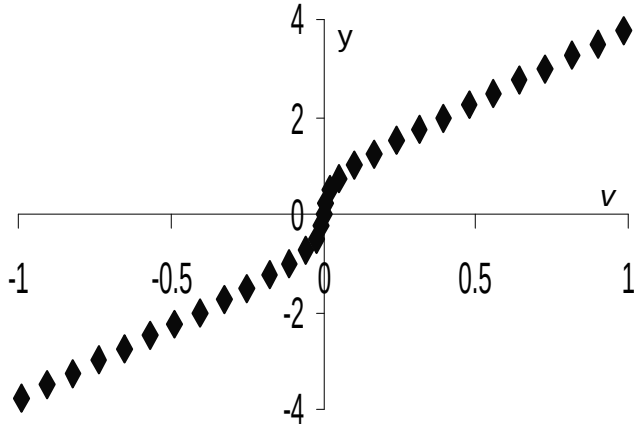

(b)

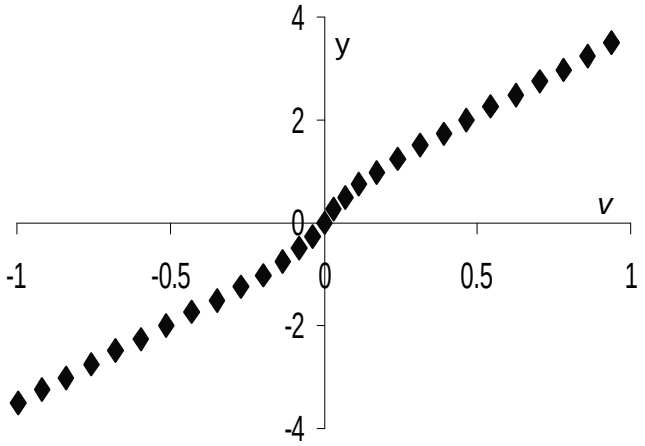

(c)

Figure 3.10: Velocity profiles in the presence of the compatibilizer for coverages higher than the minimum coverage required for suppression of slip. Plot (a) corresponds to a coverage $\Gamma = 3.2$ and $N_{AB} = 30$; (b) $\Gamma = 2.3$ and $N_{AB} = 40$; (c) $\Gamma = 2.7$ and $N_{AB} = 30$.

coverages of the copolymers. The profiles displayed suggest that even at such low coverages, copolymers act to suppress the flow in the layer occupied by the copolymers. Moreover, Fig. 3.10(b) suggests that an increase in MW of the copolymer increases the effective thickness of the friction layer, while a decrease in coverage (with fixed MW) leads to (Fig. 3.10(c)) a decrease in the effective friction itself.

In order to quantify the above dynamical effects and the mutual interplay between the roles of the coverage and the molecular weight, we model the copolymer layer as a Brinkman medium [75, 76]. There are two different length scales in the Brinkman model, namely, the Brinkman layer thickness l (representing the thickness of the friction layer), and the Brinkman friction

thickness δ (representing the effectiveness of copolymers in suppressing flow). We extract these parameters from our Brownian dynamics simulations by fitting it with the analytically obtained shear velocity profile of the Brinkman model developed below.

3.5.1 The Brinkman Model and The Friction Parameters

In this section we provide a description of the Brinkman model. The Brinkman media is characterized by two length scales: (i) The first is purely geometric (denoted as l_1 and l_2 in the figure), and represents thickness of the layer; (ii) To mimic the enhanced friction effect of the Brinkman media, the continuum hydrodynamic equations in the Brinkman layer are augmented with a term ξu, where ξ represents the friction of the Brinkman layer and u represents the velocity of the solvent relative to the Brinkman layer. The ratio $\delta = \xi/\mu$, where μ represents the viscosity of the solvent, has the dimensions of length and represents an effective friction length quantifying the depth of penetration of the flow.

3.5.2 Comparison to the Brinkman Model

In order to compare our Brownian dynamics velocity profiles with the Brinkman model solution, we need to solve the velocity profiles in the Brinkman medium and the bulk medium. To effect this comparison, we consider a system geometry, wherein the Brinkman medium is sandwiched between the two bulk mediums as shown in Fig. 3.11a. The equations, dictating the

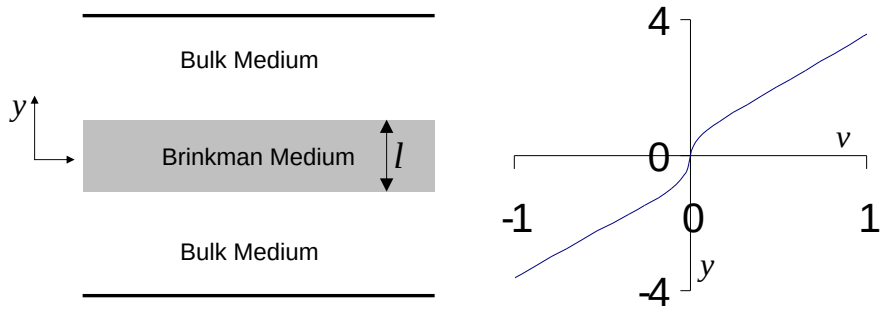

Figure 3.11: (a) Two bulk homopolymer phases, separated by an interface filled with copolymers is modeled as two bulk viscous media with a Brinkman medium between them representing the copolymer layers. (b) The velocity profile obtained by solving the Brinkman model equations.

flow in both these medias is given by,

$$\begin{aligned} \mu\frac{d^2u}{dy^2} &= 0, \quad y > l/2 \;\&\; y < -l/2 \\ \mu\frac{d^2u}{dy^2} &= \xi u, \quad -l/2 < y < l/2 \end{aligned} \tag{3.5}$$

with, l being the geometric *Brinkman layer thickness*, as shown in the figure and, $\delta = \xi/\mu$, representing the Brinkman friction thickness. Figure 3.11b displays the sample solution for the velocity profile of the above system for $l = 2.0$ and $\delta = 0.35$. We fit such Brinkman model solutions with the velocity results from the Brownian dynamics simulations for various copolymer molecular weights (lengths) and coverages and extract the Brinkman model parameters. The Brinkman layer thickness extracted by fitting our simulation results are plotted in Fig. 3.12(a) for four different values of the block copolymer lengths. Note that the length of the blend components are held a constant at 20 segments, while the MW of the block copolymer is varied. In accord with

the qualitative results presented earlier, the Brinkman layer thickness increases with the length of the dangling copolymer, suggesting that copolymers with longer arms dangling in the matrix present a thicker region for the suppression of flow. This thickness can be simply understood as corresponding to the thickness of the block copolymers swollen by the respective blend components (note that R_g in the figures correspond to unperturbed radius of gyration of the blend components). At these extremely low coverages, an increase in the coverage of the block copolymer (results not displayed) showed no significant impact upon the Brinkman layer thickness. We note that for higher coverages the latter is not expected to be true, especially as one reaches the interfacial coverages representative of the polymer brush regime. It is interesting to note that the thickness of the layer is of the order of R_g of the copolymer. For typical polymeric blends, this is of the order of a few nanometers, and is comparable to the size scales of the gap between the polymer droplets during drainage prior to coalescence. We explore the significance of these length scales in the next section.

Figure 3.12(b) displays the Brinkman friction thickness δ (expressed in units of R_g of the blend components) as a function of copolymer coverages and for different copolymer MWs. Physically, the friction thickness corresponds to the penetration thickness of the flow into the copolymer layer. As is evident from the results, even at these low coverages, the values of δ are all less than one, suggesting that the flow does not penetrate beyond a fraction of the R_g of the copolymers. Further, the penetration depth decreases almost linearly

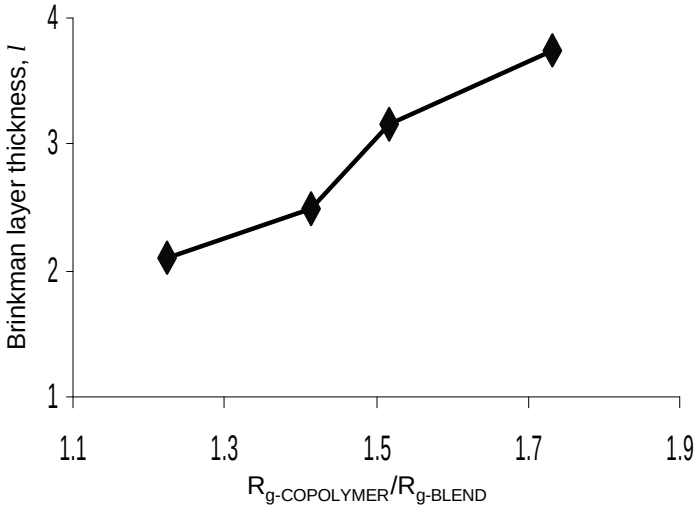

(a)

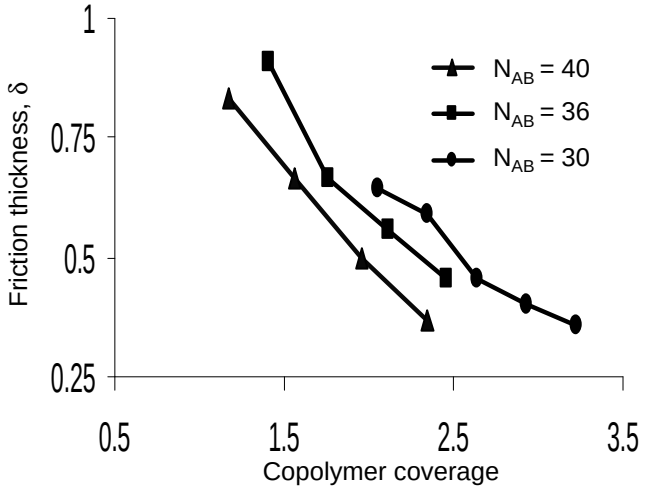

(b)

Figure 3.12: (a) The Brinkman layer thickness, l as a function of the copolymer lengths; (b) The Brinkman friction thickness δ plotted for three different molecular weights of copolymer as a function of the copolymer coverages at the interface (expressed as number of chains/R_g^2). Lines are drawn as a guide to the eye.

(at these coverages) with an increase in the coverage of the copolymer. While many earlier researches have studied the penetration of flow into brushes, our results suggest that significant suppression of flow can result even at very low fractions of compatibilizers. The latter feature contrasts with the density profiles of the different components at such low coverages (not displayed) which shows a significant mixing between the blend components and the respective blocks of the copolymer. These results serve to underline the importance of the molecular configurations and the resulting nonlocal coupling between density and the velocity profiles.

In Fig. 3.12(b), we have also displayed our results corresponding to the effect of the MW of the copolymer in influencing these friction characteristics. As is evident, longer copolymers provide more effective friction (at the same coverages, as expressed in number of chains/R_g^2 of the copolymer) in suppressing the flow of the blend components. This result is not surprising when viewed in the context of our results for the minimum coverages required for the suppression of slip, where we argued that the effective friction is due to the number of monomers of the blend components spanning the block copolymer layer, and that this quantity increases with MW of the copolymer. However, it is to be noted that this result is somewhat dependent on our idealization of the copolymer layer as a brush with uniform friction coefficient, and might lead to qualitatively different results if an alternate/more detailed model of the copolymer layer is used.

In summary, our results presented above suggests a unique role for the

block copolymers in modulating the dynamical properties of polymer blend interfaces even at extremely low volume fractions. At low coverages of the copolymer, our results confirm that the block copolymers suppress slip, albeit even in the absence of entanglements. Upon even a slight increase in copolymer fractions we have demonstrated that the compatibilizers provide an additional source of friction on a layer of thickness of the order of the R_g of the copolymer. The effective friction of the layer is sufficient to suppress the penetration of the flow to less than a fraction of the R_g of the blend components. An increase in the coverage of the copolymer serves to increase the effective friction of the layer, while it has no effect on the thickness of the friction layer. While the above results are specific to unentangled systems, we expect the results to be qualitatively valid even for entangled systems albeit with much more pronounced magnitudes for the friction effects.

3.5.3 Drainage Time Computation in The Brinkman Model

As already briefly indicated, the length scales of the copolymer friction layer are comparable to the length scales encountered during drainage and coalescence. Moreover, the resulting suppression in flow can effectively increase the lubrication force between approaching droplets leading to an increase in the drainage times. In this section, we use the values of the Brinkman parameters discerned in the previous section to quantify if indeed these can lead to enhancement in drainage times comparable to those observed in experiments. To this effect, we developed a simple model of the squeeze flow between two

fluid interfaces with Brinkman layers adjoining their interface. This physically corresponds to a scenario where the two droplets approaching each other are flattened under the action of capillary forces. Our drainage model only accounts for the effect of enhanced friction owing to the copolymers. A more realistic model of the coalescence process, would necessarily have to incorporate a combination of other important effects [77] like the Marangoni stresses and steric repulsion effects which are not considered in the present model, and is beyond the scope of this research.

The drainage time for two droplets with compatibilizer Brinkman layers approaching each other (see Fig. 3.13) [75, 76] is deduced in the present model by considering the scenario where the droplets are flattened (to a radius a) under the action of the capillary forces. Due to symmetry, it suffices to consider the half plane $z > 0$. The equations governing the radial velocity field $u(z)$ in the gap between the two droplets are given by,

$$\mu_m \frac{d^2u}{dz^2} - \frac{dp}{dr} = \begin{cases} 0, & 0 < z < h/2 - l_m \\ \xi u, & h/2 - l_m < z < h/2 \end{cases} \tag{3.6}$$

and inside the droplet phase,

$$\mu_d \frac{d^2u}{dz^2} = \begin{cases} \xi u, & h/2 < z < h/2 + l_d \\ 0, & z > h/2 + l_d \end{cases} \tag{3.7}$$

In the above equation, μ_m represents the viscosity of the matrix and μ_d the viscosity of the droplet. l_m and l_d represent the Brinkman layer thicknesses of the compatibilizer in the matrix and the droplet phases. dp/dr denotes the pressure gradient in the gap between the approaching droplets. In the

situation where the droplets are flattened by the capillary forces (to a radius a), we assume that the pressure gradient in the gap between the droplets is due to capillary forces, and use a scaling approximation to replace dp/dr by $2\sigma/a^2$ [88], where σ represents the surface tension of the drop. ξ denotes the effective friction of the Brinkman layer, which for simplicity is assumed to be the same in the droplet and the matrix phases (in the notation of the text $\delta = \sqrt{\mu_m/\xi}$). The above governing equations are supplemented by conditions ensuring continuity of the velocity fields and its derivatives and by the following boundary conditions:

$$\frac{du}{dz} = 0 \quad \text{at } z = 0, \tag{3.8}$$

representing the symmetry about the plane $z = 0$, and

$$\frac{du}{dz} = -\frac{u}{a} \quad \text{at } z = h/2 + l_d. \tag{3.9}$$

In writing the latter boundary condition at the droplet interface, we have used the Chesters's boundary condition based on the scaling idea [81] that the velocity gradient inside the drop can be approximated as the velocity scale variations over a distance a.

The solution for the Brinkman problem can be combined with the lubrication theory to obtain a modified equation governing the drainage of the fluid from the gap between the droplets. In such a situation, the drainage of the fluid is obtained as:

$$\pi a^2 \frac{dh}{dt} = -2\pi a \int_{-h/2}^{h/2} dz\, u(z). \tag{3.10}$$

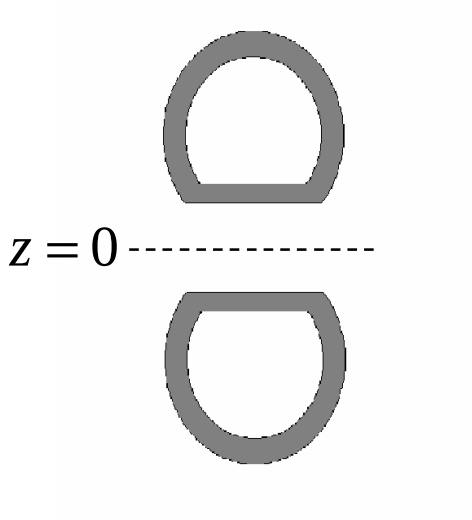

(a)

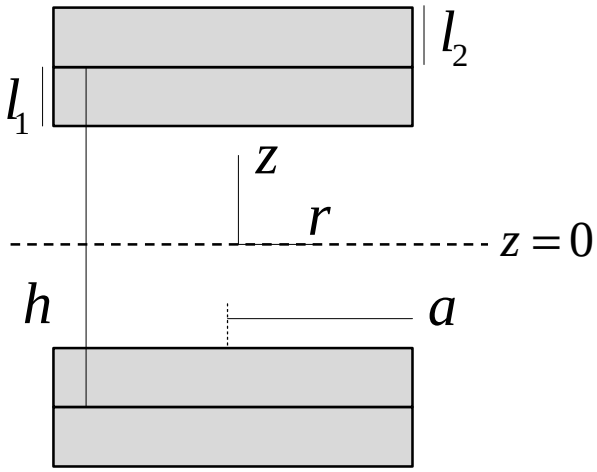

(b)

Figure 3.13: Schematics of our hydrodynamic model. (a) Drainage between droplets. The droplets are assumed to be flattened due to the capillary forces. (b) Closer view of the drainage between droplets. l_1 and l_2 respectively represent the thickness of the Brinkman layers exterior and interior to the droplet.

We solve equations (3.6) - (3.9) analytically, and combined the result with a numerical solution of equation (3.10). The latter is performed between the limits of $h_{\rm beg} = 0.1\mu$ m, corresponding to the start of the drainage, to $h_{\rm end} \sim 10 - 15$nm. The qualitative trends discussed in the main text do not depend sensitively on the exact limits we choose for the beginning and the end of drainage.

3.5.4 Compatibilizer Effects on Drainage Times: Results

Using the above Brinkman model, we derived the equations governing the drainage times of compatibilized and uncompatibilized droplets. The values of parameters appearing in the Brinkman model were chosen from the results of our numerical simulations. The rest of the parameters in our model are chosen in accordance with the previous investigations of Leal and co-workers [58]. The capillary numbers were chosen in the range $Ca \simeq 10^{-3} - 10^{-1}$. The drainage times are computed by integrating the drainage equation (3.10). The experimental definition for the beginning of the drainage process (namely, $h \sim 0.1\mu m$) is around 25 in units of R_g), while the minimum value of h in the fluid drainage process, i.e. when the film ruptures, was fixed at $\sim$10nm ($\simeq 3-4$ in units of R_g) (obtained by assuming that the film rupture begins at a proximity when the predominant driving for coalescence is the van der waals attraction). We have fixed the ratio of droplet and the matrix fluid viscosities $\mu_d/\mu_m = \lambda = 1$.

With the above set of parameters we compute the (nondimensionalized)

drainage times for the compatibilized blend (with Brinkman medium) and uncompatibilized blend. Figures 3.14a and 3.14b plots the drainage times as a function of capillary numbers for different coverages (at a fixed molecular weight) of the copolymers and for different lengths of the exterior copolymer block (at a fixed coverage). The differences in the physical characteristics of the copolymer layer translates into differences in the parameters of the Brinkman model and impacts on the drainage times. As is evident from the displayed results, the presence of the compatibilizers increases the drainage times by orders of magnitude (i.e. it takes much longer for the droplets to coalesce), especially at higher capillary numbers. This suggests that the copolymer layers can serve as effective drainage and coalescence suppressors even at very low volume fractions. Furthermore, our results in Fig. 3.14a also suggests that while an increase in coverage leads to an increased efficiency in suppression of coalescence, these increases saturate at low volume fractions of compatibilizers. These effects may serve to explain the experimental results of Hudson *et al.* [78] as well as Lyu *et al.* [74] which showed that the addition of block copolymers beyond a certain value did not impact upon the droplet size distributions of the blend. Moreover, Fig. 3.14b confirms that copolymers with the longer block in the matrix serve as more effective coalescence suppressors.

The above results are broadly consistent with the experimental results of Leal [88], Macoscko and coworkers [67] mentioned in the introduction. Our model is purely dynamical, and does not rely upon the steric repulsion between the block copolymers. In this regard, our model rationalizes suppression as

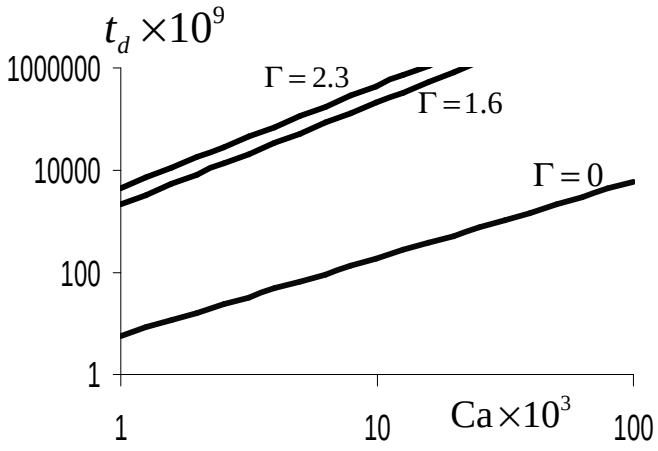

(a)

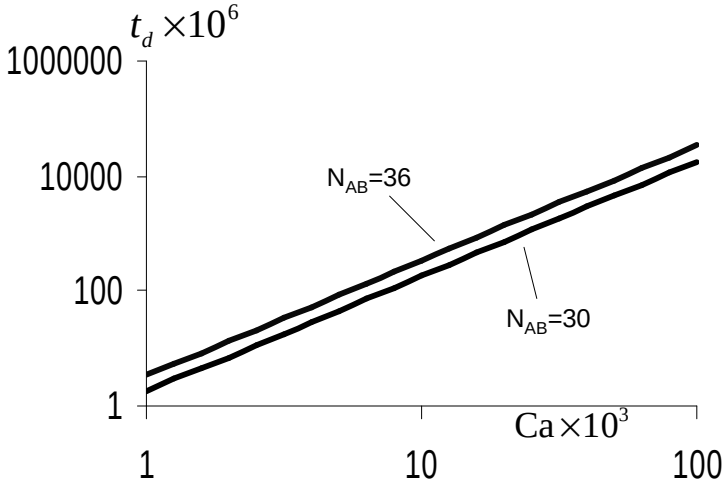

(b)

Figure 3.14: Nondimensionalized drainage times (t_d) plotted as a function of capillary number (Ca): (a) For three different copolymer coverages Γ (expressed as number of chains per R_g^2 at the interface. $\Gamma = 0$ corresponds to the absence of compatibilizer; and (b) For two different molecular weight of copolymer, N_{AB}.

arising from the suppression of drainage of the fluid. On the other hand, by including the Brinkman parameters our model accounts for the finite size effects of the block copolymers, which were absent in the studies which made analogies to surfactants. However, our model clearly overestimates the suppression due to compatibilizers. Indeed, while the earlier models of Marangoni stress driven suppression effectively corresponds to a compressible copolymer layer with an infinite friction between the blend and the copolymers, our model corresponds to an incompressible copolymer layer with a finite friction between the blend and copolymers. In reality, the copolymers influence suppression in both ways, viz., by providing an additional layer of friction for drainage, as well as through the Marangoni effects [59]. This combination, especially through the friction provided by an inhomogeneous copolymer layer, might possibly rationalize quantitatively the experimental results. Our main contribution in this section is to point out the possible impact of the friction effects, by using the parameters and insights determined from our self consistent Brownian dynamics simulations.

3.6 Summary

In this chapter we used the self-consistent Brownian dynamics simulation [54] approach to study the dynamics of inhomogeneous polymeric systems. In the context of polymer blends, we have studied binary systems of symmetric and asymmetric polymers. We demonstrated the success of our hybrid approach in capturing the equilibrium properties of both these systems. We

applied our approach to study the effect of compositional inhomogeneity on the dynamics of such systems. Slip phenomena at the interface of polymer blends was captured and compared with scaling results of deGennes and theoretical results of Fredrickson and Goveas. Our results were obtained in the contexts of both symmetric and asymmetric systems. Quantitative agreement of the extrapolation length (or slip length) with the theoretical results was observed.

On the role of block copolymers compatibilizers, we have demonstrated that the copolymers reduce the slip at the interface of a polymer blend. The minimum coverages required to eliminate slip at the interface was found to decrease with increasing length of the copolymer, suggesting that the finite size of copolymers play an important role in modifying the dynamical interfacial properties of a polymer blend. Moreover, we observed that low coverages of copolymer (more than that required to eliminate slip) could also provide an apparent layer of increased viscosity at the interface. We modeled this layer as a Brinkman friction layer and extracted the parameters appearing in the model using our numerical results. We observed order of magnitude differences in the drainage times (for two approaching droplets) of compatibilized and free droplets suggesting that enhanced friction is a potential mechanism that could suppress droplet coalescence in compatibilized blends.

Chapter 4

Flow Deformation of Polymer Blend Droplets and The Role of Block Copolymer Compatibilizers

4.1 Introduction

There has been a significant interest in the recent years on understanding the effect of surfactants upon the flow-induced deformation behavior of emulsion droplets [82–87]. These studies have been motivated by the fact that the desired properties of the end products of multiphase systems depend not only on the properties of the individual constituents but also on the morphology of the dispersion [27, 88]. In this regard, addition of surfactant compatibilizers to emulsions have been demonstrated as a versatile approach to control the flow-induced morphologies of the two phase systems. On the one hand, the presence of surfactants induces a reduction in interfacial tension, thereby making the interfaces more susceptible to deformation. On the other hand, flow-induced concentration gradients of surfactants along the interface can give rise to tangential stresses that can resist the droplet deformation and/or prevent coalescence of the droplets. Many experiments have demonstrated that these effects can together lead to a significant impact on the resulting droplet size distribution in the end product [89–92].

Theoretical studies of the above phenomena have typically relied on a continuum approach to the problem of droplet deformation by relating the resulting droplet shape to a balance between the viscous and interfacial forces [93]. The surfactant-induced reduction in the interfacial tension is commonly accounted by employing a constitutive equation relating the local surfactant concentration along the interface to the value of the local interfacial tension [88]. The fluid mechanics problem is then coupled to a transport problem which governs the flow-induced gradients (and the resulting stresses) set up in the concentration of surfactants [88]. Together, these effects lead to a complex free-boundary problem which can be solved analytically in some asymptotic limits [93, 95] and numerically by using sophisticated boundary integral[83, 84] and finite volume methods [96].

The above observations and results in the context of surfactants and simple fluid emulsions have by and large also been borne out in the context of ternary polymer blends containing two (partially) immiscible homopolymers with an added block copolymer component (the latter being the equivalent of the surfactant [97]). For instance, in the absence of compatibilizers, experiments by Leal and coworkers [89] have demonstrated that the breakup of polymer droplets occur via the capillary modes in a manner similar to the emulsion droplet systems. Also, Velankar and coworkers have visualized the steady shear deformation of compatibilized polymeric droplet systems and observed effects such as "tip streaming," which have also been observed in emulsion systems in the presence of surfactants [88].

While the analogies between polymeric and non-polymeric emulsions are clear, there are also important differences between them. On the one hand, polymeric fluids are inherently viscoelastic [40] and the non-Newtonian nature of the components can significantly influence the deformation characteristics of the droplet and the rheological characteristics of the mixture. Indeed, polymer droplet deformation experiments by Macosko and coworkers [98] have clearly demonstrated that the first and second normal stresses of the polymer components can lead to a reduced droplet deformation relative to a purely affine droplet deformation. Other novel behavior, such as droplet widening in the vorticity direction, [99] the formation of sheet-like morphologies [99] have also been observed and attributed to the viscoelastic characteristics of the matrix and droplet phases.

The presence of block copolymeric compatibilizers also introduces new molecular level physics not automatically incorporated into the continuum models. For instance, architecture and the sequence distribution of the copolymer compatibilized can influence both the reduction in interfacial tension and its dependencies upon the concentration gradients [101]. Moreover, the molecular weight of the copolymer and its architecture can by itself also influence dynamical phenomena such as slip of the matrix and droplet components near the interface [102, 103]. The precise manner in which these two distinct effects interplay with each other to affect the deformation and the macroscopic rheological characteristics has not been elucidated. For instance, theoretical predictions [104] have suggested that a symmetric copolymer should be more

effective than an asymmetric copolymer at reducing the interfacial tension and enhancing the deformation of the droplet. However, thread breaking experiments by Favis and coworkers [105] using symmetric and asymmetric copolymers suggest that the interfaces compatibilized by the asymmetric copolymer to be more prone to deformation compared to the symmetric copolymers. Similarly, Levitt and Macosko [102] attributed the results of their droplet visualization experiments to a combination of the above features without resolving their individual contributions.

Macroscopic continuum-level theoretical treatment of deforming droplet systems involving free boundaries is a complex problem which is solved for Newtonian systems by using appropriate phenomenological equations [95]. The solution of the above problem for viscoelastic systems with non-Newtonian constitutive models becomes quite complex and not surprisingly there are very few such results available [106]. Though such problems could be overcome by molecular scale numerical simulations like molecular dynamics (MD), Brownian dynamics (BD), Monte Carlo (MC) simulations etc, these simulations employ pair potentials (like LJ potential) which renders them computationally very expensive to study the system at realistic size and time scales. In contrast, recent advances in "coarse-grained" molecular level simulation approaches could prove valuable in overcoming the aforementioned limitations. They could also shed light upon the appropriate forms of the constitutive equations, the physics that need to be incorporated and the boundary conditions to be used. In this regard, we mention the recent work of Phan-Thien and

coworkers [107], who studied the dynamics of polymer droplet deformation and breakup using the method of Dissipative Particle Dynamics (DPD). They found qualitative agreement with experimental observations and were able to shed light upon the linear and non-linear regimes of droplet deformation of non-Newtonian fluids.

In this research, we primarily focus on the influence of block copolymer compatibilizers upon the deformation and rheological characteristics of polymer blend systems. An earlier article of ours [103] considered the case of a flat polymer blend interface and examined dynamical effects such as slip suppression and interfacial rheology induced by the presence of the block copolymers at the interface. The study in the present work is motivated by the question, *"how do the equilibrium influences of block copolymers (such as its effect upon the interfacial tension) interplay with the dynamical effects to influence the deformation and rheology of polymer blend droplets?"*

The use of a coarse-grained "molecular" simulation approach presents both advantages and disadvantages for addressing the problem at hand. The immediate advantage of our approach is the ability to study the influences of the physical properties of the copolymer, such as their structure, architecture and chain length effects upon polymer droplet deformation. Secondly, our approach also allows us to study the competing effects of copolymer diffusion and convection at the drop surface while accounting faithfully for their interfacial rheological characteristics. By addressing the latter effects at a molecular level, we bypass the need to specify and track the dynamical boundary con-

ditions (and the influence of the copolymer characteristics) at an evolving droplet interface. Finally, the influence of the viscoelasticity of the matrix and the droplet phases are automatically incorporated without resorting to phenomenological constitutive equations.

The main computational limitation of our method arises from its use of Brownian dynamics simulations of polymer chains to study a phenomena which is inherently macroscopic, occurring at the scales of the order of 1000 times the characteristics sizes of the polymer [27]. In the present study, since we were mainly interested in probing the qualitative aspects of the influence of the copolymers, we restricted ourselves to relatively small systems with the droplet sizes on the order of the size of the polymers (and copolymers) themselves. The latter situation renders our simulation more representative of the case of the droplet phase microemulsions which result in oil-water-surfactant (and analogous polymeric) mixtures [108, 109]. In such regimes, effects such as the bending modulus of the interface can and does become relevant in determining the droplet deformation. Secondly, again due to computational limitations, our simulations considered only the case of a two dimensional flow situation. The latter renders our simulations not directly comparable with continuum theories for surfactant effects on droplet deformations based on three-dimensional flow geometries. Despite these limitations (which can in principle be overcome by simulating larger systems), our results still provide useful insights into the influence of copolymer compatibilizers upon the deformation of polymer blend droplets.

The rest of the chapter is arranged as follows. In section 4.2 we outline the details of the simulation parameters used in this research. In sections 4.3 and 4.4 we focus on the polymer droplet deformation characteristics under an applied simple shear field and its dependencies upon the various physical characteristics of the block copolymer compatibilizer. Section 4.5 of the chapter focuses on the effect of flow induced drop deformation upon the overall rheological properties of the polymer blend. We conclude with a discussion of the results and an outlook for future work.

4.2 Simulation Details

We carried out our self-consistent Brownian dynamics simulations in a simulation cell of dimensions $12 \times 8 \times 10$ (in R_g units) containing 400 chains of the homopolymer A (droplet polymer) and 12000 chains of homopolymer B (the matrix polymer) corresponding to a volume fraction of 3.25% of the droplet phase. The homopolymers were comprised of 6 beads ($N_A = N_B$) each. Note here that all our simulations were performed with the composition and velocity fields assumed to be two dimensional (2D) in nature. However, the polymer beads were allowed to execute Brownian motion in all three dimensions. The copolymers used to compatibilize the droplets were of the form $A - B$ and the simulations were performed for different coverages Γ of the copolymers and sizes N_{AB} such that N_{AB}/N_B ranges from 0.3 to 1.3. The degree of incompatibility between the two polymers A and B, parametrized by χN_A, was set at a value of 25.0. Owing to the strong incompatibility para-

meter χN chosen for our simulations, shear-induced dissolution of the droplet is prevented, thereby maintaining the droplet volume at a constant value. The coverage of copolymers around the interface Γ is a critical parameter in our study of droplet deformations and rheological effects. We express this parameter as the number of copolymers in the system per unit interfacial area, the latter being expressed in the units of R_g^2, where R_g denotes the radius of gyration of the homopolymer.

The time step Δt for Brownian dynamics algorithm, expressed in terms of the reciprocal of the friction coefficient ζ, was chosen as 0.001. The shear rates $\dot{\gamma}$ in this chapter are non-dimensionalized using this friction coefficient ζ and the energy scale k_BT set to 1.0. The shear rate boundary conditions were applied using the Lees-Edwards boundary conditions [69] in the gradient direction. We chose the lattice grid dimensions for coarse-graining as 0.125 R_g units in x and y directions. To ensure a faster convergence to equilibrium, the initial conditions were generated by randomly assigning the positions for all A beads inside a cylindrical volume of radius $1.0R_g$ centered at around $(x, y) \equiv (0, 0)$, while the B beads were initially assigned random positions outside this cylindrical volume. Random initial conditions were assigned for the potentials w and π at all the lattice points. All the fields were assumed to be periodic in the velocity direction.

At a continuum level, the physical parameters relevant for droplet deformation of surfactant-free Newtonian emulsions include [88], the matrix fluid viscosity μ, the droplet viscosity $\lambda\mu$, the interfacial tension σ, the radius of the

undistorted spherical drop R_o, and the externally applied shear rate $\dot{\gamma}$. We would like to note here that the interfacial tension σ employed in this research is an *effective non-equilibrium interfacial tension* computed from small drop deformation and it comprises of two contributions from the copolymers at the interface: (i) The equilibrium interfacial tension reduction by the copolymers (denoted by Σ) and (ii) The increase in bending modulus (denoted by K) owing to the presence of copolymers at the interface. The latter effect, viz. increase in bending modulus is negligible in large droplet systems with droplet radius is far greater than the copolymer radius of gyration, however it becomes very important in small droplet systems when droplet radius is comparable to the copolymer radius of gyration, as is the case under investigation. The above parameters can be combined into two nondimensional quantities which influence the droplet deformation of nonpolymeric emulsions: (i) The Capillary number $\mathrm{Ca} = \mu R_o \dot{\gamma}/\sigma$; and (ii) The viscosity ratio λ. In this work, we study the case where the droplet and the matrix viscosities are identical and $\lambda = 1$. Other non-dimensional parameters which can influence the deformation characteristics in our system include the surface Peclet number of the compatibilizer, Pe, and the Weissenberg numbers of the matrix and the droplet phases, Wi. The Peclet number, $\mathrm{Pe} = \dot{\gamma} R_o^2/D_s$, characterizes the relative strengths of the convective and the diffusive motion of the compatibilizers (D_s denotes the surface diffusion coefficient of the surfactant along the droplet interface). Interfacial diffusion of copolymers is promoted when copolymer concentration gradient develops along the interface of the droplet and the matrix. Such a situation

is witnessed (as elucidated later) when the droplet interface is extended under shear. For the range of shear rates employed in this study, the Peclet numbers for the copolymers are found to extend from a minimum of 0.9 to a maximum value of 18.0 by assuming the surface diffusion of the copolymers to be same as the bulk diffusion of a Rouse melt. The Weissenberg number quantifies the importance of viscoelastic effects and is given by $\mathrm{Wi} = \dot{\gamma}\tau$, where τ denotes the Rouse relaxation time of polymer chain and is given by $\zeta N_i^2 a^2/3\pi^2 k_B T$. In this research, we have probed shear rates for which Wi vary from 0.12 at the lowest applied to shear to 3.6 at the highest shear rate. At the higher shear rates probed, the Weissenberg numbers are large enough for the viscoelasticity effects to play a non-trivial role in the droplet deformation. However, within the framework of a Rouse model, such viscoelastic effects are somewhat screened. Signatures of viscoelasticity like shear thinning and second normal stress differences are absent in a Rouse model. But the model does predict a squared shear rate ($\dot{\gamma}^2$) dependence of first normal stress difference resulting from chain stretching (under shear) and chain connectivity in polymeric systems. This would in turn affect the droplet deformation which plays an important role in affecting the resulting rheological behavior of the system.

The two quantities that are often used to describe the geometry of a deformed drop in a shear flow are the deformation parameter D and the orientation angle θ [113]. The deformation parameter D is given by the ratio $(L-B)/(L+B)$, where L and B are the major and minor axis of the ellipsoidal drop in the plane perpendicular to the vorticity direction and θ is the angle

of the major axis with respect to the velocity direction. To compute the deformation D, we make use of the droplet composition field ϕ_A,which is closer to 1.0 inside the droplet and nearly zero outside. Subsequently, we compute the major and minor axes of the ellipsoidal droplet by calculating the following moments of this field as [114],

$$\begin{aligned} b &= G\sum_{\mathbf{x}} \phi_A \\ c_\alpha &= G\sum_{\mathbf{x}} x_\alpha \phi_A \\ d_{\alpha\beta} &= G\sum_{\mathbf{x}} \phi_A (x_\alpha - c_\alpha)(x_\beta - c_\beta) \end{aligned} \tag{4.1}$$

$(\alpha, \beta = x, y)$, where b represents the non-dimensional area of the droplet and $\mathbf{c}/b$ represents the position vector of its center. The summations are performed over the two-dimensional system coordinates with G denoting the non-dimensional lattice grid area (=0.125×0.125). The eigenvalues of $d_{\alpha\beta}/b$ yield then the two length scales L and B while its eigenvectors yield the orientation θ.

4.3 Qualitative Aspects of The Deformation Behavior of Droplets

In this section, we discuss the qualitative aspects of the influence of the shear rates and the coverage of the copolymer compatibilizers upon the droplet deformation and flow characteristics. The objective of this section is to compare these aspects with corresponding results obtained using other theoretical approaches.

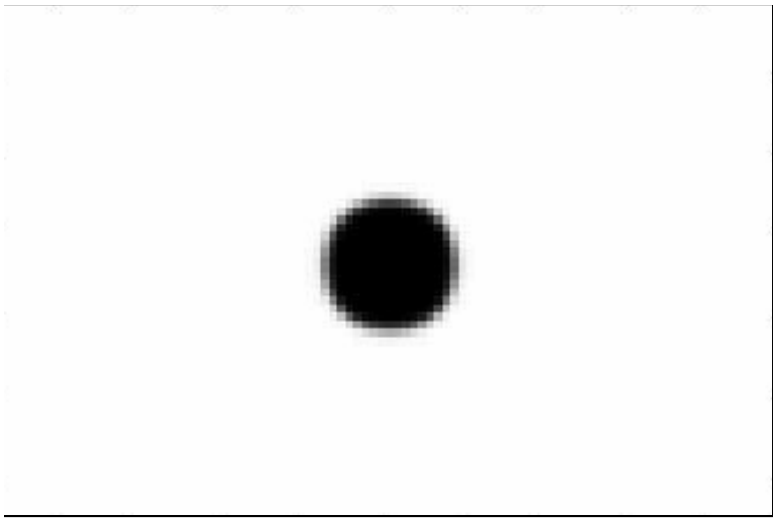

(a)

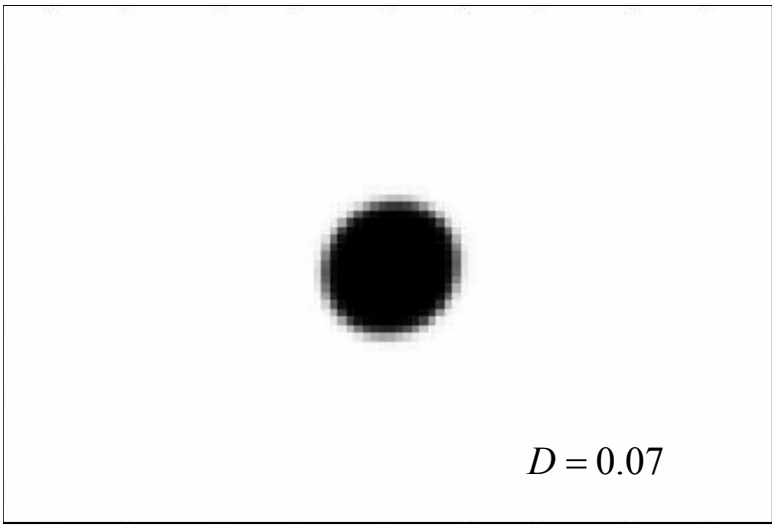

(b)

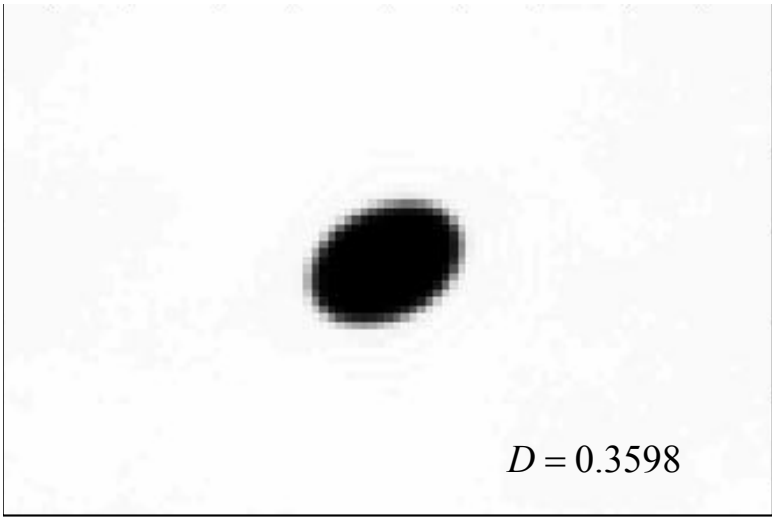

(c)

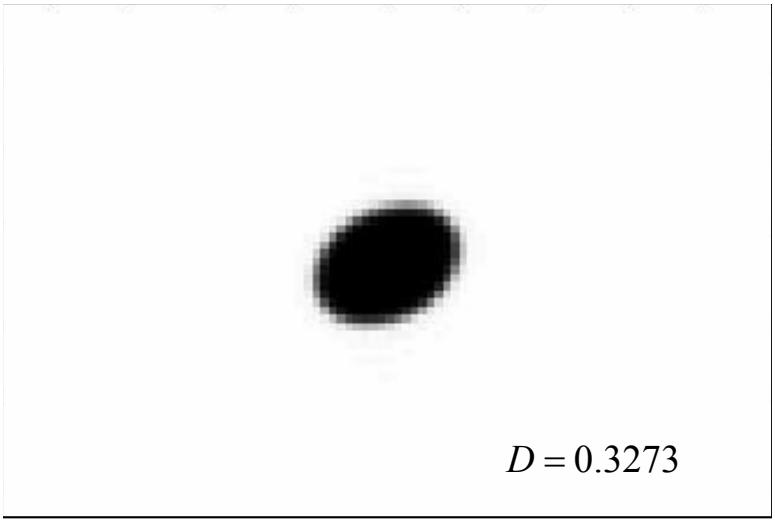

(d)

Figure 4.1: Steady state composition profiles of the droplet phase polymers: (a) $\Gamma = 3.18, \dot{\gamma} = 0.0$, Wi=0.0; (b) $\Gamma = 3.18, \dot{\gamma} = 0.15$, Wi=0.18; (c) $\Gamma = 3.18, \dot{\gamma} = 1.0$, Wi=1.2; (d) $\Gamma = 0.0, \dot{\gamma} = 1.0$, Wi=1.2. "$D$" denotes the deformation parameter for the droplet (The black color denotes the droplet phase).

Figures 4.1a-c display the steady-state composition profiles of the droplet phase for a fixed copolymer coverage Γ of 3.18 and for three different shear rates $\dot{\gamma} = 0, 0.15$ and 1.0 with corresponding Wi $= 0, 0.18$ and 1.2. The compatibilizer is a symmetric diblock-copolymer (i.e. the block sizes of A and B are equal) with $N_{AB} = 4$. We observe that with increasing shear rate there is a deformation of the droplet into an ellipsoidal shape accompanied both by an increase in the deformation parameter D and the orientation of the drop along the shear direction (the D values are displayed in the captions accompanying the figures). This increase in D is qualitatively consistent with the expectations based on theories for surfactant-free emulsion droplets, and is a result of the shear-induced elongation of the droplet along the major axis and its concomitant compression along the minor axis [113, 115].

More interesting are the effects of the copolymer upon these deformation characteristics, which is illustrated in Figs. 4.1c and d by contrasting the composition profiles at a fixed shear rate of $\dot{\gamma} = 1.0$ for the cases of a compatibilized droplet at 3.18 coverage and an uncompatibilized droplet (zero coverage). We notice that in the presence of a compatibilizer, there is almost a 10% increase in the deformation compared to the uncompatibilized droplet. The latter observations are broadly in accord with other theoretical [85] and experimental [89] results which demonstrate that for a fixed shear-rate, surfactants typically enhance the deformation of emulsion droplets. While the latter behavior arises due to the interfacial tension effects of surfactants, we note that in the context of block copolymer compatibilizers [88, 102], the increased

deformations can also arise due to the suppression of slip at the polymer blend interface [102]. In the next section we decouple these effects to understand mechanistically the origins of the deformation behaviors.

How does shear impact the copolymer composition profiles along the interface ? Figures 4.2a-c display the steady state copolymer composition profiles of the B part of the AB copolymer at shear rates $\dot{\gamma} = 0, 0.15$ and 1.0 and corresponding Weissenberg numbers Wi $= 0, 0.18$ and 1.2. We observe that as the shear rate is increased (Figs. 4.2b,c), there is a depletion of the copolymers from the equatorial region of the droplet and is accompanied by an accumulation at the poles of the droplet. This displacement of the copolymers is driven by the convective effect of the flow field and is resisted by the diffusive motion of the copolymers. As elaborated earlier, the relative magnitudes of these effects are parametrized using the non-dimensional Peclet number, Pe. Experiments [99] on polymeric droplet systems normally involve a high Pe $\simeq$O(10^5) owing to the small diffusion coefficients of the copolymer. In such cases, the convective effects dominate and visualization experiments by Macosko and coworkers [99] have demonstrated that even moderate shear rates can lead to highly non-uniform interfacial compositions. In contrast, our simulations involve a moderate Pe $\simeq O(10)$, and it is interesting to note that the qualitative aspects of the copolymer composition around the droplet interface in Figs. 4.2a-c are still similar to that observed in experiments of Macosko and coworkers (where Pe $\sim 10^6$). The latter suggests that the asymptotic limit of dominance of convective effects and the non-uniformity of compositions are

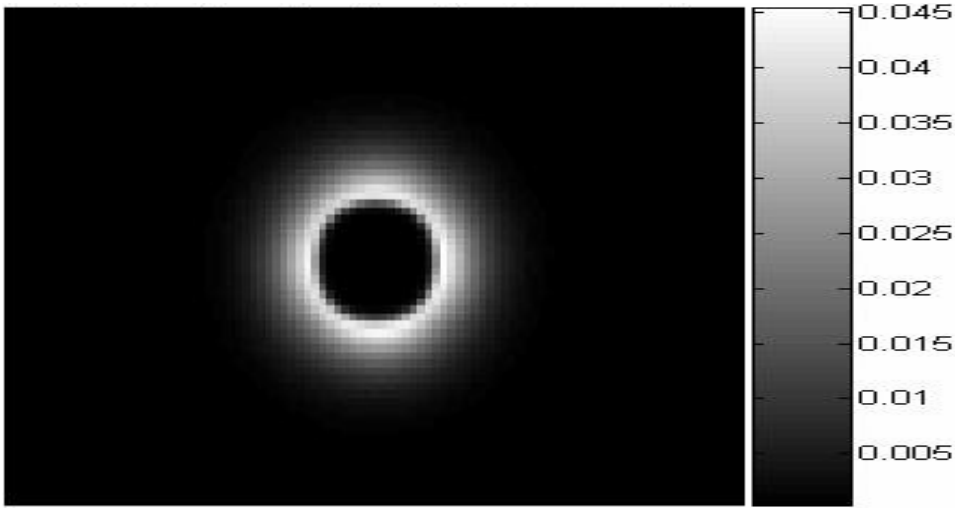
0.045
0.04
0.035
0.03
0.025
0.02
0.015
0.01
0.005

(a)

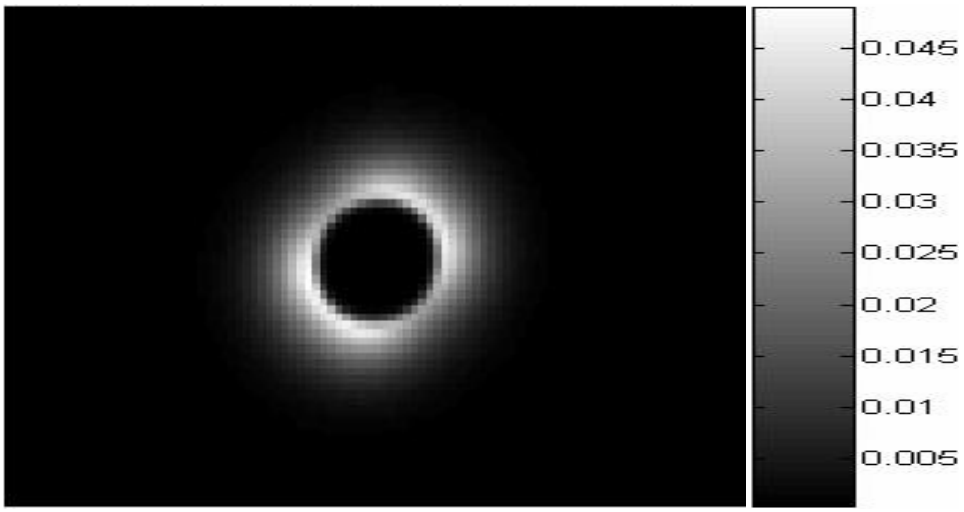
0.045
0.04
0.035
0.03
0.025
0.02
0.015
0.01
0.005

(b)

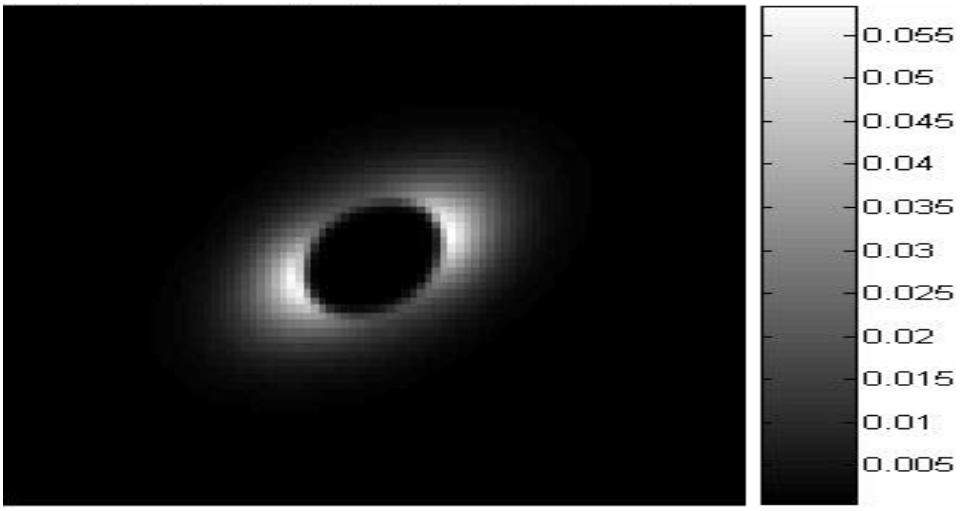

(c)

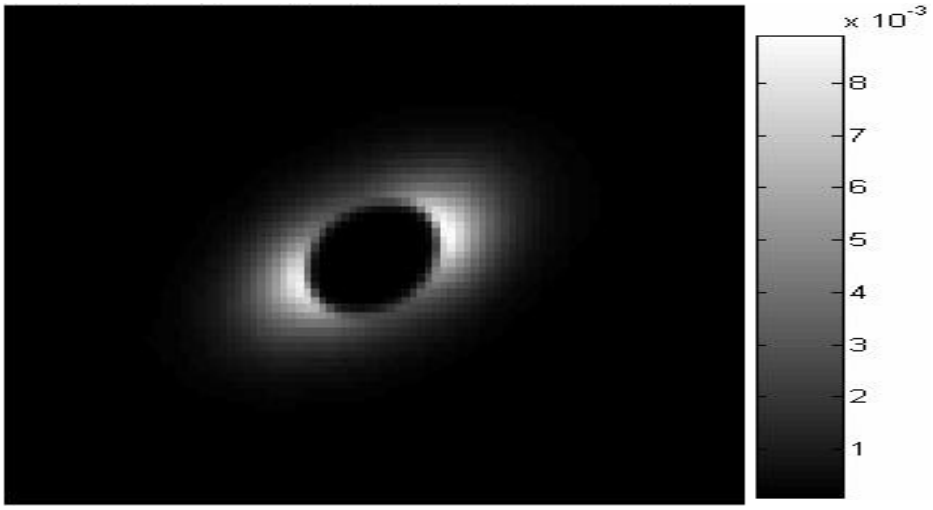

(d)

Figure 4.2: Steady state composition profiles of the copolymers: (a) $\Gamma = 3.18, \dot{\gamma} = 0.0$, Wi=0.0; (b) $\Gamma = 3.18, \dot{\gamma} = 0.15$, Wi=0.18; (c) $\Gamma = 3.18, \dot{\gamma} = 1.0$, Wi=1.2; (d) $\Gamma = 0.477, \dot{\gamma} = 1.0$, Wi=1.2 (The white color denotes the copolymer phase).

achieved at even relatively low shear rates. This effect is seen more clearly also in comparing Figs. 4.2c and d, which contrasts the composition profile characteristics for two different coverages ($\Gamma = 0.477$ and 3.18) at a fixed shear rate. From the intensity scales we notice increased concentration of copolymers in the vicinity of the poles for the higher coverage case, again suggesting the dominance of the convective effects. We note that these observations are qualitatively consistent with the conclusions of Pozrikidis *et al.* [100] which used finite element and finite volume simulations to study the effect of surfactants on drop deformation for a range of Pe. There again similar concentration profiles can be noted for the case of $\mathrm{Pe} = 10$. In the next section, we discuss the quantitative aspects of the composition profiles and its impact upon the droplet deformation.

Next we illustrate the effects of the physical characteristics of the copolymer and the droplet deformation in modifying the resulting flow field. First we focus on the structure of the flow at different magnitudes of the applied shear rate. Figures 4.3a,b display the flow streamlines for the case of a pure polymer droplet at shear rates $\dot{\gamma} = 2.0$ and 3.5. The relatively noisy streamline patterns arises from the use of a stochastically averaged velocity profiles defined at every point on the continuum grid. However, it is still observed from the streamlines that the averaged matrix velocity of the polymers near the droplet is tangential to the deformed droplet interface. Moreover, it is also seen that the velocity disturbances propagate to a distance of the order of the deformed droplet radius in the normal direction. Finally, we observe a

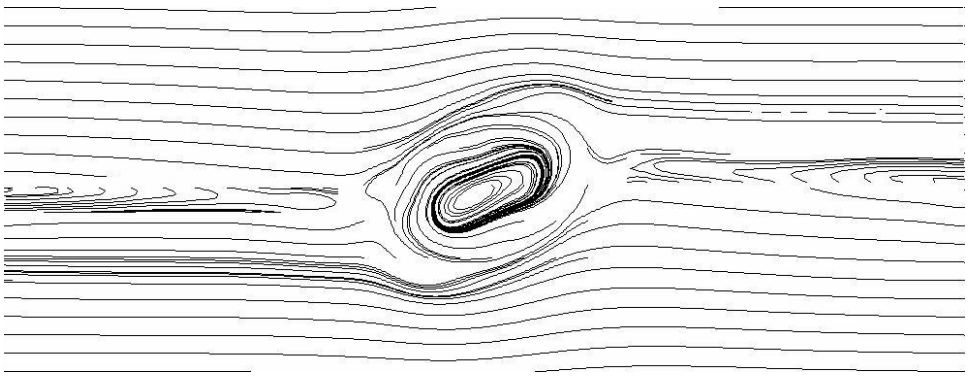

(a)

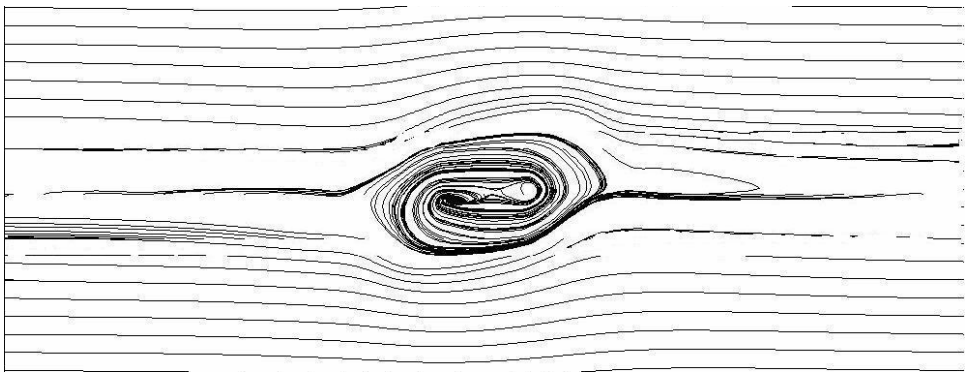

(b)

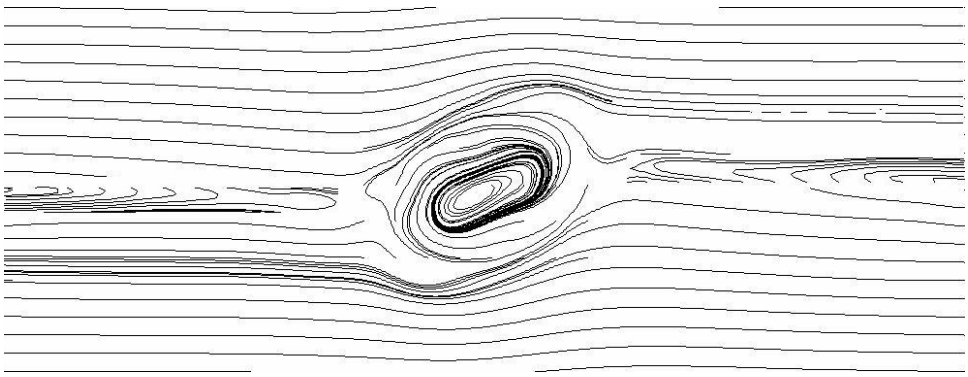

(c)

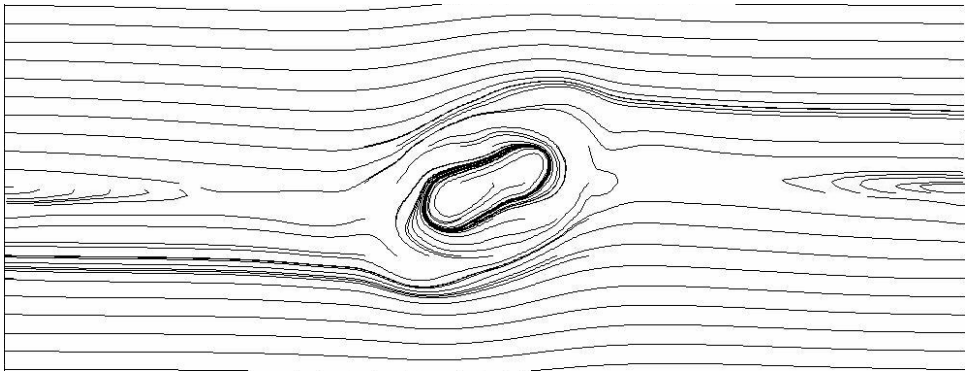

(d)

Figure 4.3: Steady state streamline profiles: (a) $\Gamma = 0.0, \dot{\gamma} = 2.0$; (b) $\Gamma = 0.0, \dot{\gamma} = 3.5$; (c) $\Gamma = 0.0, \dot{\gamma} = 2.0$; (d) $\Gamma = 3.18, \dot{\gamma} = 2.0$.

single vortex in the flow field inside the droplet, which gets distorted depending on the flow strength and droplet orientations. These observations, while consistent with continuum deductions [115], has to our knowledge never been simulated using a (quasi) molecular/Brownian dynamics simulation approach. Consistency with continuum expectations (and other related work noted below) serves to emphasize the validity of our simulation approach in capturing hydrodynamical phenomena.

In terms of the influence of shear rates, it is evident by comparing Figs. 4.3a,b that while the droplet is more deformed and oriented towards the shear direction at $\dot{\gamma} = 3.5$ (Fig. 4.3b), the overall patterns of the flow are relatively insensitive to the droplet shape, and in both cases we observe a single eddy inside the droplet. One difference evident between the two streamlines is with respect to the width of the recirculating region along the x-axis resulting from flow separation. The recirculation region is comparatively longer (along the shear direction) at the lower shear rate of $\dot{\gamma} = 2.0$ and its size progressively decreases with an increase in the shear rate and at a shear rate of $\dot{\gamma} = 3.5$ there is almost a lack of recirculation region. These observations can be rationalized by noting that with an increase in the applied shear the droplet elongates and aligns towards the direction of applied shear. This decreases the effective radius of the ellipsoidal droplet along the y direction. This in turn reduces the obstruction to flow in the x-direction and hence reduces and eventually eliminates the recirculation patterns. Flow separation and recirculation patterns are observed in Newtonian flow over a stationary cylinder. This is

a result of an "adverse" pressure gradient along the cylindrical surface. In a two-dimensional framework, our system corresponds to a situation with flow over a cylindrical droplet with deformable surface. We note that boundary integral simulations by Zhou and Pozrikidis [115] have also reported similar streamline patterns and recirculation phenomena.

Finally, we compare the flow streamlines for an uncompatibilized droplet and a compatibilized droplet (3.18 coverage) at a fixed shear rate of 2.0 (see Figs. 4.3c,d). Again we notice a qualitatively similar flow pattern in both the cases, with however the width of the recirculation region being smaller for the compatibilized case compared to that of the uncompatibilized droplet. The latter can be explained by invoking our earlier observations that at a fixed shear rate, the presence of the compatibilizers increases the overall deformation of the droplet (the mechanism behind this effect will be explored in the following section). This increase in droplet deformation results in a corresponding reduction in the width of the recirculating region, by the mechanism discussed in the above paragraph.

In this section, we have presented some visual evidence of the qualitative effects resulting from the externally applied shear field and the compatibilizer coverage upon the deformation and the flow characteristics. Our main observations are that the presence of the compatibilizer influences the deformation characteristics while having only a lesser effect on the gross aspects of the flow field. Our results mirror many of the theoretical predictions and experimental observations pertaining to the same features, thereby suggesting

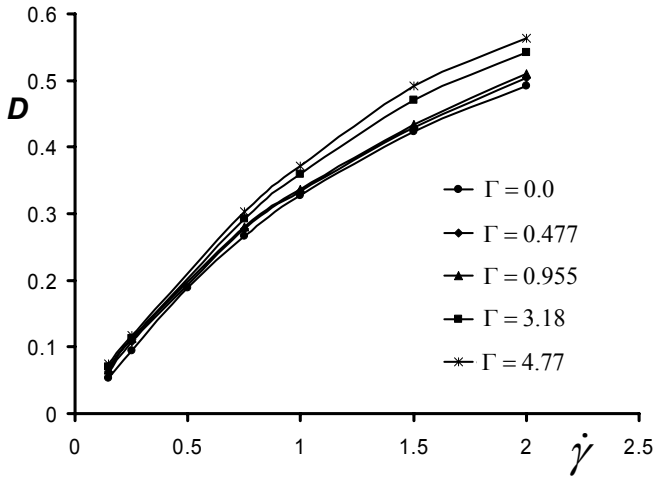

Figure 4.4: Droplet deformation parameters D as a function of applied shear rate $\dot{\gamma}$ for different compatibilizer coverages Γ.

the validity of our "molecular simulation" approach for capturing hydrodynamics of macroscopic phenomena. In the following section, we consider in more detail the quantitative aspects of droplet deformation.

4.4 Quantitative Aspects of The Deformation Behavior of Droplets

In this section, we consider the quantitative aspects of the deformation of the droplets and identify the mechanistic basis for our observations. In Fig. 4.4 we display our simulation values of the deformation parameter D as a function of shear rate $\dot{\gamma}$ for compatibilized droplets at different coverages Γ ($\Gamma = 0$ corresponds to the case of uncompatibilized droplet). We observe that for a given coverage of the copolymer, the deformation parameter monotoni-

cally increases with an increase in the shear rate approaching the asymptotic maximum deformation $D = 1$. We note that this monotonic trend as a function of shear rate contrasts somewhat with the predictions [83] and observations[118] for emulsion droplets, which typically undergo a breakup at higher shear rates due to capillary and other instability mechanisms. We believe that this discrepancy is due to the two-dimensional nature of our flow simulations. Indeed, Lattice-Boltzmann simulations by Wagner and coworkers [114] have suggested that in the absence of inertial effects there are no droplet breakup mechanisms in two dimensions and that the drops continue to elongate (upto the maximum deformation) as a function of the shear rate.

More pertinently it is evident from Fig. 4.4 that at a fixed shear rate the deformation of the droplet *increases monotonically with an increase in the copolymer coverage*. To elucidate the mechanisms behind this effect, we first recall the different means by which compatibilizers have been proposed to influence the deformation characteristics: (i) The compatibilizer can induce a reduction in the overall interfacial tension σ of the polymer blend interface [104]. The latter is expected to lead to a concomitant reduction in the interfacial forces resisting the deformation, resulting in an overall increase in the deformation of the droplet; (ii) Marangoni stresses can arise from the nonuniformity of the copolymer concentrations (cf. Fig. 4.2) and tends to resist the deformation of the droplet [87, 116]; (iii) Convection of the surfactants to the tips of the droplet can lead to a concomitant increase in the deformation if it leads to a substantial lowering of the interfacial tension at the poles (tip

stretching effect) [117, 118]; (iv) Droplet deformations increase the interfacial area, leading to an effective dilution of the copolymers which can result in an overall decrease in the deformation [82]; (v) Copolymer-induced suppression of slip can result in more efficient interfacial stress transfer to the drop, leading to an increased deformation.[102]

To identify the actual manner in which the above mechanisms impact the behavior in Fig. 4.4, we first account for the overall reduction in the equilibrium interfacial tension. While our simulations can be used directly to determine the surface tensions of copolymer-covered flat interfaces, we opt here for an indirect approach (cf. also Leal and coworkers [89]) which uses our D values at low shear rates but also accounts for the possible curvature effects upon the interfacial tension. We use ideas motivated by the results of small deformation theories of drop deformation [88, 119] (in three dimensions), which suggests that for *weak shear rates* the only role played by the compatibilizer is its effect on the interfacial tension and $D \propto \mu R_o \dot{\gamma}/\sigma(\Gamma)$. Explicitly, we find the coverage dependent interfacial tension $\sigma(\Gamma)$ by rescaling the shear rates $\dot{\gamma}$ such that at low values of this normalized shear rate the deformation parameters D match identically at different coverages of the copolymers.

Figure 4.5 presents the results of the so-determined "equation of state" relating the interfacial tension σ to the copolymer coverage Γ. We observe that there is a relatively strong decrease in the interfacial tension at lower coverages followed by a much weaker lowering for higher coverages of the compatibilizer. We have explicitly verified that at higher coverages there is no change in the

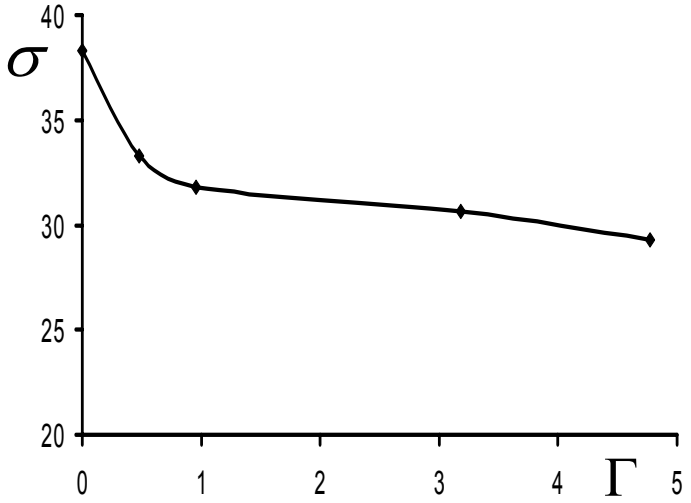

Figure 4.5: Effective surface tension σ (note: the interfacial energy is non-dimensionalized with energy scale $k_BT = 1.0$ and length scale of $R_g = 1.0$) plotted as a function of the copolymer coverage Γ.

interfacial coverage from the expected values and hence we believe that this behavior does not arise from a diffusive leakage of the compatibilizer into the bulk phases (cf. experiments of Anastasiadis *et al* [120]). Instead, the trends observed in Fig. 4.5 can be rationalized by considering two competing interfacial effects that result specifically from the addition of block copolymer compatibilizers: (i) On the one hand they lower the interfacial tension Σ (we distinguish this from the above effective interfacial tension, σ and explain this distinction below); (2) Secondly, block copolymers lead to an increase in the bending modulus of a polymer blend interface. Explicitly, theoretical

calculations by Matsen [121] (cf. also Wang and Safran [108]) suggest that

$$\Sigma = \Sigma_0 - \frac{\pi^2}{4}\Omega_0^3 \tag{4.2}$$

$$K = K_0 + \frac{3\pi^2}{64}\Omega_0^5 \tag{4.3}$$

where Ω_0 is a measure of the interfacial coverage of the copolymer, Σ_0 and K_0 denotes the bare (copolymer-free) surface tension and bending modulus of the interface, while Σ and K represent the surface tension and bending modulus at a local copolymer coverage of Ω_0. Whence it is evident that at lower coverages of the compatibilizer, the copolymer has a more dominant effect in decreasing the interfacial tension, while at higher coverages the compatibilizer has a more dominant effect in increasing the bending modulus of the interface. Alternately, at lower droplet sizes the bending modulus plays an important role, while at higher droplet sizes, the bending modulus effects are negligible. Bending modulus effects on the deformation of an elastic interface have been studied by Pozrikidis and coworkers within the context of red blood cells. They have observed progressively decreasing deformation of an elastic interface with increasing bending moments. To rationalize the behavior in Fig. 4.5 in terms of bending modulus effects we note that the indirect approach used to measure $\sigma(\Gamma)$ essentially measures an effective interfacial tension as mentioned before, representing a composite of the increased deformability arising from a reduction in the actual interfacial tension Σ, and the enhanced rigidity which arises from the increase in the bending modulus K. At low coverages, the former dominates, leading to the steep decrease evident in σ, followed by a

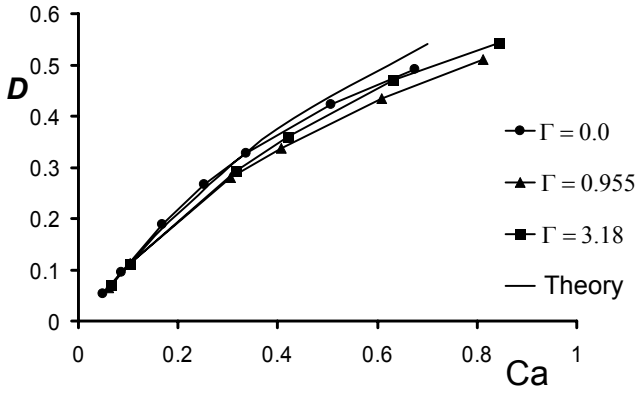

Figure 4.6: Droplet deformation parameter D is displayed as a function of capillary number Ca. In the above, theory refers to the predictions of [94].

crossover to the influence of the bending modulus effect at higher coverages which renders the droplet less deformable. This effect is manifested in Fig. 4.5 as a plateauing of effective interfacial tension at higher coverages.

Having determined the effective interfacial tension $\sigma(\Gamma)$, we can now examine the different mechanisms by which copolymers affect the deformation of the droplet. Figure 4.6 displays the deformation parameter D now as a function of the capillary number $\text{Ca} \equiv \mu R_o \dot{\gamma}/\sigma(\Gamma)$. Also displayed (solid line) are the D values obtained from the small deformation theories [93, 94] proposed for three dimensional droplets in Newtonian systems. We observe that the deformations predicted by the theories agree very well at low capillary numbers. However, there exists a consistent negative deviation of deformation from the theoretical prediction at higher capillary numbers, which we speculate to be either due to the two dimensional nature of our simulations [114] or due to the effect of viscoelasticity owing to high Wi. Recent experimental determination

of droplet deformation for a viscoelastic system by Guido and coworkers [122] have also shown negative deviations from the theoretical predictions. More interestingly, it is evident that in this representation the D values at a given Ca are all *lower* than that of the pure polymer droplets. Secondly, we also note a non-monotonic dependence of the deformations as a function of the copolymer coverage with a decrease in the deformations upto a coverage of $\Gamma = 0.955$, followed by an increase in the deformations at higher coverages (albeit the deformation for the compatibilized drop being still lower than the deformation observed for the pure polymer droplet).

We note that the above results are in qualitative agreement with the experimental observations of Velankar and coworkers [118] where increasing copolymer coverage was shown to lead to a significant decrease in the deformability of the droplets (in the Ca representation). The results in Fig. 4.6 already provide insights into the mechanisms by which copolymers influence deformation. By comparing the relative deformations of the compatibilized and the uncompatibilized droplets in the $\dot{\gamma}$ (Fig. 4.4) and Ca (Fig. 4.6) representations we deduce that the *dominant mechanism behind the copolymer-induced increase in droplet deformations in Fig. 4.4* arises due to the influence of the copolymers upon the interfacial tension of the polymer-polymer interface. Further, the fact that upon incorporating the interfacial tension effects, block copolymers actually reduce the deformation of the polymer droplets relative to the uncompatibilized droplet suggesting that *slip suppression* effects of the copolymers play, if any, only a secondary role in influencing the defor-

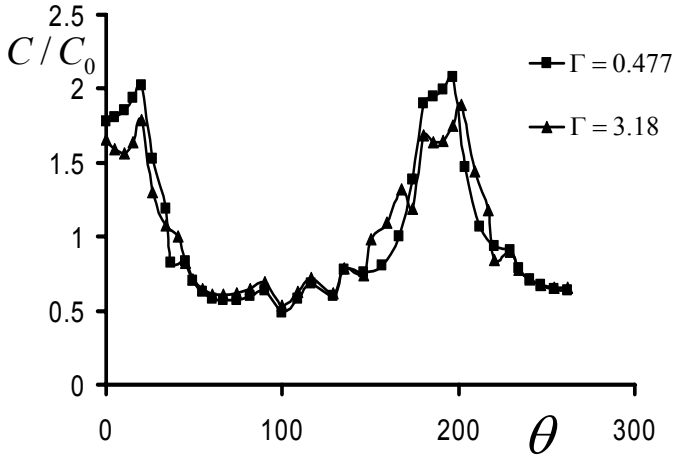

Figure 4.7: The variations of copolymer composition C (normalized by its uniform value, C_0) as a function of the meriodonal angle θ for two different copolymer coverages Γ.

mations.

However, our observations so far provide only a partial explanation of mechanistic basis of the copolymers. Indeed, in the absence of additional effects, the D values at a given Ca for the uncompatibilized drop is expected to be identical to the deformation parameter for a droplet with uniform coverage of copolymers along the droplet surface. "What causes the coverage effects observed in Fig. 4.6?" To explain these observations we recall that even moderate flows lead to a significant inhomogeneity in the copolymer distribution around the interface. Below we examine these concentration profiles to shed light on their role in influencing the deformations.

In Fig. 4.7 we display the average, normalized copolymer composition profiles along the interface at two different coverages (representative of low

and high coverages) as a function of the meriodonal angle along the interface. In accordance with the Fig. 4.2, we observe that at all coverages there is an accumulation of the copolymers at the tips of the droplet and a concomitant depletion at the equatorial regions. As discussed earlier, accumulation of copolymers at the tip is expected to lead to a decrease in the local interfacial tension and an increase in the deformation at the droplet poles [84]. However, it is evident from the equation of state presented in Fig. 4.5 that this effect becomes relatively less pronounced upon increasing the coverage beyond a certain value, and hence we speculate that its influence upon the deformations is not a dominant effect. In contrast, the depletion of the compatibilizers from the equatorial region can lead to a significant increase in the interfacial tension of those regions, thereby reducing the deformability of the droplet. We believe that the preceding effect underlies the reduced deformations observed for the compatibilized droplet in comparison to the uncompatibilized droplet.

To explain the nonmonotonic trends noted as a function of the copolymer coverage, we observe from Fig. 4.7 that at lower coverages the concentration gradients are relatively stronger compared to the situation at higher coverages. At higher copolymer coverages, the Marangoni stresses resulting from the concentration gradients are expected to become more pronounced leading to the reduced copolymer concentration gradients as displayed in Fig. 4.7. The situation for higher coverages then resembles more closely the case of a uniform copolymer coverage along the interface. We believe that the relatively weaker depletion-induced increase in interfacial tension that results in such a scenario

leads to the observed increase in deformation parameter for the coverages of $\Gamma = 3.18$ and 0.477.

It is interesting to probe if the above arguments can be equally applied in consideration to other physical characteristics of the copolymer. To address this issue, we consider briefly the effects of the copolymer chain length upon the above deformation characteristics. Figure 4.8a displays the D values as a function of the rescaled Ca for droplets compatibilized with copolymers of different chain lengths but at the same fixed coverage. While we observe only weak chain length effects, it is still evident that an increase in the chain length leads to an increase in deformations. To rationalize these trends, we again consider the copolymer concentration profiles along the interface (see Fig. 4.8b) for different copolymer lengths. It can be observed that for longer copolymer chains the concentration gradients tend to be much weaker. We rationalize the latter by noting that for longer copolymers the Marangoni elasticity and the resulting stresses arising from the coverage dependence of interfacial tensions are much stronger [118] leading to more uniform coverage of copolymers along the interface. As mentioned earlier, a more uniform coverage of the drop reduces the effects arising from the depletion of copolymers and hence promotes the increased droplet deformation as observed in Fig. 4.8a.

In summary, we have considered the different effects by which the copolymers influence the deformation characteristics of the polymer droplet. Of these effects we identify the reduction in interfacial tension as a dominant effect influencing the droplet deformation. However our results suggest that

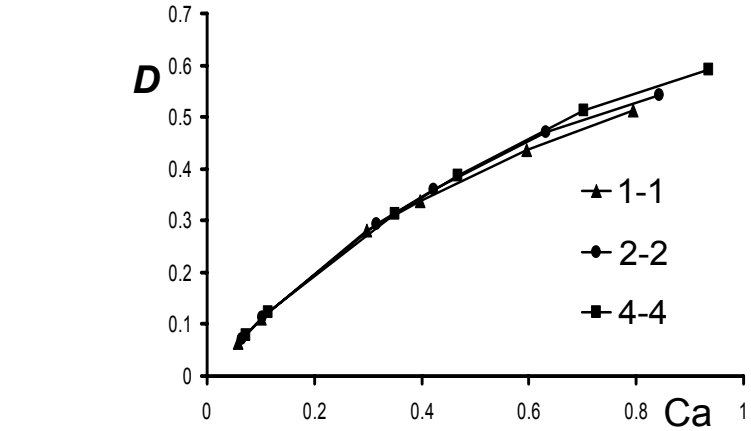

(a)

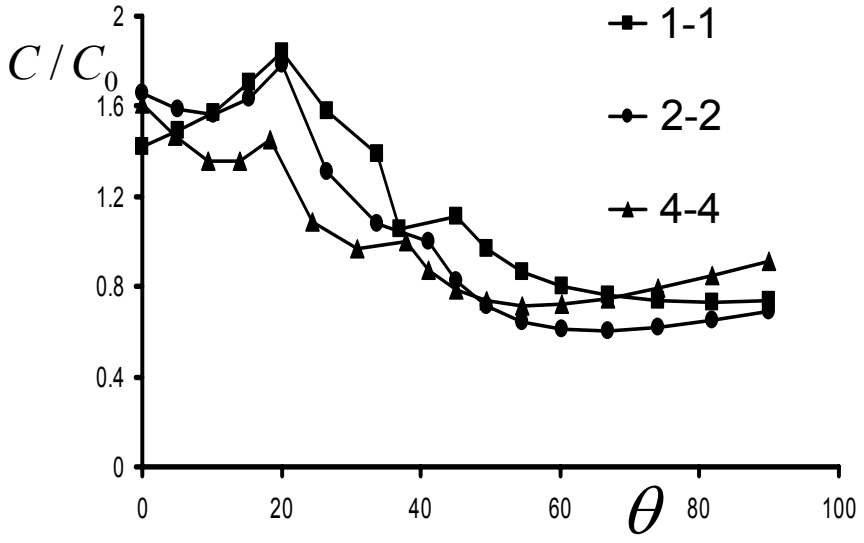

(b)

Figure 4.8: (a) Droplet deformation parameter D displayed as a function of the capillary number Ca at a coverage $\Gamma = 3.18$ for different copolymer lengths N_A-N_B; (b) Normalized copolymer compositions as a function of the meriodonal angle θ for three different copolymer lengths N_A-N_B.

effects arising from non-uniform copolymer coverage along the interface can also affect the coverage dependence of the deformation characteristics. For the parameters considered in our simulations, we identify "equatorial depletion" (and the lack thereof) as the next most important mechanism controlling the deformation of the droplet. We point out that this observation is qualitatively identical to the results of Li and Pozrikidis [84] who used boundary integral numerical techniques to address the analogous surfactant problem. They demonstrated that the equatorial depletion effect plays a dominant role in determining the deformation characteristics in simple shear flows when the $\mathrm{Pe} \simeq O(1)$ (the regime considered in this work).

4.5 Rheology

The rheological characteristics of a homogeneously mixed polymer blend exhibits a rich variety of phenomena arising from the viscoelastic nature of the individual polymer matrices [40, 123]. In the case of a phase-separated polymer blend, additional features manifest to influence the rheology, including: (i) The stresses resulting from the interfaces and their shear-induced deformation [98, 119, 124] and (ii) Contributions due to slip at the polymer-polymer interfaces [102, 103]. Addition of copolymer compatibilizers to the mixture influences each of the above characteristics and in turn the overall rheology of the mixture [125]. On the one hand, the deformation characteristics of the droplet (and interfaces) are affected by the copolymer. Secondly, slip at polymer-polymer interfaces is lowered due to the additional friction provided by the

copolymers [67, 126]. Finally, the rheological characteristics of the copolymer layer can by itself contribute to the overall rheology of the system.

In this section we complement our deformation results by discussing the effects of the copolymer in modifying the rheological characteristics of the mixture. The main question we address is, "Do the rheological properties of the mixture track the deformations (as is true for simple emulsions) or do additional dynamical effects, such as slip, play a role?" We note that the unentangled, Gaussian chain model employed in this study exhibits a simple rheological behavior which eliminates some of the richness possibly observable in experiments. Indeed for a homogeneous system, our model exhibits a constant, shear rate independent viscosity and a first normal stress difference characteristic of the Rouse model. Whence shear rate dependent viscoelastic effects must necessarily arise from the deformation of the interface and the slip effects.

The shear stress and the normal stress differences are computed using the Kramer's stress expression for bead-spring systems. This expression explicitly accounts for the elastic stress stored in the springs connecting the beads. Figure 4.9 displays the low shear viscosity (determined at a shear rate $\dot{\gamma} = 0.15$) for polymer blend droplets at different coverages Γ and for different chain lengths N_{AB}. Note here that the viscosities are normalized by the rouse viscosity of a completely homogeneous polymeric system. The lower viscosity at zero copolymer coverage is a direct consequence of slip at the interface of the droplet and matrix polymers. For comparison we have also displayed the

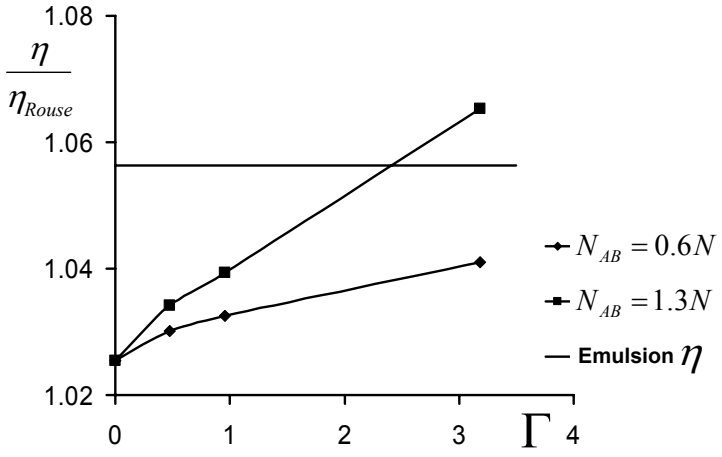

Figure 4.9: Low shear viscosities η_0 as a function of coverage for two different copolymer lengths. The thin line indicates the theoretical prediction for the emulsion viscosity [127] at zero copolymer coverage.

corresponding theoretical predictions for the effective viscosity of a suspension of Newtonian emulsions droplets at the volume fraction corresponding to our simulations. We observe that for both chain lengths, at low coverages Γ, the effective viscosity of the compatibilized polymer blend is lower than the theoretically predicted values. However, with an increase in the coverage of the compatibilizer, the low shear viscosity is seen to increase and for high enough coverages exceed that of the emulsion predictions. Secondly, it is also evident that at a given coverage, the effective viscosities are larger for the case of the larger copolymer chain when compared with the smaller compatibilizer.

The above observations can be rationalized by invoking considerations of slip at the polymer-polymer interface and its suppression by the addition of copolymers. Indeed, earlier experimental [67] and theoretical[103] studies

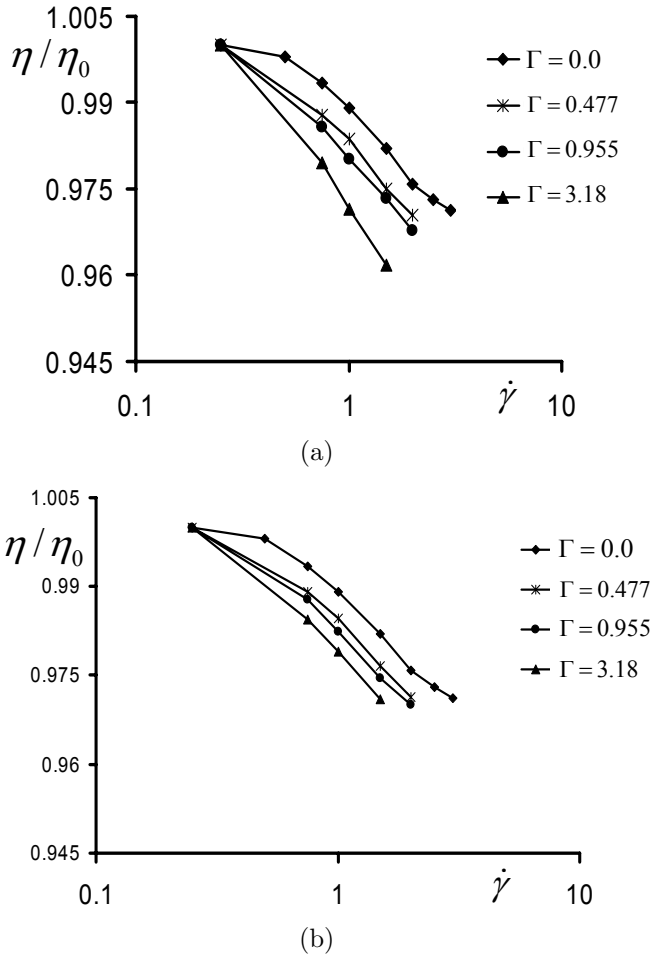

Figure 4.10: Normalized shear viscosity as a function of shear rate $\dot{\gamma}$ for different coverages and for copolymer chain lengths: (a) $N_{AB} = 1.3N$; (b) $N_{AB} = 0.6N$.

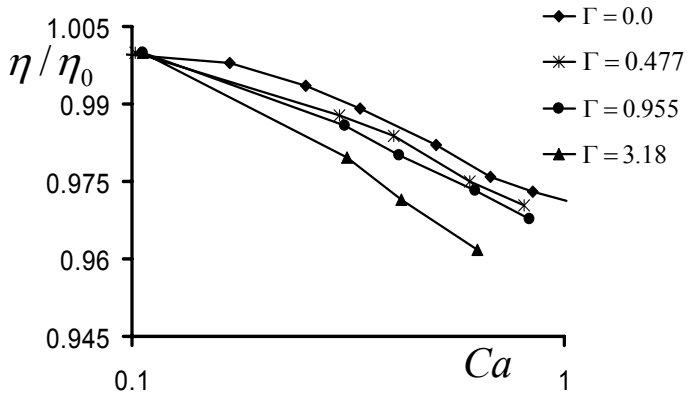

(a)

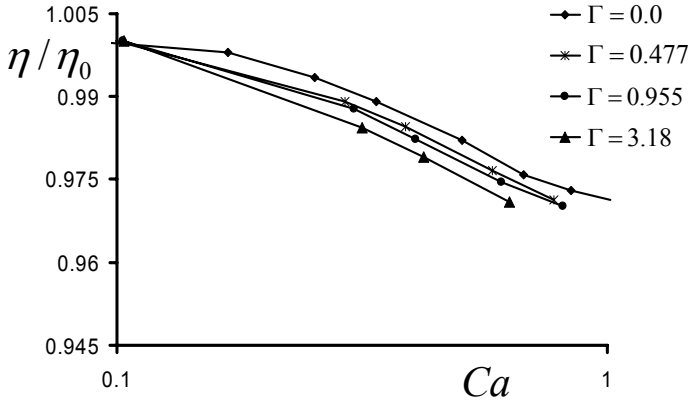

(b)

Figure 4.11: Normalized shear viscosity as a function of capillary number Ca for different coverages and for copolymer chain lengths: (a) $N_{AB} = 1.3N$; (b) $N_{AB} = 0.6N$.

have demonstrated that even in the case of unentangled polymers, the velocity profiles can exhibit a slip at polymer blend interfaces. In fact, the latter has been implicated in the anomalously low mixture viscosities that have been reported in many polymer blend systems. More recent works have suggested that even trace amount of copolymers can lead to a suppression of the slip and render the interface more akin to a "solid" boundary. Furthermore, this slip suppression efficacy has been predicted to increase with an increase either in the coverage Γ or the copolymer chain length, N_{AB}. These considerations are consistent with the results in Fig. 4.9a and suggests that the lower than expected viscosities at low coverages can be attributed to the slip occurring at the polymer blend interfaces and the eventual increase at higher coverages (or with the chain length N_{AB}) can be ascribed to the slip suppression resulting from the addition of copolymers.

Figure 4.10 displays the results for the steady shear-rheology for droplets compatibilized by copolymers at different coverages and chain lengths. It is evident that all the polymer droplet systems exhibit shear thinning behavior, albeit only weak within the shear rates probed in our simulation. We note that shear thinning behavior observed in the boundary integral simulations of Pozrikidis and coworkers [115] was also only of the order of a 3% decrease in the viscosities, which is consistent with our results. Shear thinning rheology is a generic characteristic of droplet systems and can be understood as resulting from the increased deformation and orientation of the droplet with increasing shear [124]. The latter in turn leads to a reduction in the dissipation resulting

from the presence of the droplet and hence a lower viscosity of the suspension. We observe that the trends evident in Figure 4.10 are overall in accord with this deformation mechanism. Explicitly, we note that shear thinning becomes more pronounced with an increase in the coverages and the chain lengths of the copolymer, which is consistent with the enhanced deformation observed (Figs. 4.8) at a given shear rate for increasing coverages and chain lengths of the compatibilizers.

Is droplet deformation the only mechanism responsible for results in Fig. 4.10? We recall that in the preceding section we suggested that the deformations exhibit a non-monotonic behavior (as a function of coverage) when represented as a function of capillary number, Ca. In contrast the results displayed in Fig. 4.11 demonstrates that the normalized viscosities, η/η_0 exhibit a monotonic trend as a function of Ca, suggesting the influence of additional mechanisms in shear thinning. To rationalize these observations we recall that copolymers influence the shear rheology also by an additional mechanism, viz. the suppression of slip. It is evident from the composition profiles displayed in Fig. 4.7, that shear leads to convection of the copolymers from the equatorial region of the droplet to its poles. The latter is expected to lead to a more pronounced slip, especially for droplets with higher coverage where the copolymer had effectively suppressed the slip effects. We speculate that this mechanism is possibly responsible for the monotonic and lower viscosities observed at higher coverages.

Next, we consider the first normal stress difference behavior of our

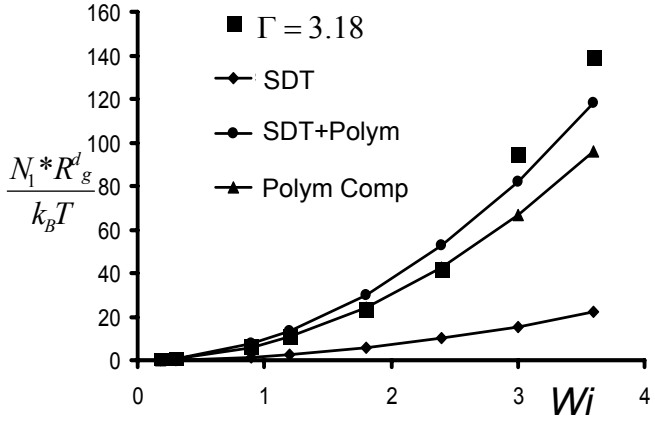

Figure 4.12: First normal stress difference obtained at a copolymer coverage of 3.18 is compared with the results of small deformation theory (SDT [119]), Polymer component of normal stress difference [40] (indicated above by Polym Comp) and the polymer corrected normal stress difference (SDT+Polym).

system, the results of which are displayed in Fig. 4.12. There are two contributions to the first normal stress differences in our system. On the one hand, since the polymer matrix and the droplet are both viscoelastic in nature, they exhibit individually a first normal stress difference. In Fig. 4.12 we display this contribution (indicated by "Polym Comp") for a homogeneously mixed polymer blend system containing unentangled Rouse polymers [40]. A comparison of our results with this viscoelastic N_1 indicates a semi-quantitative match at lower Wi, with deviations notable at higher Wi. The latter can be rationalized as a consequence of ignoring the droplet deformation contribution to the normal stress, which becomes more pronounced with increasing shear rates and Weissenberg numbers. The latter manifests even for a simple emulsion droplet and has been calculated theoretically by Schowalter *et al* [119]. for small de-

formations of the droplet. Its dependence on Wi is displayed (indicated by "SDT") in Fig. 4.12. It is evident by comparing our results to the predictions of small deformation theory that the latter grossly underpredicts the values of N_1. This can be understood easily since the latter predictions were obtained for Newtonian droplets while making no allowance for the viscoelastic nature of components in a polymeric system.

In order to crudely incorporate both the aforementioned effects, we add the N_1 values obtained for a homogeneous viscoelastic system of completely non-interacting Rouse chains, to the small-deformation theory predictions of Schowalter *et al* [119]. This value, referred in this research as "polymer-corrected" N_1 values, is also depicted in Fig. 4.12. We observe that while this polymer corrected contribution provides a better estimate of our results, positive deviations from the latter are still witnessed at higher Weissenberg numbers. At this moment, we do not have a satisfactory explanation of these discrepancies. In the numerical studies of Li and Pozrikidis [84], a positive deviation from the small deformation theory was also observed for high shear rates which was attributed to the Marangoni stresses. As noted earlier, we expect significant Marangoni stresses to also manifest in our system at high shear rates (or Wi), and can rationalize the positive deviations in the first normal stress difference values. Alternatively, the latter discrepancies can also be a result of the 2D situation considered in this research. In the absence of a theory for 2D viscoelastic fluids, we are unable at this time to resolve the interplay of the preceding contributions. Independent of these latter discrep-

ancies, our results at lower Wi clearly suggest the polymer contribution to the N_1 to be the dominant effect compared to the droplet N_1.

Our results presented in this section suggest that copolymer compatibilizers around the droplet have a non-trivial effect not only upon the deformation phenomena but also upon the overall rheological behavior of the droplet-matrix system. Explicitly, while the steady shear rheology tracks the deformation behaviors, both the low shear viscosities and the shear rheology display effects arising from the slip suppression feature of the copolymers. The latter renders the rheological properties nontrivially dependent upon the copolymer coverages and chain lengths. The behavior of the first normal stress differences also differs from conventional emulsion predictions. While the majority of these discrepancies can be accounted by the contributions to N_1 from the matrices themselves, remnant discrepancies were still visible at higher shear rates which were attributed to the Marangoni stresses.

4.6 Conclusion

In this work we have used Brownian dynamics simulations to study the free-boundary problem involving a deforming polymer droplet interface under externally applied steady shear flow. Our focus was specifically on the effects of the physical characteristics of copolymer compatibilizer (coverage, chain length) upon the polymer droplet deformation characteristics and inturn on the rheological properties of such polymer melt systems. We have presented the deformation characteristics of a compatibilized droplet as a function of shear

rate with increase in length and coverage of copolymer compatibilizer. The copolymer coverage affects the deformation in a non-trivial and non-monotonic manner when plotted against the rescaled capillary number. The interfacial tension, bending modulus, Marangoni stresses were identified as playing competing roles in influencing the droplet shape, with the reduction in interfacial tension being the dominant mechanism affecting the droplet deformation. For the rheological characteristics, we found noticeable change in shear-thinning properties with increasing copolymer coverage around the droplet interface. Moreover, the low shear viscosities show an increase with increasing coverage and chain length of copolymers. Our results serve to highlight the role of physical characteristics of the copolymer in influencing the droplet deformational and the rheological characteristics of the polymer blend mixture.

One shortcoming of this study is that it was performed in two-dimensions. Novel effects observed in experiments, such as widening of the viscoelastic droplets in the vorticity direction could not be studied using in this framework. Also, some of the effects of coverage upon deformation and the rheology observed in this work could become more pronounced in the context of three dimensional simulations. Another natural extension of our study is to incorporate the effects of contrasting viscoelastic properties for the matrix and droplet polymers. Future works will focus on extensions along these directions.

Chapter 5

Dynamical Phenomena in Ternary Polymer Blends

5.1 Introduction

From the researches detailed in previous chapters, it is evident that complex polymeric fluids such as polymer blends exhibit fascinating rheological properties while undergoing a multitude of morphological transformations under external flow [33–36, 130, 132]. In the previous two chapters we focused on dynamical phenomena in binary polymer blends of two homopolymers. In the present chapter we focus on a different class of polymeric systems, viz., ternary polymer blends formed by mixing immiscible homopolymers A and B with comparable amounts of block copolymer AB. As mentioned earlier, binary blends of polymeric systems tend to exhibit macroscopic phase separation [27–29], which often results in poor property characteristics for the polymeric material. This problem is typically overcome by the addition of compatibilizers [67, 101], like block, graft or random copolymers to the binary blend. Such compatibilizers, preferentially position themselves at the interfaces of bulk domains and contribute to the stabilization of the interfaces by reducing the interfacial tension, or by triggering the formation of *micro*-phase separated morphologies like lamellar phases or bicontinuous microemulsion phases

[135–139]. For instance, Fig. 5.1 displays the experimental phase diagram of a symmetric ternary blend of homopolymers PDMS and PEE blended with block copolymer PDMS-*b*-PEE (adapted from [140]). Here the block copolymer molecule is symmetric in block lengths and is roughly 5 times longer than the homopolymer molecule with $\alpha = N_{AB}/N_A = 5.0$. In such ternary blends, at low values of volume fraction, ϕ, (corresponding to a predominantly block copolymer system) lamellar phases are obtained and at high ϕ values, (corresponding to a predominantly binary blend) two phase coexistence is obtained. However, at intermediate values of ϕ, the existence of bicontinuous microemulsion phases and three phase coexistence is observed [130, 132].

In the above system, bicontinuous microemulsion like phases have received particular attention. These phases, first observed in oil/water/surfactant (o/w/s) systems [141], have intriguing complex structures as shown in Fig. 5.3a. They possess a complicated, delicately balanced microstructure, with large interfacial area and negligible interfacial tension due to the presence of the surfactants at the interface. The rich morphologies are also expected to lead to complex rheological phenomena, albeit, the experimental studies of which has been limited owing to fast microstructural dynamics in o/w/s systems. However, there exists a vast amount of theoretical and experimental research on the flow effects on bicontinuous phases of surfactant systems, which have demonstrated that shear flows either tend to stabilize the lamellar phases or disorder the microemulsion phases. For example, Cates and Milner [9] have shown that suppression of fluctuations by steady shear, results in

raising the transition temperature for isotropic microemulsion like phase to a lamellar phase. In a certain range of temperatures, they find that the lamellar phase can actually be induced by applying shear. Yamamoto and Tanaka [128] and Mahjoub and coworkers [129] have provided experimental evidence for isotropic-lamellar transition under steady shear. Other researches [131, 133] have investigated the stability of the lamellar phase itself under shear field in such systems. They have noticed a decrease in the lamellar spacing owing to elastic deformation of the fluctuating interfaces under shear. This deformation leads to an effective increase in the number density of the layers and weakening of steric repulsion.

In this above context, ternary polymer blends have attracted significant attention due to their ability to serve as models for the broad class of o/w/s systems [142]. The longer length and time scales in polymeric systems leads to slower relaxation behavior (compared to o/w/s systems) and opens up the possibility to probe the origins and mechanisms of morphological and rheological transitions in this general class of systems. Recently, Krishnan and coworkers [132] carried out a detailed study of the effects of shear flow on a polymeric bicontinuous microemulsion. They studied a ternary blend system of poly(ethyl ethylene) (PEE), poly(dimethyl siloxane) (PDMS), and a PEE-PDMS diblock copolymer. They studied a symmetric system, wherein the sizes and the volume fraction of the homopolymers were almost identical and the different block lengths of the block copolymer were comparable. The two parameters in the system were the ratio of the lengths of copolymer to the homopolymer

(fixed at a value of 5.0), and the homopolymer volume fraction (fixed at 0.8). At equilibrium, such a ternary blend had a microstructure comprising of two percolating microphases (PEE rich and PDMS rich) separated by an interface containing the copolymer molecules (as shown in the inset of Fig. 5.1). Under the application of shear, they studied the scattering function patterns and deduced the occurrence of three different structural phase transitions. At very low shear rates, they observed scattering patterns signaling a transition of the system from a bicontinuous microemulsion phase to a streaked lamellar pattern, similar to o/w/s systems. However, with increase in shear rates they observed the lamellar phase giving way to a three phase coexistence (of a lamellar-phase coexisting with macrophase separated homopolymer phases). At stronger shear rates, they noticed the three phase system transitioning into a structure with macrophase separated bulk homopolymers (characterized by an increase in scattering intensity at low wave vectors). Furthermore, they also noticed a rich rheological behavior in this system. Under the application of steady shear they found four distinct regimes of rheological response as a function of the applied shear rate. At low shear rates, they observed Newtonian behavior (regime I). Further increase in shear rates led to the beginning of shear thinning behavior owing to the development of anisotropy in the morphology (regime II). At higher shear rates, the system shear thins more, at which point the lamellar like structure breaks down resulting in flow-induced phase separation into three phase coexisting patterns (regime III). Rheologically, this regime is characterized by shear rate independent, constant value

of shear stress. Upon further increase in shear rate (regime IV), the system viscosity plateaus to a constant value resembling the viscosity of an immiscible binary homopolymer blend, with the block copolymers playing no role.

The complex interplay between flow and structure and the rich rheological behavior exhibited by these ternary polymeric systems have prompted us to investigate the molecular scale phenomena in such systems. Some of the questions we wish to answer from this research are, "What are the mechanisms for differences. if any, in the flow behaviors of multicomponent polymeric systems?.", "What are the origins and mechanisms of this rheology-thermodynamics coupling in multicomponent polymeric systems?" In this work, we employ the recently developed non-equilibrium, self-consistent Brownian dynamics simulations [54, 103], to study shear induced phase transitions in ternary polymer blend systems formed using homopolymers A and B and block copolymer AB consisting of homopolymer blocks. Our main focus in this chapter is on shear induced microstructural transformations of polymeric bicontinuous microemulsions. In this work we emphasize the novel role of chain conformations and their flow deformations in influencing both the thermodynamical and rheological characteristics of multicomponent systems. As will be shown later, our results match qualitatively with the recent experimental observations on ternary polymer blend systems, but differ significantly from the behavior expected and observed in the analogous system of surfactants. We rationalize this contrast from a molecular viewpoint suggesting that the interplay between polymer chain conformations and their flow deformations can

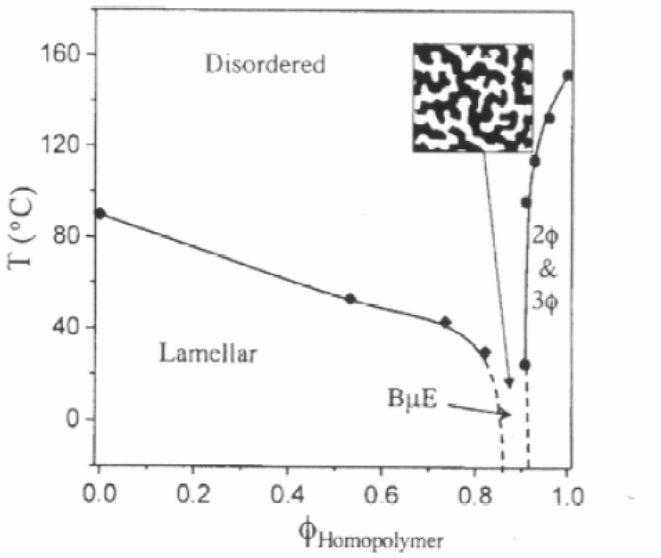

Figure 5.1: Phase diagram for a ternary PEE-PDMS system, at a constant 1:1 ratio of PEE and PDMS homopolymer. A bicontinuous microemulsion phase exists in a narrow composition channel at a total homopolymer concentration of around 90% by volume (adapted from [140]) (The white and black colors denote the two components in the inset).

lead to novel flow effects upon the phase, structural, and rheological behavior multicomponent polymer systems.

The rest of the chapter is divided as follows. Section 5.2 details the parameters used in the self consistent Brownian dynamics approach. Section 5.3 presents results on the shear-induced transformations of bicontinuous microstructures. The rheology resulting from the effects of inhomogeneities are detailed in section 5.4. Section 5.5 quantifies the effect of flow field upon polymer chain distortion, and relates these characteristics to the phase transformations presented in section 5.3. In conclusion, the flow-induced chain distortion is proposed as a possible mechanism rationalizing the discrepancies in the flow behavior between polymeric microemulsions and surfactant systems.

5.2 Simulation Algorithm & Details

In the current research, the polymer chains are modeled as FENE chains with the beads connected together with FENE (Finitely Extensible Non-linear Elastic) springs [45]. Our simulations were performed in a simulation box of size $40\times40\times10$ (in R_G units of the homopolymer) containing 25000 chains each of homopolymer A and B and 2500 chains of block copolymer. In different runs, the copolymer chains were discretized into 10, 20 and 28 beads each, while the homopolymer chains consisted of 4 beads each, corresponding to $\alpha = N_{AB}/N_H = 2.5, 5.0$ and 7.0. Initially all the beads were assigned random positions inside the simulation cell, while ensuring that none of the springs were excessively stretched. The length units were non-dimensionalized using

the radius of gyration of homopolymer. Our Brownian dynamics algorithm was non-dimensionalized by expressing time in terms of the reciprocal of friction coefficient ζ and setting the energy scale $k_BT = 1.0$. The beads in our simulation cell were allowed to execute Brownian motion in all 3 dimensions, however, the self consistent potential were evolved in 2 dimensions with no axial variations. Moreover, the velocity field was evolved in 1 dimension allowing variations only in shear gradient direction. Preliminary runs for a $2D$ velocity field yielded qualitatively similar as the $1D$ velocity assumption.

The parameters in our model include: the Flory interaction parameter quantifying the strength of repulsion between unlike monomers [20], χN_{AB}; the phenomenological parameters for the evolution of the potential and velocity fields Γ_1, Γ_2, ϵ (see equations (2.41), (2.42) and (2.45)) and the FENE b_f parameter. We performed our simulations for $\chi N_{AB} = 15.0$ and with 0.05, 0.1 and 0.0016 (in the units discussed above) respectively for Γ_1, Γ_2 and ϵ. The FENE b_f parameter was fixed at 30 and viscoelastic asymmetry between the 2 components is introduced within the system using a parameter $\beta = \zeta_A/\zeta_B$, with $\beta = 1$ representing a viscoelastically symmetric system. The time step for the Brownian dynamics was chosen as 0.01 for low shear rates and 0.001 at higher shear rates. Convergence of both composition and velocity fields were used as criteria for the attainment of steady state. The convergence was assumed to be achieved when there was no visible change in the composition profiles and less that 1% change in the velocity profiles obtained from two consecutive block averagings performed for an interval of 200τ, where τ is

the Rouse relaxation time of the homopolymer. All the shear rates employed this research are non-dimensionalized with this time scale. The computational time for our runs took an average of around 96hrs in a single 2.5GHz processor system.

5.3 Equilibrium Microemulsion Structure

We first present the equilibrium results obtained from our simulations. The points on the Fig. 5.2 (adapted from [112]) displays the equilibrium phase diagram of ternary polymer blend system for $\alpha = 5.0$, obtained using the methodology of Field Theoretic Simulation (FTS) [110]. The solid line depicts the phase boundary obtained from equilibrium self-consistent field theory. In self-consistent field theory, an ordered lamellar phase is predicted for homopolymer compositions below $\phi_H = 0.85$. A three phase coexistence channel (a lamellar phase in coexistence with macrophase separated A and B) is predicted for higher homopolymer compositions and two phase macrophase separated structures are predicted towards the right of this channel. While self-consistent field theory (a mean field theory) does not predict bicontinuous phases in ternary blends, in experiments, the regions around the three phase coexistence region are destroyed by fluctuations resulting in a bicontinuous microemulsion phase. Fredrickson and Helfand [134] have quantified the fluctuations in polymeric systems using a parameter denoted as C:

$$C = mR_{g0}^{d}/V \tag{5.1}$$

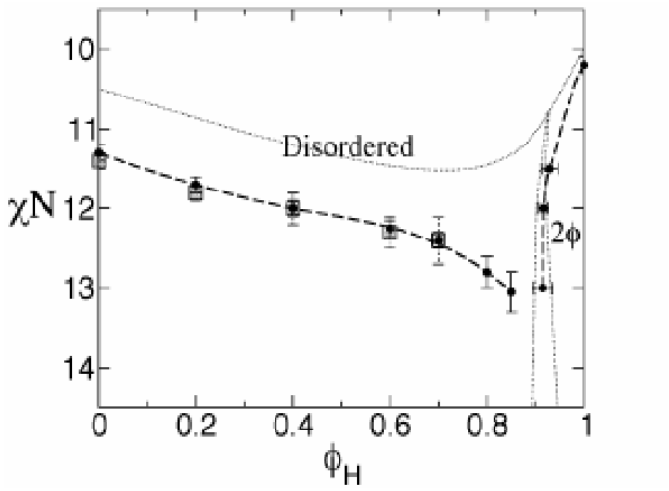

(a)

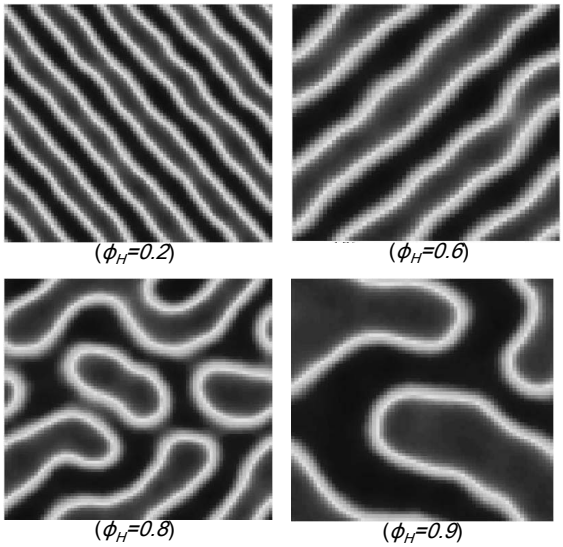

(b)

Figure 5.2: (a) Equilibrium phase diagram of a ternary system obtained using Field Theoretic Simulations [112] (FTS), (b) Two dimensional composition profiles obtained from SCBD at various homopolymer compositions indicated (The gray areas denote the total composition of component A).

where, m is the total number of polymers in a system of volume V, and R_{g0} is the radius of gyration of the polymer at equilibrium and d is the dimensionality of the system. $C \to \infty$, is the limit predicted by self-consistent field theory and it corresponds to the absence of fluctuations. The method of FTS accounts for fluctuations, and the points in Fig. 5.2 depict the phase boundary obtained by accounting for such fluctuations (with $C = 50$). It is observed that indeed the phase boundaries shift, and opens up a channel of disordered phases between the lamellar phase and the two phase regions.

For the system density employed in our simulations, C parameter corresponds to a value 35. To compare with the theoretical results, we compared equilibrium SCBD simulations for $\chi N = 13$ and a range of homopolymer compositions ϕ_H. The insets in Fig. 5.2 display the time averaged two dimensional composition profile obtained (the total homopolymer composition, ϕ_H, indicated in parenthesis). At $\phi_H = 0.2$ and 0.6, we obtain the lamellar microstructures as predicted by mean field theory. In such phases, the homopolymers position themselves within the lamellar phase formed by the block copolymers, leading to an overall swelling of the layers. At a higher homopolymer composition of 0.8, we observe that the lamellar microstructure is destroyed by fluctuations, giving rise to a bicontinuous microemulsion phase. Increasing the homopolymer composition any further gives rise to macrophase separation within the system resulting in two homopolymer rich phases with the block copolymers present at the interface of the homopolymer rich phases.

Comparing the equilibrium phase diagram from field theoretic simu-

lations, alongside the experimental phase diagram (Fig. 5.1) by Bates and coworkers [136], we observe a reasonable qualitative agreement. The lamellar phase at low ϕ_H and the two phase region at high ϕ_H, being separated near the Lifshitz point [135], $\phi_L = \alpha^2/(2+\alpha^2)$, by a narrow channel of bicontinuous microemulsion like phases. This equilibrium phase diagram is captured by our Brownian dynamics simulation as well.

5.4 Effect of Shear on Structure

In this section we present the effect of shear on the microstructure in a ternary blend ($A + B + AB$) system. We also draw qualitative comparisons of our results with the findings of shear experiments on ternary polymeric bicontinuous systems performed by Burghardt, Bates and coworkers [132]. As shown in the inset of Fig. 5.2, the ternary blend with homopolymer concentration, ϕ_H of 0.8, at a $\chi N = 13.0$, under quiescent conditions forms a bicontinuous microemulsion structure. We notice that the A and B type monomers occupy equal areas inside the cell. This is because we have symmetric compositions of A and B homopolymers and the AB diblock copolymer is symmetric in A and B as well. Initially, we apply a very low shear rate $\dot{\gamma}\tau$ of 0.0081 to this equilibrium configuration and we notice that the bicontinuous structure transforms to a modulated lamellar type of structure with the lamellae oriented along the shear direction (see Fig. 5.3b) indicative of a shear-induced alignment of the interfaces of the microemulsion case. This is equivalent to a shear-induced shift in the phase diagram to the left of the bicontinuous chan-

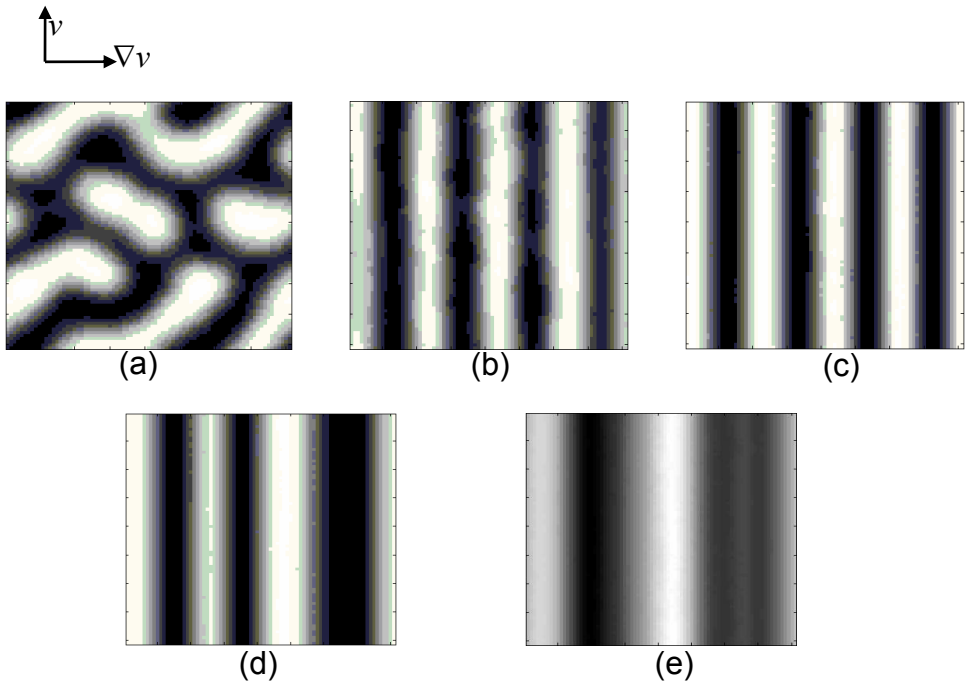

Figure 5.3: Two dimensional composition profiles obtained at various shear rates, (a) $\dot{\gamma}\tau$=0.0, Equilibrium; (b) $\dot{\gamma}\tau$=0.0081; (c) $\dot{\gamma}\tau$=0.081; (d) $\dot{\gamma}\tau$=0.81; (e) $\dot{\gamma}\tau$=2.025 (The white areas denote the total composition of component A).

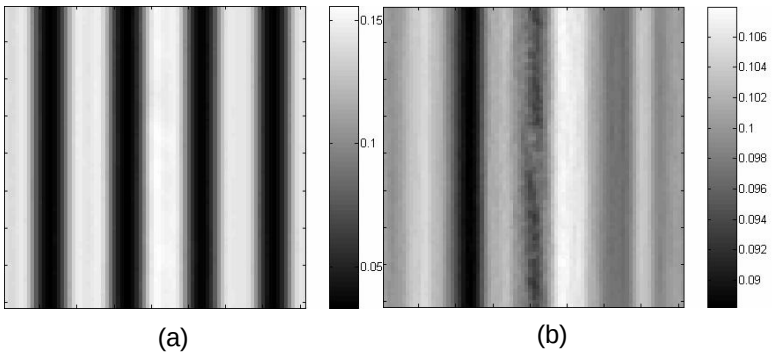

Figure 5.4: Two dimensional composition profiles of just the block copolymers in the system, at shear rates (a) $\dot{\gamma}\tau$=0.2; (b) $\dot{\gamma}\tau$=2.025 (The grayscale denotes the composition of component A of the copolymer).

nel where lamellar structures are obtained at quiescent conditions. Modulated lamellae persist until a shear rate of $\dot{\gamma}\tau = 0.081$ as shown in Fig. 5.3c. Upon increase the shear rate to even higher values ranging from $\dot{\gamma}\tau$ of 0.081 to 0.2 (not shown in figure), we observe that the modulated lamellae stabilize to form perfectly aligned lamellae of equal thickness (see Fig. 5.3c). This shear-alignment of interfaces at low shear rates is a manifestation of suppression of capillary wave fluctuations and is consistent with earlier predictions and observations in block copolymer and surfactant systems [9, 10]. In order to understand the block copolymer organization within the system, in Fig. 5.4a we display the $2D$ compositions profiles of just the block copolymers within the system at an applied shear rate of 0.2. These time averaged composition profiles are obtained by considering only the block copolymer bead positions within the system. The lamellar microstructure of the copolymer in Fig. 5.4a reinforce that the copolymer links position themselves mainly at the interfaces

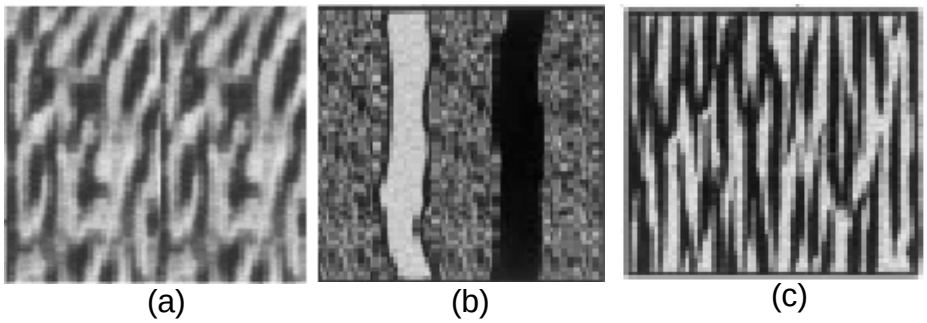

Figure 5.5: Microphase structures predicted by Krishnan and coworkers at (a) Low; (b) High and (c) Intermediate, shear rates.

and dictate the lamellar microstructure. These results compare favorably with the experimental findings of Krishnan and coworkers [130, 132]. Indeed as seen in Fig. 5.5, at low shear rates Krishnan et al., noticed that the isotropic bi-continuous structures give rise to anisotropy in the form of streaked lamellar microphase separated structures. However, experimental results from Fig. 5.5 do not match exactly with the well aligned microphase separated lamellar patterns obtained in our simulations (Fig. 5.3). Indeed our simulations were constrained by computational costs which allowed us to study small systems where the lamellar patterns tend to align very well even at low applied shear rates.

As we increase the shear rate to 0.81 (Fig. 5.3d), we notice that the lamellar structure begins to breakdown forming a non-periodic lamellar phase. Owing to small system sizes employed, a true three phase coexistence cannot be observed in our simulation, and consequently this non-periodic lamellar phase is interpreted as a signature of the three phase coexistence. With fur-

ther increase in shear rates to higher values ($\dot{\gamma}\tau = 2.025$ and higher) we notice that all the lamellae breakdown to form a completely macrophase separated two phase system with homopolymer rich domains as shown in Fig. 5.3e. Qualitatively, the above sequence of shear-induced phases matches very well with the observations of Krishnan et al. [132] (reproduced in Figs. 5.5a, 5.5b and 5.5c). Experimentally observed series of phase transformations include microphase separation at low shear rates (Fig. 5.5a), three phase coexistence with micro and macrophase separated regions (Fig. 5.5b) and completely macrophase separated blend (Fig. 5.5c) at very high shear rates [132]. In the macrophase separated system (Fig. 5.5c) it was speculated that the copolymers are uniformly solubilized in the blend with phase separation occurring mainly between homopolymer phases. This is also evident from our results in Figs. 5.4a and 5.4b which displays the copolymer composition inside the system for the shear rates of $\dot{\gamma}\tau = 0.2$ and 2.025. We notice that while there exists microphase separation of copolymers at the lower shear rate, at higher shears the copolymers are uniformly solubilized in the blend.

We provide more evidence for the above claimed phase transitions by comparing the 1D averaged composition profile of the above transformations. These 1D composition profiles are obtained by averaging the $2D$ compositions in the velocity gradient direction. Figure 5.6a displays the 1D time averaged composition profiles of component A in the system obtained for the shear rate of $\dot{\gamma}\tau = 0.081$. At this shear rate, the system has a lamellar microstructure with four identical lamellae inside the simulation cell. An increase in shear rate

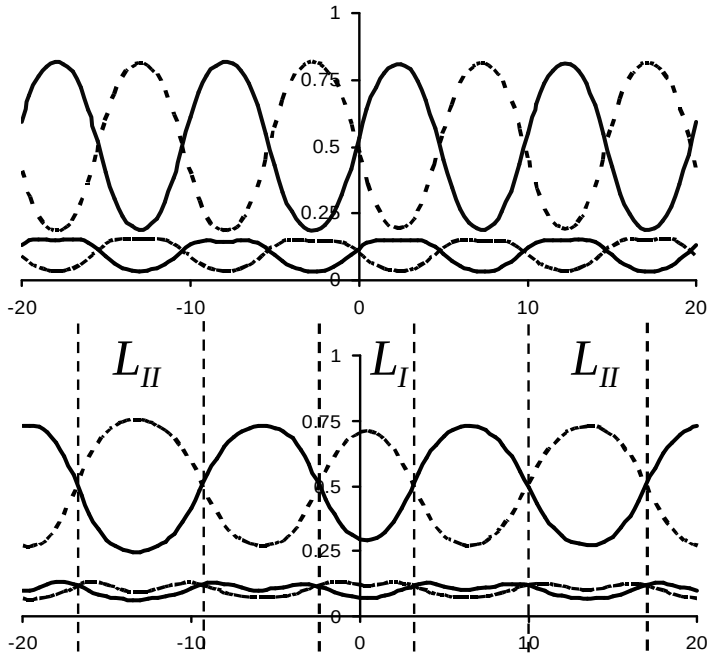

Figure 5.6: One dimensional averaged composition profiles at shear rates (a) $\dot{\gamma}\tau$=0.081; (b) $\dot{\gamma}\tau$=0.81.

to $\dot{\gamma}\tau = 0.81$ triggers macrophase separation and takes the system into the non-periodic lamellar phase (≡three phase coexistence) in Fig. 5.6b. The presence of two distinct kinds of lamellar at $\dot{\gamma}\tau = 0.81$ (labeled L_I and L_{II}) is evident from Fig. 5.6b. Figures 5.6a and 5.6b also display the copolymer composition profiles (of A block) for the shear rates $\dot{\gamma}\tau = 0.081$ and 0.81. Under closer examination we notice a dip in the composition profile in the middle of each lamella. This is due to higher concentrations of homopolymer chains between the copolymer monolayers thus reducing the copolymer concentration at the centers of the lamellae. A careful comparison of the composition profiles at $\dot{\gamma}\tau = 0.081$ and 0.81, shows that the lamellae regions of the three phase system are broader then the lamellae observed at lower shears. Moreover, the dip in the copolymer concentration at the lamellae centers is also more pronounced at the higher shear. We discuss the implications of these results in a later section.

5.4.1 Effect of Viscoelastic Asymmetry

All the above results were obtained for a viscoelastically symmetric ternary blend with the friction coefficients of the two components (ζ_A, ζ_B) being equal. However, all experimental multicomponent polymeric systems are inherently asymmetric, and specifically, the experiments of Krishnan et al. [132] focused on a system of viscosity contrast $\equiv 10^3$. In order to study the effect of viscoelastic asymmetry on shear rheology and the shear induced phase transitions, we incorporate asymmetry in our ternary blend system us-

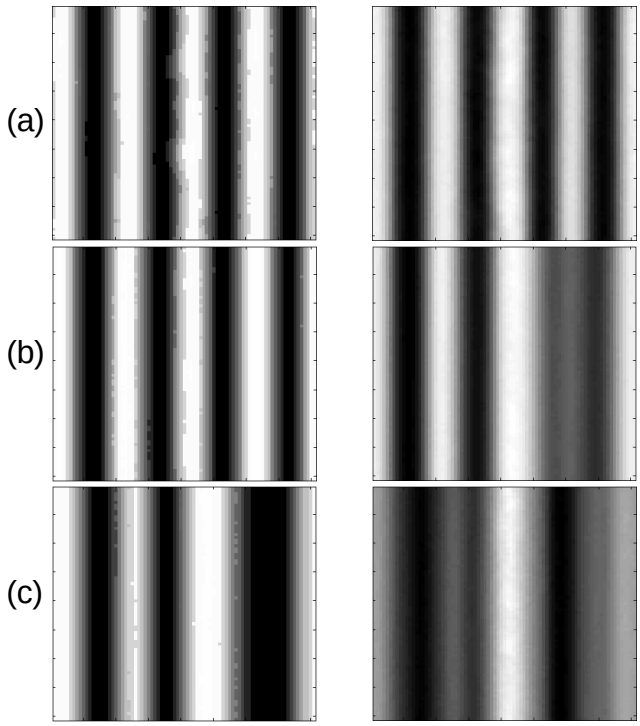

Figure 5.7: Two dimensional compositional profiles obtained for viscoelastically symmetric (left column) and viscoelastically asymmetric (right column) system with $\beta = 10.0$, at shear rates (a) $\dot{\gamma}\tau$=0.04; (b) $\dot{\gamma}\tau$=0.6; (c) $\dot{\gamma}\tau$=1.21 (The grayscale denotes the total composition of component A).

ing a parameter $\beta = \zeta_A/\zeta_B$. We note that the viscoelastic asymmetry does not affect the equilibrium morphology in the system. However, we notice quantitative changes in the shear induced morphology owing to the asymmetry in response of the two components to applied shear. Figure 5.7 displays the two dimensional composition profiles obtained under shear for a viscoelastically asymmetric system with $\beta = 10$ plotted alongside with the symmetric system composition profiles to effect a comparison. From the lowest applied shear rate of $\dot{\gamma}\tau = 0.04$ until a shear rate of $\dot{\gamma}\tau = 0.2$ (see Fig. 5.7a), we obtain perfectly aligned lamellae in the asymmetric system. However, for the viscoelastically symmetric system, at $\dot{\gamma}\tau = 0.04$, a modulated lamellar phase is observed. As we increase the applied shear to $\dot{\gamma}\tau = 0.6$ in the asymmetric system, we observe the initiation of shear induced macrophase separation resulting in three phase coexistence (see Fig. 5.7b). However at the same shear rate the viscoelastically symmetric system is still observed in the lamellar phase. Further increase in shear rate to $\dot{\gamma}\tau = 1.21$ in the asymmetric system results in an entirely macrophase separated two phase system (see Fig. 5.7c), whereas the symmetric system exhibits morphology characteristics of three phase coexistence. In summary, while the asymmetric system phase separates under shear giving rise to morphologies qualitatively similar to that observed in symmetric systems, *the transitions from equilibrium bicontinuous phase to various shear morphologies happen at lower shear rates in asymmetric systems as compared to the symmetric systems.*

5.4.2 Effect of Copolymer Size

The previous results (equilibrium and shear) have been obtained for a unique value of copolymer size to homopolymer size ratio $\alpha = N_{AB}/N_H = 5$. Now, we study the effect of varying copolymer size (and hence the size ratio α) on the above flow-induced phase transitions. We have considered the shear induced phase transitions in two more systems corresponding to $\alpha = 2.5$ and 7.0. We note that the value of α does impact the equilibrium morphology within the system, and consequently we have modified the volume fraction of the copolymers to obtain a bicontinuous structure at equilibrium. Our main observation is the delayed onset of macrophase separation into a two phase system upon decreasing α's. This trend is displayed explicitly in Figs. 5.8a,b,c, which plot the time averaged 1D composition profiles (total composition and copolymer composition) at $\dot{\gamma}\tau = 0.61$ for $\alpha = 2.5, 5.0$ and 7.0 respectively. We notice that at this shear rate, the systems with $\alpha = 2.5$ and 5.0 are still in the lamellar phase with equally spaced lamellae within the system, however, non-periodic lamellae (signifying three phase coexistence) is witnessed for $\alpha = 7.0$. Indeed, three phase coexistence is observed in the system with $\alpha = 7.0$ at even the lowest applied shear. Furthermore, at a shear rate of $\dot{\gamma}\tau = 4.05$, both the systems with $\alpha = 5.0$ and 7.0, are already in the two phase region, while the system with $\alpha = 2.5$ has coexistence of three phases. Hence, we observe that shear leads to sooner onset of phase transitions with increasing copolymer sizes (or α). This effect of varying α on the shear induced phase transition is elaborated in the final section of the article.

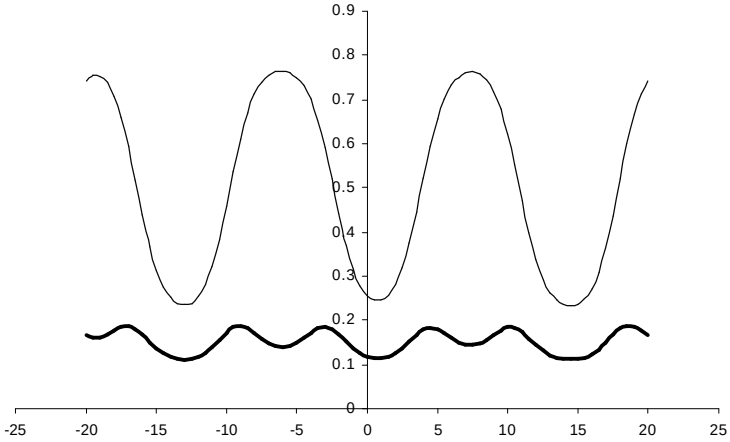
0.9
0.8
0.7
0.6
0.5
0.4
0.3
0.2
0.1
0
-25
-20
-15
-10
-5
0
5
10
15
20
25

(a)

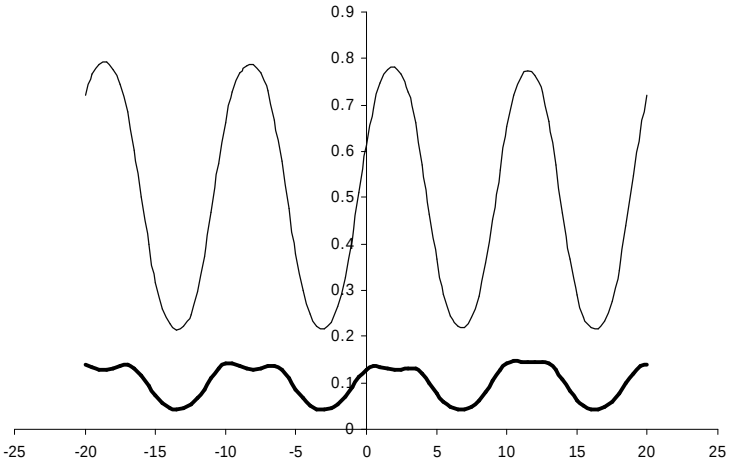
0.9
0.8
0.7
0.6
0.5
0.4
0.3
0.2
0.1
0
-25
-20
-15
-10
-5
0
5
10
15
20
25

(b)

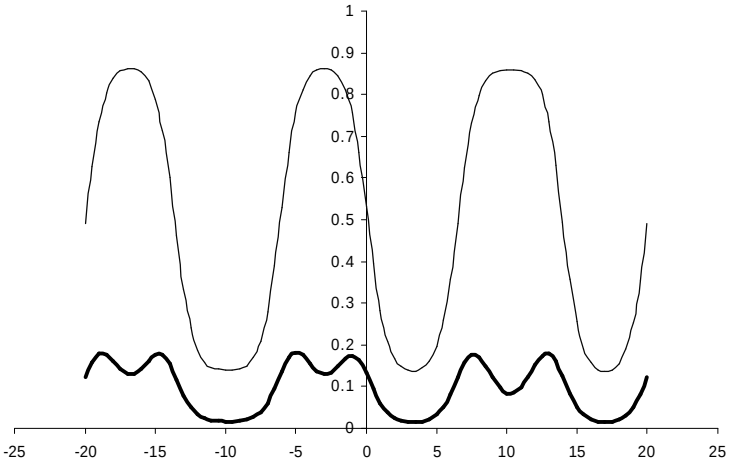

(c)

Figure 5.8: One dimensional, total (thin line) and copolymer (thick line) composition profiles at a shear rate of $\dot{\gamma}\tau$=0.61, for three different values of copolymer lengths characterized by (a) $\alpha = 2.5$, (b) $\alpha = 5.0$ and (c) $\alpha = 7.0$.

5.5 Effect of Morphology on Rheology

In the previous section, we presented results for the effect of externally applied flow field on the microstructure of the ternary blend system. Now, we study the effect of inherent microstructure of the system on the induced flow field and the rheological properties of the system. The microstructure induced flow field on the system could in fact be very different from the externally applied flow field, which in this case is just a simple shear. For example, Krishnan and coworkers [132] have observed microstructure induced thermo-rheological complexity in a ternary polymer blend system. In X-ray scattering experiments, Burghardt and coworkers [17] have attributed the discrepancy in scattering patterns between their experiments and the theoretical prediction

of Patzold and Dawson [18] to the assumption of uniform velocity field.

The self-consistent velocity profile evolved in our simulations (in $1D$) allows for different components to respond differently to the applied shear field. As detailed in the *Algorithm Development* section, the convergence criterion for the flow-induced self consistent velocity profile is the constancy of shear stress. The microscopic stress profile is obtained using the Kramer's expression for stress in polymeric systems (equation (2.44)). Our velocity profiles were obtained when the shear stress converges to within 10% deviation from the mean value. Figure 5.9 displays the velocity profile for a system with $\alpha = 5.0$ and $\beta = 1.0$, for three different shear rates $\dot{\gamma}\tau = 0.0081, 0.081$ and 4.05. We have also displayed the 2D composition profile at these shear rates alongside the velocity profile. We notice that, at the two lower shear rates when the system is has the lamellar morphology, the velocity profiles qualitatively resemble a steplike pattern with decreased velocity gradients at the interfaces owing to the segregated copolymer chain. This finding is consistent with our results in chapter 3 for compatibilized polymer blends saturated with copolymers at the interface, wherein the copolymers at the interface is shown to impart friction to the bulk flow. At the highest shear rate of $\dot{\gamma}\tau = 4.05$, we see that the system has a two phase morphology, wherein the copolymer chains are well mixed. This system has a linear, simple shear like velocity profile. Hence, morphology of the system, strongly affects the induced velocity profile.

In order to study the effect of morphological characteristics on the rheology of the system, we computed the average viscosities of the entire,

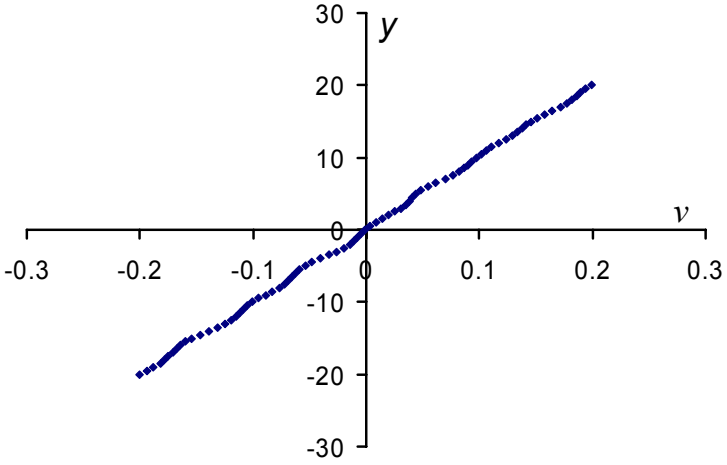
30
y
20
10
v
0
-0.3
-0.2
-0.1
0
0.1
0.2
0.3
-10
-20
-30

(a)

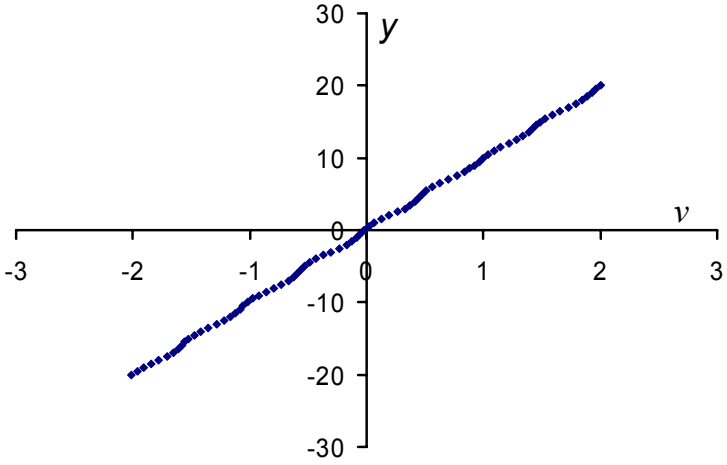
30
y
20
10
v
0
-3
-2
-1
0
1
2
3
-10
-20
-30

(b)

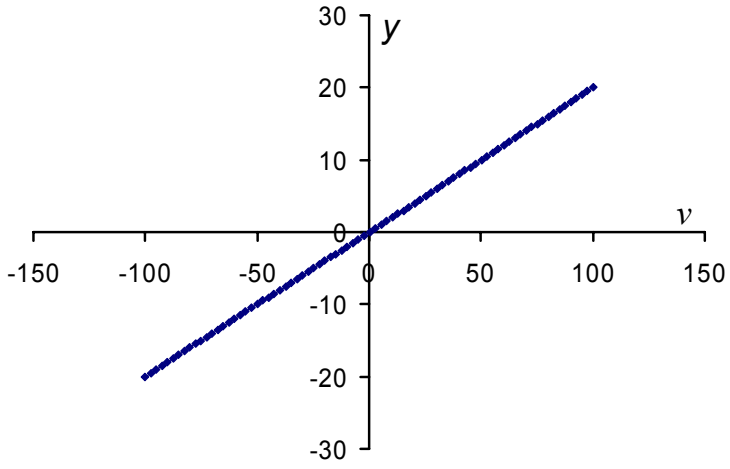

(c)

Figure 5.9: Velocity profiles for a system with $\alpha = 5.0$ and $\beta = 1.0$, for shear rate values of (a) $\dot{\gamma}\tau$=0.0081, (b) $\dot{\gamma}\tau$=0.081 and (c) $\dot{\gamma}\tau$=4.05.

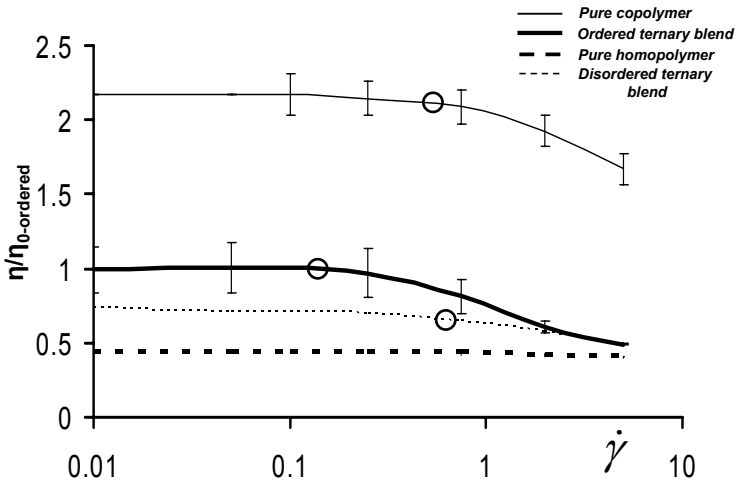

Figure 5.10: Shear viscosities normalized by low shear viscosity of an ordered ternary blend, for the cases of pure homopolymer, ordered ternary blend, pure homopolymer and disordered ternary blend. The rings denote the approximate shear rate where the respective systems begin to shear thin.

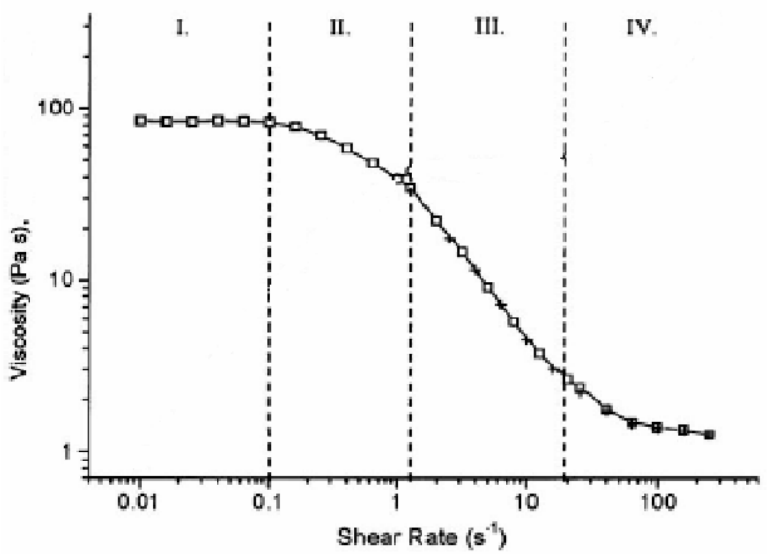

Figure 5.11: Shear thinning viscosity for PEE-PDMS ternary blend (adapted from [130]).

ordered, symmetric ternary blend (with $\beta = 1, \alpha = 5.0$) for a wide range of shear rates. Figure 5.10 displays the steady shear viscosity of the ternary blends (normalized by the zero-shear viscosity of the ordered blend). The point where shear thinning begins is marked by a ring in the figure. We observe the existence of a linear regime at low shear when the system retains the lamellar (modulated/aligned) microstructure. At moderate shear rates, the system starts shear thinning corresponding approximately to when the lamellae begin to merge together giving rise to a three phase microstructure. At even higher shear rates the lamellae breakdown completely and the system progressively shear thins further. Figure 5.10 also displays the corresponding viscosities of pure homopolymer and pure disordered block copolymer. While it is observed that the longer block copolymer shear thins sooner than the homopolymer (see Fig. 5.10), however the ordered ternary blend system shear thins earlier than the block copolymer (see Fig. 5.10), which can be attributed solely to the transition in microstructure with applied shear. Hence, by comparing the shear thinning plot (Fig. 5.10) with the morphological modifications under shear (Fig. 5.3), we notice that shear thinning is normally accompanied with a decreasing number of interfaces.

Steady shear experiments by Krishnan and coworkers [132] have resulted in qualitatively similar viscosity vs shear rate plots. They observed that in the linear regime there exists either a bicontinuous microstructure or streaked microphase separated structure. Also, they noticed three phase coexistence around the same shear thinning regime as observed in our simulations.

However, with increase in shear rate, when the two phase macrophase segregated structure develops, they observe a plateau in the viscosity (see Fig. 5.11), corresponding to the viscosity of the homopolymer phases. We fail to capture this last viscosity plateau in our Brownian dynamics simulation due to shear thinning of homopolymers.

5.5.1 Effect of Copolymer Size

In the current subsection, we study the effect of changing copolymer to homopolymer size ratio (=α), on the rheological behavior of the system. In order to render the interfacial effects on rheology more explicit, the viscosity profiles are plotted in Fig. 5.12. Comparing this local viscosity profile along with the composition profile, we notice that the peaks in the profile again correspond to the interfaces while the troughs correspond to the center of the lamellae.

A high concentration of block copolymer links at the interfaces give rise to increased viscosities by imparting resistance to flow. Figure 5.13 compares the shear thinning behavior of the ternary blend systems with $\alpha = 2.5, 5.0$ and 7.0. The figure displays the viscosity (normalized by the low shear viscosity) as a function of the applied shear rate for varying α's. We notice that the system with a smaller size asymmetry is less shear thinning than the higher α system. Shear thinning behavior doesn't start for $\alpha = 2.5$ system until an applied shear rate of 0.6075, whereas the $\alpha = 7.0$ system is already started shear thinning at the lowest applied shear rate of 0.0081.

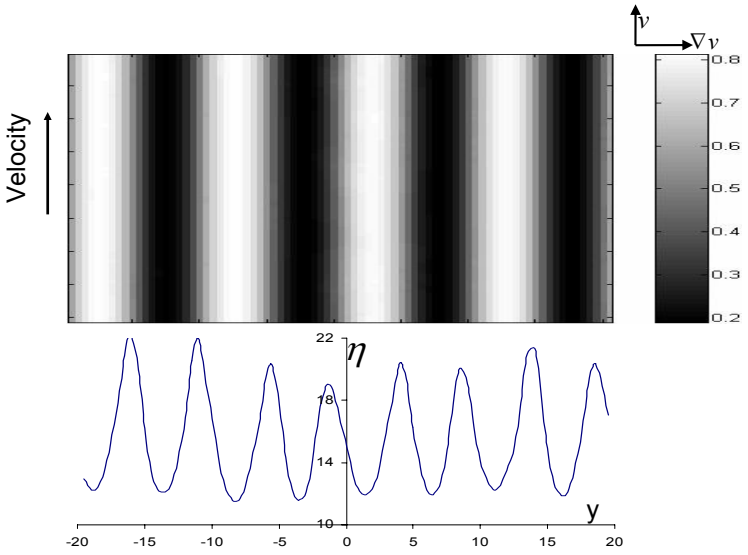

(a)

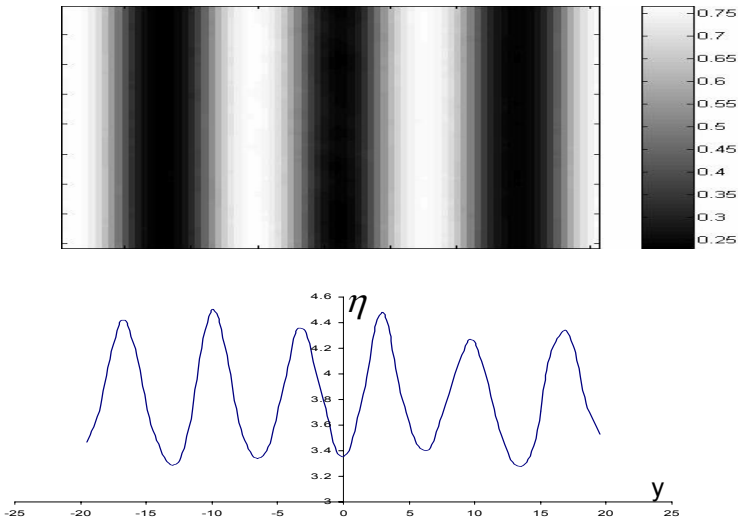

(b)

Figure 5.12: Two dimensional composition and 1D averaged viscosity profiles for shear rate of $\dot{\gamma}\tau$=0.081, for systems with two different copolymer lengths given by, (a) $\alpha = 5.0$ and (b) $\alpha = 7.0$.

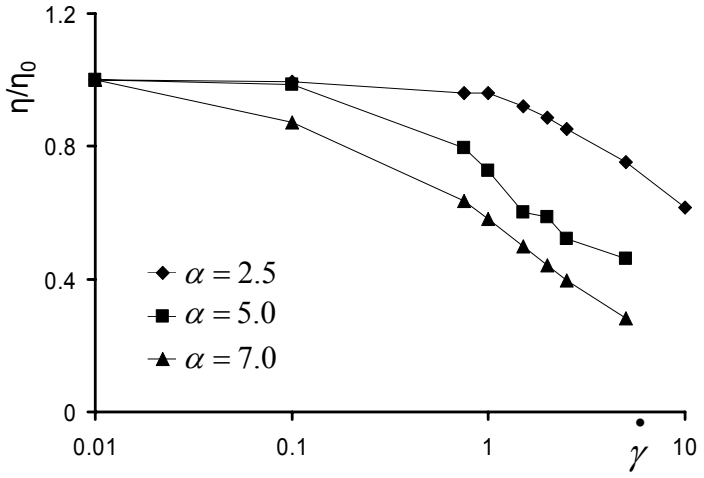

Figure 5.13: Shear viscosities (normalized by the respective low shear viscosity) for systems with three different copolymer lengths, given by, (a) $\alpha = 2.5$, (b) $\alpha = 5.0$ and (c) $\alpha = 7.0$.

These rheological characteristics can in turn be rationalized by the inherent microstructural features at those shear rates. While the $\alpha = 2.5$ system retains the lamellar microstructure throughout the applied range of shear rates, the $\alpha = 7.0$ system has already phase separated into the three phase coexistence at the lowest applied shear rate. This difference in microstructure manifests in the shear thinning behavior of these respective systems.

5.5.2 Effect of Viscoelastic Asymmetry

In this subsection, we focus on the effect of viscoelastic asymmetry (by varying the β parameter) on the rheological behavior of the system. Figure 5.14 displays the viscosity profile obtained for an asymmetric system with $\beta = 10$ (with $\alpha = 5.0$). This is the highest asymmetry we have studied in our

simulation and hence we expect profound differences between the local velocity profile of phase separated domains and the overall velocity. From Fig. 5.14, we notice that the interfacial viscosity, with the 8 peaks in the profile corresponding to the 8 interfaces in the system, is equal at all the interfaces in the system regardless of the component present on either side of the interface. However, viscosities at the centers of the lamellae, corresponding to the 8 troughs, are quite different depending on the component that forms the particular lamellar. Note that the ratio of the pure homopolymer viscosities in this case is equal to β (=10). However, the ratio of trough viscosities corresponding to the viscosity ratio of the centers of lamellae formed with components A and B is less than 2.0. This could be construed as a *rheological compatibilization* of different components effected by the block copolymers. The presence of copolymer chains reduces the apparent asymmetry between different phase separated domains. To our knowledge, this is the first visualization of microscopic velocity profile in a lamellar micro-segregated system.

We compare the shear thinning rheology of the ternary blend systems with $\beta = 1, 5$ and 10. Figure 5.15 displays the viscosity versus shear rate for the three systems, normalized by the linear, zero shear viscosity of the ordered system. We notice that the increase in asymmetry progressively decreases the shear rate at which the system begins to shear thin. Our results on shear-induced phase transitions and shear rheology are consistent with the experimental results [132] in the context of ternary polymer blends. With increase in shear rate, when the two phase macrophase segregated structure

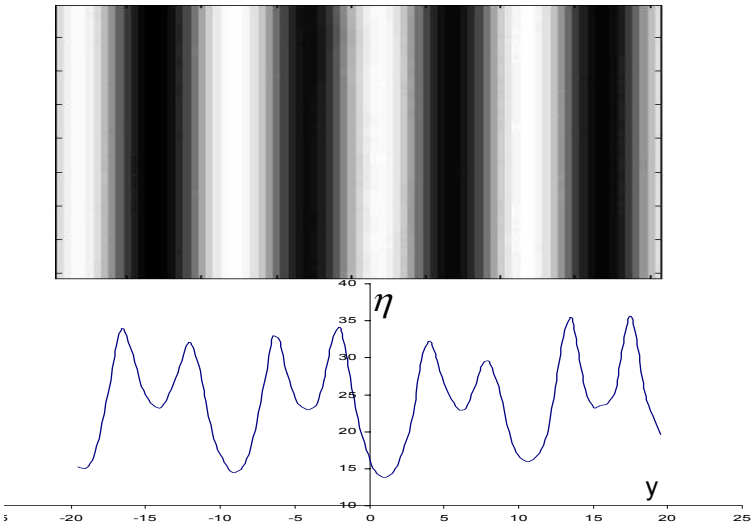

Figure 5.14: Two dimensional composition and 1D averaged viscosity profiles for a viscoelastically asymmetric system with $\beta = 10.0$ and $\alpha = 5.0$.

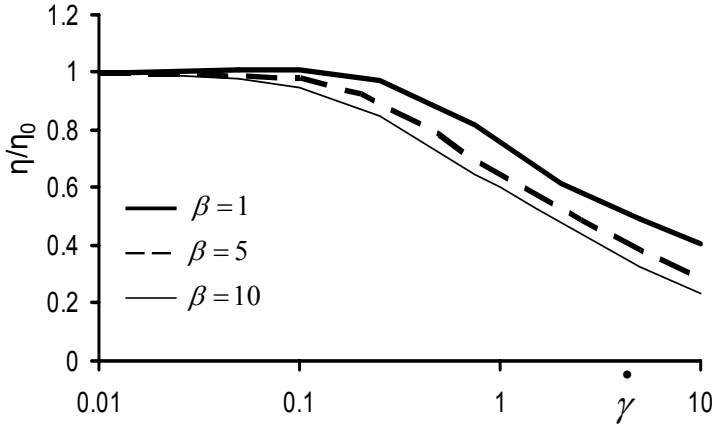

Figure 5.15: Shear viscosities (normalized by the respective low shear viscosity) for systems with three different viscoelastic asymmetries, given by, (a) $\beta = 1.0$, (b) $\beta = 5.0$ and (c) $\beta = 10.0$.

develops, Krishnan and coworkers observed a plateau in the viscosity as shown in Fig. 5.11 (reproduced from [130]). We fail to capture this viscosity plateau in our Brownian dynamics simulation.

5.6 Mechanism for Shear-Induced Phase Transitions

In this section, we provide molecular and scaling arguments for the structural and rheological characteristics of the ternary blend system under steady shear. Qualitatively all the above sequence of shear-induced phases (section 5.3) matches with the experimental results of Krishnan and coworkers [132]. While the shear alignment of interfaces is common to both surfactant and polymeric systems, the subsequent phase transitions to three phase coexistence and macrophase separation appear to be quite unique to polymeric systems. This prompts us to raise the question, "what are the mechanisms underlying the above shear induced phase transitions in polymeric systems?"

Chain Deformations: Experimental and theoretical works on equilibrium ternary polymer blend systems have identified two competing effects stabilizing the lamellar phases [143] (a) The interfacial tension between the homopolymer phases due to the presence of the copolymer layer at the interface; and (b) The homopolymer mediated effective interactions between the copolymer layers. Addition of homopolymers to lamellar phases increases the interfacial tension which is countered by the system by reducing the interfacial area or the number of interfaces. The latter effect viz. the effective interactions between copolymers is correlated with the energetic gain resulting from their

localization at the interface of homopolymers [144]. This is especially true in ternary polymeric microemulsions with the size asymmetry $\alpha \equiv N_{AB}/N_H > 1$. In Fig. 5.16 we portray the effects of shear by first displaying the shear rate dependencies of the R_g of the copolymer chains in the Y direction. The copolymer size in the direction normal to the shear reduces with increase in applied shear rate. The copolymer chain contraction has already been implicated in the reduction in degree of interpenetration copolymers in Figs. 5.6a and 5.6b. An outcome of this deformation is the concomitant increase in the unfavorable overlap between A (B) component of the block copolymer and the B (A) components of copolymers and homopolymers. The latter is elucidated in Fig. 5.16 which portrays a measure of this unfavorable overlap, and displays an increase at around the same shear rates at which chain deformation effects manifest. We suggest that this shear-induced lowering of energetic gain of localization of the copolymers increases the effective interfacial tension between the homopolymers. This reasoning certainly explains the driving force for reducing the number of interfaces observed in the phase transitions in Fig. 5.3 where higher shear rates leads to lamellae with less number of interfaces followed by a transition to a macrophase separated system at even higher shear rates.

While chain deformation and its resulting non-linear rheology typically manifest at higher shear rates in the non-linear flow regime in homogeneous systems, we point out that in highly structured systems like $A+B+AB$ blends, the copolymer chain deformation effects give rise to non-linear rheology even with in the linear regime of the homopolymers. In [132] also, the shear induced

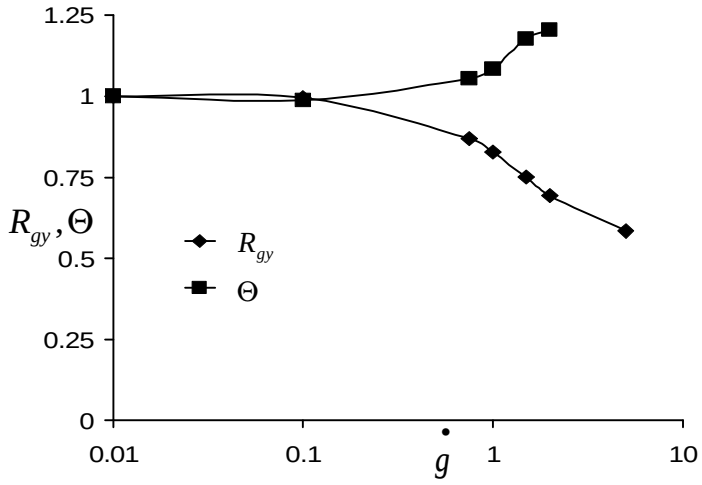

Figure 5.16: Shear rate dependencies of R_{gy} of the copolymer chains and the enthalpic overlap functions defined as: $\Theta = \int_L dy[\phi_A^C(y)\phi_B^C(y) + \phi_A^C(y)\phi_B^H(y) + \phi_A^H(y)\phi_B^C(y)]$, where the integration is over an AB interface. The superscripts H and C denote the homopolymer and copolymer respectively. L denoted the lamellar phase and T denotes the nonperiodic lamellar and macrophase separated phase. Both Θ and R_{gy} are normalized by their zero shear values.

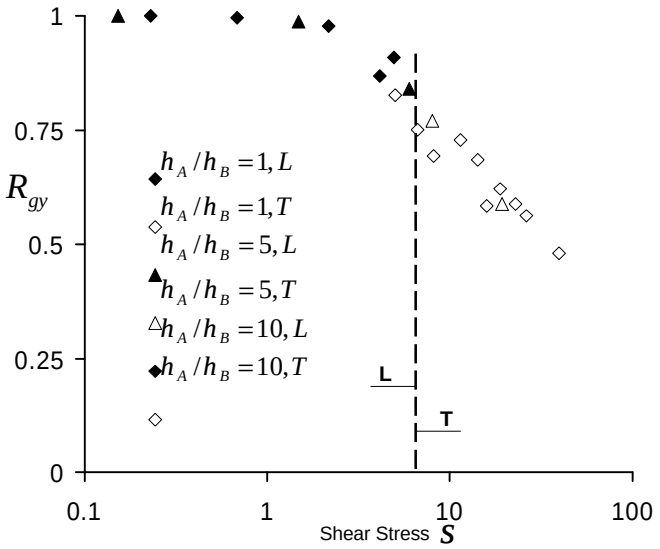

Figure 5.17: Shear stress dependence of R_{gy} of the copolymer for different viscosity contrast systems. Solid symbols correspond to L phase and open symbols correspond to T phase.

phase transformations and non-linear rheology were observed to manifest in the linear regime of the homopolymers. The reasons for earlier onset of non-linearity in these systems are two fold. On the one hand, the size asymmetry with $\alpha \equiv N_{AB}/N_H > 1$ leads to an asymmetric stress division concentrated on the longer copolymer chains. On the other hand, the conformation of the copolymer chains normal to the lamellar interface, exposes them to more of the shear flow and hence they experience more stress. This proposes a novel scaling for systems with viscosity contrasts. As the chain deformations relate to stress experience by the individual chains, we expect that the shear-induced phase transitions at different shear rates should collapse into a unified plot if it were plotted as a function of the shear stress. In Fig. 5.17 we confirm this proposal by displaying the collapse of the radius of gyration of the copolymer in the normal direction (R_{gy}) for varying viscosity contrast systems. Moreover, it is also observed that the transition from lamellar (L) to three phase coexistence (T) happen approximately at the same shear stress independent of the viscosity contrast within the system. Since systems with a viscosity contrast exhibit a higher average viscosity (in our non-dimensionalization), this translates into the occurrence of phase transformations at lower shear rates for systems with viscosity contrast (or viscoelastic asymmetry).

The above results with extensive role of polymer chain deformation has prompted us to perform a simple scaling analysis to ascertain the predictions for different values of α. The enthalpic gain of having copolymer molecules at the interface of homopolymers can be written in a scaling form as,

$$g/k_BT = \int_0^a \phi_{cA}\phi_{hB}dx + \int_0^a \phi_{cA}\phi_{hB}dx + \int_a^l \phi_{hA}\phi_{hB}dx \tag{5.2}$$

where, ϕ_{cK} and ϕ_{hK}, are the copolymer and homopolymer volume fractions of beads of type K ($\equiv A, B$). Here, a is the length of copolymer molecules and l is the interfacial length. Assuming a step composition profile for copolymers and a hyperbolic tangent profile for the homopolymers (ϕ_{hA}, ϕ_{hB}), the above expression reduces to,

$$\frac{g(a,l)}{k_BT} \propto \int_a^l \tanh\left(\frac{x}{l}\right)\left[1 - \tanh\left(\frac{x}{l}\right)\right]dx \tag{5.3}$$

Note here that in the limit of high α the first 2 terms on the right hand side of the free energy equation vanishes. The enthalpic cost under shear can be obtained as, $\Delta g = g(a,l) - g(a_o,l)$, where a_o is the unperturbed equilibrium size of the copolymer molecules. The only 2 parameters in the equation for interfacial tension are a/a_o and a_o/l. For shear rate dependence of a/a_o, we use the scaling description proposed by Semenov [145] for FENE chains: $(\dot{\gamma}\tau)^{-1/3}N_{AB}^{-1/2}$, and a_o/l is found from our composition profiles to closely match with $\sim (1 - (2/\alpha^2))$. Incorporating these observations, the shear rate dependence of enthalpic cost can be written as,

$$\Delta g/k_BT \sim \log\left(\cosh(a_o/l)/\cosh(\frac{a}{a_o}\frac{a_o}{l})\right) + \frac{a_o}{l}(a/a_o - 1) + \tanh(a_o/l) - \tanh(\frac{a}{a_o}\frac{a_o}{l}) \tag{5.4}$$

Figure 5.18 displays the enthalpic cost as a function of shear rate $\dot{\gamma}\tau$, for two different values of α as indicated. It can be seen from Fig. 5.18 that for a larger

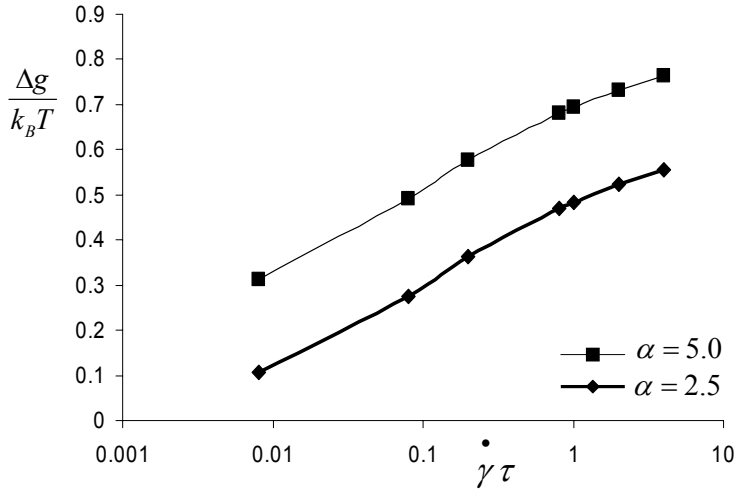

Figure 5.18: Enthalpic cost displayed as a function of shear rate for two values of α.

value of α, there is a greater enthalpic cost with shear rate, which rationalizes the reduction in the number of interfaces and macrophase separation. This is consistent with our observation of the dependence of phase behavior on α.

5.7 Conclusion

In this chapter we have used self-consistent Brownian dynamics [103] to probe the shear effects on the internal microstructure in a ternary polymer blend system. We have identified different regimes through which a bicontinuous structure at equilibrium macrophase separates under shear. Initially at low shear rates, bicontinuous structure gives rise to a modulated lamellar structure. Moderate shear rates lead to a stabilization of lamellar structure with

suppression of capillary waves resulting in perfectly aligned lamellae. Any further increase in shear rate results in merging of lamellae leading to three phase coexistence. Finally at very high shear rates, the system macrophase separates entirely giving rise to homopolymer rich domains. These different regimes are also consistent with the experimental observations of Krishnan and coworkers [132]. At low shear rates, Krishnan et al. have also observed anisotropy in the form of streaked patterns aligned at an angle to the flow direction. However, with increase in shear rate these patterns increasingly align in the shear direction, resulting in a lamellar-like microstructure. We have particularly concentrated on the transitions between lamellar phase to macrophase separated regions in these systems, hence, such a transition contrasts with that observed in traditional oil/water/surfactant systems. The non-trivial length of the copolymer chain and its flow deformation has been implicated in altering the energetic interactions and hence the modifying the interfacial tension leading to the above transitions. Though the qualitative sequence of transitions remain unchanged, the quantitative trends of phase transitions with copolymer size asymmetry and viscoelastic asymmetry has been discussed. A simple scaling analysis incorporating the polymer chain deformation under shear has been presented. This analysis was also shown to corroborate the quantitative trends observed with copolymer size and viscoelastic asymmetry. To our knowledge, the results presented above constitute the first molecular scale simulation study of flow induced phase transitions near microemulsion phases.

Chapter 6

Composition Field Dynamics in Ternary Polymer Blends

6.1 Introduction

As seen in the previous chapter, ternary polymer blends of homopolymers A and B blended with a blockcopolymer AB exhibit rich flow-structure interplay [17, 146]. In the recent experimental work of Burghardt and coworkers, bicontinuous microemulsion structures formed in the vicinity of Lifshitz point of ternary blends (see Fig. 5.1) have displayed a series of phase transitions under the application of shear field [130, 132, 147]. The experiments have suggested a transition of the bicontinuous structures into streaked lamellar like patterns, followed by three phase coexistence and macrophase separated patterns with progressively increasing shear rates (Fig. 5.5) [130, 132]. In the previous chapter, with the use of self-consistent Brownian dynamics simulations [103], we implicated the macromolecular nature of the polymeric system (namely, the interplay between flow and conformational dynamics of the polymers) as a possible mechanism behind the flow-induced structural transitions [147]. Our results presented in the previous chapter constitute the first molecular simulation study of flow-induced phase transitions near microemulsion phases. Very good qualitative agreement was noted between our simulation

results and the experiments of Burghardt and coworkers [132].

Traditional theories for flow effects on multicomponent polymeric systems typically pertain to weak shears and ignore the viscoelastic chain deformation effects discussed above [9, 131]. These theories have focused on the composition fluctuations present in multicomponent systems, and have quantified the effect of external shear on the fluctuations and its effect in turn on (de)stabilizing a particular phase. Such researches, in the context of lamellar and microemulsion phases, can in general be classified into two broad classes, namely, (a) The effect of shear on isotropic to lamellar transitions and (b) The stability of lamellar phases under external shear. As mentioned in chapter 5, Cates and Milner (class (a)) [9] have shown that steady shear suppresses the composition fluctuations in isotropic phases resulting in the increase of transition temperature, leading to a transition from isotropic to the lamellar phases. Although this suppression in composition fluctuations can explain the bicontinuous to lamellar transition in ternary blend systems, they fall short of explaining the further transitions of the lamellar phases into three phase coexistence and macrophase separation observed by Krishnan and coworkers. On the other hand, theories studying the stability of lamellar phases (class (b)) [131, 133] have observed shear induced suppression of fluctuations leading to a reduction in lamellar spacing. Other researches have also noticed shear induced reorientation of lamellae (to be discussed in detail in the following chapter).

Patzold and Dawson [18] have carried out a detailed theoretical study of

a model along the above lines to examine the structural and rheological properties of microemulsion phases. Their framework used a simple time-dependent Landau-Ginzburg model [50] for a single scalar order parameter, viz. the composition difference between A and B components, denoted by ψ, based on a Hamiltonian which incorporates some essential features microstructures observed in surfactant systems. They studied the case of steady shear and oscillatory shear and found rheology corresponding to shear thinning behavior, positive first normal stress difference and negative second normal stress differences. Their model also predicts the structure factor under shear for such self-assembling systems. *However, no shear-induced phase transitions were predicted*. Their predictions were compared recently with the experimental results of Burghardt and coworkers, but found significant discrepancies between the model and experiments. While the single order parameter model of Patzold and Dawson generally predicted a suppression of scattered intensity under steady shear, the experimental results displayed an enhancement of anisotropic structure factor with shear, due to loss of scattering intensity along the velocity direction. They also observed that the angles of peak intensity progressively rotated towards the velocity gradient direction with increase in shear, an effect not predicted by Patzold and Dawson model.

The above discrepancies between Patzold and Dawson [18] model and experiments by Burghardt and coworkers [17], have motivated us to develop a more refined order parameter model which characterizes more accurately the features of ternary polymeric blends. In this chapter, we present the results of

this model, including investigations whether such a model could explain the shear-induced phase separation using composition fluctuations alone without invoking the flow-induced polymer chain deformation phenomena discussed in the previous chapter.

6.2 Derivation of Free Energy Expression

In this chapter, we study a symmetric system of ternary polymer blends, with the system average compositions of the homopolymers of type A and type B being equal. The block copolymers AB are also assumed to be symmetric in their block composition. The ratio of the lengths of the copolymer and the homopolymer, denoted by $\alpha = 1/y$, is fixed at a value of 2.22 in this research. We consider a three order parameter model, where the order parameters are denoted by $\psi_i (i = 1..3)$, written in term of the local compositions of homopolymers and copolymers, denoted by ϕ's, as:

$$\begin{aligned}
\psi_1(\mathbf{r}) &= \phi_A^H(\mathbf{r}) - \phi_B^H(\mathbf{r}) \\
\psi_2(\mathbf{r}) &= \phi_A^C(\mathbf{r}) + \phi_B^C(\mathbf{r}) - (1 - \bar{\Phi}_1) \\
\psi_3(\mathbf{r}) &= \phi_A^C(\mathbf{r}) - \phi_B^C(\mathbf{r}) \\
\psi_4(\mathbf{r}) &= \phi_A^H(\mathbf{r}) + \phi_B^H(\mathbf{r}) - \bar{\Phi}_1. \qquad (6.1)
\end{aligned}$$

where, subscripts A and B denote monomer A, monomer B and superscripts H and C refer to the homopolymer and copolymer respectively. Here $\bar{\Phi}_1$ denotes the system average homopolymer composition ϕ^H and $\bar{\Phi}_2$ ($\equiv 1 - \phi^H$) denotes the system averaged copolymer composition. Due to the incompressibility

condition, the fourth order parameter field, ψ_4, becomes redundant and hence, we use only three order parameters ψ_1, ψ_2 and ψ_3, in the rest of the chapter.

To obtain the appropriate free energy for the above order parameters, we use a simple density functional approach proposed by Wang and coworkers [150]. The idea behind these models is to use a local Flory-Huggins description for the free energy of the system, while correcting the second order terms (in compositions) by using nonlocal correlations between order parameters. Explicitly,

$$F[\psi_1, \psi_2, \psi_3] = F_{id}[\psi_1, \psi_2, \psi_3] - F_{id}^{(2)}[\psi_1, \psi_2, \psi_3] + \Delta F^{(2)}[\psi_1, \psi_2, \psi_3]. \quad (6.2)$$

In the above, F_{id} stands for the local Flory-Huggins free energy (relative to the homogeneous state) corresponding to compositions ψ_1, ψ_2, ψ_3, while, $F_{id}^{(2)}$ stands for the quadratic terms in F_{id} (by definition, the linear terms are zero) and $\Delta F^{(2)}[\psi_1, \psi_2, \psi_3]$ correspond to the (nonlocal) free energy functional at compositions ψ_1, ψ_2, ψ_3, which is evaluated using the random phase approximation (RPA) [4, 40].

For the Flory-Huggins ideal free energy contribution, we have,

$$\frac{\beta N F_{id}}{\rho} = \frac{\phi_A^H}{2}\ln(\phi_A^H) + \frac{\phi_B^H}{2}\ln(\phi_B^H) + \frac{\phi_A^C}{2\alpha}\ln(\phi_A^C) + \frac{\phi_B^C}{2\alpha}\ln(\phi_B^C), \quad (6.3)$$

where, N is the polymerization index of the homopolymers and the compositions $\phi_A^H, \phi_B^H, \phi_A^C, \phi_B^C$ are related to the order parameters ψ_i's through the

equations (6.1). Using this we obtain,

$$\begin{aligned} F_{id} - F_{id}^{(2)} &= \frac{3\psi_2\psi_1^2}{6y\bar{\Phi}_1^2} + \frac{1}{12y\bar{\Phi}_1^3}\left(\psi_1^4 + 6\psi_1^2\psi_2^2\right) + \\ & \psi_2^3\left(\frac{1}{6y\bar{\Phi}_1^2} - \frac{1}{6\bar{\Phi}_2^2}\right) - \frac{\psi_2\psi_3^2}{2\bar{\Phi}_2^2} + \psi_2^4\left(\frac{1}{12\bar{\Phi}_1^3} + \frac{1}{12\bar{\Phi}_2^3}\right) + \\ & \frac{1}{12\bar{\Phi}_2^3}\left(\psi_3^4 + 6\psi_2^2\psi_3^2\right). \end{aligned} \tag{6.4}$$

Now, $\Delta F^{(2)}$ is evaluated within the RPA approximation as [40]:

$$\begin{aligned} \frac{\beta N \Delta F^{(2)}(\mathbf{k})}{\rho} &= -\frac{\chi N}{4}[\psi_1 + \psi_3]^2 + \frac{1}{2}[S_{AA}^{(H)}(\mathbf{k})]^{-1}\Delta\phi_A^H(\mathbf{k})\Delta\phi_A^H(\mathbf{k}) + \\ & \frac{1}{2}[S_{BB}^{(H)}(\mathbf{k})]^{-1}\Delta\phi_B^H(\mathbf{k})\Delta\phi_B^H(\mathbf{k}) + \frac{1}{2}[S_{AA}^{(C)}(\mathbf{k})]^{-1}\Delta\phi_A^C(\mathbf{k})\Delta\phi_A^C(\mathbf{k}) + \\ & \frac{1}{2}[S_{BB}^{(C)}(\mathbf{k})]^{-1}\Delta\phi_B^C(\mathbf{k})\Delta\phi_B^C(\mathbf{k}) + [S_{AB}^{(C)}(\mathbf{k})]^{-1}\Delta\phi_A^C(\mathbf{k})\Delta\phi_B^C(\mathbf{k}) \end{aligned} \tag{6.5}$$

In the above, $\Delta\phi_A^H(\mathbf{k}), \Delta\phi_B^H(\mathbf{k}), \Delta\phi_A^C(\mathbf{k}), \Delta\phi_B^C(\mathbf{k})$ represent the Fourier transform of the fields $\Delta\phi_A^H(\mathbf{r}), \Delta\phi_B^H(\mathbf{r}), \Delta\phi_A^C(\mathbf{r}), \Delta\phi_B^C(\mathbf{r})$, where for the symmetric system we have considered,

$$\begin{aligned} \Delta\phi_A^H(\mathbf{r}) &= \phi_A^H(\mathbf{r}) - \frac{\bar{\Phi}_1}{2} \\ \Delta\phi_B^H(\mathbf{r}) &= \phi_B^H(\mathbf{r}) - \frac{\bar{\Phi}_1}{2} \\ \Delta\phi_A^C(\mathbf{r}) &= \phi_A^C(\mathbf{r}) - \left(\frac{1-\bar{\Phi}_1}{2}\right) \\ \Delta\phi_B^C(\mathbf{r}) &= \phi_B^C(\mathbf{r}) - \left(\frac{1-\bar{\Phi}_1}{2}\right). \end{aligned} \tag{6.6}$$

Moreover, $S_{ij}(\mathbf{k})$ denotes the Fourier transform of the volume fraction correlation functions of the appropriate components i and j, evaluated for the *noninteracting* case (RPA idea). The latter quantities have already been cal-

culated in literature [4] as:

$$\begin{aligned} S_{AA}^{(H)} &= S_{BB}^{(H)} = \frac{\bar{\Phi}_1}{2} g[y,x] \\ S_{AA}^{(C)} &= S_{BB}^{(C)} = \frac{1-\bar{\Phi}_1}{2} g[1/2,x] \\ S_{AB}^{(C)} &= \left(\frac{1-\bar{\Phi}_1}{2}\right) \frac{1}{2} \left(g[1,x] - 2g[1/2,x]\right) \end{aligned} \tag{6.7}$$

where $x = k^2 R_g^2$ and $g[y,x]$ is the generalized Debye function [40],

$$\begin{aligned} g[y,x] &= \frac{2[yx + \exp(-yx) - 1]}{x^2} \\ &\simeq y^2/(1+yx). \end{aligned} \tag{6.8}$$

By writing equation (6.5) in terms of ψ_1, ψ_2, ψ_3 (and dropping all constant and linear terms), and expanding $g[y,x]$ as above, we obtain,

$$\begin{aligned} \frac{\beta N \Delta F^{(2)}(\mathbf{k})}{\rho} &= -\frac{\chi N}{4}[\psi_1 + \psi_3]^2 + \left(\frac{1}{2y\bar{\Phi}_1} + \frac{1}{2\bar{\Phi}_2}\right)\psi_2^2 + \frac{x\psi_2^2}{6}\left(\frac{1}{\bar{\Phi}_1} + \frac{1}{\bar{\Phi}_2}\right) + \\ &\quad \frac{1}{2y\bar{\Phi}_1}\psi_1^2 + \frac{x}{6\bar{\Phi}_1}\psi_1^2 + \frac{1.8}{2\bar{\Phi}_2}\psi_3^2 + \frac{x}{4\bar{\Phi}_2}\psi_3^2 + \\ &\quad \frac{3}{\bar{\Phi}_2 x}\psi_3^2. \end{aligned} \tag{6.9}$$

Transforming back to real space and expressing all lengths in R_g units we

obtain to the fourth order,

$$\begin{aligned}\frac{\beta NF}{\rho} &= \frac{-\chi N}{4}\left(\psi_1+\psi_3\right)^2+\left(\frac{1}{2y\bar{\Phi}_1}+\frac{1}{2\bar{\Phi}_2}\right)\psi_2^2+\frac{\left(\nabla\psi_2\right)^2}{6}\left(\frac{1}{\bar{\Phi}_1}+\frac{1}{\bar{\Phi}_2}\right)+\\ &\frac{1}{2y\bar{\Phi}_1}\psi_1^2+\frac{1}{6\bar{\Phi}_1}\left(\nabla\psi_1\right)^2+\frac{1.8}{2\bar{\Phi}_2}\psi_3^2+\frac{1}{4\bar{\Phi}_2}\left(\nabla\psi_3\right)^2+\\ &\frac{3}{\bar{\Phi}_2}\int dr\int dr'\frac{\psi_3(r)\psi_3(r')}{|r-r'|}+\frac{3\psi_2\psi_1^2}{6y\bar{\Phi}_1^2}+\frac{1}{12y\bar{\Phi}_1^3}\left(\psi_1^4+6\psi_1^2\psi_2^2\right)+\\ &\psi_2^3\left(\frac{1}{6y\bar{\Phi}_1^2}-\frac{1}{6\bar{\Phi}_2^2}\right)-\frac{\psi_2\psi_3^2}{2\bar{\Phi}_2^2}+\psi_2^4\left(\frac{1}{12\bar{\Phi}_1^3}+\frac{1}{12\bar{\Phi}_2^3}\right)+\\ &\frac{1}{12\bar{\Phi}_2^3}\left(\psi_3^4+6\psi_2^2\psi_3^2\right). \qquad (6.10)\end{aligned}$$

6.3 Cell Dynamics

In this section we provide a brief overview of the numerical scheme used to study shear behavior in ternary blend systems. The numerical scheme we used falls in the general class of cell dynamics method originally developed by Oono and Puri [15] to model interfacial dynamics in phase separating systems. This scheme corresponds to a coarse-grained discretization of the time-dependent Ginzburg-Landau (TDGL) equation for a system with a conserved order parameter. In our three order parameter system, the evolution equations read:

$$
\begin{aligned}
\frac{\partial \psi_1(\mathbf{r},t)}{\partial t} &= -\nabla \cdot (\psi_1 \mathbf{v}) + M\nabla^2 \frac{\delta F\left[\psi_1(\mathbf{r},t), \psi_2(\mathbf{r},t), \psi_3(\mathbf{r},t)\right]}{\delta \psi_1(\mathbf{r},t)} \\
&\quad + B\xi(\mathbf{r},t) \\
\frac{\partial \psi_2(\mathbf{r},t)}{\partial t} &= -\nabla \cdot (\psi_2 \mathbf{v}) + M\nabla^2 \frac{\delta F\left[\psi_1(\mathbf{r},t), \psi_2(\mathbf{r},t), \psi_3(\mathbf{r},t)\right]}{\delta \psi_2(\mathbf{r},t)} \\
&\quad + B\xi(\mathbf{r},t) \\
\frac{\partial \psi_3(\mathbf{r},t)}{\partial t} &= -\nabla \cdot (\psi_3 \mathbf{v}) + M\nabla^2 \frac{\delta F\left[\psi_1(\mathbf{r},t), \psi_2(\mathbf{r},t), \psi_3(\mathbf{r},t)\right]}{\delta \psi_3(\mathbf{r},t)} \\
&\quad + B\xi(\mathbf{r},t)
\end{aligned} \tag{6.11}
$$

In the above equations, M is a mobility coefficient (assumed constant), used to non-dimensionalize the time scale and B is the amplitude of a Gaussian noise ξ. The velocity field $\mathbf{v}(r,t)$ is assumed to be equal to $\dot{\gamma} y$ in disordered, viscoelastically symmetric systems. However, in the case of phase separating systems *with viscosity contrast*, the velocity field is determined self-consistently as a function of the structural characteristics. Explicitly, the velocity field is evolved at every step using the Navier-Stokes equation, which is written allowing for the inclusion of viscosity contrast as,

$$
\rho \frac{\partial \mathbf{v}(r,t)}{\partial t} = \left\{ \nabla \cdot \left[\eta \left(\psi_1(r,t) + \psi_3(r,t) \right) \left(\nabla \mathbf{v} + \nabla \mathbf{v}^T \right) \right] \right\}_{\perp} \tag{6.12}
$$

where $\eta(\psi(r))$ is the order parameter dependent viscosity and $\mathbf{v}(r,t)$ denotes the local velocity and ρ is a fictitious density used to evolve the equations to steady state. While equations (6.11) are solved in the real space, the Navier-Stokes equation (6.12) is solved in the Fourier space. The Fourier transformed

Navier-Stokes equation is written as,

$$\frac{\partial \mathbf{v}(\mathbf{k},t)}{\partial t} = (\mathbf{I} - \mathbf{kk}/\mathbf{k}^2) \,.\, \mathbf{F}(\mathbf{k},t) \tag{6.13}$$

where $\mathbf{v}$(**k**,t) and $\mathbf{F}$(**k**,t) represent the Fourier components of local velocity, $\mathbf{v}$(r,t) and the driving force $\mathbf{F}(r,t) = \nabla \,.\, [\eta(\psi_1 + \psi_3)(\nabla \mathbf{v} + \nabla \mathbf{v}^T)]$, respectively.

In our simulations, the length and time scales are non-dimensionalized using the radius of gyration of the homopolymer R_g and the inverse of the mobility coefficient M. We have chosen x, as the flow and y as the velocity gradient direction. Our simulations are performed in a 128×128 2D square lattice where each lattice bin is $0.25R_g$ in length. In shear flows, we also employ the shear periodic boundary condition proposed by Ohta [148] as,

$$\psi(i,j,\tau) = \psi\left(i + N_x L + \gamma N_y L, j + N_y L, \tau\right) \tag{6.14}$$

where N_x and N_y are arbitrary integers and $\gamma = \dot{\gamma}\tau$ is the shear strain. This shear periodic boundary condition is enforced in the reciprocal Fourier space (for solving velocity evolution equation) by defining a new shifted Fourier variable $\mathbf{k}'$ ($k_x' = k_x, k_y' = k_y + \dot{\gamma} t k_x$) as proposed by Zhang and coworkers [151]. Under this shifted variable, the Navier-Stokes equation is now rewritten as,

$$\frac{\partial \mathbf{v}(\mathbf{k}',t)}{\partial t} = (\mathbf{I} - \mathbf{kk}/\mathbf{k}^2) \left[\mathbf{F}(\mathbf{k}',t) - \gamma k_x' \frac{\partial \mathbf{v}(\mathbf{k}',t)}{\partial k_y'}\right] - \mathbf{k}\mathbf{v}(\mathbf{k}',t)/\mathbf{k}^2 \,.\, \frac{\partial \mathbf{k}}{\partial t} \tag{6.15}$$

where **k** is related to $\mathbf{k}'$ as $k_x = k_x'$, $k_y = k_y' - \dot{\gamma} t k_x'$. In order to obtain faster convergence and to enable us to employ a larger timestep, we have solved the

above equation using an Alternate-Direction-Implicit (ADI) scheme [152]. The timestep Δt used in our simulations is 0.001 in the units mentioned earlier. The initial conditions for velocity is set at $\dot{\gamma} y$, for the solution of viscoelastic asymmetric systems. The initial conditions for the order parameters are taken as zero and the amplitude for white noise, B is chosen as 0.01.

6.4 Results for Disordered Phase

In order to understand shear effects on ternary polymer blends, we have focused on both disordered and ordered phases. In the disordered phases we study the shear effects on structure factor to probe the shear effect on composition fluctuations. In the ordered system we directly obtain information on the structure and composition fields and the effects of shear on possible phase transitions in the ordered phases. In this section we display our results on the flow induced changes in the structure factor in a ternary polymer blend system. However, before displaying the non-equilibrium results, we first present the equilibrium results obtained for the ternary system in order to confirm the accuracy of free energy expression.

Figure 6.1 displays the equilibrium line of order-disorder transitions, for α=2.22, obtained using the free energy functional developed (equation (6.10)) above. The Lifshitz point is given as $\phi_L = \alpha^2/(2+\alpha^2) \equiv 0.71$ [135] is the composition that separates the lamellar phases (formed at lower ϕ^H's) and the two phase region (formed at high values of ϕ^H). Experiments have observed a bicontinuous, sponge like phases in the vicinity of the Lifshitz point. A sys-

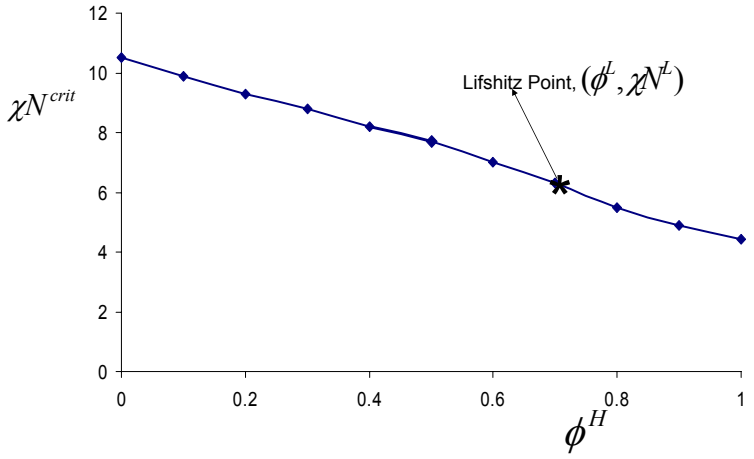

(a)

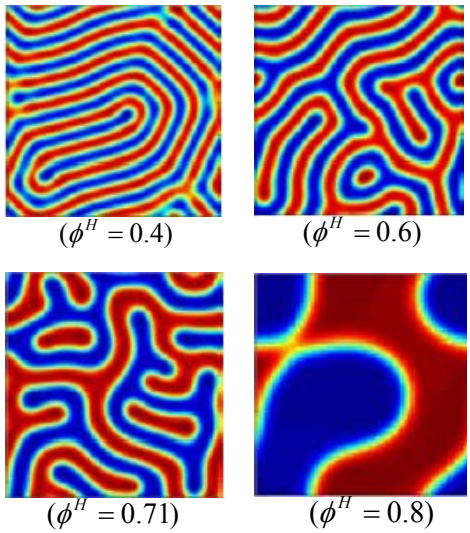

(b)

Figure 6.1: (a) Order disorder transition for ternary blend system with $\alpha = 2.22$ (b) Cell dynamics solution of the equilibrium composition profile at various homopolymer compositions indicated.

tematic exploration of the entire equilibrium phase diagram is out of scope of this research, and instead we have performed our cell dynamics simulations for selected values of homopolymer compositions ϕ^H. Figure 6.1b displays the time averaged two dimensional composition profile obtained for the homopolymer compositions ϕ^H indicated in the parenthesis. At $\phi^H = 0.4$ and 0.6 (compositions in the lamellar phase), we observe a lamellar microstructure formed in our equilibrium simulation. The lamellae thickness is larger for the system with larger homopolymer composition, $\phi^H = 0.6$, a phenomenon seen in experiments, and which arises due to the swelling of block copolymer layers. Bicontinuous microemulsion like phases are found in the vicinity of the Lifshitz point ($\phi^H = 0.71$). At higher homopolymer compositions of $\phi^H = 0.8$, we observe macrophase separated homopolymer rich domains. Furthermore, we have checked that the disordered phase prevails for all χN's less than the critical χN for the corresponding homopolymer composition. This exercise demonstrates the validity of the free energy functional for ternary polymer blends (equation 6.10) employed in the cell dynamics scheme.

Now we present the equilibrium structure factor results for two distinct homopolymer compositions of $\phi^H = 0.2$ and $\phi^H = 0.67$, in the disordered phase. Figure 6.2 displays the 2D scattering intensity plot for $\phi^H = 0.2$, $\chi N = 9.3$ and $\phi^H = 0.67$, $\chi N = 6.5$ systems respectively. The critical values of χN (for transition to ordered phases) at these homopolymer compositions are $\chi N = 9.5$ and $\chi N = 6.8$ respectively. These scattering functions are computed as, $S(k) =< \psi_t(k)^2 >$, where $\psi_t(k)$ is the Fourier component of

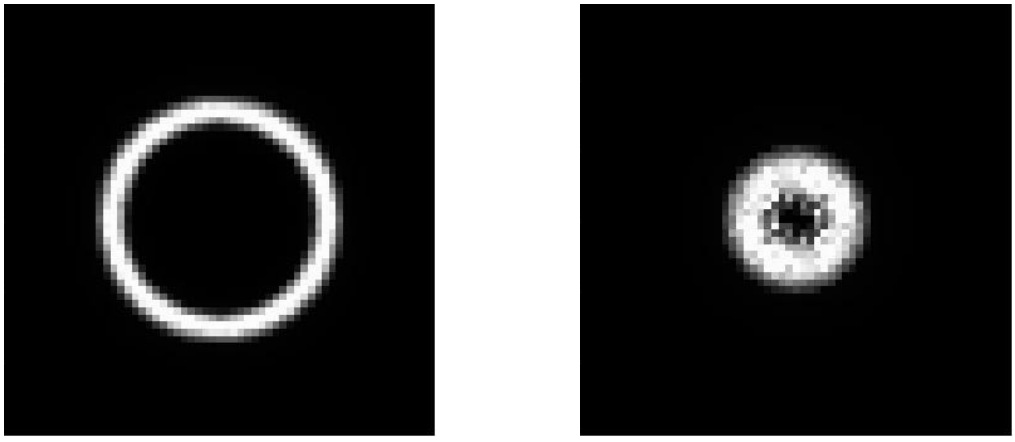

(a) (b)

Figure 6.2: Equilibrium structure factor in the disordered phase, for homopolymer compositions of (a) $\phi^H = 0.2$ and (b)$\phi^H = 0.67$.

the composition field, $\phi_t(r) = \psi_1(r) + \psi_3(r)$. In the 2D scattering patterns of Fig. 6.2, the dark areas denote the regions of lower scattering intensity. The radius of the ring for the $\phi^H = 0.2$ case is seen to be larger than that for the $\phi^H = 0.67$ system. This radius corresponds to the absolute value of the most unstable wave vector with which the lamellar pattern will develop at the order-disorder transition temperature. As noted earlier, the lamellar thickness in the ordered phases are smaller in the $\phi^H = 0.2$ system, which is consistent with a larger radius of scattering intensity in the reciprocal $\mathbf{k}$ space.

Figure 6.3 displays the structure factor of the system ($\phi^H = 0.67$) under the application of shear. Note here that under the shear boundary condition (equation (6.14)), the Fourier components are calculated by performing an

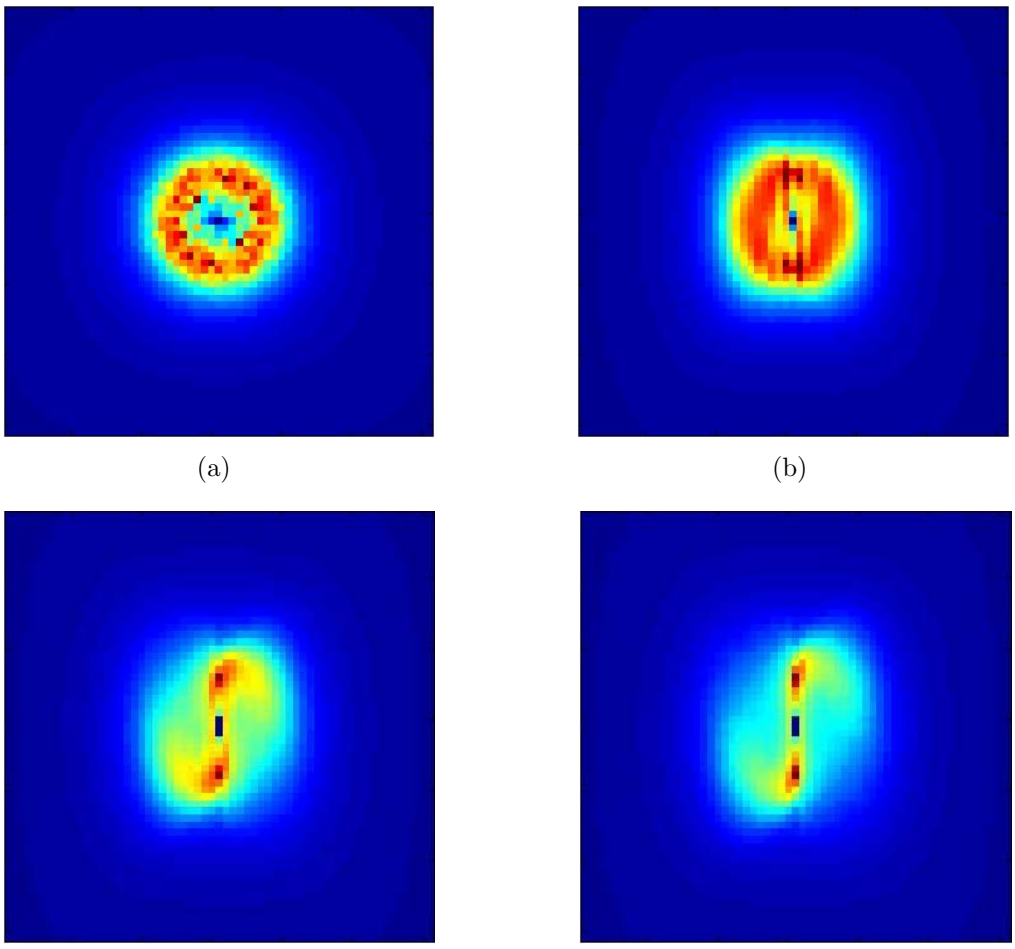

(a) (b)

(c) (d)

Figure 6.3: Structure factor for ternary blend with $\phi^H = 0.67$ at four different shear rates of (a) $\dot{\gamma} = 0.0$; (b) $\dot{\gamma} = 0.005$; (c) $\dot{\gamma} = 0.05$ and (d) $\dot{\gamma} = 0.1$.

affine transformation as [149],

$$\psi_t(k_x, k_y, t) = \int_0^L dx^{'} \int_0^L dy \psi_t(x, y, t) \exp[i(k_x x + k_y y)], \tag{6.16}$$

where, $x^{`} = x - \gamma y$ and $K = (k_x, k_y) = (2\pi/L)(m, n - \gamma m)$ where, m and n are integers. The applied shear rates in Fig. 6.3, correspond to (a) $\dot{\gamma} = 0$, (b) $\dot{\gamma} = 0.005$, (c) $\dot{\gamma} = 0.05$, (d) $\dot{\gamma} = 0.1$. At low shear rate of $\dot{\gamma} = 0.005$, (Fig. 6.3b) we observe that there is very little change in the structure factor compared to its equilibrium value. With increasing shear rate however, we observe that the structure factor becomes anisotropic and elliptical in shape (Fig. 6.3c, d), with the areas of peak intensity rotating closer towards $q_x = 0$.

In order to quantify the above results and effect a comparison with experiments, we follow the lines of Caputo et al. [17], by computing a second moment tensor of the dimensionless scattering vector $\hat{\mathbf{q}}$ weighted by the normalized structure factor,

$$\langle \hat{q}_i \hat{q}_j \rangle = \int \int \hat{q}_i \hat{q}_j \hat{S}(\hat{\mathbf{q}}) d\hat{q}_x d\hat{q}_y \tag{6.17}$$

where, the $\hat{q}_i$'s are obtained by normalizing q_i's by their values at which the highest scattering intensity is obtained at quiescent conditions ($\hat{q}_i = q_i/q_{max}$), where q_{max} is the value of q corresponding to the maximum scattering intensity at equilibrium. Here the integral is carried out over $|\hat{q}_x, \hat{q}_y| \leq 1.5$ (the range covered by the 2D scattering patterns). The anisotropic second moments are normalized by the diagonal element of this tensor for isotropic, quiescent

structure factor values, given by,

$$\frac{1}{2}\left\langle \hat{q}^2 \right\rangle_0 = \frac{1}{2}\int\int \hat{q}^2 \hat{S}_0(\hat{\mathbf{q}}) d\hat{q}_x d\hat{q}_y \tag{6.18}$$

Other measures of characterizing the anisotropy in the structure factor include the normalized anisotropy (Δ) and orientation angle (θ). These values are computed using the expressions given by Caputo and coworkers as [17],

$$\Delta = \frac{\sqrt{(\langle \hat{q}_x^2 \rangle - \langle \hat{q}_y^2 \rangle)^2 + 4\left\langle \hat{q}_x \hat{q}_y \right\rangle^2}}{\frac{1}{2}\left\langle \hat{q}^2 \right\rangle_0} \tag{6.19}$$

$$\theta = \frac{1}{2}\tan^{-1}\left(\frac{2\left\langle \hat{q}_x \hat{q}_y \right\rangle}{\langle \hat{q}_x^2 \rangle - \langle \hat{q}_y^2 \rangle}\right) \tag{6.20}$$

where $\left\langle \hat{q}^2 \right\rangle_0$ is given by,

$$\frac{1}{2}\left\langle \hat{q}^2 \right\rangle_0 = \frac{1}{2}\int\int \hat{q}^2 \hat{S}_0(\hat{\mathbf{q}}) d\hat{q}_x d\hat{q}_y \tag{6.21}$$

In Fig. 6.4, we display the various moments (xx, yy, -(xx-yy), -xy) obtained from our numerical scheme, alongside the experimental and numerical results of Burghardt and coworkers [17]. The numerical results of [17] were obtained using a single parameter model similar to that of Patzold and Dawson [18]. The xx component of the tensor is seen to monotonically decrease with increase in shear rate, quantitatively consistent with the experimental values. We also find a qualitative agreement of the xy component with the experiments, which is characterized by a maxima. Moreover, compared to the single parameter model, our results for the -(xx-yy) components show better quantitative agreement with experimental results. However, there still exists quantitative

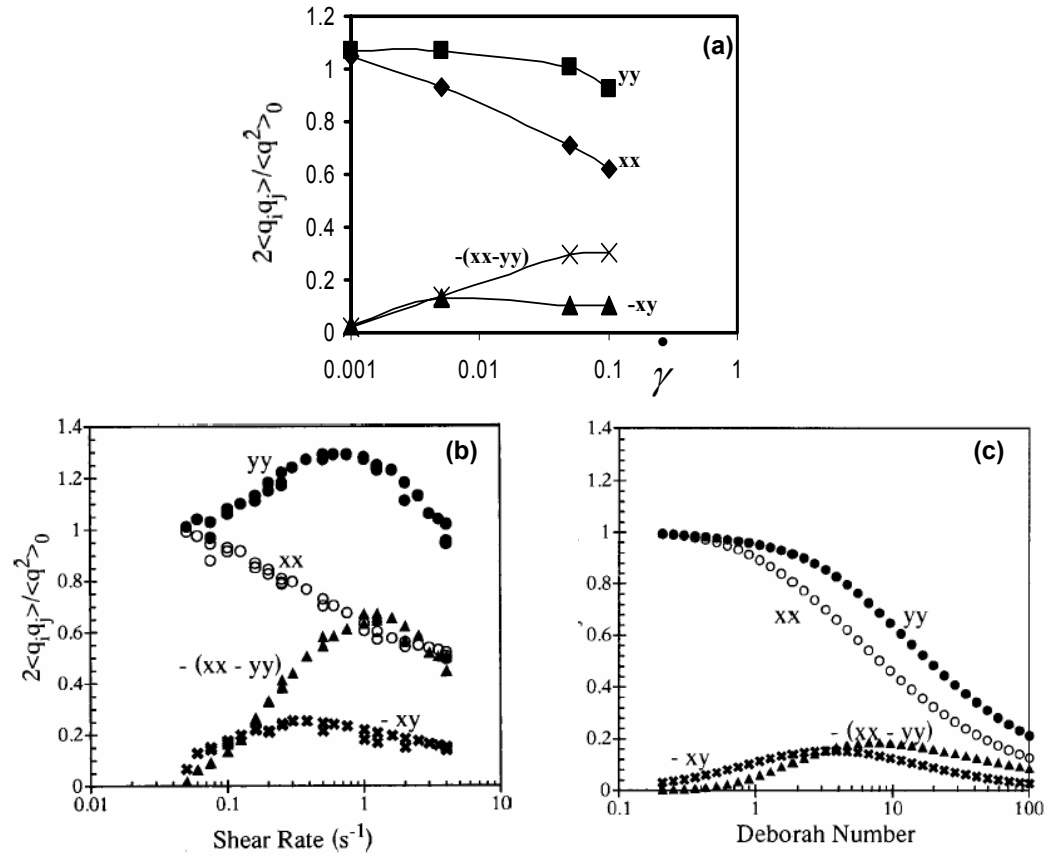

Figure 6.4: The structure factor weighted second moments displayed as a function of the shear rate, obtained from cell dynamics in (a) and the experimental and numerical scheme results of [17] in (b) & (c) respectively.

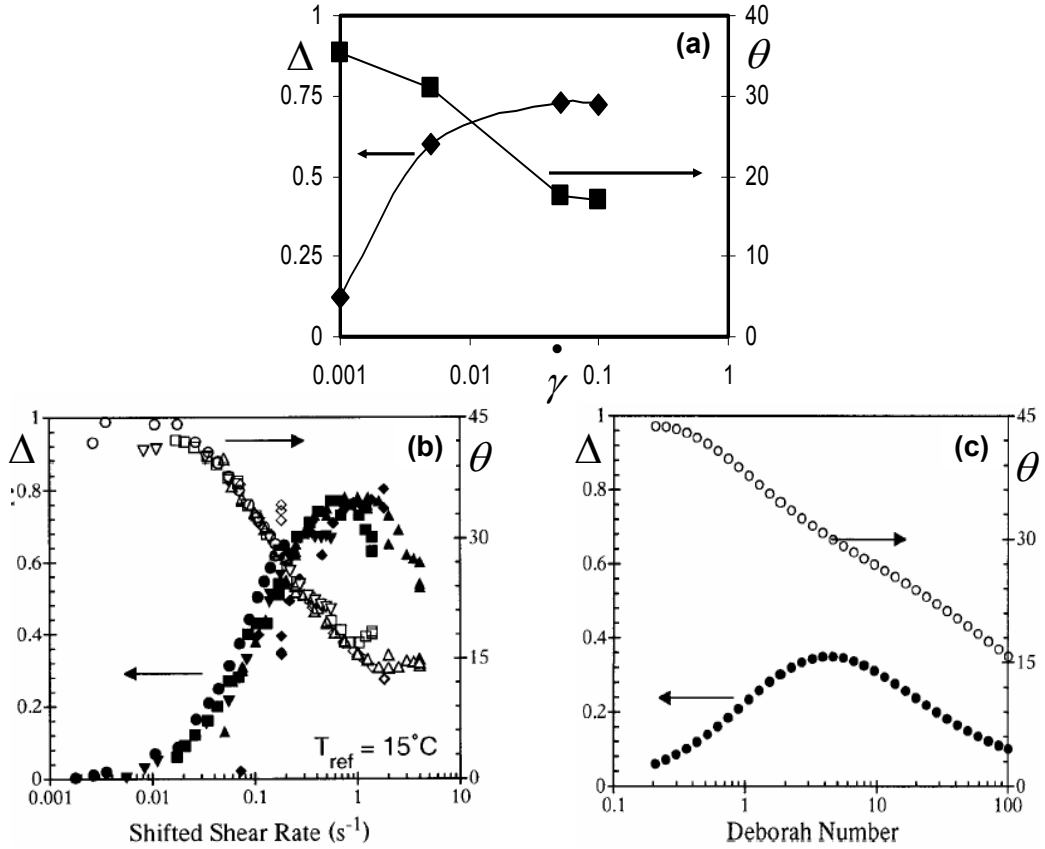

Figure 6.5: Normalized anisotropy Δ and orientation angle θ displayed as a function of shear rate, obtained from cell dynamics in (a) and the experimental and numerical scheme results of [17] in (b) & (c) respectively.

and qualitative discrepancies. For instance, our yy component is a monotonically decreasing function of shear rate, while the experimental results show a maxima. We return to this feature later.

Next, we compared the normalized anisotropy (Δ) and orientation angle (θ) with the experimental and single order parameter model results in Fig. 6.5. Here again, compared to the single order parameter model, we find better quantitative agreement. The normalized anisotropy values are much higher that the single parameter model, and compare very well quantitatively with experiments. We also obtain quantitative agreement of the orientation angles with the experimental data and we also capture the plateauing of orientation angle at higher shear rates (not captured by single parameter model).

Next, we compare the scattering intensity at $q_x = 0$, of our system at equilibrium and under shear, with the experimental results of Caputo and coworkers [17]. The experiments have seen an increase in the scattering intensity at low q_y's with increasing shear rates as seen in Fig. 6.6. This increase in scattering intensity is not captured in our model, wherein, as seen in Fig. 6.6, the scattering intensity under shear remains clearly unchanged from its equilibrium values.

Overall, we find a reasonably good agreement between our results and the experiments. Moreover, a comparison with the single order parameter model results show that our results have better agreement with the experiments. However, some quantitative discrepancies still remain. In the experimental research of Burghardt and coworkers [17], they have implicated

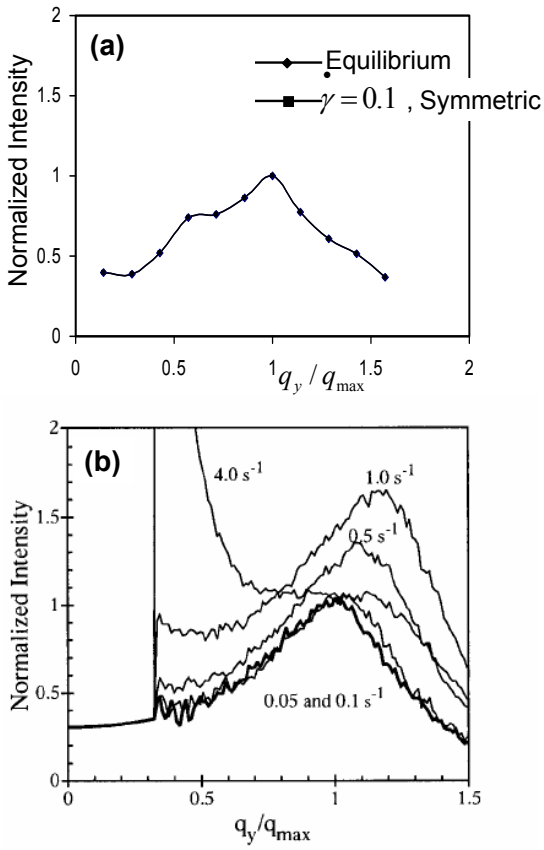

Figure 6.6: (a) Normalized intensity obtained from cell dynamics, at equilibrium and under shear ($\dot{\gamma} = 0.1$) for a viscoelastically symmetric system; (b) Normalized intensity under shear for a PEE-PDMS ternary blend, adapted from [17].

the extreme viscosity contrast between the PEE and PDMS polymers as a possible reason behind the discrepancies between the experiments and single parameter model. Indeed any theory which assumes that the local velocity field is unaffected by the microemulsion structure (such as we assumed in the absence of viscoelastic contrast), predicts no change in the structure factor along $q_x = 0$. Such an assumption is questionable, especially in systems like PEE-PDMS ternary blends, with significant viscosity contrast between the components.

Such discrepancies motivated us to study viscoelastically asymmetric systems. Explicitly, the viscosity is related to the order parameter using an expression of the form $\eta(\psi) = \eta_0 + \eta_1(\psi_1(r) + \psi_3(r))$, where η_0 and η_1 are chosen as 1.0 and 100.0 respectively (this corresponds to a 100 fold difference in viscosities). In order to probe the effect of the viscosity contrast on the shear-induced changes in the structure factor, in Fig. 6.7a we display the normalized intensity at $q_x = 0$ for an asymmetric system under various applied shear rates. We notice a progressive increase in intensity with shear rate, at low values of q_y. This behavior is qualitatively consistent with the observations of Caputo and coworkers [17] displayed in Fig. 6.7b. However, Caputo et al., observe an increase in the peak intensity with applied shear, an effect not captured in our model even including the viscosity contrast.

Next, we display the second moment tensors and the normalized anisotropy and orientation angle for a viscoelastically asymmetric system in Figs. 6.8 and 6.9. Our results compare better with the experiments of Burghardt and

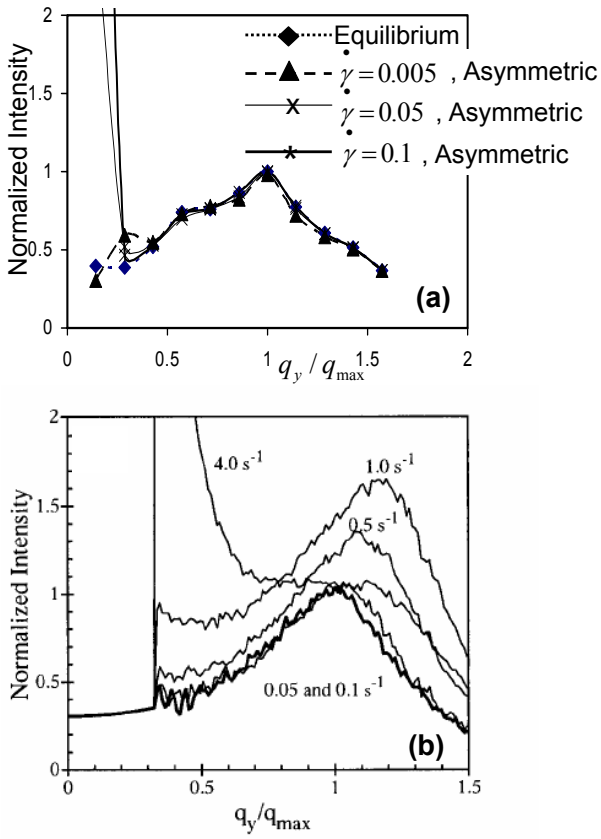

Figure 6.7: (a) Normalized intensity obtained from cell dynamics, at equilibrium and under shear rates indicated, for a viscoelastically asymmetric system; (b) Normalized intensity under shear for a PEE-PDMS ternary blend, adapted from [17].

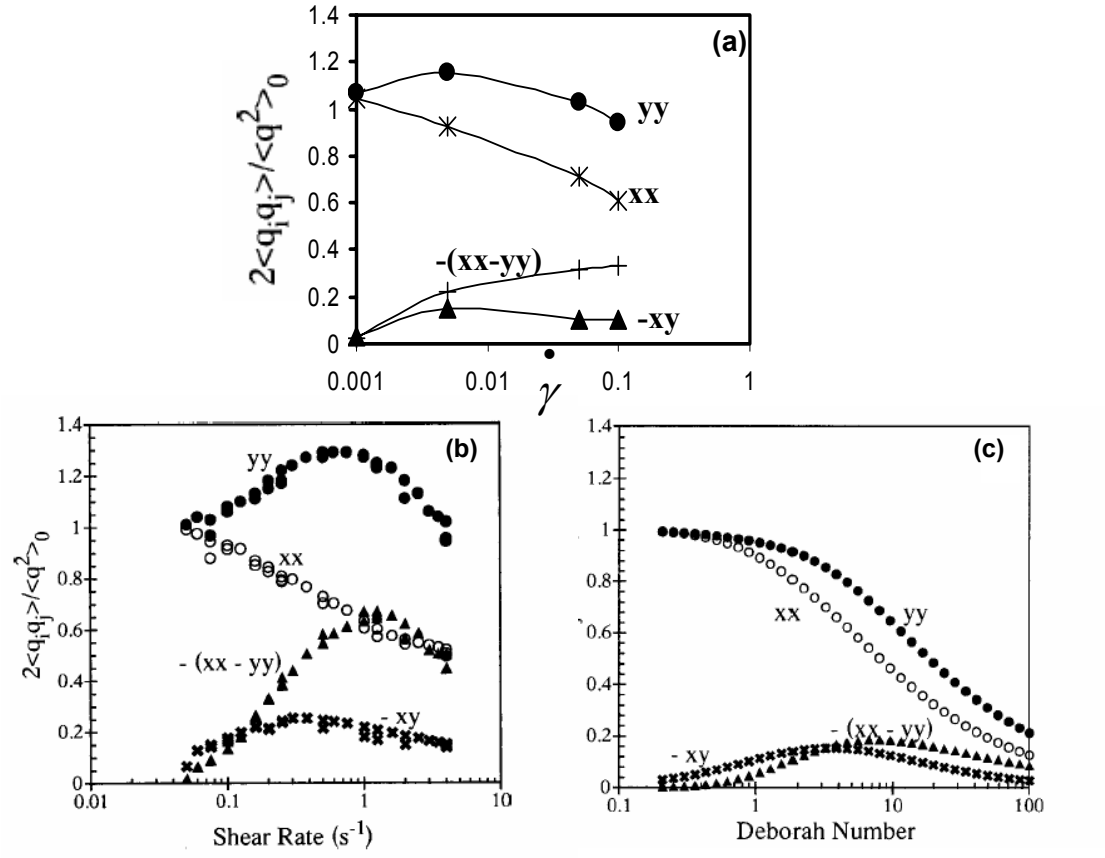

Figure 6.8: The structure factor weighted second moments displayed as a function of the shear rate, obtained from cell dynamics (for a viscoelastically *asymmetric* system) in (a) and the experimental and numerical scheme results of [17] in (b) & (c) respectively.

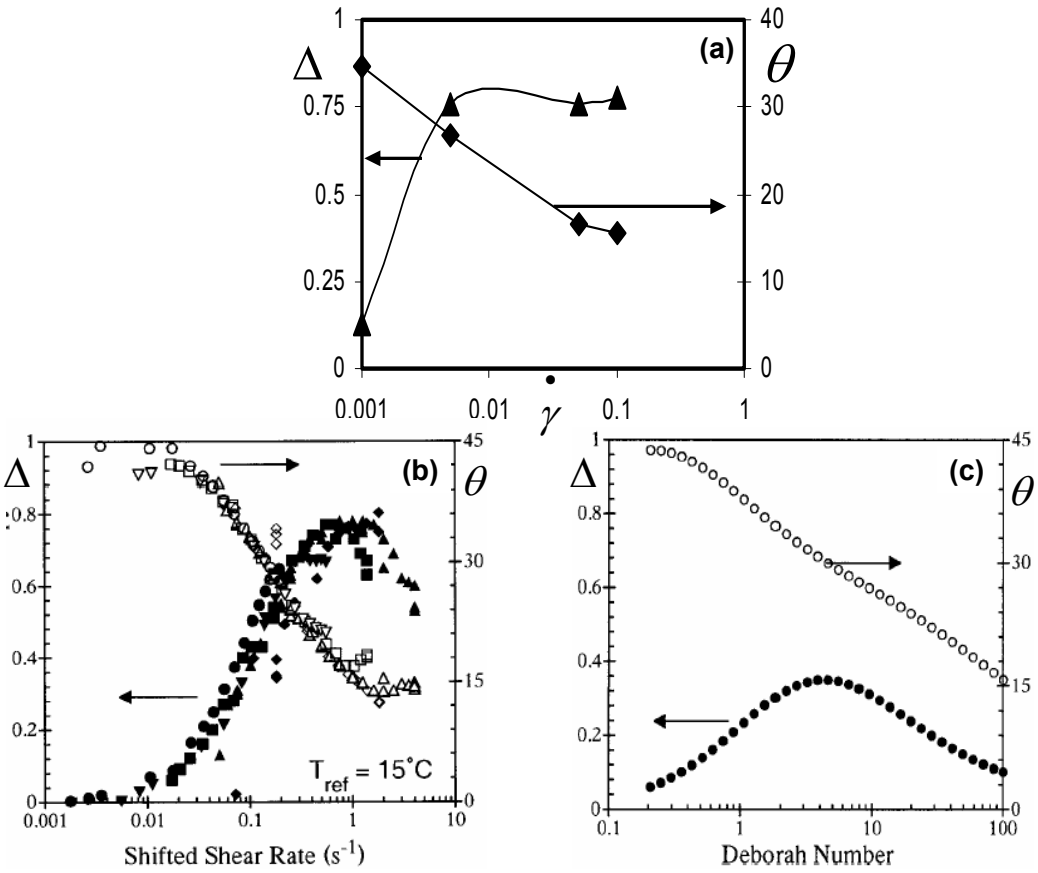

Figure 6.9: Normalized anisotropy Δ and orientation angle θ displayed as a function of shear rate, obtained from cell dynamics (for a viscoelastically *asymmetric* system) in (a) and the experimental and numerical scheme results of [17] in (b) & (c) respectively.

coworkers than the single parameter model. Owing to enhanced scattering in the asymmetric system, we capture the maxima in the yy component of the tensor, which is absent in the single parameter model. Although, we notice little difference between the symmetric and asymmetric system in their second moments, Δ and θ values, our results are in better quantitative agreement with the experiments.

In summary, we have probed features of the disordered state under shear in this section. We have studied the development of asymmetry in the disordered state structure factor under shear and quantified the asymmetry using second moment tensors, normalized anisotropy and orientation angle. We observe very good agreement with the experimental results of Burghardt and coworkers [17] except for a few discrepancies. We also find better quantitative agreement, showing significant improvement over the existing single parameter model of Patzold and Dawson [18].

6.5 Ordered System Results: Cell Dynamics

To probe the occurrence of shear-induced phase transitions, we have also studied shear-induced structural phase transitions in *ordered* ternary blend systems (slightly below ODT) using cell dynamics simulations. We have studied a range of homopolymer compositions (from $\phi^H = 0.68$ to $\phi^H = 0.8$), corresponding to near the Lifshitz point ($\phi^H \equiv 0.71$). To account for metastable states, we have followed two different protocols in probing shear effects in phase separated ternary blends. In the first protocol, we progressively increased the

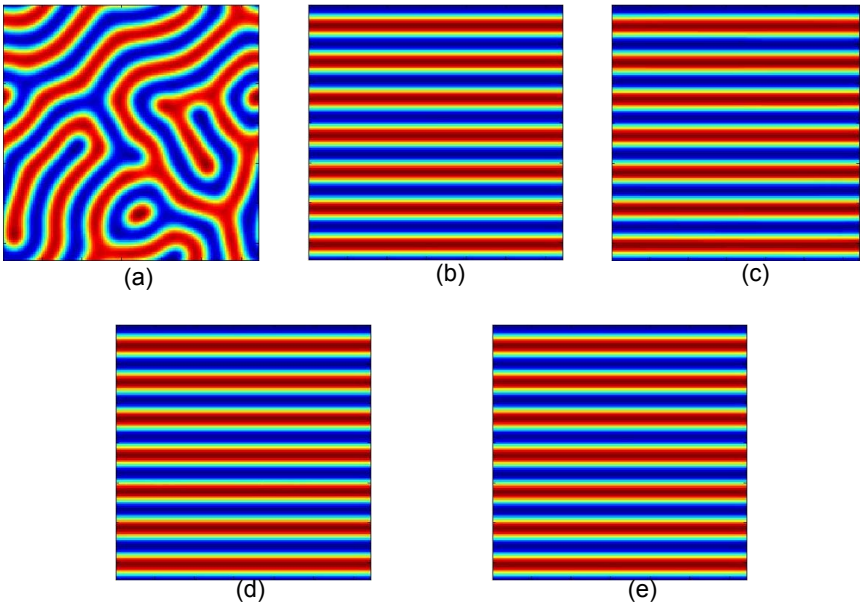

Figure 6.10: Two dimensional composition profiles obtained using the first protocol for a ternary blend with $\phi^H = 0.68$, at equilibrium in (a) and at four different shear rates of (b) $\dot{\gamma} = 0.001$; (c) $\dot{\gamma} = 0.005$; (d) $\dot{\gamma} = 0.05$ and (e) $\dot{\gamma} = 0.5$.

shear rates in small increments starting from equilibrium. In the second protocol, we applied the desired shear rate directly to the equilibrated system. In the following, we present our results obtained for both protocols for viscoelastically symmetric and asymmetric systems.

Figures 6.10, 6.11, 6.13 and 6.14 display the 2D composition profiles (with χN fixed at 6.8), obtained using the first protocol described above, for a range of homopolymer compositions indicated. Figure 6.10 displays the equilibrium and the shear composition profiles for four different shear rates as indicated for a system with $\phi^H = 0.68$ (corresponding to a homopolymer com-

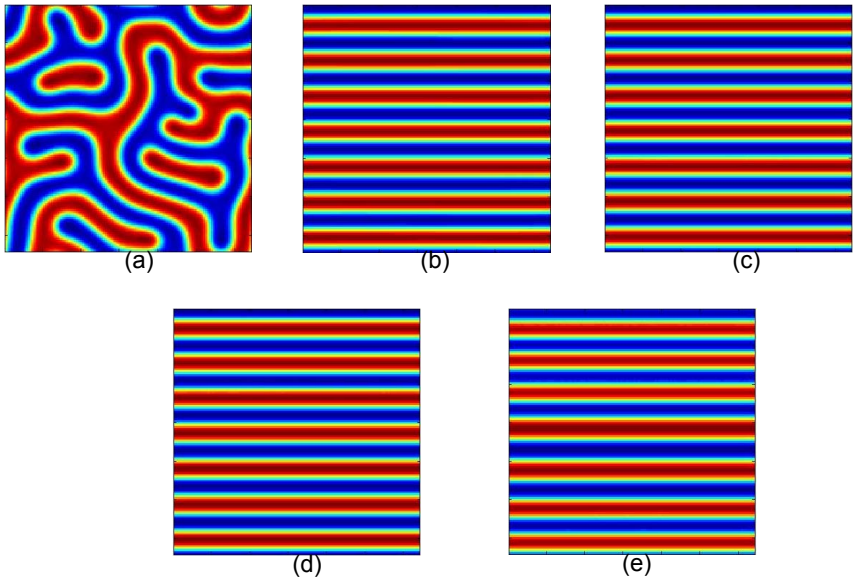

Figure 6.11: Two dimensional composition profiles obtained using the first protocol for a ternary blend with $\phi^H = 0.71$, at equilibrium in (a) and at four different shear rates of (b) $\dot{\gamma} = 0.001$; (c) $\dot{\gamma} = 0.005$; (d) $\dot{\gamma} = 0.05$ and (e) $\dot{\gamma} = 0.5$.

position below the Lifshitz point, where at equilibrium the system is predicted to be in the lamellar phase). We notice that under the application of the lowest shear rate, the system transforms into a lamellar structure, and this structure is retained upto a 500 fold increase in the shear rate from a value of $\dot{\gamma}$=0.001 to $\dot{\gamma}$=0.5. Figure 6.11 displays the composition profiles for the same set of shear rate conditions, for a system with $\phi^H = 0.71$ (corresponding to a homopolymer composition exactly at the Lifsitz point). We find similar composition profiles, with the system attaining an aligned lamellar structure which is retained as we increase shear rates in small increments. In order to verify the lamellar nature of the microstructure, we display (in Fig. 6.12) the composition profile of just the copolymer components in the system ($\equiv \psi_3 = \phi_A^C - \phi_B^C$), for $\phi^H = 0.68$ and 0.71 systems respectively. We notice that these block copolymer composition profiles are similar to the total composition profiles (Figs. 6.10e and 6.11e) at the same shear rate, confirming the existence of a copolymer dictated lamellar structure.

Next, we display the composition profiles under shear for systems with $\phi^H = 0.73$ and 0.77 (corresponding to a homopolymer compositions above the Lifshitz point) in Figs. 6.13 and 6.14 respectively. We notice that the system readily transitions into a macrophase separated system. Such a macrophase separated system is again seen to be retained for the entire range of shear rates. When we again consider just the copolymer compositions (at the highest shear rate of 0.5 for the two systems), in Figs. 6.12c & d, it is seen that the copolymers are concentrated mainly at the interfaces, with zero copoly-

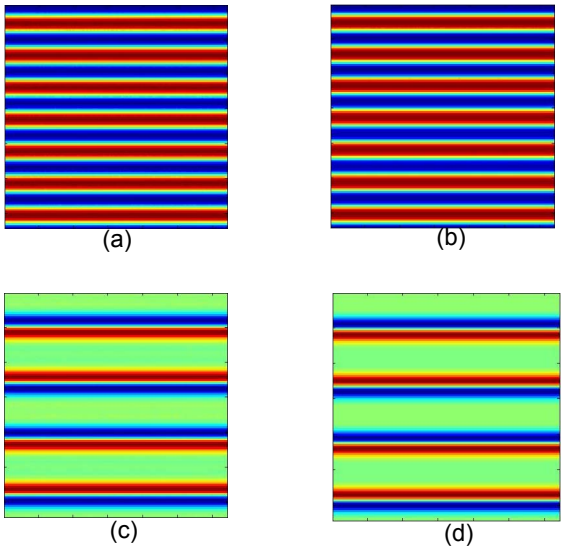

Figure 6.12: Two dimensional composition profiles (of just the copolymers) obtained using the first protocol for a shear rate $\dot{\gamma} = 0.5$ for a ternary blend with homopolymer composition of (a) $\phi^H = 0.68$; (b) $\phi^H = 0.71$; (c) $\phi^H = 0.73$ and (d) $\phi^H = 0.77$.

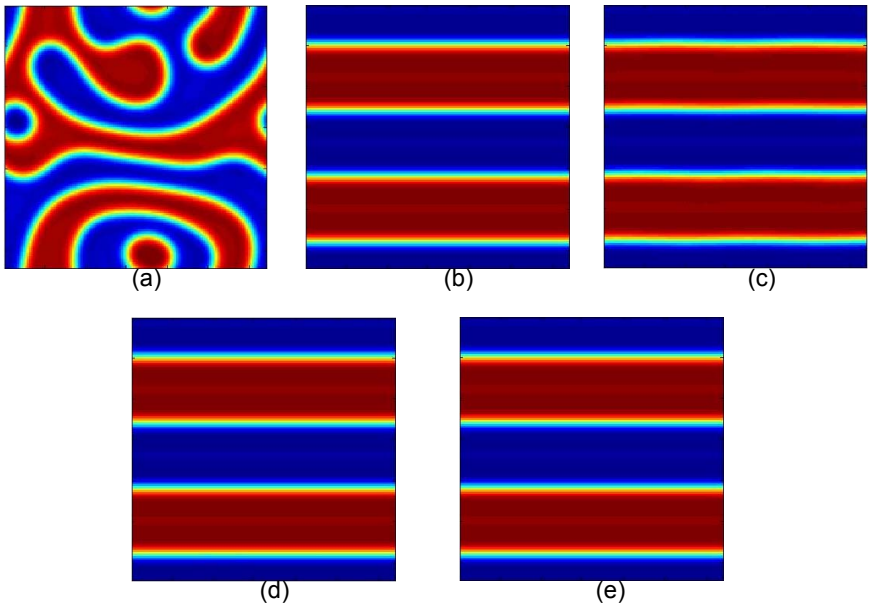

Figure 6.13: Two dimensional composition profiles obtained using the first protocol for a ternary blend with $\phi^H = 0.73$, at equilibrium in (a) and at four different shear rates of (b) $\dot{\gamma} = 0.001$; (c) $\dot{\gamma} = 0.005$; (d) $\dot{\gamma} = 0.05$ and (e) $\dot{\gamma} = 0.5$.

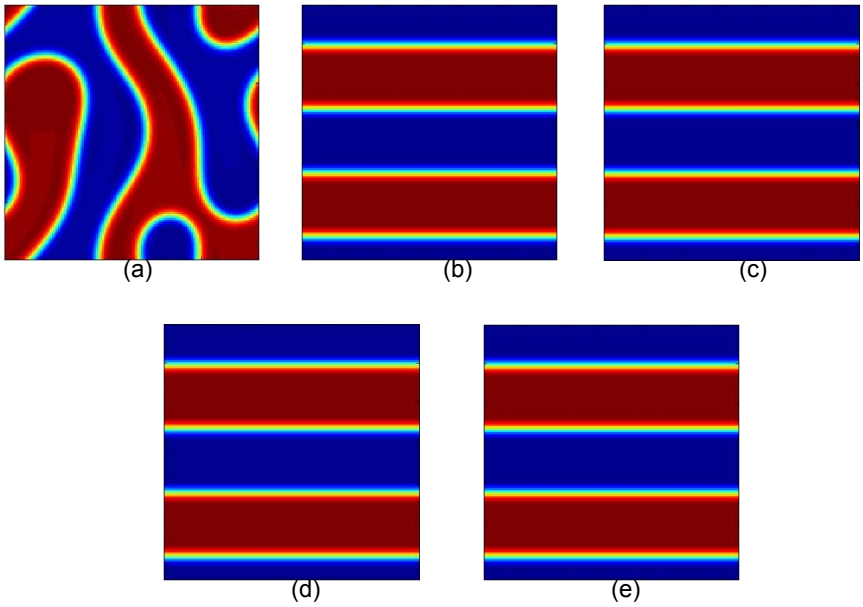

Figure 6.14: Two dimensional composition profiles obtained using the first protocol for a ternary blend with $\phi^H = 0.77$, at equilibrium in (a) and at four different shear rates of (b) $\dot{\gamma} = 0.001$; (c) $\dot{\gamma} = 0.005$; (d) $\dot{\gamma} = 0.05$ and (e) $\dot{\gamma} = 0.5$.

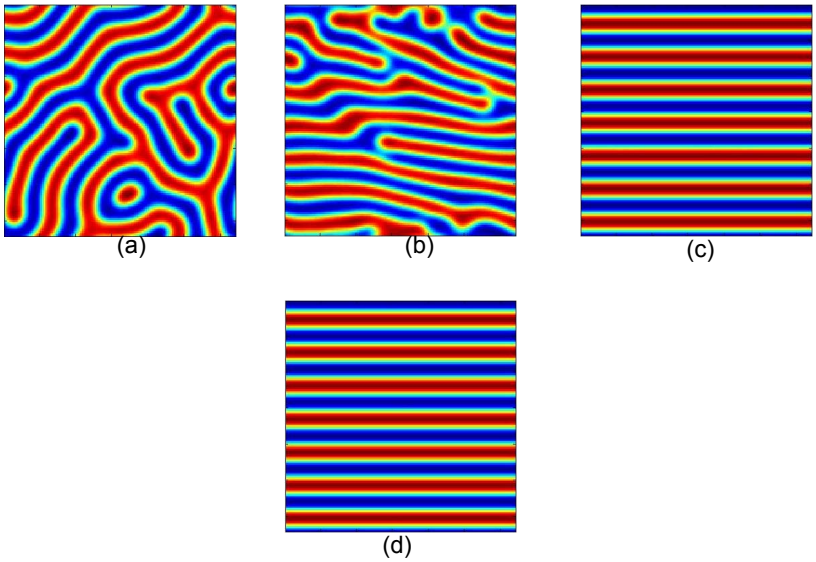

Figure 6.15: Two dimensional composition profiles obtained using the second protocol for a ternary blend with $\phi^H = 0.68$, at equilibrium in (a) and at three different shear rates of (b) $\dot{\gamma} = 0.001$; (c) $\dot{\gamma} = 0.005$ and (d) $\dot{\gamma} = 0.05$.

mer composition inside the bulk of the macrophase separated domains. This confirms the two phase nature of morphologies obtained under shear.

Now we display the results obtained using the second protocol, namely, by applying the final value of the shear rate directly to an equilibrated system. Figures 6.15 and 6.16 display the 2D composition profiles for the range of shear rates for the two systems below the Lifshitz point, with $\phi^H = 0.68$ and 0.71. For the $\phi^H = 0.68$ system, we notice that the defective lamellar structure at equilibrium (Fig. 6.15a) gives rise to modulated lamellar like structure (Fig. 6.15b) at the lowest shear rate of 0.001. However, at higher shear rates of 0.005 and 0.05, the system transitions to a perfectly aligned lamellar state

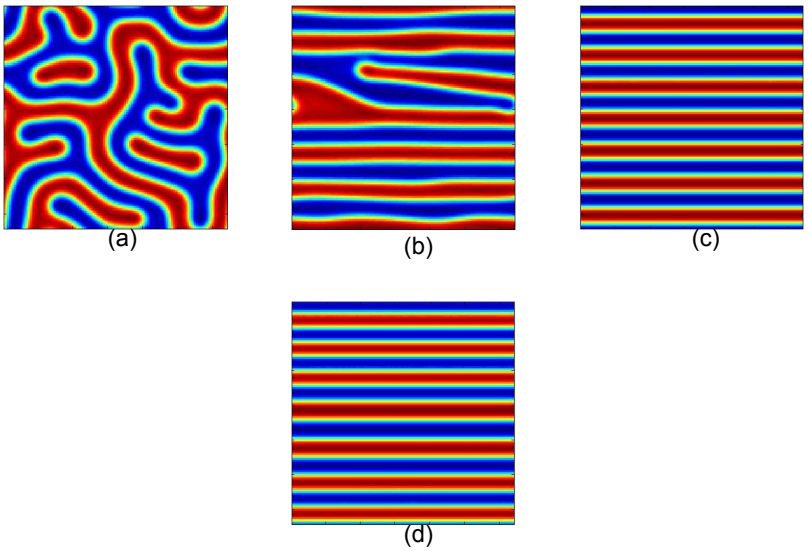

Figure 6.16: Two dimensional composition profiles obtained using the second protocol for a ternary blend with $\phi^H = 0.71$, at equilibrium in (a) and at three different shear rates of (b) $\dot{\gamma} = 0.001$; (c) $\dot{\gamma} = 0.005$ and (d) $\dot{\gamma} = 0.5$.

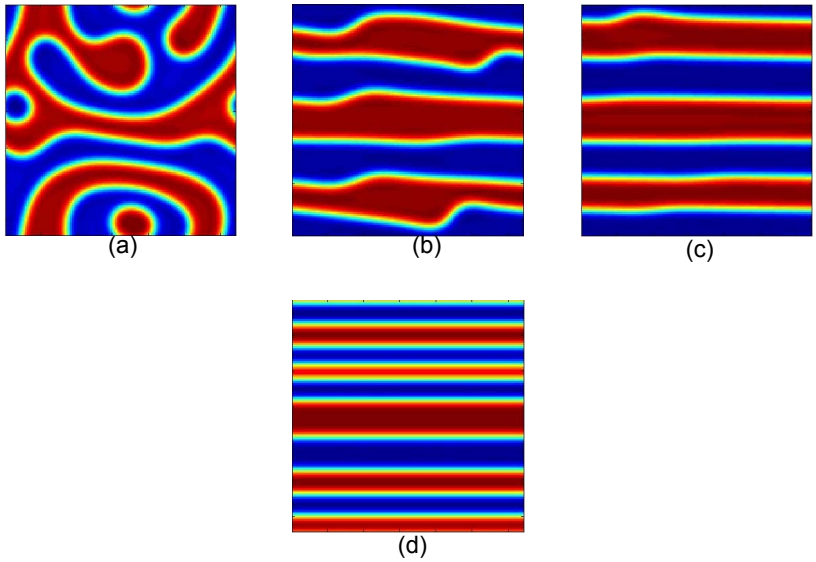

Figure 6.17: Two dimensional composition profiles obtained using the second protocol for a ternary blend with $\phi^H = 0.73$, at equilibrium in (a) and at three different shear rates of (b) $\dot{\gamma} = 0.001$; (c) $\dot{\gamma} = 0.005$ and (d) $\dot{\gamma} = 0.05$.

(Figs. 6.15c,d) similar to the microstructural patterns obtained using the first protocol (see Figs. 6.10). Similarly, the $\phi^H = 0.71$ system, which exists in a bicontinuous phase at equilibrium (Fig. 6.16a), transforms into a modulated lamellar type structure (Fig. 6.16b)at the low shear rate of 0.001, which in turn transforms into a well aligned lamellar like structure at high shear rates, akin to the structural patterns obtained using the first protocol. However, for the systems above the Lifhitz point, namely, $\phi^H = 0.73$ and 0.77, the composition profiles obtained using the second protocol are quite different from those obtained from the first protocol. Figure 6.17 displays the composition profile for system with $\phi^H = 0.73$, under the shear rates of 0.001, 0.005 and

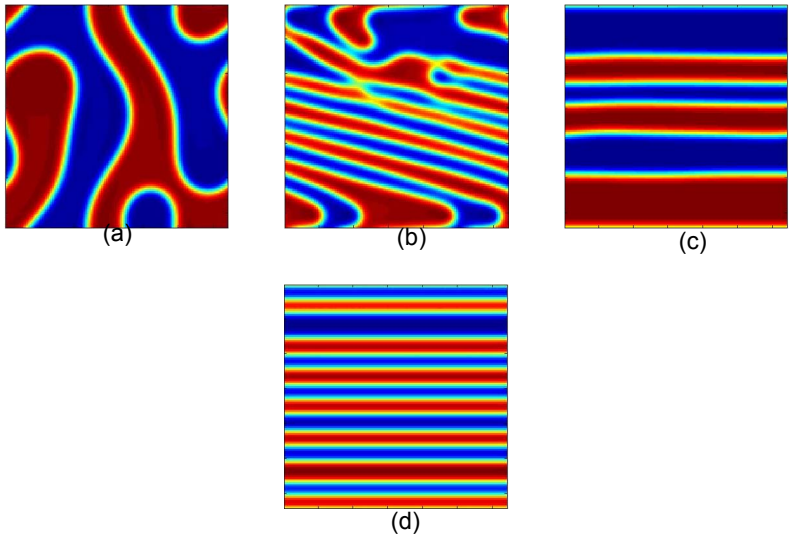

Figure 6.18: Two dimensional composition profiles obtained using the second protocol for a ternary blend with $\phi^H = 0.77$, at equilibrium in (a) and at three different shear rates of (b) $\dot{\gamma} = 0.001$; (c) $\dot{\gamma} = 0.005$ and (d) $\dot{\gamma} = 0.5$.

0.05, obtained by directly ramping up the shear rates to their final values. We notice that at the low shear rates of 0.001 and 0.005 (Figs. 6.17b,c) the system has lamellar type structure, with three lamellae. At the highest shear rate of 0.5 (Fig. 6.17d), there exists more lamellae in the system, with smaller lamellar thicknesses. Figure 6.18 plots similar composition profiles obtained for $\phi^H = 0.77$ system. At a low shear rate of 0.001, there exists partially aligned lamellae and at higher shear rates, the lamellae are completely aligned which show behaviors qualitatively similar to $\phi^H = 0.73$ system. The second protocol is seen to lead to more lamellar like phases above the Lifshitz point, in contradiction with the results obtained using the first protocol. This can be rationalized by noting that the direct application of shear to its final value

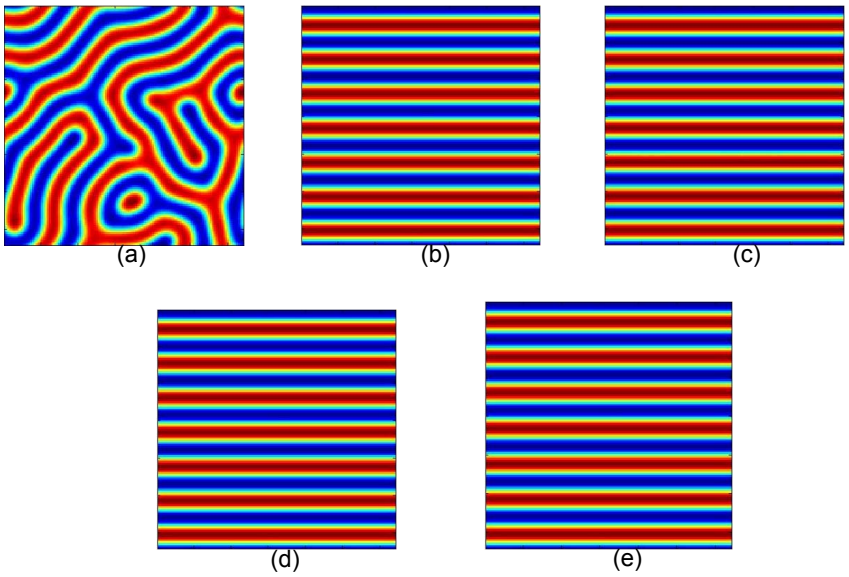

Figure 6.19: Two dimensional composition profiles obtained using the first protocol for a ternary blend (*with viscosity contrast*) with $\phi^H = 0.68$, at equilibrium in (a) and at four different shear rates of (b) $\dot{\gamma} = 0.001$; (c) $\dot{\gamma} = 0.005$; (d) $\dot{\gamma} = 0.05$ and (e) $\dot{\gamma} = 0.5$.

results in the likely formation of metastable lamellar phases which retain their structure. Such metastable structures have also been observed in the context of binary polymer blends, which have shown metastable string phases or sheet-like phases, under the application of very high shear rates.

We have also probed the effects of viscoelastic asymmetry and obtained identical results for composition profiles. Figures 6.19, 6.20, 6.21 and 6.22 display the 2D composition profiles obtained for various shear rates indicated, for the four different homopolymer compositions of $\phi^H = 0.68, 0.71, 0.73$ and 0.77. We can see that these plots are identical to the structural patterns of a

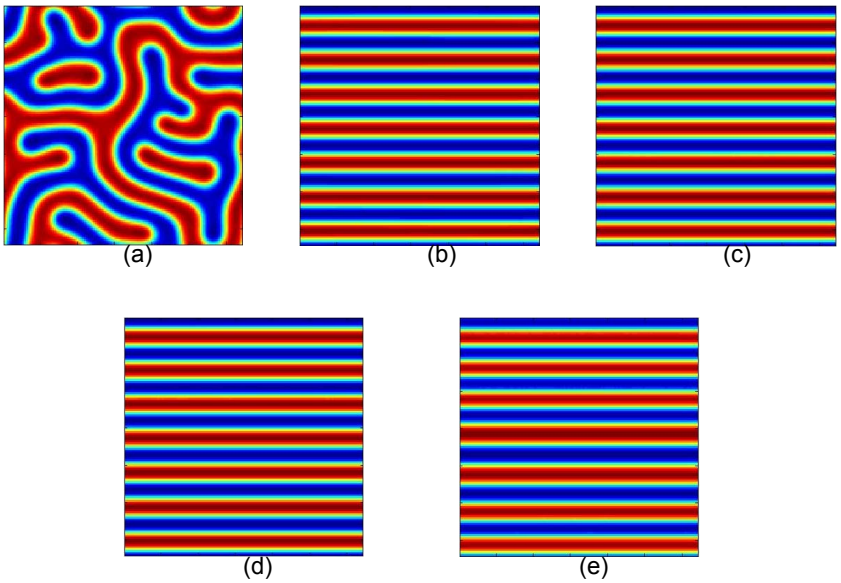

Figure 6.20: Two dimensional composition profiles obtained using the first protocol for a ternary blend (*with viscosity contrast*) with $\phi^H = 0.71$, at equilibrium in (a) and at four different shear rates of (b) $\dot{\gamma} = 0.001$; (c) $\dot{\gamma} = 0.005$; (d) $\dot{\gamma} = 0.05$ and (e) $\dot{\gamma} = 0.5$.

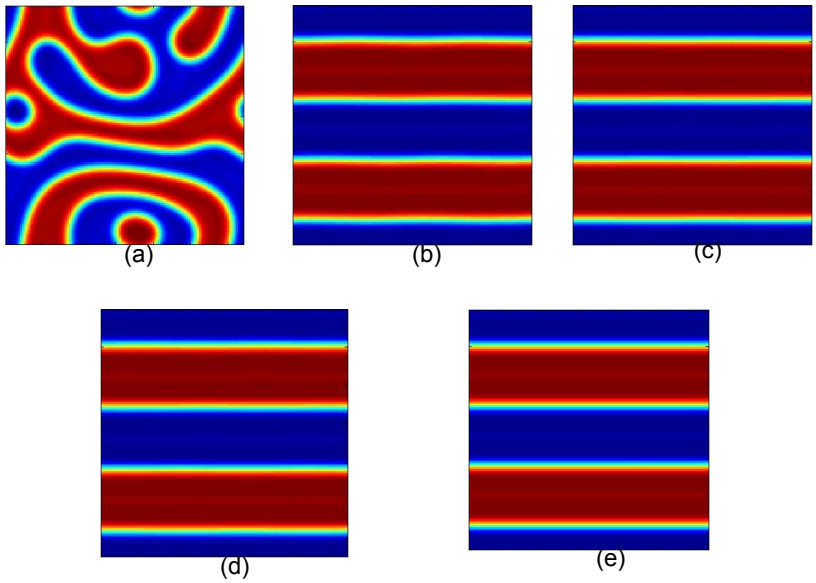

Figure 6.21: Two dimensional composition profiles obtained using the first protocol for a ternary blend (*with viscosity contrast*) with $\phi^H = 0.73$, at equilibrium in (a) and at four different shear rates of (b) $\dot{\gamma} = 0.001$; (c) $\dot{\gamma} = 0.005$; (d) $\dot{\gamma} = 0.05$ and (e) $\dot{\gamma} = 0.5$.

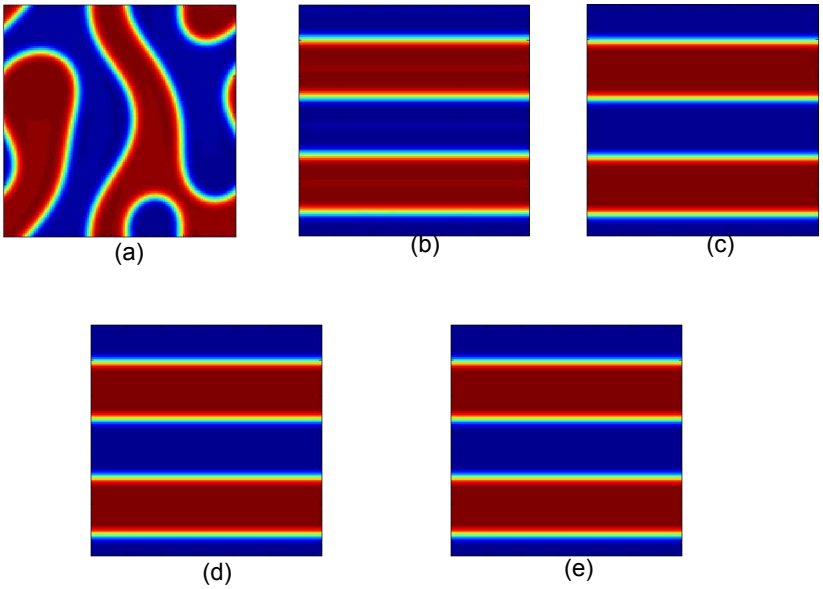

Figure 6.22: Two dimensional composition profiles obtained using the first protocol for a ternary blend (*with viscosity contrast*) with $\phi^H = 0.77$, at equilibrium in (a) and at four different shear rates of (b) $\dot{\gamma} = 0.001$; (c) $\dot{\gamma} = 0.005$; (d) $\dot{\gamma} = 0.05$ and (e) $\dot{\gamma} = 0.5$.

viscoelastically symmetric system.

From the above set of results we notice that the main effect of the applied shear is equivalent to an effective reduction in fluctuations leading to the mean-field solution, wherein the Lifshitz point demarcates the lamellar phase and the macrophase separated structure. *We found no evidence for progressive shear-induced phase separation into three phase coexistence and macrophase patterns observed in our earlier Brownian dynamics simulations. This suggests that under the model assumptions, just the pure effect of shear on composition field models can not rationalize the occurrence of shear-induced phase transitions.*

6.6 Summary and Conclusions

The shear-induced phase transitions and the rheological behavior observed by Krishnan and coworkers [17] in ternary polymer blend systems cannot be understood using existing models which primarily have been developed to describe flow behavior in oil-water-surfactant systems. In order to address such discrepancies, we have carried out a detailed analysis of the effect of composition fluctuations on the ordered and disordered phases of ternary polymer blends. For this purpose, we have developed a three order parameter model with a Leibler-type fourth order free energy expansion, which provides a more accurate description of a ternary blend system. We have employed a *cell dynamics* type numerical scheme to evolve the three order parameters. Such a numerical scheme has allowed us to study the dynamical phenomena in both

ordered and disordered phases of ternary blends.

The disordered phase structure factor results provided in section 6.4 agree qualitatively and in many cases, semi-quantitatively with the experimental observations. The structure factor results obtained for the viscoelastically asymmetric system provides better agreement with experiments than the single order parameter model of Patzold and Dawson [18]. Better quantitative agreement of the anisotropy factors and orientation angles with experiments were also obtained.

In ordered phase, we found no evidence of shear-induced phase transitions or instabilities. As mentioned before, the only effect of applied shear is seen to be an effective reduction of fluctuations leading to the mean-field solution, with lamellar phases being stabilized for homopolymer compositions below the Lifshitz point and a stable macrophase separated structure observed for homopolymer compositions above the Lifshitz point.

Some caveats need to be mentioned before concluding the inadequacies of composition models for predicting shear-induced phase transitions in ternary blends. Since (as described in chapter 5), microemulsion phases result from strong fluctuation effects, and proper treatment of fluctuations is needed in coarse-grained models [153]. Moreover, a true bicontinuous phase can only be obtained in a 3D system, requiring us to incorporate the compositional fluctuations in a three dimensional study (our study was 2D). Another possible reason for the failure of three parameter model in capturing shear-induced phase transition could be the need to include higher order terms in the free

energy expansion to accurately reflect suitable thermodynamic characteristics. Our future studies will examine these extensions.

Chapter 7

Rheology of Ordered Phases of Multiblock Copolymers

7.1 Introduction

Block copolymers typically exhibit exquisite nanoscale self-assembled patterns due to incompatibility between different blocks of the block copolymers [1, 154]. For instance, diblock copolymers with two chemically distinct segments can easily be tuned to attain cubic arrays of spheres of the minor phase dispersed in a matrix of the major phase, hexagonal arrays of cylinders of the minor phase, bicontinuous patterns or phase separated lamellar like structures depending on the relative lengths of the blocks [6, 41]. There is an active interest in engineering such microstructurally arranged systems to obtain tailor made materials for user specific applications.

A major hurdle in the successful realization of the above objective is that while periodicity of the structure is preserved in the short scales, it is usually difficult to obtain materials which exhibit long range order [30, 33]. Similar to a variety of other complex fluid systems such as liquid crystalline materials, colloidal crystals etc., owing to defects created from thermal and mechanical fluctuations, block copolymers are seldom found in a coherently ordered

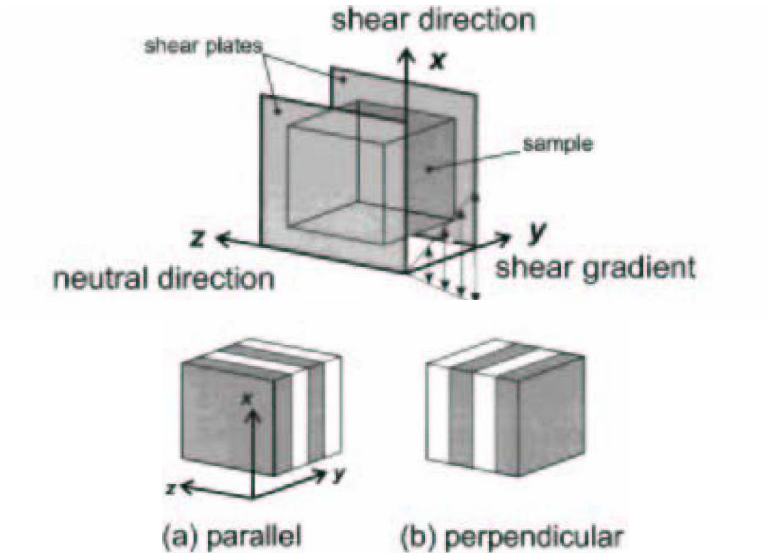

Figure 7.1: Schematic representing the (a) parallel and (b) perpendicular orientations of block copolymer lamellae under shear.

state. Unfortunately, experimental and theoretical investigations relating the morphology to the final properties (or structure-property relationships) are meaningful only in defect free systems that retain long-range order. Furthermore, such macroscopic order is also essential in various potential applications of block copolymers in biomaterials, optics and microelectronics.

Symmetry breaking fields, such as the external flow fields and electric fields have been explored as a possible route to induce macroscale order and alignment [10–12, 30, 33, 140, 155]. Over the last decade, flow processing of block copolymer melts has emerged as an efficient and inexpensive route to achieve alignment. Various forms of external flow fields have been investigated, including, extrusion [155], oscillatory and steady shear [10, 11, 30, 33],

extensional flow, roll-casting [156] etc. Although, application of external flow-field is promising in achieving long range order, many experiments have also witnessed a variety of intriguing *additional* effects of external flow on block copolymer morphology. One such effect is the shear induced order to disorder transition in symmetric block copolymers reported by Bates and coworkers [136], and has been rationalized by the theory of Cates and Milner [9]. Another effect which has sparked significant interest is the flow-induced changes in block copolymer orientation. Koppi and coworkers [10] were the first to observe a macroscale flip in ordering of block copolymer lamellae (PEP-*b*-PEE) from the parallel orientation configuration to a perpendicular orientation under the application of oscillatory shear. (Figure 7.1 displays the parallel and perpendicular orientations of the block copolymer lamellae. When the shear is applied in the x-direction and y the shear gradient direction, lamellae aligned in the xz-plane is said to be in the parallel orientation, whereas lamellae aligned in the xy-plane (vorticity plane) is said to be in the perpendicular orientation). Until Koppi's experiments, it was generally believed that parallel alignment of lamellae was the only orientation obtainable under reciprocating shear. These observations became more significant when an opposite trend was reported by Winey and coworkers [11, 12]in a different system. They found that polystyrene-polyisoprene (PS-PI) diblock lamella flips from an initial perpendicular orientation to a parallel orientation when shear frequency was increased. Later researches have also implicated the strain amplitude as another parameter in determining the orientation changes [159].

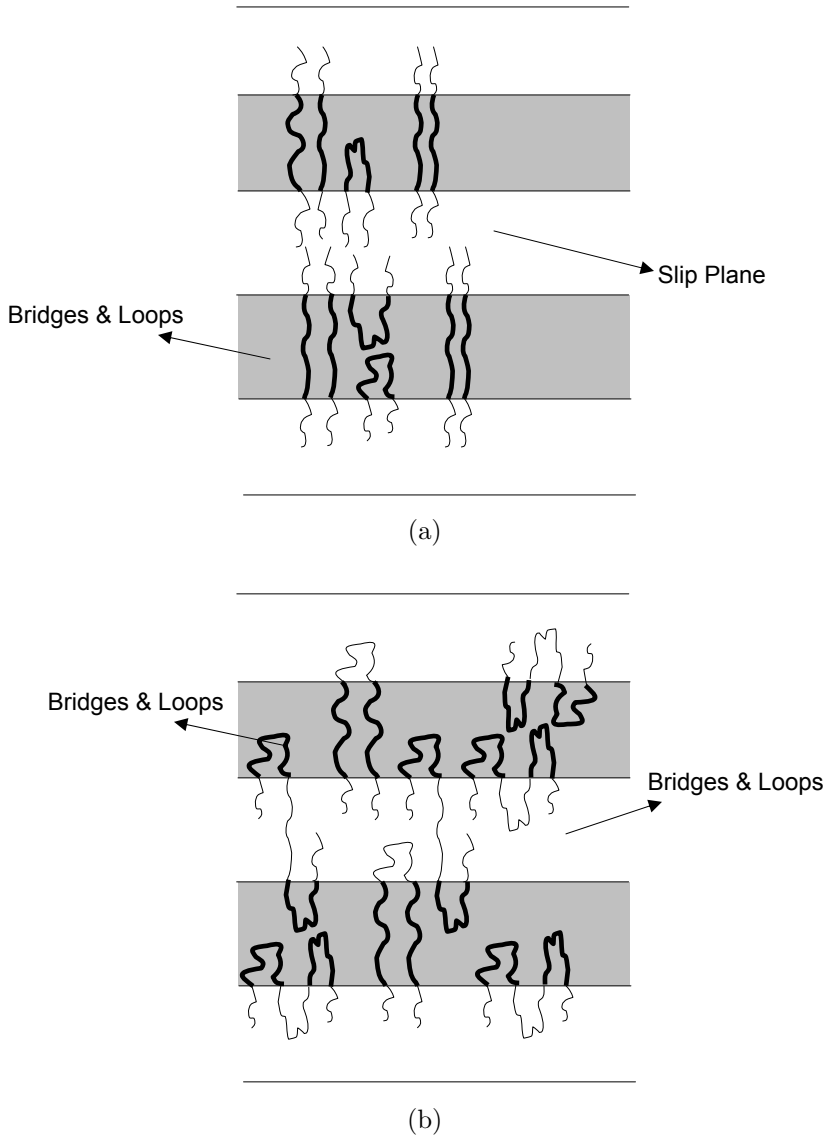

Figure 7.2: (a) Schematic of a *triblock* copolymer lamella displaying the alternate *bridges and loops* layer and *slip* layer; (b)Schematic of a *pentablock* copolymer lamella displaying the *bridges and loops* in every layer.

More recently, interest has expanded to the flow-induced microdomain alignment of multiblock copolymer architectures, such as triblock and pentablock copolymers [8, 34]. CEC triblock copolymers have been found to exhibit parallel orientations at either high frequencies or large strain amplitudes, while only perpendicular orientation has been found in CECEC pentablock copolymers (here C and E refer to polycyclohexylethylene and polyethylene respectively) [34]. A partial explanation of these effects have been provided by invoking the concept of slip planes. Figure 7.2a shows a schematic of lamellae in a triblock copolymer, with the bridges and loops layer and the alternate slip layer. The bridges present in multiblock copolymer layers resist deformation under shear. In contrast, the layers of lamellae formed by the end blocks of the triblock copolymer do not have any bridges and are more susceptible to slip (slip plane) and have correspondingly a lower viscosity than the layer with both bridges and loops [157]. The presence of slip planes in triblock copolymer were speculated to accommodate a larger fraction of the applied strain and hence permit alignment in parallel orientations. In contrast, as can be seen in Fig. 7.2b, longer multiblock copolymer like tetrablock, pentablock and heptablock copolymers, have bridges in every layer of the lamella. In such case one would expect an absence of *slip planes* rendering the perpendicular orientations favorable than parallel (as found in CECEC pentablock copolymers).

Recent experiments by Wu and coworkers [8] have added another degree of complexity to the problem. They have observed parallel orientation of macrodomains in the heptablock copolymer of SISISIS (where S is polystyrene

and I is polyisoprene). By delaminating in a selective solvent for isoprene blocks after alignment, they found higher fraction of looping conformations than bridges in the interior layers. These results suggest that by the application of carefully selected flow fields we can also *change* the chain conformations and hence select the orientations of the layers. We note that a simple toy model proposed by Gansean and Fredrickson [157] anticipates such flow-induced bridges to loop transitions.

On the theoretical side, while there have been several attempts at understanding the effect of reciprocating shear field on the lamellar orientation, though the exact process(es) leading to re-orientation has yet defied a complete understanding. A set of theories have focused on the relative stability (or lack thereof) under flow of lamellar structures [131, 133]. Small perturbations have been introduced into regular lamellar pattern to study the secondary stability of various orientations. Other studies have investigated the effect of thermal fluctuations near the order-disorder transition on a layered structure and their coupling to the shear field. Fredrickson [159] has investigated the suppression of fluctuations about the mean lamellar pattern by steady shear flows and found that parallel orientation is preferred for small shear rates while perpendicular alignment is found at large shear rates. He also incorporated the effect of different viscosities of the pure block components in the lamellae architecture. Viscosity contrast is found to affect the formation of parallel orientation from a perpendicular lamellae with decrease in temperature of the sample. The effect of such viscoelastic contrast rationalized some of the earlier dis-

crepancies in experimental observations. For instance, in relation to Winey's experiments [11, 12], Fredrickson and Bates [135] noted that PI is largely entangled while PS is not and they attributed the parallel orientation under high oscillatory shear frequency in PS-PI diblock melts to the viscoelastic contrast between the PS and PI blocks.

However, many unresolved questions still remain on the orientation selection of block copolymer lamellae. For instance, recent experiments by Wu and coworkers [8] have shown the existence of three frequency regimes in the orientation selection. They observed a parallel orientation in PS-PI system at low frequency, perpendicular orientation at intermediate frequencies and parallel orientation again at high frequencies. Theoretically, the existence of three such regimes of lamellar reorientation is not completely understood. Fraaije and coworkers have been able to capture the parallel to perpendicular reorientation, by considering the suppression of composition fluctuation by the reciprocating shear field. However, only speculative arguments exist to explain the latter regimes.

In this chapter we present our preliminary contributions in the study of the ordered phases of block copolymers layered under oscillatory shear. The current formalism of self-consistent Brownian dynamics is restricted to 2D, and we cannot directly observe the lamellar reorientations. Instead, we compute the orientation selection in an indirect manner, by making use of empirical evidence from numerous studies [8] correlating the lamellar orientation with the complex modulus $|G^*|$ $(=\sqrt{(G')^2 + (G'')^2})$. Many experiments have suggested

that the system chooses an orientation with the *lower value* of $|G^*|$ is selected. This could be physically understood by noting that the complex modulus $|G^*|$, comprises of an energetic contribution ($G^{'}$) as well as a dissipative component ($G^{''}$). While there exists no theoretical proof as to why the combination of $|G^*|$ is appropriate, heuristically a lower complex modulus system would correspond to a system with a lower combination of energetic and dissipation components.

In order to pursue the above framework, we adopt our self-consistent Brownian dynamics algorithm [54, 103] to study the rheological behavior of block copolymer lamellae. The first contribution of this study is the development of a novel way of incorporating self-consistent oscillatory shear velocity into the self-consistent Brownian dynamics simulations. Note that, our algorithm mainly pertained to polymeric systems under steady shear conditions. The manner in which oscillatory shear effects are accommodated was outlined in chapter 2, and is a new development of this research. The first part of the present chapter deals with the effects of viscoelastic contrast and the strain rate on the macroscopic rheology of diblock copolymer lamellar system. Though we cannot actually simulate a reorientation of the lamella from a parallel (perpendicular) to perpendicular (parallel) orientation, we make use of the above mentioned empirical criterion based on $|G^*|$ to comment on the effect of viscosity contrast on the frequency of the transition from a perpendicular to a parallel orientation. The latter part of the chapter elaborates the oscillatory shear rheology results for parallel and perpendicular orientations of di-, tri-

and penta- block copolymer blend, wherein again we comment on the role of chain conformations on the orientation selection.

7.1.1 Simulation Details

Our simulations for the case of diblock copolymer melt were performed inside a simulation box of size 6×6×6 (in R_g units) containing 8000 chains. Each chain was discretized into 20 beads, with 10 beads of type A and 10 beads of type B with $N_A = N_B$. All our simulations were performed with composition fields ranging in two spatial dimensions (x and y). The velocity field however was assumed to only have the x-component. The beads of the polymer chain were allowed execute Brownian motion in all three dimensions. The degree of incompatibility between unlike monomers, parametrized by $\chi(N_A + N_B)$, was set at a value of 20.0. Note that for a symmetric diblock copolymer $\chi(N_A + N_B) \geq 10.5$, corresponds to ordering into the lamellar phase. The center of mass positions for the chains were assigned randomly inside the simulation box. The connector vector lengths and orientations were also assigned randomly while ensuring that the springs are not stretched above the maximum extensibility of FENE springs. Random initial conditions were assigned for the potential fields w and π at all the lattice points. The inital condition for the velocity field was set by fixing the in-phase and out-of-phase velocity amplitudes to $\gamma_0 \omega y$ and 0.0 respectively. We also non-dimensionalize our simulation by expressing the length in the chain radius of gyration (R_g) units and expressing time in terms of the reciprocal of the friction coefficient,

ζ and setting the energy scale $k_BT = 1.0$.

In such a non-dimensionalized formulation, there exists four parameters in our simulations: the Flory interaction parameter between unlike monomers, χN ($N = N_A + N_B$); Γ_1 and Γ_2, the phenomenological mobilities for the evolution of the potential fields $w(r)$ and $\pi(r)$ respectively and ϵ, the phenomenological viscosity for the velocity field evolution (see equations (2.41), (2.42) and (2.45)). In our runs we used values of 0.05, 0.1 and 0.0016 for Γ_1, Γ_2 and ϵ respectively in the non-dimensionalized units discussed above. The timestep for Brownian dynamics evolution was chosen as 0.0025 and the lattice cell dimensions for coarse-graining was chosen to be $0.1R_g$ in the x and y directions. We have studied the block copolymer orientations for various values of strain amplitudes γ_o and shear frequencies ω. The shear frequencies have ranged from $1.0/\tau_R$ to $10.0/\tau_R$, whereas the strain amplitudes was set at a value of 0.5. Here τ_R is the Rouse relaxation time of the block copolymer chain.

The convergence criterion for *equilibrium simulations* was the convergence of composition profiles. In case of oscillatory shear, the convergences of compositions profile and the simultaneous convergences of the in-phase and out-of-phase velocity amplitudes were used to obtain results. Their convergences were assumed to be achieved when there was less than 5% change in the composition and the velocity amplitudes for two consecutive block averagings performed over an interval of $5\tau_R$. The simulations were performed for a further period of $20\tau_R$ after convergence to sample the desired quantities. The computational time for our runs took an average of around 60 hours in a

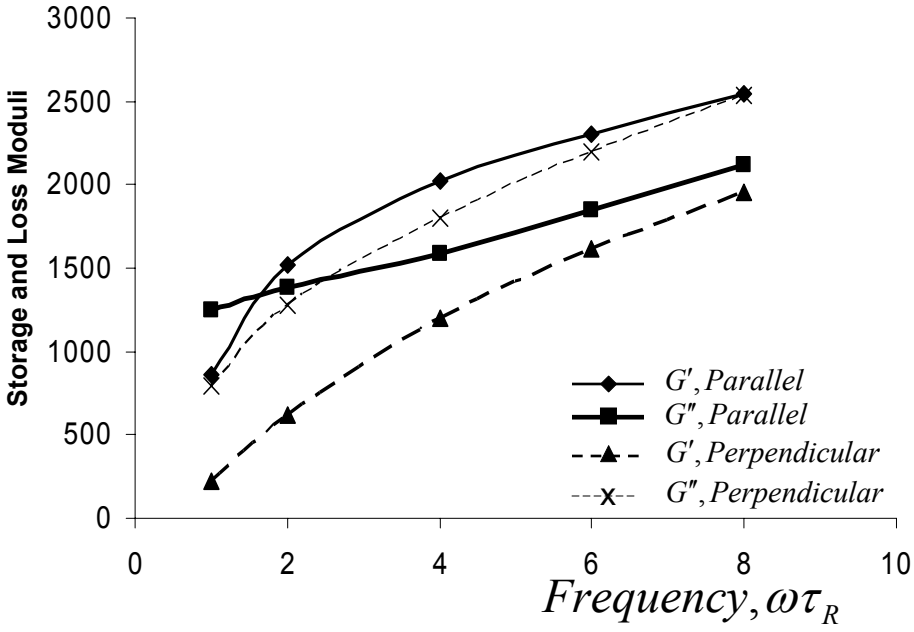

Figure 7.3: Storage($G^{'}$) and loss ($G^{''}$) moduli as a function of oscillatory shear frequency, for lamellae oriented in parallel and perpendicular directions.

single 2.5 GHz processor system.

7.2 Oscillatory Shear Rheology of Diblock Copolymer Lamellar: Role of Viscoelastic Asymmetry

We study the oscillatory shear rheology in block copolymer systems in two sections. In this section, we focus on the effect of viscoelastic asymmetry between the different blocks of the copolymer on the resulting rheological response. In Fig. 7.3 we display the loss ($G^{''}$) and storage ($G^{'}$) moduli of both

parallel and perpendicular lamella, for a viscoelastically symmetric system ($\beta = 1.0$). We observe that in the parallel orientation, for higher frequencies, the storage modulus is higher than that of the loss modulus. This behavior can be rationalized by noting that, in the parallel orientation, the chains localized are the lamellar interfaces and are oriented perpendicular to the layers. Hence, the viscous contribution mainly arises from the overlap between layers (which is small) compared to the elastic contribution (arising from the non overlapping parts of the chain) [160]. In contrast, for the perpendicular orientation, the loss modulus is seen to be greater than the storage modulus for the entire range of frequencies. This can be understood by noting that in the perpendicular configuration, the system resembles a simple homopolymer melt in the plane of shear and hence exhibits Rouse like viscous characteristic with $G^{''} > G^{'}$ [40]. Such frequency dependence of the moduli have also been observed in the experiments of Bates and coworkers [8] for a PS-PI block copolymer system.

In Figs. 7.4a, b, c & d, we display the frequency dependence of storage and loss moduli for a parallel and perpendicularly oriented systems for four different contrast in viscoelasticity (β represents the ratio of bare viscosities of different blocks). By comparing these figures we notice that the qualitative behavior of the different moduli, noted in the previous paragraph, remain unchanged even with the incorporation of viscoelastic asymmetries. However, the absolute magnitudes of the moduli is seen to increase with an increase in the degree of viscoelastic asymmetry, a feature easily rationalized by noting that

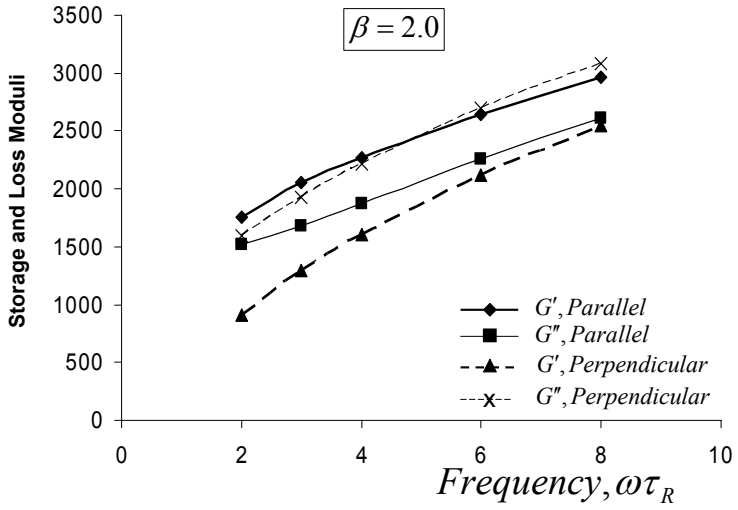
$\beta = 2.0$
Storage and Loss Moduli
3500
3000
2500
2000
1500
1000
500
0
0
2
4
6
8
10
$Frequency, \omega\tau_R$
$G', Parallel$
$G'', Parallel$
$G', Perpendicular$
$G'', Perpendicular$

(a)

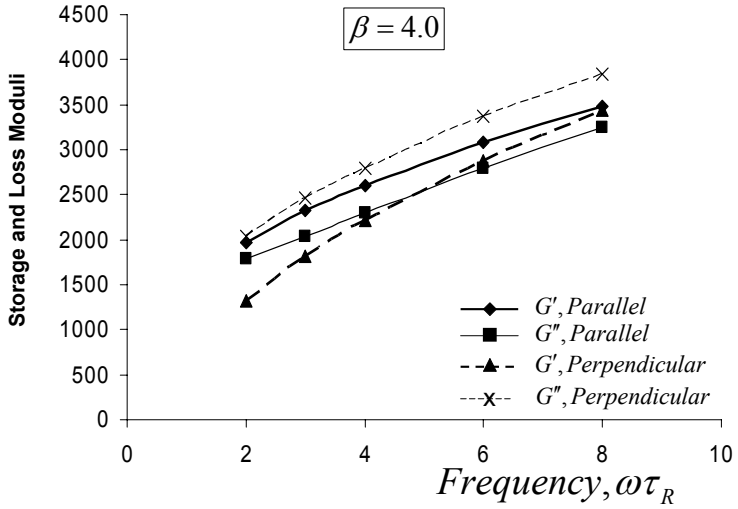
$\beta = 4.0$
Storage and Loss Moduli
4500
4000
3500
3000
2500
2000
1500
1000
500
0
0
2
4
6
8
10
$Frequency, \omega\tau_R$
$G', Parallel$
$G'', Parallel$
$G', Perpendicular$
$G'', Perpendicular$

(b)

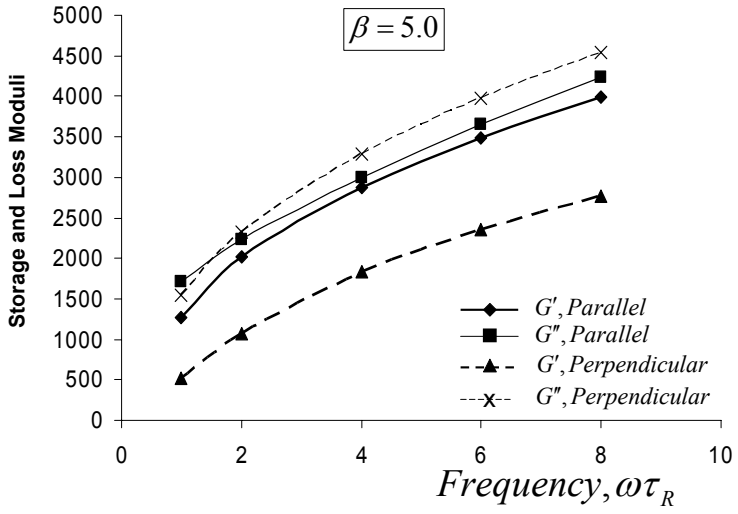

(c)

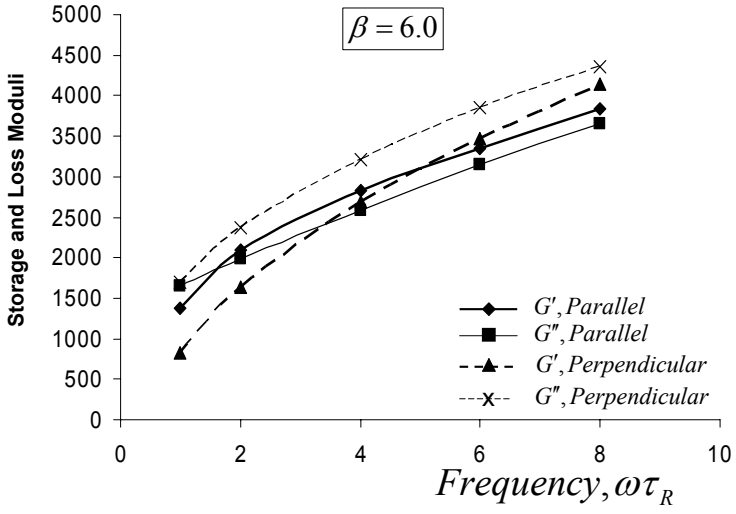

(d)

Figure 7.4: Storage($G^{'}$) and loss ($G^{''}$) moduli as a function of oscillatory shear frequency, for lamellae oriented in parallel and perpendicular directions, for four different viscoelastic asymmetries characterized by (a) $\beta = 2.0$; (b) $\beta = 4.0$; (c) $\beta = 5.0$ and (d) $\beta = 6.0$.

increase in β increases the relaxation time τ of the polymer and correspondingly the low frequency responses of both the storage and loss moduli is also enhanced. Moreover, on closer observation, we notice that both the storage and loss moduli of the perpendicular system increase by a greater extent with increase in viscoelastic asymmetry, compared to that of the parallel system. The latter can be understood by noting that the parallel configuration allows a inhomogeneous chain localization on the lower viscosity plane and hence the effective moduli is less enhanced compared to perpendicular configuration [148, 157].

In order to obtain more information on the effect of viscoelastic asymmetry on rheological behavior of parallel and perpendicular systems, we compute the complex modulus $|G^*|$ $(=\sqrt{(G')^2 + (G'')^2})$, of both the systems for the range of viscoelastic asymmetries (see Fig. 7.5). From Figs. 7.5a, b, & c, we observe that in accordance with the storage and loss moduli, the complex modulus values show a quantitative increase with increase in asymmetry β. We notice that, for the $\beta = 1$ case, the complex modulus for the parallel orientation is higher than that of the perpendicular orientation for all values of the frequencies studied. However, for all values of $\beta > 1$, there exists a crossover frequency over which the complex modulus of the perpendicular system becomes higher than that of the parallel system. We have denoted this crossover frequency by ω_c. Further, we notice from Figs. 7.5a, b & c, that this crossover happens at lower frequencies with increase in asymmetry, with ω_c decreasing monotonically with increase in the viscoelastic asymmetry β. This behavior

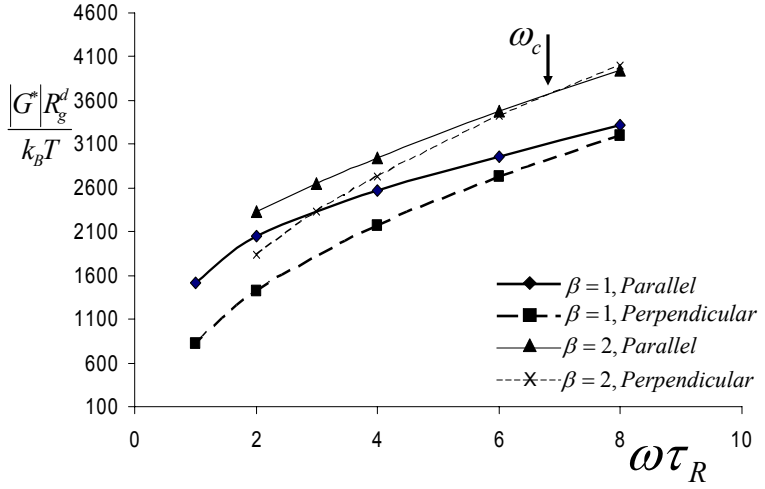
4600
4100
3600
3100
2600
2100
1600
1100
600
100
0
2
4
6
8
10
$\frac{|G^*|R_g^d}{k_BT}$
ω_c
$\omega\tau_R$
$\beta = 1, Parallel$
$\beta = 1, Perpendicular$
$\beta = 2, Parallel$
$\beta = 2, Perpendicular$

(a)

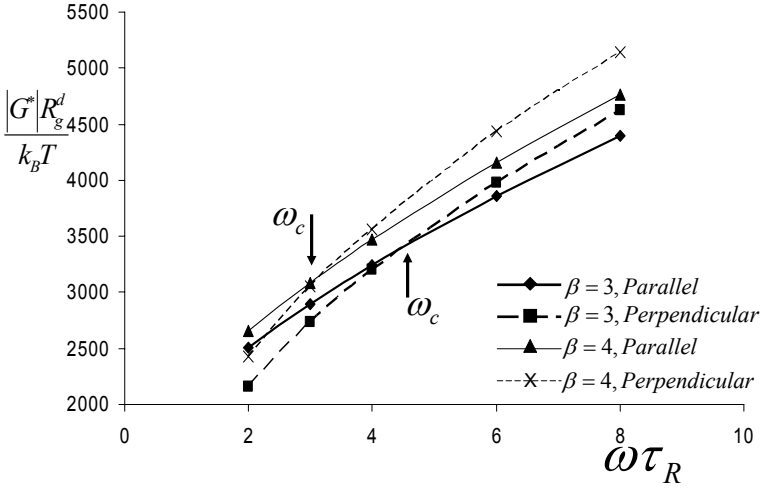
5500
5000
4500
4000
3500
3000
2500
2000
0
2
4
6
8
10
$\frac{|G^*|R_g^d}{k_BT}$
ω_c
ω_c
$\omega\tau_R$
$\beta = 3, Parallel$
$\beta = 3, Perpendicular$
$\beta = 4, Parallel$
$\beta = 4, Perpendicular$

(b)

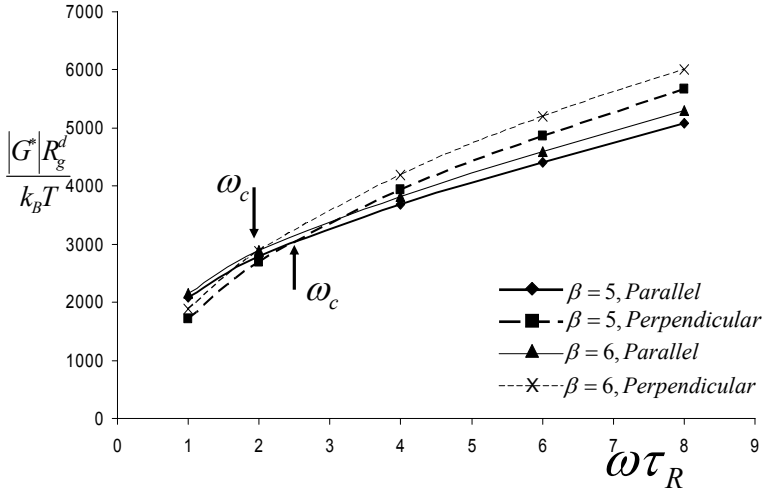

(c)

Figure 7.5: Complex modulus for parallel and perpendicular orientations of lamellae as a function of frequency, comparing three different viscoelastic asymmetries, (a) $\beta = 1.0$ & $\beta = 2.0$; (b) $\beta = 3.0$ & $\beta = 4.0$; (c) $\beta = 5.0$ & $\beta = 6.0$. Here, ω_c is the crossover frequency defined in the text.

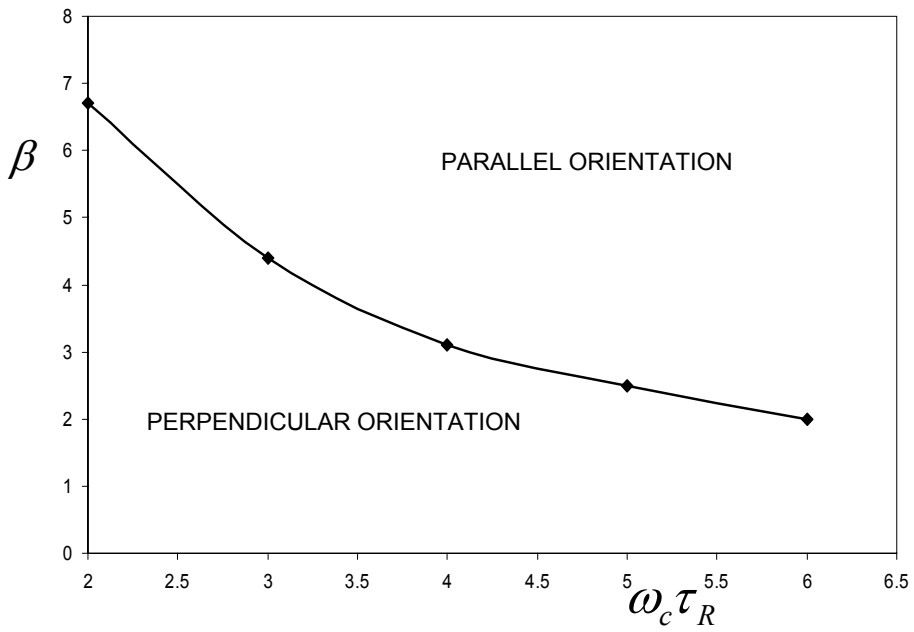

Figure 7.6: Phase diagram for parallel and perpendicular orientation selection as a function of viscoelastic asymmetry β and crossover frequency ω_c.

is displayed explicitly in Fig. 7.6.

As mentioned earlier, various experimental research on block copolymer lamellae reorientation under oscillatory shear have provided empirical evidence showing that the crossover frequency (ω_c) in complex modulus is roughly the frequency at which the lamellae reorient themselves. Based on this, we can determine the orientation phase diagram in the scale of crossover frequency ω_c and viscoelastic asymmetry β. From Fig. 7.6 we observe that the parallel orientation is preferred for systems with higher viscoelastic asymmetry between

the components, in contrast, for more rheologically symmetric system, the perpendicular orientation is preferred. This result corresponds very well with the experimental research of [8], wherein the high viscoelastic contrast between the PS and PI components were speculated to give rise to predominantly parallel orientations.

In summary, we have quantified the oscillatory shear rheology in parallel and perpendicular systems in this section. We have studied the effect of viscoelastic asymmetry on the storage, loss and complex modulus and their dependence on frequency for both orientations. To our knowledge this is first study of the effect of microscopic quantities such as the individual component viscosities on the macroscopic rheological properties of the system. Further, we have used an empirical criterion to obtain an approximate copolymer reorientation phase diagram. However, three dimensional simulations of these systems (currently underway), would enable us to actually visualize the orientational phase transition and determine the accuracy of this empirical phase diagram.

7.3 Oscillatory Shear Rheology: Multiblock Copolymers

In this section, we focus on the oscillatory shear rheology of symmetric di-, tri-, and penta-block copolymer lamellar system but restrict our considerations to systems which do not exhibit any contrast in the individual component mobilities (*i.e.* $\beta = 1.0$). Although, various experimental researches have shown that the different chain architectures in multiblock copolymer lamellae

exhibit a rich variety of flow phenomena [10–12, 30], there has been little numerical or theoretical research addressing the fundamental question, namely, "What is the role of chain architecture in the macroscopic rheological properties in lamellar systems?". Our main contribution in this section is to address this question by drawing a comparison between the oscillatory shear rheology of di-, tri- and penta-block copolymer lamellae. As in the previous section, we effect this comparison in both parallel and perpendicular lamellar systems.

In Fig. 7.7 we display the storage modulus and loss modulus for a parallel oriented di-, tri- and penta-block copolymer system. For parallel orientations, it is seen that at low frequencies $G''_{di} > G''_{tri} > G''_{penta}$, whereas, $G'_{di} < G'_{tri} < G'_{penta}$. These differences can be rationalized by noting that the pentablock has bridges and loops in all layers (elastic & viscous components), and diblock copolymer has only viscous components. Hence the elastic (viscous) components of *pentablock* $>$ ($<$) *triblock* $>$ ($<$) *diblock*. At high frequency, response of all chains are expected to be predominantly elastic. In such a case, $G'_{penta} > G'_{tri} > G'_{di}$, due to the higher elasticity of bridges (which act as crosslinks). Consistent with this, the viscous responses are seen to asymptotically approach each other at high frequency.

Despite the fact that we did not observe direct rheological effects from bridge to loop conversions, such conversions do occur in our system. To demonstrate this, we computed the time averaged number distribution based on the distance between links in tri- and penta-block copolymer lamellar systems. Figure 7.8 displays the number of successive links N_{link} with a distance d be-

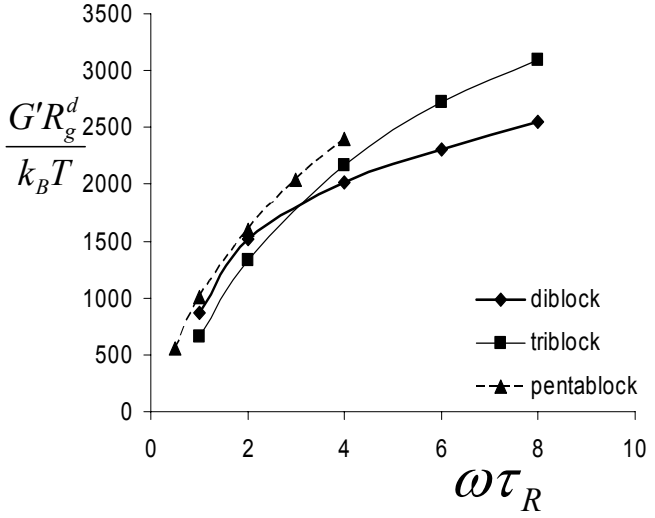

(a)

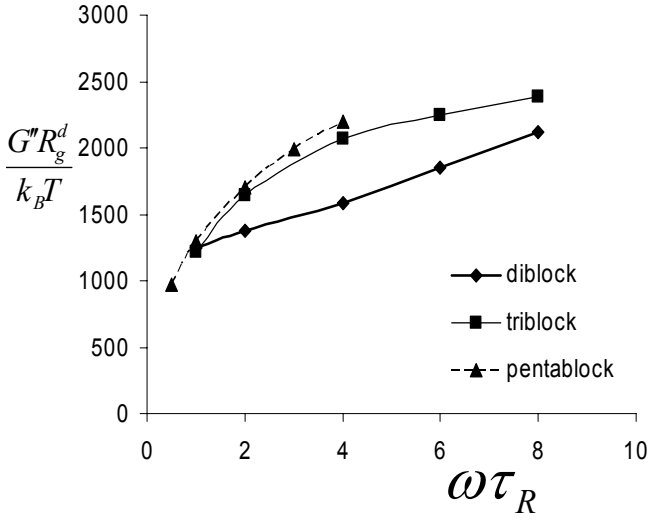

(b)

Figure 7.7: (a) Storage modulus of viscoelastically symmetric, di-, tri- and penta-block copolymer as a function of frequency. (b) Loss modulus of viscoelastically symmetric, di-, tri- and penta-block copolymer as a function of frequency.

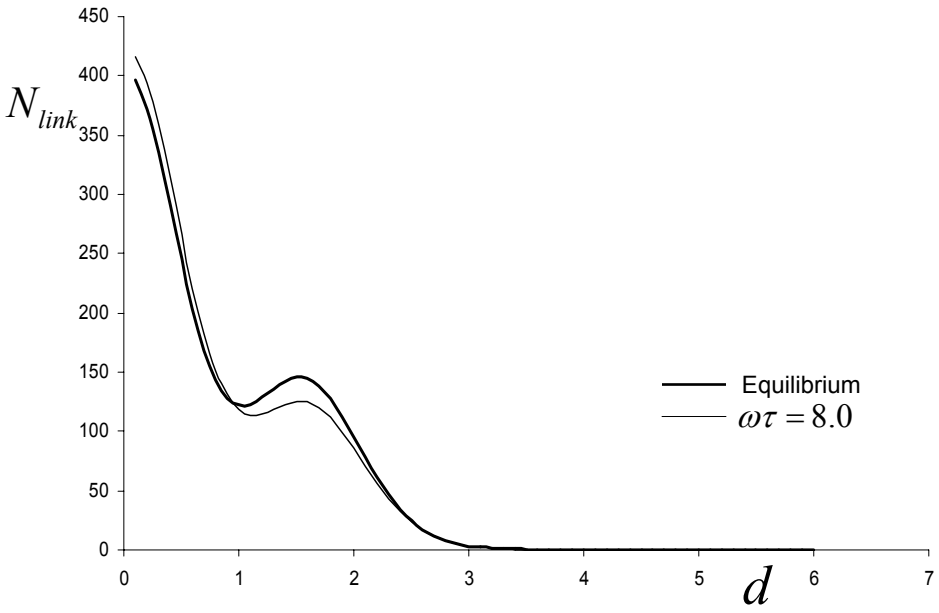

Figure 7.8: Time averaged link distribution as a function of the distance between the links, for a pentablock copolymer system oriented in the parallel direction, at equilibrium (thick line) and under shear with $\omega\tau = 8.0$ (thin line).

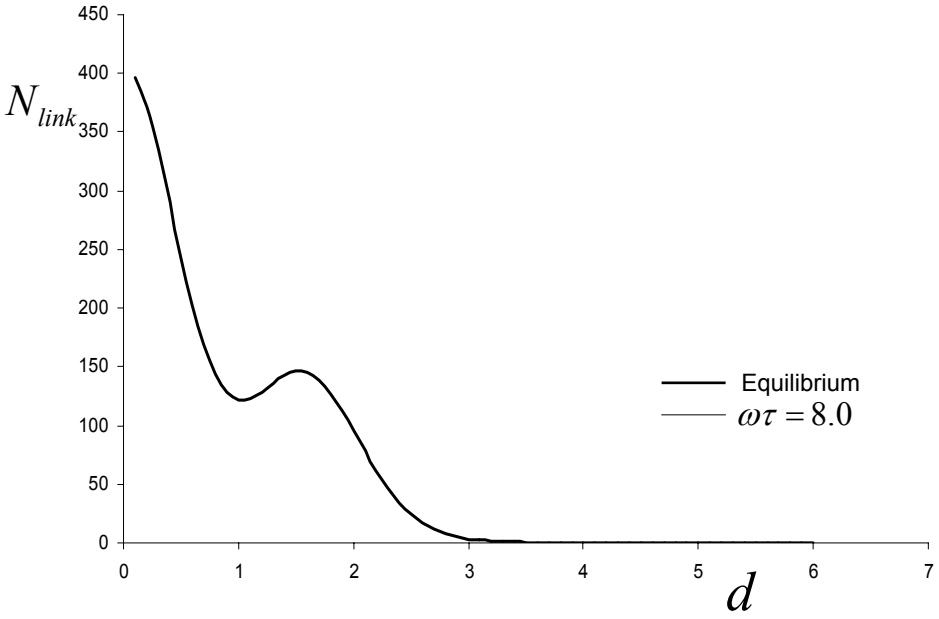

Figure 7.9: Time averaged link distribution as a function of the distance between the links, for a pentablock copolymer system oriented in the perpendicular direction, at equilibrium (thick line) and under shear with $\omega\tau = 8.0$ (thin line, coincides with the thick line).

tween them in a pentablock copolymer system at equilibrium and under shear with $\omega\tau = 8.0$. The peak near $d = 0$, corresponding to the number of successive links with almost zero distance between them, corresponds to the loop configuration. As expected, we observe that under the application of oscillatory shear, there is an enhanced number of loops at the cost of bridges. This provides direct evidence for bridge to loop transitions under shear. In contrast, we do not see any bridge to loop transition in a perpendicular lamella (see Fig. 7.9).

In Fig. 7.10, we display the complex moduli of the di-, tri- and pentablock copolymer systems in parallel and perpendicular orientations. In the previous section, we determined the crossover frequency (corresponding to the perpendicular to parallel reorientation) in the diblock system (for $\beta = 1$) to be around 10. In contrast, we note that these complex moduli values for both triblock and pentablock copolymer systems diverge with increasing frequencies. This suggests that the perpendicular orientation is preferred for triblock and pentablock copolymer lamellar systems for the entire range of frequencies we have examined. This is in very good agreement with the experimental results of Bates and coworkers [8]. They have observed the persistence of perpendicular orientation in both triblock (SIS) and pentablock copolymers (SISIS), for wide ranges of both frequencies and strain amplitudes.

In this section, we have been able to quantify the effect of chain architecture on their macroscopic rheological behavior. Our contribution in this section includes, quantifying the effect of chain architecture (loops and bridges)

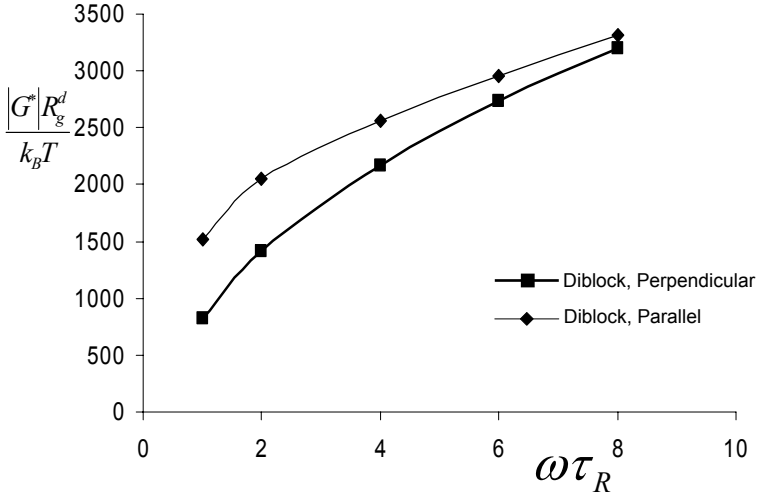
3500
3000
2500
2000
1500
1000
500
0
0
2
4
6
8
10
$\frac{|G^*|R_g^d}{k_BT}$
$\omega\tau_R$
Diblock, Perpendicular
Diblock, Parallel

(a)

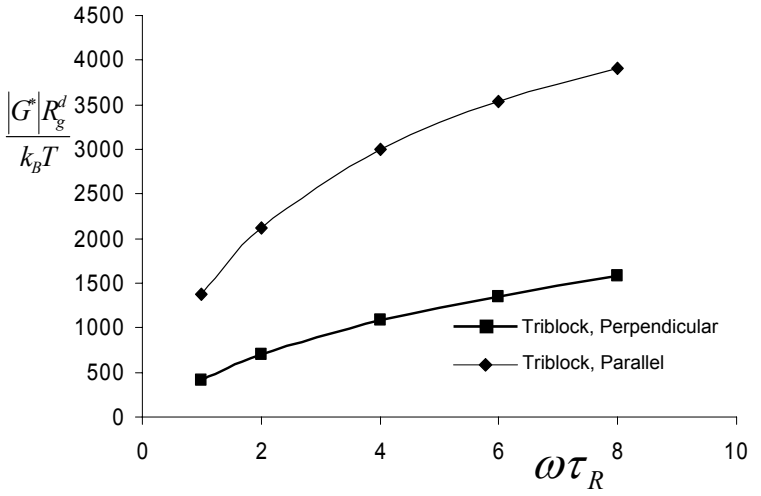
4500
4000
3500
3000
2500
2000
1500
1000
500
0
0
2
4
6
8
10
$\frac{|G^*|R_g^d}{k_BT}$
$\omega\tau_R$
Triblock, Perpendicular
Triblock, Parallel

(b)

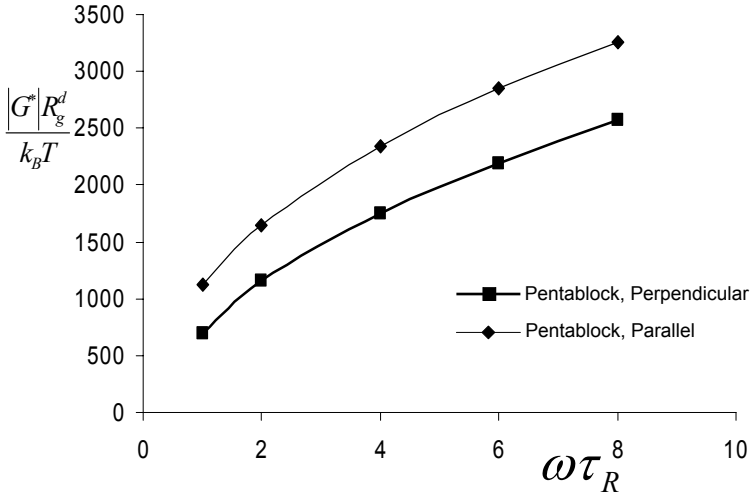

(c)

Figure 7.10: Complex modulus as a function of frequency for parallel and perpendicular orientations of (a) diblock (b) triblock and (c) pentablock copolymer systems.

on the oscillatory shear rheology (loss and storage moduli, shear thinning viscosity). Moreover, we provide an approximate prediction for the preferred orientation of the lamellar phases. Further research is required to study both these effects in detail. We also computed the bridge to loop transition as a function of the strain amplitude and frequency. This data could be used in the development of constitutive equations that could accurately predict the non-linear rheological behavior in multiblock copolymer systems.

7.4 Summary and Conclusions

Numerous unanswered questions remain in the context of rheology of copolymer lamellar phases and the orientations selected under oscillatory shear. Theoretical predictions on the role of viscoelasticity and viscoelastic asymmetry on rheology of ordered phases do not exist. Also, theoretical predictions for shear-induced lamellar reorientation phenomena remain incomplete. Our first contribution in this research is the refinement of the existing self-consistent Brownian dynamics simulation approach (which has been used to study steady shear phenomena) by incorporating the capability to study oscillatory shear in a novel way.

We employed the above approach to compare the oscillatory shear rheology of viscoelastically symmetric and asymmetric diblock copolymer lamellae. In this context, we further compared the rheology of both parallel and perpendicular orientations of the lamellar system. Moreover, by using the values of the complex modulus of the systems oriented in parallel and perpen-

dicular directions, we have been able to provide approximate predictions for perpendicular to parallel reorientation with increase in frequency. Our results show qualitative agreements with experiments.

We also studied the effect of chain architecture on the oscillatory shear rheology of lamellar systems (parallel and perpendicular). Specifically, we effected a rheological comparison of di-, tri- and penta-block copolymer. Rheological differences observed in these three systems have been rationalized using the chain conformations (as loops and bridges). For instance, there are no loops and bridges in a diblock copolymer lamella, while every alternate layer consists of loop and bridge architectures in a triblock, and every layer of a pentablock copolymer comprises of both loops and bridge conformations. Further, we also capture the bridge to loop transition of the chains under oscillatory shear.

We have presented a rich variety of oscillatory shear phenomena in multiblock copolymer systems. Our contributions in this chapter opens up the possibility for further numerical research that would help us gain a better understanding of their complex rheology. Possible future research should include a three dimensional investigation of the flow-behavior which could directly visualize the lamellar reorientation phenomena. Further research quantifying the bridge to loop transition under flow is also required. This would help us understand the rheological behavior and also let us manipulate the material properties by fine-tuning the chain conformations.

Chapter 8

Summary and Future Directions

8.1 Summary and Conclusions

This chapter summarizes the contributions of the research detailed in this dissertation. The later part of the chapter provides recommendations for future work in understanding dynamical phenomena in multicomponent polymeric systems. The contributions of this doctoral research can primarily be categorized into two parts, namely, (a) Development of a hybrid, multiscale approach to address dynamical phenomena in multicomponent polymeric systems (viz. Self-Consistent Brownian Dynamics Approach) (b) Application of the above approach to study various multicomponent polymeric systems. The flow chart below shows the various systems studied and the issues addresses. In the following, a summary of all the contributions is provided.

A novel simulation approach, termed self-consistent Brownian dynamics [54, 103], was developed, which combined Brownian dynamics simulations with polymer self-consistent field theory and continuum mechanics. Such a procedure enables us to capture the viscoelastic effects within the framework of a coarse-grained simulation approach. Owing to the high computational costs involved in atomistic computer simulations of dense polymeric systems

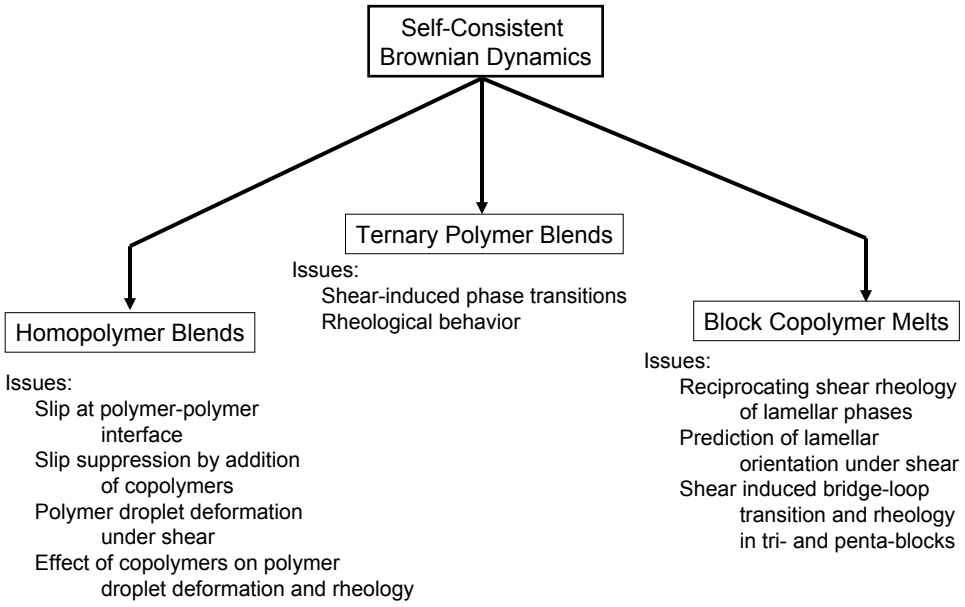

Figure 8.1: A chart depicting the main contributions and issues addressed in the thesis.

[13, 14], many researchers have turned to coarse-grained formalisms to model a polymer chain and employ, *particle-based*, mesoscopic models, including molecular dynamics (MD), Monte Carlo (MC) and Brownian dynamics (BD) [69]. Despite the successes of these techniques in the context of homogeneous systems, they still remain quite expensive to simulate inhomogeneous systems that exhibit nanoscale or macroscale phase separation. In contrast, due to the hybrid framework adopted, the self-consistent Brownian dynamics algorithm results in the speeding up of simulations by orders of magnitude, which makes it ideally suitable to study situations involving dense phases.

Our first approach addressed the interfacial slip phenomena at polymer-polymer interfaces [67, 68, 103]. Many experiments have pointed to blends of immiscible polymers with a very high degree of immiscibility exhibiting anomalously low viscosities. This lowering of viscosity has been attributed to the slip at the interface of the polymeric blend. Slip phenomena is a direct result of a sharp composition gradient at the thin interface, the size of which is comparable to the molecular size. Using self-consistent Brownian dynamics, we have been able to capture the effects of such composition gradients on the velocity field, allowing us to quantify this slip phenomena. We have quantified the interfacial slip by considering both symmetric (in terms of molecular lengths and friction coefficients or mobilities) as well as asymmetric polymer blends. We have studied the interfacial slip as a function of the degree of immiscibility between the two homopolymers and effected a quantitative comparison with the existing theories predicting slip.

Next, we studied the suppression of slip by the addition of block copolymers to the polymer blend [59, 72, 73, 103]. Block copolymers are known to position themselves at the interface of the polymer blend, thereby reducing the interfacial slip. However, to our knowledge, this reduction in slip has never been directly visualized in experiments. By employing the self-consistent Brownian dynamics approach, we have provided a molecular scale visualization of the slip suppression phenomena by block copolymers at the interface. Moreover, we have quantified the slip suppression as a function of the physical characteristics of the block copolymer, such as the length and the coverage of the copolymers at the interface.

Within the context of polymer blends, we next focused on polymer droplet deformation under shear [161]. Droplet deformation under steady shear has been well understood for Newtonian fluids [93, 94, 113]. However, many issues in viscoelastic droplet deformation and the effect of copolymer compatibilizers on such features are unresolved [72, 116–118, 161]. Despite the comparatively small size of our droplets and the 2-D nature of our simulations, our results agree semi-quantitatively with the asymptotic predictions for the droplet deformations. We also presented results elucidating the influence of block compatibilizers upon the droplet deformations. Our results suggest that even trace fractions of compatibilizers can lead to significant changes in the flow fields around the droplets and their deformation characteristics. We studied the influences of the molecular weight of the block copolymer and the coverage of block copolymers upon the deformation and rheological properties

of polymer droplets.

Recently, Burghardt and coworkers [17, 130, 132, 146], observed a novel phenomena in ternary polymer blends formed using poly(ethyl ethylene) (PEE), poly(dimethyl siloxane) (PDMS) and PEE-PDMS block copolymer. They noticed a series of shear induced phase transitions from an equilibrium bicontinuous microemulsion phase. They have also reported novel rheological behavior exhibited by such bicontinuous structures under shear flow. In the context of ternary polymer blends, we used SCBD to study the shear-induced phase transitions and their effect on the bulk rheology of the system. Our results match qualitatively with the experimental observations and suggests that flow transforms the microemulsion phases into a lamellar like phase and into a three-phase coexistence (of a lamellar-phase coexisting with phase separated homopolymer phases) at strong shears followed by a macrophase separation of the homopolymers at even stronger shear flows. These transitions are also accompanied by a strong shear-thinning behavior in the rheological response. The results suggest significant differences between shear effects on bicontinuous phases of ternary polymeric systems and microemulsion phases of oil-water-surfactant systems, which we rationalized from a molecular viewpoint.

Independently, we also studied the shear induced phase transition in ternary blend system using a Landau-Ginzburg type model [151]. We developed a fourth order free energy expansion with three order parameters. This method was shown to capture the structure of disordered phase under shear better than the available models, but it did not entirely capture the shear-

induced phase transitions.

Finally, we studied the dynamical phenomena in block copolymer melts aligned as lamellae. We have studied the oscillatory shear rheology and the effect of shear frequency and viscosity contrast of different blocks on the lamellar orientation. In the context of multiblock copolymers, we have compared the oscillatory shear rheology of lamellae formed by di-, tri- and penta-block copolymers. The results were rationalized using the polymer chain conformations (bridges and loops) in these systems. We have further observed the shear-induced transition in polymer chain conformation from a *bridge* conformation to a *loop* conformation under oscillatory shear in multiblock copolymer systems.

In conclusion, we have addressed an array of dynamical phenomena in a variety of multicomponent polymeric systems, typically inaccessible by traditional theoretical and modeling approaches [39, 40, 50]. Our multiscale, hybrid approach towards studying the aforementioned systems, has provided valuable insights into the molecular scale phenomena and their correlation to the macroscale properties. However, there still exists a wide range of applications, that are fertile grounds for exploration. The following section provides some possible directions for future research.

8.2 Recommendations for Future Work

The ambitious goal in the theoretical study of multicomponent polymeric systems would be the development of continuum models that couple

polymer thermodynamics and rheology, while incorporating means to predict phenomena unique to inhomogeneous polymeric systems. In order to achieve this goal, we need to gain a better understanding of fundamental issues in polymeric systems and use this knowledge to bolster the existing kinetic theory models and phenomenological approaches, making way for a unified theory coupling thermodynamics and rheology in multicomponent systems. Having this goal in mind, there still remains plenty of intriguing dynamical phenomena yet to be addressed. The rest of this section provides an outline of the possible future directions in developing our simulation approach (SCBD) and identifies some phenomena that could be addressed in the context of multicomponent polymeric systems.

8.2.1 Entanglements

The self-consistent Brownian dynamics approach (elaborated in chapter 2) [54, 103], has been used extensively in this research to address various dynamical phenomena in polymeric systems. We have mainly used simple Rouse and FENE (Finitely Extensible Non-linear Elastic) models to describe a polymer chain in SCBD. However, these models do not incorporate topological constraints such as entanglements typically seen in polymeric systems [40, 65, 71]. One of the first improvements to the algorithm would be the incorporation of better single chain models that can accurately capture dynamical behavior in polymeric systems. For instance, the slip link model developed by Schieber and coworkers [162] can incorporate the essentials of the tube model

for reptation in entangled systems.

By incorporating entanglement effects, one could study interfacial slip phenomena at entangled polymeric interfaces. Interfacial slip and slip suppression phenomena by copolymers at the interface, which entangle into the bulk phases are some of the possible extensions of the research outlined in this work. In the context of ternary polymer blends, with the inclusion of slip-link model [162] or other *entanglement mimicking* models, one could carry out a detailed analysis of shear-induced phase transitions in entangled bicontinuous phases. In the context of block copolymer systems, inclusion of entanglements could change their rheology dramatically. For instance, rheological phenomena of a lamellar system with entangled loops and bridges could be quite different from that observed in unentangled systems.

8.2.2 Transients

Further future work could be done on enabling the SCBD algorithm to be able to capture transient dynamical phenomena in polymeric systems. The self-consistent Brownian dynamics algorithm in its current form uses phenomenological prescriptions for the evolution of self-consistent potentials and velocity profiles to their steady state values. Hence, the unsteady-state, real time behavior is not captured in SCBD. One possible future work could be in the identification of a relation between the phenomenological parameters in the algorithm (like $\Gamma_1, \Gamma_2, \epsilon$ etc.), such that, they correspond to the real-time evolution of the system. This would enable us to perform a quantitative

comparison of various properties such as stress relaxation, domain relaxation behavior etc.

In ternary polymer blends, transient rheological measurements of bi-continuous microemulsion phases could be made possible. For instance, the development of stress overshoot and decay in different regimes of morphology development could be characterized. Moreover, transient morphology development has been observed in experiments, with a development of a *double-streak* pattern on flow inception, evolving into a single streak pattern [146]. Hence, a detailed analysis of both transient morphology and rheology could be effected

In block copolymer systems, a transient study could shed light on the time evolution of change in copolymer orientation. Computational study of such systems are extremely difficult to perform and to our knowledge, never been attempted. However, they would provide us with enormous information from a molecular viewpoint, which in turn can be used to develop better theories and models predicting their behavior.

8.2.3 Parallelization of Algorithm To Enable 3D Simulations

All our SCBD simulations studying various polymeric systems have been performed either in 1D or 2D. The polymer density required for performing SCBD simulations prove too expensive in three dimensions with the computational power available today. Another possible future work, would be enabling three dimensional simulations by parallelizing the SCBD algorithm. In view of the single-chain framework employed in SCBD, wherein different

chains do not interact with each other, its parallelization is rendered straightforward using algorithms such as MPI. Again the implementation of three dimensional simulations would enable one to perform a quantitative comparison with experiments.

After the implementation of the above mentioned improvements to the self-consistent Brownian dynamics algorithm, it could be used to study a variety of phenomena previously inaccessible. In the context of binary polymer blends, it would allow for the study of capillary wave fluctuations of polymer blend interfaces. Thermally driven, density fluctuations along the polymer interfaces are termed capillary fluctuations. Capillary fluctuations [163], unlike critical fluctuations can survive deep into the two phase region and influence quantities such as interfacial width and interfacial tension. Such effects are largely unclear and extremely difficult to study in experiments. However, a three dimensional simulation would enable to quantify not only the capillary fluctuations, but also the effect of external shear flow on capillary wave fluctuations. In the context of polymer droplets under shear, a three dimensional simulation opens up the study of a variety of phenomena in such systems. For instance, a two dimensional droplet deforms continuously under shear without breakup. However, a three dimensional droplet breakup into daughter droplets under high shear [83, 88, 89, 97, 114]. We could perform both droplet breakup and coalescence studies in a 3D system. Furthermore, by incorporating 3D and transients into SCBD, one will be able to quantify effects like droplet widening in the vorticity direction [99], time evolution of droplet breakup and

coalescence [58] and validate the predictions of drainage times and the effect of copolymer characteristics on drainage times and eventual coalescence [58]. Finally, in the context of block copolymer lamellar systems, a three dimensional study of lamellar phases would enable the visualization of reorientation [8, 10, 11, 34] of these lamellar phases under shear.

8.2.4 Model Development

As mentioned before, an ambitious goal in the theoretical understanding of *multicomponent polymer dynamics* is the development of continuum models that could successfully couple polymer thermodynamics and their rheology. Pioneering work by various researchers have given rise to successful viscoelastic models [51, 164], such as the *two-fluid model*, for phase separated polymeric systems. However, such models do suffer from various shortcomings. As mentioned before, one of the main drawbacks of such approaches is the neglect of molecular deformations and their interplay with the thermodynamics and system rheology. Advances in coarse-grained computational methods have opened up a window of possible research at understanding flow-thermodynamics interplay from a molecular perspective [80, 103]. One of the possible future research direction would be to recast such interplay in the form of constitutive equations that could be employed with viscoelastic models such as the two-fluid models in order to overcome the drawbacks in their current form.

Bibliography

[1] W. Zheng and Z. G. Wang, *Macromolecules* **28**, 7215 (1995).

[2] S. F. Edwards, *Proc. Phys. Soc. (London)* **85**, 613, (1965).

[3] E. Helfand, *J. Chem. Phys.* **62**, 999 (1975).

[4] L. Leibler, *Macromolecules* **13**, 1602 (1980).

[5] K. Freed, *Renormalization Group Theory of Macromolecules*; Wiley, New York, 1987.

[6] A. K. Khandpur, S. Forster, F. S. Bates, I. W. Hamley, A.J. Ryan, W. Bras, K. Almdal, K. Mortensen, *Macromolecules* **28**, 8796 (1995).

[7] L. Levitt, C. W. Macosko and S. D. Pearson, *Polym. Eng. Sci.* **36**, 1647 (1996).

[8] L. Wu, T. P. Lodge and F. S. Bates, *J. Rheol.* **49**, 1231 (2005).

[9] M. E. Cates and S. T. Milner, *Phys. Rev. Lett.* **62**, 1856 (1989).

[10] K. A. Koppi, M. Tirrell, F. S. Bates, K. Almdal and R. H. Colby, *J. Phys. II* **2**, 1941 (1992).

[11] K. I. Winey, H. H. Patel, R. G. Larson and H. Watanabe, *Macromolecules* **26**, 2542 (1993).

[12] K. I. Winey, H. H. Patel, R. G. Larson and H. Watanabe, *Macromolecules* **26**, 4313 (1993).

[13] K. Binder and M. Muller, *Curr. Opin. Colloid Interface Sci.* **5**, 315 (2000).

[14] M. Murat, G. S. Grest and K. Kremer, *MRS Bull.* **22**, 27 (1997).

[15] Y. Oono and S. Puri *Phys. Rev. Lett.* **58**, 836 (1987); *Phys. Rev. A* **38**, 434 (1988).

[16] Y. Oono and Y. Shiwa *Mod. Phys. Lett. B* **1**, 49 (1987).

[17] F. E. Caputo, W. R. Burghardt, K. Krishnan, F. S. Bates and T. P. Lodge, *Phys. Rev. E* **66**, 041401 (2002).

[18] G. Patzold and K. Dawson *Phys. Rev. E* **54**, 1669 (1996).

[19] I. C. Sanchez and R. H. Lacombe, *Macromolecules* **11**, 1145 (1978).

[20] P. J. Flory, *Principles of Polymer Chemistry* Cornell University Press, Ithaca, 1953.

[21] G. S. Grest, M. D. Lacasse and M. Murat, *MRS Bull.* **22**, 27 (1997); K. Binder *Monte Carlo and Molecular Dynamics Simulations in Polymer Science;* Oxford University Press, New York, 1995.

[22] K. Kremer and F. Muller-Plathe *MRS Bull.* **26**, 205 (2001)..

[23] T. W. Liu, *J. Chem. Phys.* **90**, 5826 (1989).

[24] P. E. Rouse, *J. Chem. Phys.* **21**, 1272 (1953).

[25] M. Somasi, B. Khomami, N. J. Woo, J. S. Hur and E. S. G. Shaqfeh *J. Non-Newtonian Fluid Mech.* **108**, 227 (2002).

[26] E. Van Hemelrijck, P. Van Puyvelde, C. W. Macosko and P. Moldenaers, *J. Rheol.* **49**, 783 (2005).

[27] D. R. Paul and C. B. Bucknall, *Polymer Blends*, Wiley, New York, 2000.

[28] C. W. Macosko, *Macromol. Symp.* **149**, 171 (2000).

[29] S. P. Lyu, F. S. Bates, and C. W. Macosko, *Aiche J.* **48**, 7 (2002).

[30] Z. R. Chen and J. A. Kornfield, *Polymer* **39**, 4679 (1998).

[31] I. W. Hamley, *J. Phys.-Condes. Matter* **13**, R643–R671 (2001).

[32] T. Tepe, D. A. Hajduk, M. A. Hillmyer, P. A. Weimann, M. Tirrell, F. S. Bates, K. Almdal, and K. Mortensen, *J. Rheol.* **41**, 1147 (1997).

[33] U. Wiesner, *Macromol. Chem. Phys.* **11**, 3319 (1997).

[34] M. E. Vigild *et al*, *Macromolecules* **34**, 951 (2001).

[35] M. L. Fernandez, J. S. Higgins and S. M. Richardson, *J. Mat. Proc. Tech.* **56**, 807 (1996).

[36] I. A. Hindawi, J. S. Higgins and R. A. Weiss, *Polymer* **33**, 2522 (1992).

[37] W. Soontaranun, J. S. Higgins and T. D. Papathanasiou, *Fluid Phase Equilibria* **121**, 273 (1996).

[38] F. S. Bates *et al*, *Macromolecules* **35**, 4685 (2002).

[39] R. B. Bird, C. F. Curtiss, R. C. Armstrong, and O. Hassager, *Dynamics of Polymeric Liquids: Vol.2: Kinetic Theory* (Wiley, New York, 1987).

[40] M. Doi and S. F. Edwards, *The Theory of Polymer Dynamics* (Oxford University Press, Oxford, 1986).

[41] M. W. Matsen and M. Schick, *Phys. Rev. Lett.* **72**, 2660 (1994).

[42] G. H. Fredrickson, V. Ganesan and F. Drolet, *Macromolecules* **35**, 16 (2002).

[43] M. W. Matsen, *Phys. Rev. Lett.* **74**, 4225 (1995); M. W. Matsen, *Macromolecules* **28**, 5765 (1995).

[44] M. W. Matsen, *J. Chem. Phys.* **106**, 7781 (1997); H. Y. Chen and G. H. Fredrickson, *J. Chem. Phys.* **116**, 1137 (2002).

[45] H. C. Ottinger, *Stochastic Processes in Polymeric Fluids* (Springer, Berlin, 1996).

[46] Y. Masubachi *et al.*, *J. Chem. Phys.* **115**, 4387 (2001).

[47] J. T. Padding and W. J. Briels, *J. Chem. Phys.* **117**, 925 (2002).

[48] M. Doi and J. Takimoto, *Philos. Trans. Roy. Soc. Lond. A* **361**, 641 (2003).

[49] R. M. Jendrejack *et al.*, *J. Chem. Phys.* **120**, 2513 (2004).

[50] J. G. E. M. Fraaije, *J. Chem. Phys.* **99**, 9202 (1993); H. Hasegawa and M. Doi, *Macromolecules* **30**, 3086 (1997).

[51] M. Doi and A. Onuki, *J. Phys. II* **2**, 1631 (1992); S. T. Milner, *Phys. Rev. E* **48**, 3674 (1993); G. H. Fredrickson, *J. Chem. Phys.* **117**, 6810 (2002).

[52] T. Shima *et al.*, *Macromolecules*, **36**, 9199 (2003).

[53] Y. Schnidman, D. Gersappe, Personal Communication.

[54] V. Ganesan and V. Pryamitsyn, *J. Chem. Phys.* **118**, 4345 (2003).

[55] F. Brochard-Wyart and P. G. deGennes, *C. R. Acad. Sci. Ser. II* **310**, 1169 (1990).

[56] J. L. Goveas and G. H. Fredrickson, *Eur. Phys. J. B* **2**, 79 (1998).

[57] T. P. Lodge and M. C. Dalvi, *Phys. Rev. Lett.* **75**, 657 (1995); M. E. Vigild, C. Chu, M. Sugiyama, K. A. Chaffin, and F. S. Bates, *Macromolecules* **34**, 951 (2001).

[58] J. W. Ha, Y. Yoon and L. G. Leal, *Phys. Fluids* **15**, 849 (2003).

[59] S. T. Milner and H. W. Xi, *J. Rheol.* **40**, 663 (1996).

[60] N. Clarke and T. C. B. McLeish, *Phys. Rev. E* **57**, R3731 (1998).

[61] N. Clarke and T. C. B. McLeish, *Macromolecules* **32**, 4447 (1999).

[62] L. A. Utracki and M. R. Kamal, *Polym. Eng. Sci.* **22**, 96 (1982); L. A. Utracki, *Poly. Eng. Sci.* **23**, 602 (1983).

[63] C. D. Han and T. C. Yu, *J. Appl. Polym. Sci.* **15**, 1163 (1971); C. D. Han and T. C. Yu, *Polym. Eng. Sci.* **12**, 81 (1972).

[64] L. A. Utracki, *J. Rheol.* **35**, 8 (1991).

[65] de Gennes, P. G. *C. R. Acad. Sci. Paris, Ser. B* **288**, 219 (1979).

[66] S. Barsky and M. O. Robbins, *Phys. Rev. E* **63**, 021801 (2001).

[67] R. Zhao and C. W. Macosko, *J. Rheol.* **46**, 145 (2002).

[68] Y. C. Lam *et al*, *J. Rheol.* **47**, 795 (2003).

[69] M. P. Allen and D. J. Tildesley, *Computer Simulation of Liquids* (Oxford University Press, Oxford, 1987).

[70] M. Bousmina, J. F. Palierne and L. A. Utracki *Polym. Eng. and Sci.*, **39**, 1049 (1999).

[71] P. G. de Gennes, *C. R, Acad. Sci., Ser. II: Mec., Phys., Chim., Astron.* **308**, 1401 (1989); F. Brochard, P. G. de Gennes, S. Troian, *C. R, Acad. Sci., Ser. III:* **310**, 1169 (1990).

[72] L. Levitt and C. W. Macosko, *Macromolecules* **32**, 6270 (1999).

[73] U. Sundararaj and C. W. Macosko, *Macromolecules* **28**, 2647 (1995).

[74] S. Lyu, T. D. Jones, F. S. Bates and C. W. Macosko, *Macromolecules* **35**, 7845 (2002).

[75] S. T. Milner, *Macromolecules*, **24**, 3704 (1991).

[76] G. H. Fredrickson and P. Pincus, *Langmuir*, **7**, 786 (1991).

[77] J. Blawzdzeiwicz, E. Wajnryb and M. Loewenberg, *J. Fluid Mech.* **29**, 395, (1999).

[78] S. D. Hudson *et al*, *Macromolecules* **33**, 371 (2000).

[79] K. Binder, in *Computational Modeling of Polymers*, edited by J. Bicerano (Springer, berlin, 1992); K. Kremer, in *Soft and Fragile Matter: Nonequilibrium Dynamics, Metastability and Flow*, edited by M. E. Cates and M. R. Evans (IOP Publishing, Edinburgh, 2000).

[80] R. D. Groot and P. B. Warren, *J. Chem. Phys.* **107**, 4423 (1997).

[81] A. K. Chesters, *Trans. Inst. Chem.* **69**, 259 (1991).

[82] W. J. Milliken, H. A. Stone and L. G. Leal, *Phys. Fluids A* **5**, 69 (1993).

[83] W. J. Milliken and L. G. Leal, *J. Colloid Interface Sci.* **166**, 275 (1993).

[84] X. Li and C. Pozrikidis, *J. Fluid Mech.* **341**, 165 (1997).

[85] S. Yon and C. Pozrikidis, *Computers and Fluids* **27**, 879 (1998).

[86] Y. T. Hu and A. Lips, *Phys. Rev. Lett.* **91**, 044501 (2003).

[87] C. D. Eggleton, Y. P. Pawar and K. J. Stebe, *J. Fluid Mech.* **385**, 79 (1999).

[88] H. A. Stone and L. G. Leal, *J. Fluid Mech.* **220**, 161 (1990).

[89] Y. T. Hu, D. J. Pine and L. G. Leal, *Phys. of Fluids* **12**, 3 (2000).

[90] J. J. M. Janssen, A. Boon and W. G. M. Agterof, *AICHE. J.* **43**, 1436 (1997).

[91] R. A. De Bruijn, *Chem. Eng. Sci.* **48**, 277 (1993).

[92] A. Williams, J. J. M. Janssen and A. Prins, *Colloid Surf., A* **125**, 189 (1997).

[93] J. M. Rallison, *Ann. Rev. Fluid Mech.* **16**, 45 (1984).

[94] P. L. Maffettone and M. Minale, *J. Non-Newtonian Fluid Mech.* **78**, 227 (1998).

[95] F. Greco, *J. Non-Newtonian Fluid Mech.* **107**, 111 (2002).

[96] Y. Y. Renardy, M. Renardy and V. Cristini, *Euro. J. Mech. B* **21**, 49 (2002).

[97] U. Sundararaj and C. W. Macosko, *Macromolecules* **28**, 2647 (1995).

[98] L. Levitt and C. W. Macosko, *Pol. Eng. Sci.* **36**, 1647 (1996).

[99] H. K. Jeon and C. W. Macosko, *Polymer* **44**, 5381 (2003).

[100] C. Pozrikidis, *J. Fluid Mech.* **37**, 601 (1969).

[101] D. Gersappe and A. C. Balazs, *Phys. Rev. E* **52**, 5061 (1995); M. S. Lee, T. P. Lodge and C. W. Macosko, *J. Pol. Sci. B* **35**, 2835 (1997).

[102] L. Levitt and C. W. Macosko, *Macromolecules* **32**, 6270 (1999).

[103] B. Narayanan, V. A. Pryamitsyn and V. Ganesan, *Macromolecules* **37**, 10180 (2004).

[104] L. Leibler, *Makromol. Chem., Macromol. Symp.* **16**, 1 (1988).

[105] J. C. Lepers and B. D. Favis, *AICHE. J.* **45**, 887 (1999).

[106] P. L. Maffettone and F. Greco, *J. Rheol.* **48**, 83 (2004).

[107] S. Chen, N. Phan-Thien, X. J. Fan and B. C. Khoo, *J. Non-Newtonian Fluid Mech.* **118**, 65 (2004).

[108] Z. G. Wang and S. A. Safran, *J. Chem. Phys.* **94**, 679 (1991).

[109] K. M. Palmer and D. C. Morse, *J. Chem. Phys.* **105**, 11147 (1996).

[110] V. Ganesan and G. H. Fredrickson, *Europhys. Lett.* **55**, 814 (2001).

[111] E. Helfand and Y. Tagami, *J. Pol. Sci., Pol. Lett.* **9**, 741 (1971).

[112] D. Duchs *et al.*, *Macromolecules* **36**, 9237 (2003).

[113] G. I. Taylor, *Proc. R. Soc. A* **138**, 41 (1932).

[114] A. J. Wagner, L. M. Wilson and M. E, Cates, *Phys. Rev. E* **68**, 045301 (2003).

[115] H. Zhou and C. Pozrikidis, *Phys. Fluids A* **5**, 311 (1993).

[116] P. Van Puyvelde, S. Velankar and P. Moldenaers, *Current Opinion in Colloid and Interface Sci.* **6**, 457 (2001).

[117] P. Van Puyvelde, S. Velankar, J. Mewis and P. Moldenaers, *Pol. Eng. Sci.* **42**, 1956 (2002).

[118] P. Van Puyvelde, S. Velankar, J. Mewis and P. Moldenaers, *J. Rheol.* **45**, 1007 (2001).

[119] W. R. Schowalter, C. E. Chaffey and H. Brenner, *J. Colloid and Interface Sci.* **26**, 152 (1968).

[120] S. H. Anastasiadis *et al.*, *Macromolecules* **22**, 1449 (1989).

[121] M. W. Matsen, *J. Chem. Phys.* **110**, 4658 (1998).

[122] V. Sibillo, S. Guido, F. Greco and P. L. Maffettone, *Macromol. Symposia* **228**, 31 (2005).

[123] S. T. Milner, *J. Rheol.* **40**, 303 (1996); J. Descloizeaux, *Europhys. Lett.* **5**, 437 (1988).

[124] M. Doi and T. Ohta, *J. Chem. Phys.* **95**, 1242 (1991).

[125] P. Van Puyvelde, S. Velankar, J. Mewis and P. Moldenaers, *J. Rheol.* **48**, 725 (2004).

[126] P. Van Puyvelde *et al.*, *Pol. Eng. Sci.* **43**, 71 (2003).

[127] J. G. Oldroyd, *Proc. R. Soc. Lond. A* **232**, 567 (1955).

[128] J. Yamamoto and H. Tanaka, *Phys. Rev. Lett.* **77**, 4390 (1996).

[129] H. F. Mahjoub, C. Bourgaux, P. Sergot and M. Kleman, *Phys. Rev. Lett.* **81**, 2076 (1998).

[130] K. Krishnan, K. Almdal, T. P. Lodge, F. S. Bates and W. R. Burghardt, *Phys. Rev. Lett.* **87**, 098301/1 (2001).

[131] S. W. Marlow and P. D. Olmsted, *Eur. Phys. J. E* **8**, 485 (2002).

[132] K. Krishnan, K. Almdal, T. P. Lodge, F. S. Bates, B. Chapman and W. R. Burghardt, *J. Rheol.* **46**, 529 (2002).

[133] S. Rudiger, *Eur. Phys. J. E* **17**, 45 (2005).

[134] G. H. Fredrickson and E. Helfand, *J. Chem. Phys.* **87**, 697 (1987).

[135] G. H. Fredrickson and F. S. Bates, *J. Pol. Sci. B* **35**, 2775 (1997).

[136] F. S. Bates, W. W. Maurer, P. M. Lipic, M. A. Hillmyer, K. S. Almdal, K. Mortensen, G. H. Fredrickson, J. F. Berret and D. C. Roux, *Phys. Rev. Lett.* **79**, 849 (1997).

[137] M. A. Hillmyer, W. W. Maurer, T. P. Lodge, F. S. Bates and K. Almdal, *J. Phys. Chem. B* **103**, 4814 (1999).

[138] M. W. Matsen, *J. Chem. Phys.* **110**, 4658 (1999).

[139] L. Keilhorn and M. Muthukumar, *J. Chem. Phys.* **107**, 5588 (1997).

[140] T. L. Morkved, P. Stepanek, K. Krishnan, F. S. Bates and T. P. Lodge, *J. Chem. Phys.* **114**, 7247 (2001).

[141] L. E. Scriven, *Nature (London)* **263**, 123 (1976).

[142] N. R. Washburn, T. P. Lodge and F. S. Bates, *J. Phys. Chem. B* **104**, 6987 (2000).

[143] A. N. Semenov, *Langmuir* **11**, 3560 (1995); J. R. Naughton and M. W. Matsen, *Macromolecules* **35**, 8926 (2002).

[144] J. Noolandi and K. M. Hong, *Macromolecules* **17**, 1531 (1984); L. Leibler, *Makromol. Chem., Makromol. Symp.* **16**, 1 (1988).

[145] A. N. Semenov, *Macromolecules* **25**, 4967 (1992).

[146] K. Krishnan, W. R. Burghardt, T. P. Lodge and F. S. Bates *Langmuir* **18**, 9676 (2002).

[147] B. Narayanan, V. Pryamitsyn and V. Ganesan, *Phys. Rev. Lett.* **96**, 028302-1 (2006).

[148] T. Ohta, Y. Enomoto, J. L. Harden and M. Doi, *Macromolecules* **26**, 4928 (1993).

[149] S. Komura and J. Fukuda, *Phys. Lett. A* **208**, 108 (1995).

[150] Y. Bohbot-Raviv and Z. G. Wang, *Phys. Rev. Lett.* **85**, 3428 (2000).

[151] Z. Zhang, H. Zhang and Y. Yang, *J. Chem. Phys.* **115**, 7783 (2001).

[152] W. H. Press, W. T. Vetterling, S. A. Teukolsky and B. P. Flannery, *Numerical Recipes in Fortran* Cambridge University Press, 1988.

[153] Z. G. Wang, *J. Chem. Phys.* **117**, 481 (2002).

[154] F. S. Bates and G. H. Fredrickson, *Phys. Today* 32, Feb 1999.

[155] A. Keller, E. Pedemonte and F. M. Willmouth, *Colloid Polym. Sci.* **25**, 238 (1970); M. J. Folkes, A. Keller and F. P. Scalisi, *Colloid Polym. Sci.* **1**, 251 (1973).

[156] R. J. Albalak and E. L. Thomas, *J. Polym. Sci: Polym. Phys.* **31**, 3766 (1993).

[157] V. Ganesan and G. H. Fredrickson, *J. Rheol.* **45**, 161 (2001).

[158] R. Car and M. Parrinello, *Phys. Rev. Lett.* **55**, 2471 (1985).

[159] G. H. Fredrickson, *J. Rheol.* **38**, 1045 (1994).

[160] A. Johner and J. F. Joanny, *Macromolecules* **24**, 5299 (1990).

[161] B. Narayanan and V. Ganesan, *Phys. of Fluids.* **18**, 042109 (2006).

[162] C. C. Hua and J. D. Schieber, *J. Chem. Phys.* **109**, 10018 (1998).

[163] K. Binder, M. Muller, F. Schmid and A. Werner, *Adv. in Colloid and Interface Sci.* **94**, 237 (2001).

[164] E. Helfand and G. H. Fredrickson, *Phys. Rev. Lett.* **62**, 2648 (1989).

Vita

Bharadwaj Narayanan was born in Chennai, TamilNadu, India, on 24 July 1979, the son of Mr. Thiruvengadasami Narayanan and Aruna Narayanan. He graduated from Padma Seshadri Bala Bhavan Senior Secondary School in the summer of 1996. He was accepted into the undergraduate program in Engineering at the Indian Institute of Techonology (Chennai), in the fall of 1997, from where he received the Bachelor of Technology degree (equivalent to the Bachelor of Science degree) in Chemical Engineering in July 2001. He was accepted and started his graduate program in Chemical Engineering at The University of Texas at Austin, in spring of 2002. He passed his preliminary defense in March 2004 and was later enrolled in doctoral candidacy.

Permanent address: 6 Jawahar St
K. K. Nagar (west)
Madras, Tamilnadu 600072, India

This dissertation was typeset by the author.